Flexible operation of grid-interfacing converters in distribution networks : bottom-up solutions to voltage quality enhancement

Flexible Operation of Grid-Interfacing Converters in Distribution Networks:
Bottom-up Solutions to Voltage Quality Enhancement

Fei Wang

Flexible Operation of Grid-Interfacing Converters in
Distribution Networks: Bottom-up Solutions
to Voltage Quality Enhancement

PROEFSCHRIFT

ter verkrijging van de graad van doctor aan de
Technische Universiteit Eindhoven, op gezag van de
rector magnificus, prof.dr.ir. C.J. van Duijn, voor een
commissie aangewezen door het College voor
Promoties in het openbaar te verdedigen
op maandag 29 november 2010 om 16.00 uur

door

Fei Wang

geboren te Jiangxi, China

Dit proefschrift is goedgekeurd door de promotor:

prof.dr. E.A. Lomonova MSc

Copromotoren:
ir. M.A.M. Hendrix
en
dr. J.L. Duarte

To Yan and my parents

Abstract

Flexible Operation of Grid-Interfacing Converters in Distribution Networks: Bottom-up Solutions to Voltage Quality Enhancement

Due to the emerging application of distributed generation (DG), large numbers of DG systems are expected to deliver electricity into the distribution network in the near future. For the most part these systems are not ready for riding through grid disturbances and cannot mitigate unwanted influences on the grid. On the one hand, with the increasing use of sensitive and critical equipment by customers, the electricity network is required to serve high voltage quality. On the other hand, more and more unbalanced and nonlinear equipment, including DG units, is negatively affecting the power quality of distribution networks. To adapt to the future distribution network, the tendency for grid-interfacing converters will be to integrate voltage quality enhancement with DG functionality.

In this thesis, the flexible operation of grid-interfacing converters in distribution networks is investigated for the purpose of voltage quality enhancement at both the grid and user sides. The research is carried out in a bottom-up fashion, from the low-level power electronics control, through the realization of individual system functionality, finally arriving at system-level concepts and implementation.

Being essential to the control of grid-interfacing converters, both stationary-frame techniques for voltage detection and synchronization in disturbed grids, and asymmetrical current regulation are investigated. Firstly, a group of high performance filters for the detection of fundamental symmetrical sequences and harmonics under various grid conditions is proposed. The robustness of the proposed filters to small grid-frequency variation and their adaptability to large frequency change are discussed. Secondly, multiple reference frame current regulation is explored for dealing with unbalanced grid conditions. As a complement to the existing proportional resonant (PR) controllers, sequence-decoupled resonant (SDR) controllers are proposed for regulating individual symmetric sequences. Based on the modeling of a four-leg grid-connected system in different reference frames, three types of controllers, i.e. PI, PR, and proportional plus SDR controllers are compared.

Grid-interactive control of distributed power generation, i.e. voltage unbalance

compensation, grid-fault ride-through control and flexible power transfer, as well as the modeling of harmonic interaction, are all investigated. The in-depth study and analysis of these grid interactions show the grid-support possibilities and potential negative impact on the grid of inverter-based DG units, beyond their primary goal of power delivery.

In order to achieve a co-operative voltage unbalance compensation based on distributed DG systems, two control schemes, namely voltage unbalance factor based control and negative-sequence admittance control, are proposed. The negative-sequence voltages at the grid connection point can be compensated and mitigated by regulating the negative-sequence currents flowing between the grid and DG converters.

Flexible active and reactive power control during unbalanced voltage dips is proposed that enables DG systems to enhance grid-fault ride-through capability and to adapt to various requirements for grid voltage support. By changing adaptable weighting factors, the compensation of oscillating power and the regulation of grid currents can be easily implemented. Two joint strategies for the simultaneous control of active and reactive power are derived, which maintain the adaptive controllability that can cope with multiple constraints in practical applications. The contribution of zero-sequence currents to active power control is also analyzed as a complement to the proposed control, which is based on positive- and negative-sequence components.

Harmonic interaction between DG inverters and the grid is modeled and analyzed with an impedance-based approach. In order to mitigate the harmonic distortion in a polluted grid, it is proposed to specify output impedance limits as a design constraint for DG inverters. Results obtained from modeling, analysis, and simulations of a distribution network with aggregated DG inverters, show that the proposed method is a simple and effective way for estimating harmonic quasi-resonance problems.

By integrating these proposed control strategies in a modified conventional series-parallel structure, we arrived at a group of grid-interfacing system topologies that is suitable for DG applications, voltage quality improvement, and flexible power transfer. A concrete laboratory system details the proposed concepts and specifies the practical problems related to control design. The introduction of multi-level control objectives illustrates that the proposed system can ride through voltage disturbances, can enhance the grid locally, and can continue the power transfer to and from the grid while high voltage quality is maintained for the local loads within the system module. A dual-converter laboratory set-up was built, with which the proposed concepts and practical implementation have been fully demonstrated.

Contents

IV   System-level concepts and implementation   167

8   Converter systems with enhanced voltage quality   169

V   Closing   197

9   Conclusions and recommendations   199

VI   Appendices   207

A   Derivation of decoupling transformation matrix   209

B   Power calculation of zero-sequence components   213

Part I

Background and motivation

Chapter 1

Introduction

Grid-interfacing converters, as the name indicates, are power electronic systems that interface electrical loads and distributed generation to the grid. The interface refers to the connection point between the grid and the added systems, where voltage/current interactions and power exchange are dependent on the hardware and the software of the grid-interfacing converters.

Therefore, by choosing appropriate circuit topologies, optimally configured system functionality and implementing smart control strategies, grid-interfacing converters are expected to maintain good voltage quality for the local loads under various grid conditions, enhance the grid locally at the connection point, and achieve reliable power transfer. The flexible operation of grid-interfacing converters will facilitate the integration of distributed generation into the future distribution network and will provide alternative solutions to voltage quality enhancement. From this broad perspective, the goals of the research that this thesis aims at will be formulated in the following sections.

1.1 Distributed generation in power systems

Distributed generation (DG) refers to an electric power source connected directly to the distribution network or to the customer side of the meter [1, 2]. It includes:

- Generators powered from renewable energy sources (except large-scale hydro and wind farms);

- Combined heat and power (CHP) systems, also known as co-generation;

- Grid connected generators operating at standby, particularly when centralized generation is inadequate or expensive.

Most DG systems are installed in distribution networks where they introduce bi-directional power flow, breaking the traditional one-way power flow from the high to the low voltage network in the centralized power system.

A basic requirement in connecting any generator to a power system is that it must not adversely affect the quality of electricity supplied to other customers on the network [1]. Although significantly increasing number of DG systems are expected to deliver electricity into the grid in the near future, they might not offer the desired voltage quality level automatically. So far, conventional grid-interfacing techniques are not ready for riding through grid disturbances and for mitigating unwanted influence on the grid. On the contrary, with increasing grid-connected application of renewable energy sources, combined DG systems may cause power quality problems [3].

Due to the power injection from DG to the grid, the resulting voltage drop on the feeder impedance will lead to steady-state voltage rise when there are no loads or the loads located close to the DG systems consume less power than supplied by the DG systems.

Consequently, asymmetrical distribution of single-phase DG systems will cause voltage unbalance in the grid. Ideally, a large number of single-phase DG systems would be evenly distributed among the three-phase feeders and therefore no voltage unbalance problems should occur. In practice, any difference will cause voltage imbalance.

Moreover, the DG system also introduces harmonic currents and causes voltage distortion at the grid connection point. More and more electrical loads as well as the DG systems are designed based on high-frequency power electronic converters, which can reduce the system size and cost. However, more harmonic components are produced and the harmonic interactions within the grid are also aggravated.

Because of the rapid variation of active or reactive power flow from DG systems such as wind turbines or solar farms, voltage fluctuations can appear in the grid. As a consequence, flicker problems (an impression of unsteadiness of the visual sensation) can be observed in lighting systems [4].

Another important concern is that, following a grid disturbance such as the tripping of a large generator or a voltage dip due to grid faults in a neighbor feeder, many DG systems will be disconnected from the grid. This situation will aggravate the shortage of power generation and make the matter of grid frequency control more complicated.

In order to adapt to future emerging applications of DG systems, they should be used for the enhancement of low voltage grid through grid-interfacing converters with flexible power/current control.

1.2   Conventional power quality enhancement

Besides the influence of DG on the grid, unbalanced or nonlinear loads also introduce power quality problems. Details on power quality phenomena at the point of connection to the grid have been studied and reported in [3].

To deal with voltage quality problems, many existing power quality compensation technologies have been reported in the literature [5–13]. They are applied either by grid operators to improve the quality of the supplied voltage, or by customers to protect critical loads from grid disturbances and to prevent harmonic

currents from flowing into the grid. As will be explained in the next section, there are different types of applications of compensators.

1.2.1 Specialized power quality compensators

Compensators for harmonics

Harmonic problems are introduced by distorted grid voltages and/or caused by harmonic currents from nonlinear loads (including DG). Hence, compensation systems for harmonics should be installed in between the grid and the loads to isolate the influence of harmonic components from each other.

Fig. 1.1 shows several commonly used methods for harmonic compensation. Because of the variety of practical systems, the blocks simply remind a collection of components instead of concrete circuit diagrams. It should be noticed that isolation/step-up transformers, which may be required according to the application, are not indicated. The same remarks apply to other block diagrams in this chapter.

To protect the grid from current harmonics introduced at the user side, in Fig. 1.1 (a) passive filters or in Fig. 1.1 (b) front-end power converters can be used to isolate the electrical loads. Otherwise, as shown in Fig. 1.1 (c) additional shunt-connected active power filters can be installed close to nonlinear loads to filter out the harmonic components from the grid current [5].

When the grid voltages are distorted, series-connected active power filters can be used to compensate the harmonic voltages of the grid, thereby maintaining sinusoidal voltages at the connection point of the loads, as shown in Fig. 1.1 (d). Besides these individual compensators, hybrid compensators, which are the combination of series-/shunt-connected active power filters and passive filters, are employed to optimize the filtering performance and the cost of entire systems [6].

Compensators for unbalanced voltages

To compensate voltage unbalance, which is mainly resulted by unbalanced distribution of loads or comes from upstream grids, two types of compensators can be used to protect the end-user loads. The shunt-connected converter in Fig. 1.1 (c) can be used. However, this regulates the voltage at the grid connection point by injecting reactive currents that introduce voltages across the grid impedance for compensating unbalanced voltages [7]. It should be noticed that this way of compensation will be ineffective when the grid impedance is too low, or requires active power when the grid impedance is dominantly resistive.

Alternatively, balanced voltages at the load side can be achieved by using a series-connected converter as shown in Fig. 1.1 (d), where it injects negative-sequence or zero-sequence voltages to compensate the unbalanced components of the grid voltage. However, when three-phase loads are asymmetrical, due to the active power generated by symmetrical sequence components, the series-connected converter has to provide active power.
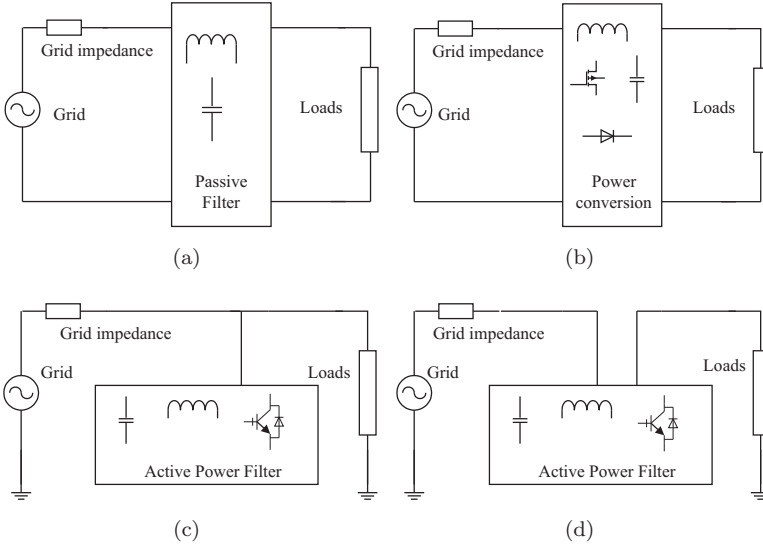
Figure 1.1: Single-line block diagrams of different compensation topologies: (a) passive filter, (b) front-end power converter, (c) shunt-connected active power filter, and (d) series-connected active power filter.

Compensators for voltage dips

The compensator for voltage dips has the same structure as the compensator used for unbalanced voltage correction. The so-called dynamic voltage restorer (DVR) is a series-connected custom power device to protect sensitive loads from adverse effects of voltage dips by injecting series voltages [8]. The static compensator (STATCOM) with shunt-connected structure is an alternative method to compensate voltage dips through providing fast reactive power injection [9]. Similarly, the drawbacks of voltage unbalance compensators are also found in these two compensation mechanisms.

In summary, the series- and shunt-connected active power filters shown in Fig. 1.1 (c) or (d) are mostly used for power quality improvement. They are specially designed for compensating certain power quality problems by either injecting current or voltage. However, it is already mentioned that in some situations both the series- and shunt-connected converters require active power to achieve the needed compensation. Unfortunately, there is no long-term active power available for these two compensators, or it is quite limited due to one or other storage method. As an alternative, systems based on multiple compensators have been proposed, of which the most comprehensive one is the unified power quality conditioner.

1.2.2   Unified power quality conditioners

A unified power quality conditioner (UPQC), as shown in Fig. 1.2, consists of two voltage source converters (VSC) sharing a common dc bus. One converter is
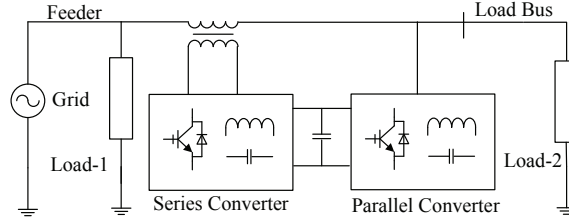
Figure 1.2: Single-line diagram of a UPQC compensated distribution system.

connected in series with the distribution feeder, while the other is connected in parallel with the same feeder. The critical load, "Load-2" on the right-hand side, requires balanced and sinusoidal voltages, and non-sensitive loads, "Load-1", are close to the grid side [11].

The main purpose of the series converter is harmonic isolation between the grid and the local distribution system. In addition, the series converter has the capability of voltage flicker and imbalance compensation, as well as voltage regulation and harmonic compensation at the grid connection point of the critical load bus in Fig. 1.2. The main purpose of the parallel converter is to absorb current harmonics, to compensate for reactive power and negative-sequence current, and to regulate the dc-bus voltage.

In such a way, the UPQC can protect the bus voltage of critical loads against unbalance, harmonics, voltage dips and other grid disturbances occurring in the distribution network. However, when the voltage of the load bus collapses to a low value, the parallel converter fails to draw the required amount of power to recharge the dc capacitor. To tackle such large voltage dips, the dc-bus capacitor can be supported by energy storage with a large power capacity, such as super-capacitors or batteries [12], or can be supplied with distributed sources [13].

1.3 Future application of grid-interfacing converters

Due to the increasing use of sensitive/critical equipment by the customers, the electricity network is continuously required to serve high power quality. It is suggested that the future direction of power quality performance standards should mention at least [14]:

- interruptions (including momentary);
- voltage dips;
- steady-state voltage regulation;
- voltage unbalance (negative sequence);
- harmonic distortion in the voltage;
- transient voltages.

On the other hand, because of the increasing use of distributed generation systems and non-linear loads, the power quality of the utility grid can also be negatively affected, as presented in Section 1.1. Taking into account all these factors associated with power quality problems, it is therefore desirable to have a
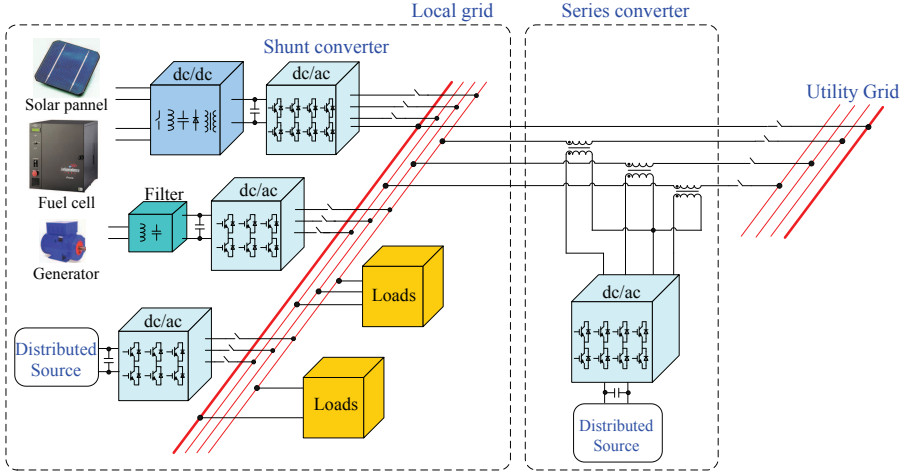
Figure 1.3: An example of future application of grid-interfacing converters for connecting multiple DG systems to the utility grid.

solution that can enhance the voltage quality at both the grid and the customer sides.

Fortunately, grid-interfacing converters have the same circuit structure as series or parallel active power filters. Being supplied with distributed sources (may also including energy storages), they have already the hardware necessary to achieve comprehensive power quality compensation.

Therefore, to adapt to emerging DG applications, it will be a tendency of grid-interfacing converters to integrate voltage quality enhancement and DG together; and besides the basic function of power delivery it will become the responsibility for DG systems to help enhancing the low voltage grid locally. For instance, ideas and considerations on the grid support via DG converters have been reported recently together with simulation results in [15].

Figure 1.3 shows an example of future application of grid-interfacing converters. Multiple DG systems are interconnected to construct a small-scale grid, also called micro-grid, which powers the loads locally and exchanges power with the utility grid through series converters. More auxiliary functions and advanced control are integrated into the system to maintain good quality voltage within the local grid and to improve the voltage quality at the grid connection point.

1.4   Background techniques

It should be remarked that, at the beginning of this thesis work, details of the power electronics control technology related to the idea of the described grid-interfacing systems had not yet received extensive attention. This gave the research flexibility in conceiving system-level concepts and subsystem functionality, but also brought the design challenges for the creation and implementation of control

methods and strategies. This section briefly introduces the background of the techniques that will be come across.

High-performance voltage detection and synchronization

For the control of grid-interfacing converters, synchronization with the grid voltage is essential. Not only the detection of grid voltages but also the separation of specific symmetric-sequence components from grid voltages should be accurately achieved under unbalanced and/or distorted conditions. In addition, though the frequency in the utility grid is usually very stable, frequency fluctuations will be caused by faults on the grid and load/generation changes, and often occur in weak grids. This problem results in system malfunctions or trips. Therefore, it is necessary to search for frequency insensitive or frequency adaptive schemes.

To synchronize with the grid, different closed-loop control algorithms have been developed based on a conventional phase-locked-loop (PLL) structure [16–18]. Alternatively, in the manner of open-loop control, symmetrical sequences at fundamental frequency can be directly derived based on delayed signal cancelation methods [19–21]. However, these approaches are usually sensitive to grid frequency change and react badly to voltage harmonics. Recently, some methods were proposed to deal with unbalanced, distorted, and variable-frequency grid conditions. A method to eliminate signals in different reference frames based on mathematical transformations [22], and a nonlinear method based on the concept of an adaptive notch filter [23] were proposed. Both methods require massive calculations.

In order to facilitate the control of grid-interfacing converters in the stationary frame, a simple, fast, and high performance stationary frame detection mechanism is required for grid voltage detection and synchronization.

Regulation of symmetrical sequence components

The design of voltage and current regulators of grid-interfacing converters are also very important for the purpose of voltage quality improvement under different grid conditions. In particular, the situation of an unbalanced grid, which can be caused by asymmetrical source impedance or loads, or grid faults, should always be taken into account. Various current controllers are therefore proposed in order to improve the transient and steady-state performance of grid-connected converters and to simplify complex control structures without compromising system performance under unbalanced grid situations.

Conventionally, three-phase quantities (voltage and current) are regulated with proportional and integral (PI) controllers in the synchronous reference frame (SRF). Adapted to unbalanced grid conditions, the well-known dual current control scheme has been applied in many applications by controlling positive-sequence and negative-sequence components separately in dual SRFs [24, 25]. The dual current control scheme is complex and requires multiple reference-frame transformations. Alternatively, the stationary-frame proportional resonant (PR) controllers were introduced to regulate ac signals without any stationary-to-synchronous transformation, while the achieved performance with PR controllers are similar to that of PI controllers

[26, 27]. Compared with PI controllers in the SRF, the complexity of control design with PR controllers under unbalanced conditions is considerably reduced.

The PR controller is suitable for regulating positive- and negative-sequence quantities together and for regulating zero-sequence quantities separately. However, there are some situations where only individual sequence quantities need to be regulated. To complement the method of PR controllers, a new stationary-frame controller for independently regulated symmetrical sequences components is desirable.

Distributed compensation for unbalanced grids

As expected in the Section 1.3, in addition to conventional delivery of electricity, more auxiliary functions for the reduction of power quality problems should be introduced into grid-interfacing converters. In [28], the capability of active filtering is integrated into an inverter-based DG unit. A control algorithm is proposed to spread the voltage-control burden over many DG units [29]. To compensate unbalance within microgrids, a reactive power-conductance droop control for regulating negative-sequence currents is distributed among inverters [30]. A similar idea for controlling negative sequence currents is presented in [31], where the control of a doubly fed induction generator system is studied. In this thesis, it is proposed to ease the responsibility of the network for voltage unbalance correction with distributed generation systems by integrating voltage unbalance correction into the control of grid-interfacing converters.

Flexible power control during voltage dips

Conventionally, a DG system would be required to be disconnected from the grid when voltage dips occur, and to be reconnected to the grid when faults are cleared. However, this requirement is changing. In order to maintain active power delivery and reactive power support to the grid, grid codes now require wind energy systems to ride through voltage dips without interruption [32] [33]. For the future scenario of a grid with significant DG penetration, it is necessary to investigate the ride-through control of wind turbine systems and other DG systems as well.

Concerning the control of DG inverters under voltage dips, especially unbalanced situations, two aspects should be noticed. Firstly, fast system dynamics and good reference tracking are necessary. Current controllers must be able to deal with all the symmetric-sequence components and to have fast feedback signals for closed-loop control. Secondly, in case of unbalanced voltage dips, the employment of different power control strategies, i.e., the generation of reference currents, is also very important.

During unbalanced voltage dips, current reference generation is constrained by trade-offs. Considering the power-electronics converter constraints, a constant dc-link voltage is desirable, [34] and [35]. On the other hand, the effects of the grid currents on the utility side should also be taken into account when assigning reference currents for DG inverters. As presented in [36] and [37], several specific strategies are proposed in order to get specific power quality levels at the grid connection point in terms of instantaneous power oscillation and current distortion.

Since voltage dips are as diverse as grid faults, there are always multiple objectives constrained by converters or by grid requirements for grid-fault ride-through control. These objectives have to be compromised and be adapted under different grid faults so as to optimize system overall performance. Therefore, a flexible power control strategy will enable grid-interfacing converters to easily adapt to different constraints under voltage dips.

Harmonic distortion impact of aggregated DG inverters

Either for auxiliary grid support or for conventional power delivery, a significant contribution to the grid side will require a collective action of many DG systems equipped with the same functionality. However, a large number of DG inverters coupled to the grid may cause harmonic interactions. As a result, the DG systems may collectively aggravate grid voltage distortion and even lead to abnormal operation of grid-connected users.

In [38], such phenomena had been observed and investigated in an existing residential grid where a large number of distributed photovoltaic (PV) inverters were installed. Previous work in [39] and [40] has already shown that inverter topologies together with control certainly influence harmonic interactions in distorted grids. Depending on the penetration levels of DG inverters and practical grid parameters, harmonic resonances can also appear at frequencies within the inverter control bandwidth. This is the frequency range of interest for which harmonic interactions of DG inverters will be studied in this work. By now, specific modeling and analysis of the harmonic interactions between DG inverters and polluted grids have not been fully explored. An analytical method is expected to be developed for understanding the problem of harmonic distortion impact on the grid.

Converter systems with enhanced voltage quality

With the above mentioned technique details, it comes to the system-level concern, that is voltage quality enhancement at both the user side and the grid side. Based on the example system in Fig. 1.3, a simplified structure that consists of only one series converter and one parallel converter in the local grid will be focused on. Similar structures used for the connection of micro-grid to electric power system have been recently reported [41–43], but the system functionalities are different from the ideas proposed in this thesis [44], which make a significant difference with respect to control objectives and implementations. Issues about system configuration, functionalities, and realization are the main points to be addressed.

1.5 Research goal and objectives

The goal of this thesis is to explore a grid-interfacing converter system that optimally combines the functions of voltage quality improvement and flexible power transfer when applying distributed generation. To achieve this goal, main research objectives are formulated as follows:
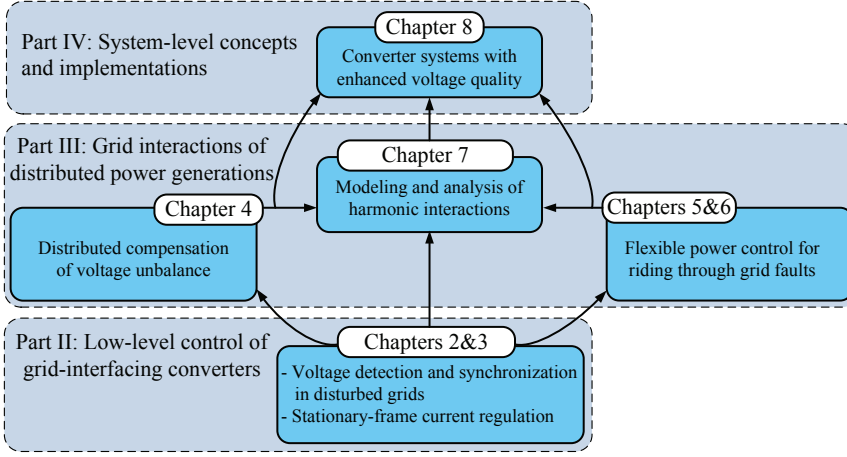
Figure 1.4: Bottom-up structure of the main research contents within the thesis.

1. **Low-level control of grid-interfacing converters**
   Research into high performance techniques for voltage detection and synchronization in disturbed grids, and into fundamental controllers suitable for dealing with unbalanced/distorted grids so as to facilitate the control design of grid-interfacing converters.

2. **Grid interaction of distributed power generation**
   • Studies on grid-support strategies of DG systems aiming at improving voltage quality at the grid side: distributed voltage unbalance compensation, grid-fault ride-through control, and flexible power transfer to the grid;
   • Modeling harmonic interaction between the grid and aggregated DG inverters with the intention to find an analysis tool for minimizing grid harmonic distortion and for estimating possible harmonic interaction problems.

3. **System modules with enhanced voltage quality**
   Integrate the proposed control methods and grid-support strategies for a dual-converter system module, and develop comprehensive system-level concepts for voltage quality enhancement at both the grid side and the user side.

4. **Realization of a laboratory set-up**
   Develop a flexible dual-converter laboratory set-up to verify the control methods and to demonstrate the system-level concepts.

1.6   Outline of the thesis

Including this introduction, the thesis consists of nine chapters. Fig. 1.4 shows the structure of the main research line. From the low-level power electronics

control, through the study of individual system functionality, and up to system-level concepts and implementations, this research work is carried out in a bottom-up manner.

Chapter 2 presents the techniques of voltage detection and synchronization in disturbed grids. As an essential part for the control of the final laboratory set-up, a group of high performance filters for the detection of fundamental symmetrical sequences and harmonics under varied grid conditions are proposed and validated by experiments.

Irrespective of specific functionality, controllers used for the inner-loop reference tracking are investigated in **Chapter 3**. These controllers are fundamental to the final system performance and overall control structure. Three types of stationary-frame current controllers, namely proportional integral (PI), proportional resonant (PR), and sequence-decoupled resonant (SDR) controllers are presented, together with the modeling of four-leg converter systems in multiple reference frames. The control design based on the PR/SDR controllers are highlighted with two practical application cases.

The low-level control presented in Chapters 2 and 4 is applied to the grid-interactive study of distributed power generation. Starting with **Chapter 4**, the distributed compensation of voltage unbalance is presented. The functionality to decrease the negative-sequence voltage at the grid connection point is added to the control of distributed generation inverters. Two compensation strategies, which are voltage unbalance factor based control and negative-sequence admittance control of DG inverters, are proposed and analyzed in detail.

In order to facilitate the fault ride-through control of DG inverters under voltage dips, **Chapter 5** first proposes a flexible active power control strategy based on positive- and negative-sequence components. This strategy enables DG inverters to be optimally designed from the perspective of both the power-electronic converters and the power system. Furthermore, the contribution of zero-sequence current to active power control is also addressed.

By including reactive power control, **Chapter 6** further investigates the power control strategies of DG inverters under unbalanced voltage dips. This is an extension of Chapter 5. With the proposed strategies, the relative amplitude of oscillating power as well as the peak values of the three-phase grid currents can be independently regulated with two individually adaptable parameters.

Chapter 7 addresses the grid harmonic distortion impact of aggregated DG inverters. An impedance-based analytical method is proposed for modeling and analysis of harmonic interactions between a polluted grid and a large number of DG inverters. In order to minimize the harmonic distortion impact on grids, the concept of specifying impedance limits as a design constraint for DG inverters is illustrated.

In **Chapter 8**, by integrating the control methods and strategies in Chapters 2 to 7, system-level concepts and implementation of voltage quality enhancement at both the user side and the grid side are specified. Adapting the conventional series-parallel structure, a couple of grid-interfacing system topologies are proposed for the purpose of DG application, voltage quality enhancement, and flexible power transfer. To detail the proposed concepts and to demonstrate the practical im-
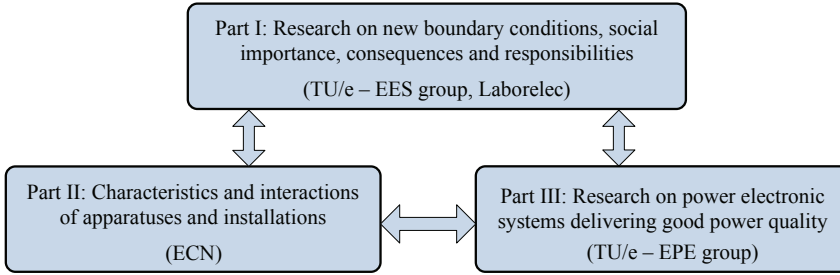
Figure 1.5: Structure of the EOS-KTI project.

plementation the final laboratory system is given; the entire system control is validated by experiments.

Finally, conclusions and recommendations are given in **Chapter 9**.

1.7   EOS-KTI project

The research presented in this thesis was performed within the framework of the "Voltage Quality of The Future Infrastructure" project, Kwaliteit van de spanning in Toekomstige Infrastructuren (KTI) in Dutch, which is part of the EOS program (Energie Onderzoek Subsidie) funded by Agentschap NL—an agency of the Dutch Ministry of Economic Affairs. The program wants to extend the knowledge concerning energy efficiency and sustainable energy in the Netherlands, which is the basis for payable, reliable and clean energy supply in the future, and covers the route from the idea until market introduction.

At Eindhoven University of Technology, including the KTI project and other 4 projects, i.e. Electrical Infrastructure of the Future (EIT), Flexible Electricity Networks (FlexibEL), Control and Reserve Power (RegelDuurzaam), and Transition Roadmap of the Energy Infrastructure in the Nederlands (TREIN), in total 7 PhD students and 2 postdoctoral researchers are involved in the EOS program.

The structure of EOS-KTI project is shown in Fig. 1.5, which consists of three parts of research activities. The first part aims at investigating the new probable boundary conditions of the electricity use and the obligation and responsibility of the society. The EES group is responsible for these aspects. Through the power quality analysis of the Dutch networks and comparisons with standard limits, suitable planning level values are suggested that can be helpful for the network operators to design future networks. Furthermore, guidelines about power quality responsibilities of different parties at the grid-connection point are investigated and proposed.

The second part, characteristics and interactions of apparatus and installations, is carried out by ECN, an energy research foundation in the Netherlands. The project mainly focuses on harmonic interactions of various power electronic devices and decentralized generations along with the network. In order to mitigate the problem of harmonic interactions and propagations, harmonic compensation and

damping techniques based on power electronic inverters are researched into.

Part III, that is the research topic covered by this thesis, is carried out in the EPE group. The project aims to propose advanced power electronic system and control strategies that can enhance the voltage quality at both the customer and the network sides. To adapt to future distribution networks, the tendency for grid-interfacing converters will be to integrate voltage quality enhancement with DG functionality, as the research background and objectives detailed in the previous sections.

The three parts of the EOS-KTI project covers different research directions but also are linked with each other. The findings of each research topic, for example, power quality consequences and responsibilities from part I, harmonic interaction problems and mitigation techniques from part II, and voltage quality enhancement technology from part III, are coupled and all together contribute to the research on voltage quality of the future infrastructure from various aspects.

1.8 List of publications

The results of this research work have been published in journals and presented at conferences, as listed in the following publications.

1. F. Wang, J. L. Duarte, and M. A. M. Hendrix, "Pliant active and reactive power control for grid-interactive converters under unbalanced voltage dips," *IEEE Transactions on Power Electronics*, accepted/in press, 2010.

2. F. Wang, J. L. Duarte, and M. A. M. Hendrix, "Design and analysis of active power control strategies for distributed generation inverters under unbalanced grid faults," *IET Generation, Transmission & Distribution*, vol. 4, iss. 8, pp. 905-916, Aug. 2010.

3. F. Wang, J. L. Duarte, and M. A. M. Hendrix, "Analysis of harmonic interactions between DG inverters and polluted grids," in *Proc. IEEE Energy Conference and Exhibition (EnergyCon)*, Dec. 2010.

4. F. Wang, J. L. Duarte, and M. A. M. Hendrix, "Active and reactive power control schemes for distributed generation systems under voltage dips," in *Proc. IEEE Energy Conversion Congress and Exposition (ECCE)*, 2009, pp. 3564-3571.

5. F. Wang, M. C. Benhabib, J. L. Duarte, and M. A. M. Hendrix, "High performance stationary frame filters for symmetrical sequences or harmonics separation under a variety of grid conditions," in *Proc. IEEE Applied Power Electronics Conference and Exposition (APEC)*, 2009, pp. 1570-1576.

6. F. Wang, M. C. Benhabib, J. L. Duarte, and M. A. M. Hendrix, "Sequence-decoupled resonant controller for three-phase grid-connected inverters," in *Proc. IEEE Applied Power Electronics Conference and Exposition (APEC)*, 2009, pp. 121-127.

7. F. Wang, J. L. Duarte, and M. A. M. Hendrix, "Active power control strategies for inverter-based distributed power generation adapted to grid-fault ride-through requirements," in *Proc. European Conference on Power Electronics and Applications (EPE)*, 2009, pp. 1-10.

8. M. C. Benhabib, F. Wang, and J. L. Duarte, "Improved robust phase locked-loop for utility grid applications," in *Proc. European Conference on Power Electronics and Applications (EPE)*, 2009, pp. 1-10.

9. F. Wang, J. L. Duarte, and M. A. M. Hendrix, "Weighting function integrated in grid-interfacing converters for unbalanced voltage correction," in *Proc. International Conference on Renewable Energy and Power Quality (ICREPQ)*, 2008, pp. 1-6.

10. F. Wang, J. L. Duarte, and M. A. M. Hendrix, "Reconfiguring grid-interfacing converters for power quality improvement," in *Proc. IEEE Young Researchers Symposium IAS/PELS/PES Benelux Chapter*, 2008, pp. 1-6.

11. F. Wang, J. L. Duarte, and M. A. M. Hendrix, "Control of grid-interfacing inverters with integrated voltage unbalance correction," in *Proc. IEEE Power Electronics Specialists Conference (PESC)*, 2008, pp. 310-316.

Part II

Low-level control of grid-interfacing converters

Chapter 2

Voltage detection and synchronization in disturbed grids

Abstract - Voltage detection and synchronization in disturbed grids are very important for the control of advanced grid-interfacing converter systems operating under various grid conditions. Being an essential part for any grid-interactive system, these issues are therefore separately detailed in this chapter, since the results will be used for all the specific applications in the next chapters.

This chapter first describes the decomposition of unbalanced and/or distorted voltages in terms of symmetrical-sequence components. Next, it presents a group of high performance filters for the detection of fundamental symmetrical sequences and harmonics under varied grid conditions. These filters are based on a basic filter cell that is demonstrated to be equivalent to a band-pass network in the stationary frame, and is easily implemented using a multi-state-variable structure. To achieve high performance for distorted and unbalanced grids, cascaded filters are developed.

This chapter also analyzes the robustness of the filter for small frequency variations, and improves its frequency-adaptive ability for large frequency changes. Furthermore, it is proved that the filter can also be applied for the synchronization and fundamental-frequency component detection in a single-phase system. Considering the digital implementation, four discretization methods and their limitations are investigated. The effectiveness of the presented filter is verified by experiments.

2.1   Introduction

For the control of power electronics-based grid-interfacing systems, synchronization with the grid voltage is essential. Depending on the applications, not only the detection of grid voltages but also the separation of specific symmetric-sequence components from grid voltages should be accurately achieved under unbalanced and/or distorted conditions. Furthermore, in order to deal with power flow control or power quality improvement (like active power filtering, voltage-dip compensation, etc.), the detection of fundamental negative-sequence components or harmonics is also always needed [24, 45–47]. In addition, though the frequency in the utility grid is usually very stable, frequency fluctuations will be caused by faults on the grid and load/generation changes, and often occur in weak grids. This problem results in system malfunctions or trips. Therefore, it is necessary to search for frequency insensitive or frequency adaptive schemes.

There are many detection methods presented in the literature for bad grid conditions. They are used for the purpose of synchronization, or for symmetrical-sequence detection under unbalanced or distorted grid conditions. To synchronize with the grid, different closed-loop control algorithms have been developed based on a conventional phase-locked-loop (PLL) structure [16–18]. Alternatively, in the manner of open-loop control, symmetrical sequences at fundamental frequency can be directly derived based on delayed signal cancelation methods [19–21]. However, these approaches are usually sensitive to grid frequency change or react badly to voltage harmonics. Recently, some methods were proposed to deal with unbalanced, distorted, and variable-frequency grid conditions. A method to eliminate signals in different reference frames based on mathematical transformations [22], and a nonlinear method based on the concept of an adaptive notch filter [23] were proposed. Both methods require massive calculations. In addition, [48] proposed an advanced PLL method based on separating the positive- and negative-sequence components in double synchronous reference frames (SRF). Apparently, this method is only preferred for power converters which are controlled with conventional SRF strategies.

On the other hand, many power converters have been designed in the stationary frame with proportional resonant (PR) controllers, which have proved to be simple and effective for the control of inverter systems under unbalanced grid conditions [26, 49, 50]. The PR controller will be presented in the next chapter. In order to facilitate the control of grid-interfacing converters in the stationary frame based on PR controllers, high performance stationary frame detection of control variables (in the form of symmetrical sequences or harmonics) are desirable. A newly developed method to detect sequence components in the stationary frame based on dual second-order generalized integrators (SOGI) was proposed in [51]. This method uses four integrators for either positive- or negative-sequence detection.

In this chapter, stationary-frame filtering technique is presented [52], of which it has been reported in practical applications [53, 54] that it can detect positive or negative sequences. Based on a multi-state-variable structure, the proposed filter is simple and easy to implement, as only two integrators are needed for positive-sequence detection. This chapter further investigates and develops an alternative

stationary frame method with a group of filters for symmetrical sequences or harmonic separation under different grid conditions. These filters are developed step by step from a basic filter cell.

This chapter is organized as follows. First, grid voltages in disturbed conditions are analyzed, also for establishing nomenclature. Secondly, the principle of the basic filter cell is presented. Following that, cascaded filters and frequency-adaptive filters are derived for the application in fixed-frequency and variable-frequency conditions. Next, the applicability to single-phase system is analytically shown, and limitations in digital implementation are investigated. Finally, experimental results and conclusions are presented.

2.2 Decomposition of disturbed grid voltages

Three-phase unbalanced or distorted voltages can be separated into three groups of balanced voltages, namely positive-sequence, negative-sequence, and zero-sequence voltages. Mathematical description is given in the following.

2.2.1 Symmetric-sequence components

With the Fourier series expansion, three-phase voltage variables in abc coordinates, Fig. 2.1, can be written as

$$
\begin{aligned}
v_a &= \sum_{n=1}^{\infty} V_{an} \cos(n\omega_1 t + \varphi_{an}), \\
v_b &= \sum_{n=1}^{\infty} V_{bn} \cos(n\omega_1 t + \varphi_{bn}), \\
v_c &= \sum_{n=1}^{\infty} V_{cn} \cos(n\omega_1 t + \varphi_{cn}),
\end{aligned}
\tag{2.1}
$$

where "n" denotes the harmonic order number and "ω_1" the fundamental angular frequency of the voltage.

Phasor notation is a proven and convenient way to describe sinusoidal quantities. Hence, the voltages in (2.1) can also be rewritten as

$$
\mathbf{v} = \begin{bmatrix} v_a \\ v_b \\ v_c \end{bmatrix} = \Re \left(\sum_{n=1}^{\infty} \mathrm{e}^{jn\omega_1 t} \begin{bmatrix} \underline{V}_{an} \\ \underline{V}_{bn} \\ \underline{V}_{cn} \end{bmatrix} \right),
\tag{2.2}
$$

where phasors are denoted with a bar subscript, that is, $\underline{V}_{an} = V_{an}\mathrm{e}^{j\varphi_{an}}$, etc, and $\Re(\cdot)$ represents the real part of a complex number. Applying symmetric-component transformation [55] to each harmonic voltage phasor yields the corresponding symmetric-sequence phasors as

$$
\begin{bmatrix} \underline{V}_n^0 \\ \underline{V}_n^+ \\ \underline{V}_n^- \end{bmatrix} = \frac{1}{3} \begin{bmatrix} 1 & 1 & 1 \\ 1 & a & a^2 \\ 1 & a^2 & a \end{bmatrix} \begin{bmatrix} \underline{V}_{an} \\ \underline{V}_{bn} \\ \underline{V}_{cn} \end{bmatrix}, \text{ with } a = \mathrm{e}^{j\frac{2\pi}{3}},
\tag{2.3}
$$
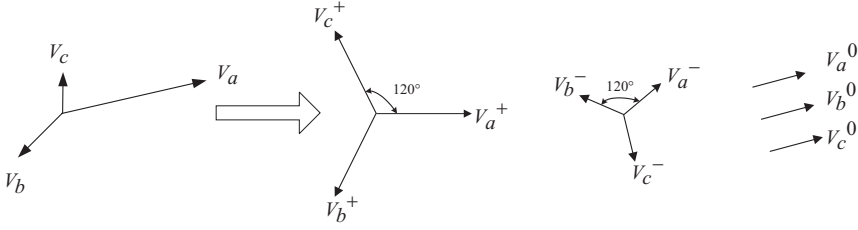
Figure 2.1: Phasor representation of the decomposition of unbalanced voltages in terms of symmetrical-sequence components.

where superscripts "+", "-", and "0" denote positive, negative, and zero sequences, respectively. The inverse transformation of (2.3) is found to be

$$
\begin{bmatrix} \underline{V}_{an} \\ \underline{V}_{bn} \\ \underline{V}_{cn} \end{bmatrix} = \begin{bmatrix} 1 & 1 & 1 \\ 1 & a^2 & a \\ 1 & a & a^2 \end{bmatrix} \begin{bmatrix} \underline{V}_n^0 \\ \underline{V}_n^+ \\ \underline{V}_n^- \end{bmatrix}.
\tag{2.4}
$$

Correspondingly, instantaneous values can be derived from the symmetric-component phasors given by (2.4). Otherwise stated, the following expressions for the *abc* voltages are applicable

$$
\mathbf{v} = \mathbf{v}^+ + \mathbf{v}^- + \mathbf{v}^0,
\tag{2.5}
$$

where $\mathbf{v}^+ = \begin{bmatrix} v_a^+ \\ v_b^+ \\ v_c^+ \end{bmatrix} = \Re \left(\sum_{n=1}^{\infty} \underline{V}_n^+ \mathrm{e}^{jn\omega_1 t} \begin{bmatrix} 1 \\ a^2 \\ a \end{bmatrix} \right),$

$$
\mathbf{v}^- = \begin{bmatrix} v_a^- \\ v_b^- \\ v_c^- \end{bmatrix} = \Re \left(\sum_{n=1}^{\infty} \underline{V}_n^- \mathrm{e}^{jn\omega_1 t} \begin{bmatrix} 1 \\ a \\ a^2 \end{bmatrix} \right), \text{ and}
$$

$$
\mathbf{v}^0 = \begin{bmatrix} v_a^0 \\ v_b^0 \\ v_c^0 \end{bmatrix} = \Re \left(\sum_{n=1}^{\infty} \underline{V}_n^0 \mathrm{e}^{jn\omega_1 t} \begin{bmatrix} 1 \\ 1 \\ 1 \end{bmatrix} \right).
$$

A graphic representation of the decomposition of unbalanced voltages is shown in Fig. 2.1. It implies that sequence-oriented observation, detection, and control can be achieved by separating unbalanced quantities. Note that fast and accurate real-time detecting methods are required in practice, because the symmetrical-component transformation presented above is only a mathematical description for understanding the decomposition of unbalanced quantities.

2.2.2   Distribution of symmetrical voltage harmonics

In polluted distribution grids, voltages may contain harmonics at any frequency due to various nonlinear loads. Generally, for three-phase systems, where the waveforms of fundamental-frequency and harmonic components should always be

half-wave symmetric, there are no even-order harmonics in the Fourier series expansion. In other words, except for special cases, it is accepted that there are no even harmonics in grid voltages.

For three-phase symmetrically distorted grids, i.e. where harmonic voltages in the three phases are balanced, the voltage quantities can be expressed by

$$
\begin{aligned}
v_a &= \sum_{n=1,3,5...}^{\infty} V_n \cos(n\omega_1 t + \varphi_n), \\
v_b &= \sum_{n=1,3,5...}^{\infty} V_n \cos(n(\omega_1 t - \tfrac{2\pi}{3}) + \varphi_n), \\
v_c &= \sum_{n=1,3,5...}^{\infty} V_n \cos(n(\omega_1 t + \tfrac{2\pi}{3}) + \varphi_n).
\end{aligned}
\tag{2.6}
$$

To decompose harmonic components of balanced voltages in terms of symmetrical sequences, applying the symmetric-component transformation of (2.3) to the phasors of the voltage harmonics in (2.6) obtains

$$
\begin{aligned}
\underline{V}_n^+ &= \tfrac{1}{3} V_n e^{j\varphi_n} \left(1 + e^{jn\left(-\frac{2\pi}{3}\right)}a + e^{jn\left(\frac{2\pi}{3}\right)}a^2\right) \\
&= \tfrac{1}{3} V_n e^{j\varphi_n} \left(1 + 2\cos\tfrac{2(n-1)\pi}{3}\right),
\end{aligned}
\tag{2.7}
$$

$$
\begin{aligned}
\underline{V}_n^- &= \tfrac{1}{3} V_n e^{j\varphi_n} \left(1 + e^{jn\left(-\frac{2\pi}{3}\right)}a^2 + e^{jn\left(\frac{2\pi}{3}\right)}a\right) \\
&= \tfrac{1}{3} V_n e^{j\varphi_n} \left(1 + 2\cos\tfrac{2(n+1)\pi}{3}\right),
\end{aligned}
\tag{2.8}
$$

$$
\begin{aligned}
\underline{V}_n^0 &= \tfrac{1}{3} V_n e^{j\varphi_n} \left(1 + e^{jn\left(-\frac{2\pi}{3}\right)} + e^{jn\left(\frac{2\pi}{3}\right)}\right) \\
&= \tfrac{1}{3} V_n e^{j\varphi_n} \left(1 + 2\cos\tfrac{2n\pi}{3}\right).
\end{aligned}
\tag{2.9}
$$

From (2.7) to (2.9), it can be found that harmonic voltages exists in terms of positive sequence when the harmonic number $n = 6m + 1$ ($m = 1, 2, 3...$), in terms of negative sequence when $n = 6m - 1$, and in terms of zero sequence when $n = 3m$. However, for three-phase asymmetrically distorted voltages, harmonic components can exist in terms of any symmetrical sequence.

2.2.3 Unbalanced voltages in the stationary reference frame

The stationary reference frame is a well-known coordinate set where, to simplify control strategies, three-phase abc quantities are mapped to $\alpha\beta\gamma$ quantities. Particularly, for three-wire systems, two independent and orthogonal quantities (α-axis, β-axis) are enough to be used for regulating the three-phase quantities since the γ term is zero. However, the calculations are complicated for unbalanced and distorted voltages because the γ quantity exists. Making use of symmetrical-sequence decomposition, the next paragraph shows that the positive- and negative-sequence components are only associated with α, β quantities, while the zero-sequence component is linked to the γ quantity.

Three-phase quantities in (2.1) can be transformed to the $\alpha\beta\gamma$ reference frame by the matrix transformation (Clarke transformation)

$$
\begin{bmatrix} v_\alpha \\ v_\beta \\ v_\gamma \end{bmatrix} = \boldsymbol{T}_{\alpha\beta\gamma} \begin{bmatrix} v_a \\ v_b \\ v_c \end{bmatrix},
\tag{2.10}
$$
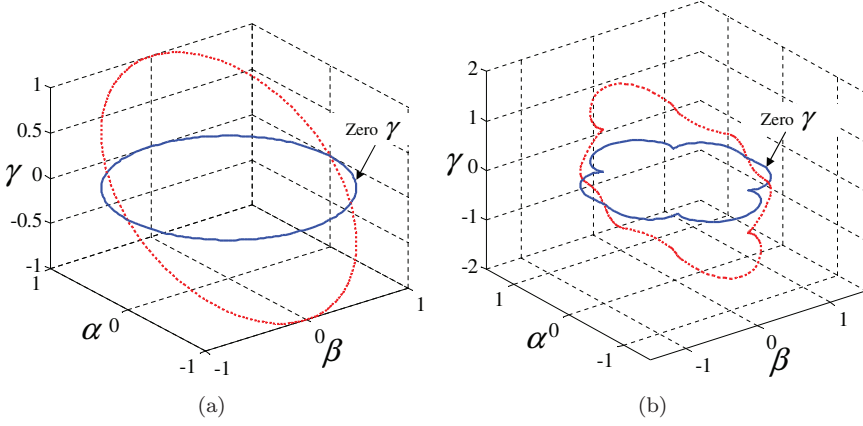
Figure 2.2: Three-phase per-unit quantities in the $\alpha\beta\gamma$-coordinate system: (a) sinusoidal grid condition and (b) distorted grid condition.

where

$$
\boldsymbol{T}_{\alpha\beta\gamma} = \frac{2}{3} \begin{bmatrix} 1 & \cos(2\pi/3) & \cos(-2\pi/3) \\ 0 & \sin(2\pi/3) & \sin(-2\pi/3) \\ 1/2 & 1/2 & 1/2 \end{bmatrix}.
$$

The coefficient "2/3" and the third-row parameters in the matrix are used for the purpose of invariant amplitude transformation. Thus, it is derived that

$$
v_\alpha = \frac{2}{3}[v_a + v_b \cos(2\pi/3) + v_c \cos(-2\pi/3)], \tag{2.11}
$$

$$
v_\beta = \frac{2}{3}[v_b \sin(2\pi/3) + v_c \sin(-2\pi/3)], \tag{2.12}
$$

$$
v_\gamma = \frac{1}{3}(v_a + v_b + v_c). \tag{2.13}
$$

Substituting the three-phase voltages of (2.5) into (2.11)-(2.13), it can be found that v_α and v_β are only composed of positive- and negative-sequence components of unbalanced voltages. It is also found that the sum of positive- or negative-sequence components is zero, which leads to only zero-sequence components left in the v_γ of (2.13), i.e.

$$
v_\gamma = \Re \left(\sum_{n=1}^{\infty} \underline{V}_n^0 e^{jn\omega_1 t} \right). \tag{2.14}
$$

For the sake of simplified computations it is convenient to group the α, β components into a single complex formula

$$
\underline{v}_{\alpha\beta} = v_\alpha + j v_\beta. \tag{2.15}
$$

From (2.11), (2.12), and (2.15),

$$
\underline{v}_{\alpha\beta} = \frac{2}{3}(v_a + v_b e^{j2\pi/3} + v_c e^{-j2\pi/3}). \tag{2.16}
$$

Substituting (2.1) into (2.16), the equation is expanded as

$$\underline{v}_{\alpha\beta} = \frac{2}{3} \sum_{n=1}^{\infty} \begin{matrix} [V_{an}\cos(n\omega_1 t + \varphi_{an}) + V_{bn}\cos(n\omega_1 t + \varphi_{bn})e^{j2\pi/3} \\ +V_{cn}\cos(n\omega_1 t + \varphi_{cn})e^{-j2\pi/3}]. \end{matrix} \tag{2.17}$$

According to Euler's formula, (2.17) is represented by

$$\underline{v}_{\alpha\beta} = \frac{1}{3} \sum_{n=1}^{\infty} \begin{matrix} [V_{an}e^{j\varphi_{an}}e^{jn\omega_1 t} + V_{an}e^{-j\varphi_{an}}e^{-jn\omega_1 t} + \\ V_{bn}e^{j\varphi_{bn}}e^{jn\omega_1 t}e^{j2\pi/3} + V_{bn}e^{-j\varphi_{bn}}e^{-jn\omega_1 t}e^{j2\pi/3} + \\ V_{cn}e^{j\varphi_{cn}}e^{jn\omega_1 t}e^{-j2\pi/3} + V_{cn}e^{-j\varphi_{cn}}e^{-jn\omega_1 t}e^{-j2\pi/3}]. \end{matrix} \tag{2.18}$$

With the phasor notation $\underline{V}_{an} = V_{an}e^{j\varphi_{an}}$ and $\overset{\circ}{\underline{V}}_{an} = V_{an}e^{-j\varphi_{an}}$, etc., where the symbol "o" denotes conjugate, it follows from (2.18) that

$$\underline{v}_{\alpha\beta} = \frac{1}{3} \sum_{n=1}^{\infty} [(\underline{V}_{an} + a\underline{V}_{bn} + a^2\underline{V}_{cn})e^{jn\omega_1 t} + (\overset{\circ}{\underline{V}}_{an} + a\overset{\circ}{\underline{V}}_{bn} + a^2\overset{\circ}{\underline{V}}_{cn})e^{-jn\omega_1 t}]. \tag{2.19}$$

Based on (2.3) and (2.19), it can be derived that

$$\underline{v}_{\alpha\beta} = \sum_{n=1}^{\infty} (\underline{V}_n^+ e^{jn\omega_1 t} + \overset{\circ}{\underline{V}}_n^- e^{-jn\omega_1 t}). \tag{2.20}$$

It is seen that the voltage $\underline{v}_{\alpha\beta}$ is the sum of two groups of phasors, which are related to the positive- and negative-sequence components. Conceptually, this means that there are two sequences rotating in opposite directions for each harmonic.

Graphic representations of various grid voltages in the $\alpha\beta\gamma$-coordinate system are shown in Fig. 2.2. If there is no zero-sequence component (zero v_γ), the resulting shape forms a circle in the $\alpha\beta$-plane for three-phase balanced and sinusoidal quantities, and are an ellipse when the three-phase quantities become unbalanced (ie. only have fundamental positive and negative sequences). When the zero-sequence component exists (non-zero v_γ), the circle or the ellipse in the $\alpha\beta$-plane rotates in the 3D $\alpha\beta\gamma$-coordinate system, as illustrated in Fig. 2.2 (a). Under distorted grid conditions irregular trajectories will be generated, as shown in Fig. 2.2 (b).

2.3 Basic filter cell

This section presents the principle of the basic filter cell that will be used to develop high performance filters. By utilizing its multi-state-variable structure, this filter cell can be easily implemented to achieve the function of a second-order band-pass filter in the stationary frame. The next paragraph mathematically demonstrates a generalized selective-harmonic band-pass filter cell for symmetric sequence decomposition. Afterwards, a series of filters that can be used for the control of grid-interfacing converter systems under a variety of grids can be constructed based on this principle.

As presented in the previous section, zero-sequence components of unbalanced voltages are decoupled from positive- and negative-sequence components, they are relatively easy to separate, simply by adding the three-phase quantities. Moreover, zero-sequence components can be regarded as single-phase quantities, which lead to an approach to the detection of fundamental-frequency components that will be addressed in a next section. Therefore, in this section, only positive- and negative-sequence components are discussed.

As already derived in the previous section, for unbalanced distorted voltages, the positive- and negative-sequence components in the $\alpha\beta$-frame are expressed by

$$
\begin{aligned}
\underline{v}_{\alpha\beta}(t) &= v_\alpha(t) + jv_\beta(t) \\
&= \sum_{n=1,3\cdots}^{\infty} (\underline{V}_n^+ e^{jn\omega_1 t} + \underline{V}_n^- e^{-jn\omega_1 t}),
\end{aligned}
\tag{2.21}
$$

where only odd harmonics are considered. Note that, for simplifying the notation, the term $\underline{\overset{\circ}{V}}_n^-$ of (2.20) is redefined and represented as phasor $\underline{V}_n^-$ in the following.

Let us look for a filter $\underline{G}_k^+(t)$, which can damp all components of $\underline{v}_{\alpha\beta}(t)$ except the kth-harmonic positive-sequence component in the stationary frame. That is

$$
\underline{v}_{\alpha\beta}(t) * \underline{G}_k^+(t) = \underline{v}_{\alpha\beta k}'(t),
\tag{2.22}
$$

where the "*" denotes a convolution product, and

$$
\underline{v}_{\alpha\beta k}'(t) = \underline{V}_k^+ e^{jk\omega_1 t} + \sum_{n=1,3\cdots,n\neq k}^{\infty} \underline{U}_n^+ e^{jn\omega_1 t} + \sum_{n=1,3\cdots}^{\infty} \underline{U}_n^- e^{-jn\omega_1 t},
\tag{2.23}
$$

with $|\underline{U}_n^+| \ll |\underline{V}_k^+|$ and $|\underline{U}_n^-| \ll |\underline{V}_k^+|$. Otherwise stated $\underline{v}_{\alpha\beta k}'(t) \approx \underline{v}_{\alpha\beta k}^+(t) = \underline{V}_k^+ e^{jk\omega_1 t}$, the kth-harmonic positive-sequence component of $\underline{v}_{\alpha\beta}(t)$ as defined in (2.21).

Multiplying (2.21) and (2.23) with $e^{-jk\omega_1 t}$, which corresponds to a transformation to a positive SRF, obtains, respectively

$$
\underline{v}_{\alpha\beta}(t)e^{-jk\omega_1 t} = \underline{V}_k^+ + \sum_{n=2,4\cdots,n\neq k-1}^{\infty} \underline{V}_n^+ e^{jn\omega_1 t} + \sum_{n=2,4\cdots}^{\infty} \underline{V}_n^- e^{-jn\omega_1 t},
\tag{2.24}
$$

$$
\underline{v}_{\alpha\beta k}'(t)e^{-jk\omega_1 t} = \underline{V}_k^+ + \sum_{n=2,4\cdots,n\neq k-1}^{\infty} \underline{U}_n^+ e^{jn\omega_1 t} + \sum_{n=2,4\cdots}^{\infty} \underline{U}_n^- e^{-jn\omega_1 t}.
\tag{2.25}
$$

It can be seen that the kth-harmonic positive-sequence voltage appears as a dc quantity in this positive SRF. Therefore, a simple first order filter $\underline{H}(t)$ with

$$
\mathcal{L}\left[\underline{H}(t)\right] = \underline{H}(s) = \frac{\omega_b}{s + \omega_b},
\tag{2.26}
$$

where $\mathcal{L}[\cdot]$ denotes Laplace transformation, and ω_b is the corner frequency, is sufficient to get $\underline{v}_{\alpha\beta k}'(t)e^{-jk\omega_1 t}$ from $\underline{v}_{\alpha\beta}(t)e^{-jk\omega_1 t}$. This can be expressed with

$$
(\underline{v}_{\alpha\beta}(t)e^{-jk\omega_1 t}) * \underline{H}(t) = \underline{v}_{\alpha\beta k}'(t)e^{-jk\omega_1 t},
\tag{2.27}
$$

or, using Laplace transformation

$$\underline{v}_{\alpha\beta}(s + jk\omega_1)\underline{H}(s) = \underline{v}'_{\alpha\beta k}(s + jk\omega_1). \tag{2.28}$$

Substituting $s - jk\omega_1 \rightarrow s$ into (2.26) and (2.28), it follows that

$$\underline{v}_{\alpha\beta}(s)\frac{\omega_b}{s - jk\omega_1 + \omega_b} = \underline{v}'_{\alpha\beta k}(s). \tag{2.29}$$

From (2.22), it can also be rewritten as

$$\underline{v}_{\alpha\beta}(s)\underline{G}^+_k(s) = \underline{v}'_{\alpha\beta k}(s). \tag{2.30}$$

Therefore, $\underline{G}^+_k(s)$, the filter being looked for in the stationary frame, should be equal to

$$\underline{G}^+_k(s) = \underline{H}(s - jk\omega_1) = \frac{\omega_b}{s - jk\omega_1 + \omega_b}. \tag{2.31}$$

By expanding (2.30) to

$$[v_\alpha(s) + jv_\beta(s)]\frac{\omega_b}{s - jk\omega_1 + \omega_b} = v'_{\alpha k}(s) + jv'_{\beta k}(s), \tag{2.32}$$

the following equations are derived

$$v'_{\alpha k}(s) = \frac{1}{s}[\omega_b(v_\alpha(s) - v'_{\alpha k}(s)) - k\omega_1 v'_{\beta k}(s)],$$

$$v'_{\beta k}(s) = \frac{1}{s}[\omega_b(v_\beta(s) - v'_{\beta k}(s)) + k\omega_1 v'_{\alpha k}(s)]. \tag{2.33}$$

Similarly, the kth-negative-sequence component follows as

$$\underline{v}_{\alpha\beta}(t) * \underline{G}^-_k(t) = \underline{v}''_{\alpha\beta k}(t), \tag{2.34}$$

where

$$\underline{v}''_{\alpha\beta k}(t) = \underline{V}^-_k\, e^{-jk\omega_1 t} + \sum_{n=1,3\cdots}^{\infty} \underline{U}^+_n e^{jn\omega_1 t} + \sum_{n=1,3\cdots,n\neq k}^{\infty} \underline{U}^-_n\, e^{-jn\omega_1 t}, \tag{2.35}$$

or $\underline{v}''_{\alpha\beta k}(t) \approx \underline{v}^-_{\alpha\beta k}(t)$. Similar to (2.28) and (2.30), it follows that

$$\underline{v}_{\alpha\beta}(s - jk\omega_1)\underline{H}(s) = \underline{v}''_{\alpha\beta k}(s - jk\omega_1),$$

$$\underline{v}_{\alpha\beta}(s)\underline{G}^-_k(s) = \underline{v}''_{\alpha\beta k}(s), \tag{2.36}$$

where

$$\underline{G}^-_k(s) = \underline{H}(s + jk\omega_1) = \frac{\omega_b}{s + jk\omega_1 + \omega_b}.$$

Correspondingly, the equations below are derived:

$$v''_{\alpha k}(s) = \frac{1}{s}[\omega_b(v_\alpha(s) - v''_{\alpha k}(s)) + k\omega_1 v''_{\beta k}(s)],$$

$$v''_{\beta k}(s) = \frac{1}{s}[\omega_b(v_\beta(s) - v''_{\beta k}(s)) - k\omega_1 v''_{\alpha k}(s)]. \tag{2.37}$$
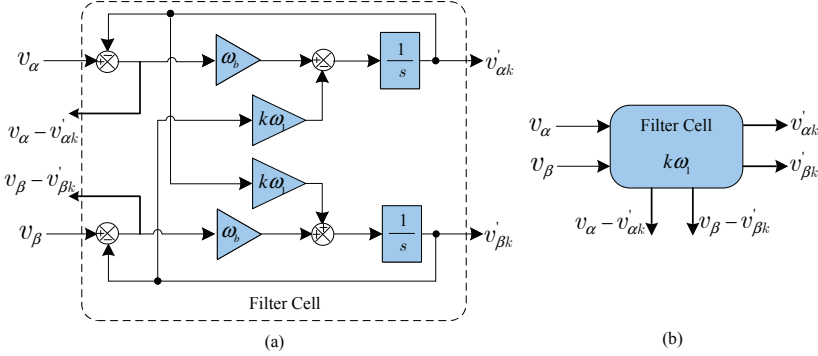
Figure 2.3: Implementation diagrams: (a) filter cell for the kth-harmonic positive-sequence component and (b) the equivalent diagram of the filter cell.

Equations (2.33) and (2.37) can be easily implemented in the $\alpha\beta$-frame by time domain digital techniques. Considerations on digital implementation will be presented in a following section. Figure 2.3 shows the implementation diagram for positive-sequence components. The filter for negative-sequence components is identical but the central frequency is changed to $-k\omega_1$. Note that two internally derived variables, $v_\alpha - v'_{\alpha k}$ and $v_\beta - v'_{\beta k}$, are taken out from the filter. These represent the residues of the two input signals minus the extracted components. In summary, the detection of $v^+_{\alpha\beta k} = v^+_{\alpha k} + jv^+_{\beta k}$ and $v^-_{\alpha\beta k} = v^-_{\alpha k} + jv^-_{\beta k}$ is achieved with (2.33) and (2.37), since $v^+_{\alpha\beta k} \approx v'_{\alpha\beta k}$ and $v^-_{\alpha\beta k} \approx v''_{\alpha\beta k}$.

2.4   Operation under fixed-frequency conditions

Based on the basic filter cell derived above, cascaded filters are constructed to output fundamental positive-sequence components, fundamental negative-sequence components, and harmonics. Applications of these filters are categorized into fixed- and variable-frequency classes. This section focuses on filter design limited to fixed-frequency conditions, that is standard frequency deviation (e.g. $\pm 1\%$ [56]).

2.4.1   Fundamental positive- and negative-sequence detection

Theoretically, when inputting unbalanced and distorted signals, the fundamental positive-sequence and negative-sequence components can be directly filtered out with the above proposed filter cells by setting the index k to 1 and -1 in Fig. 2.3, respectively. For this case, based on the transfer functions $\underline{G}^+_k(s)$ and $\underline{G}^-_k(s)$, frequency domain plots of positive-sequence and negative-sequence basic filters are drawn in Fig. 2.4. It can be seen that both symmetrical sequence filters have unity gain and zero phase-shift at the central frequency. By decreasing the bandwidth parameter ω_b, the damping ratio for other frequency components is increased,
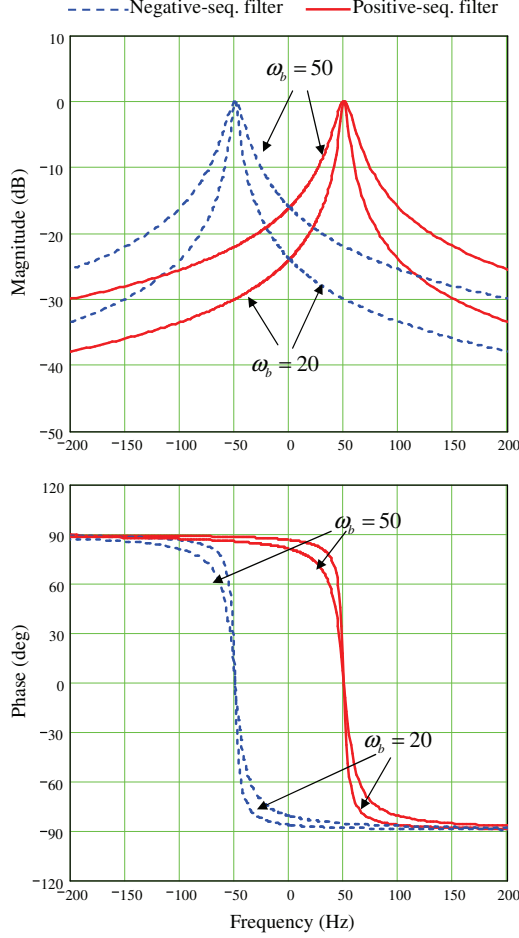
Figure 2.4: Filter plots in frequency domain of the basic filter cell with the fundamental angular frequency $\omega_1 = 314$ rad/s, $k = \pm 1$, where two different bandwidths are selected.

however, at the price of increasing response time. This will be a compromise in a practical design.

Unfortunately, in practical applications, input signals usually involve a large proportion of positive-sequence components which are difficult to damp totally. Therefore, the negative-sequence component is too small to be detected accurately by using only a basic filter cell. As a consequence, for the basic negative-sequence filter a set of input signals is required with the fundamental dominant positive sequence already removed. Thanks to the implementation structure, these signals are exactly the two variables $v_\alpha - v'_{\alpha k}$ and $v_\beta - v'_{\beta k}$ in Fig. 2.3 ($k = 1$).

It follows that a cascaded filter is constructed for the separation of two fundamental sequences. Figure 2.5(a) illustrates the implementation diagram based on the filter cell when the negative-sequence component is removed. Note that the
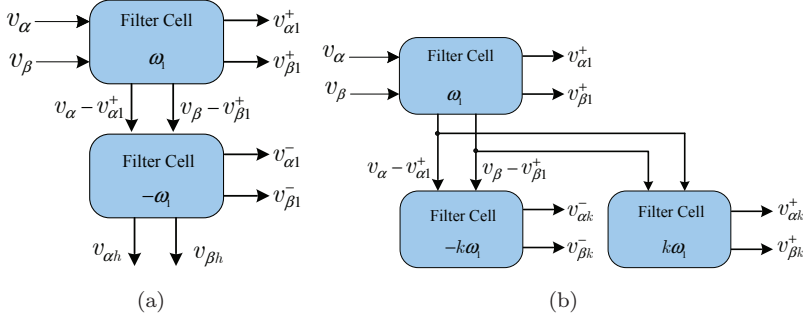
Figure 2.5: Cascaded structure for: (a) the separation of fundamental positive, negative sequences and total harmonics, and (b) the detection of the kth harmonics.

residue of harmonics $v_{\alpha h}$ and $v_{\beta h}$, that is the total of other harmonics, is output if there exist other components in the input signals than those at the fundamental-frequency.

2.4.2   Harmonic separation

The filter described above deriving the negative-sequence component and total harmonics (Fig. 2.5 (a)) can also be used by active power filters. Nevertheless, there are applications for which it is desirable to detect a specific harmonic, e.g. in the application of selective harmonic compensation. A cascaded selective-harmonic filter can be constructed to separate harmonics, as shown in Fig. 2.5 (b). For each individual filter cell, the bandwidth should be fine-tuned based on the actually present distortion.

It is pointed out that, for a three-phase system with symmetric distortion, harmonics can be divided into two groups in terms of positive and negative sequences. In other words, harmonics $v_{\alpha,\beta k}$ only exist in terms of positive sequences when $k = 6m + 1$ ($m = 1, 2, 3...$), or exists in terms of negative sequences when $k = 6m - 1$. This helps to make the implementation easier since each individual harmonic needs either a positive- or a negative-sequence filter cell. Otherwise, twice the number of filter cells are needed and therefore the computation time is doubled. A frequency domain plot for the cascaded filter is drawn in Fig. 2.6, illustrating the frequency response of the filters of Fig. 2.5 (a) and (b). As an example, the 5th negative-sequence filter and the 7th positive-sequence filter are applied. It can be seen that the filter operates equivalently to a notch filter at the positive fundamental frequency, hence improving the filter's accuracy for negative-sequence components at the fundamental frequency. In fact, other structures can be constructed in a similar manner as those cascaded filters presented in this section, depending on practical needs.
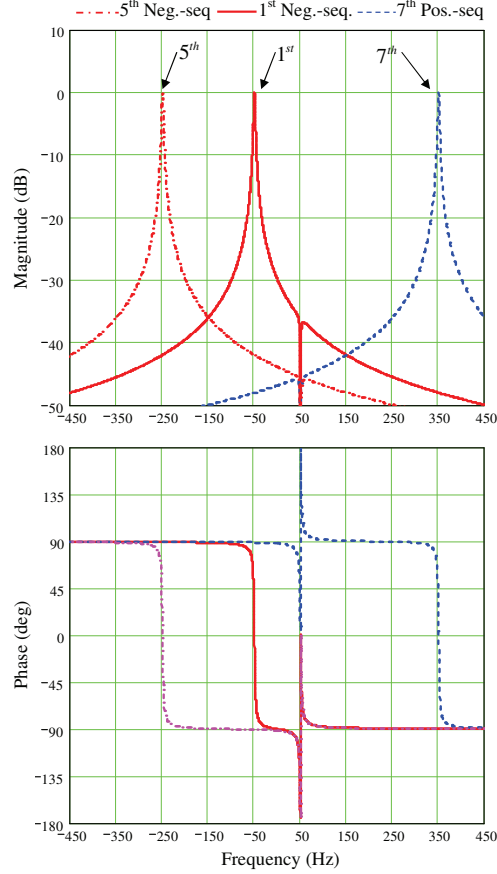
Figure 2.6: Filter plots in frequency domain of the cascaded filters with the bandwidth $\omega_b = 10$ rad/s and the fundamental angular frequency $\omega_1 = 314$ rad/s.

2.5 Operation under variable-frequency conditions

The previously designed filters were developed for a fixed-frequency situation. It is relevant to investigate their frequency behavior when applied to variable-frequency conditions.

2.5.1 Robustness for small frequency variations

It is worth noticing that the proposed filters are robust to small frequency variations. This can be explicitly analyzed from the frequency response characteristics, as shown in Fig. 2.7, where the central frequency of the filter is fixed at 50 Hz and the frequency of the input signals vary between 47 Hz and 53 Hz. It can be seen that the magnitude change and phase shift are small within 49 Hz to 51 Hz, i.e., $\pm 2\%$ deviation from the central frequency, and the effects decrease when extending
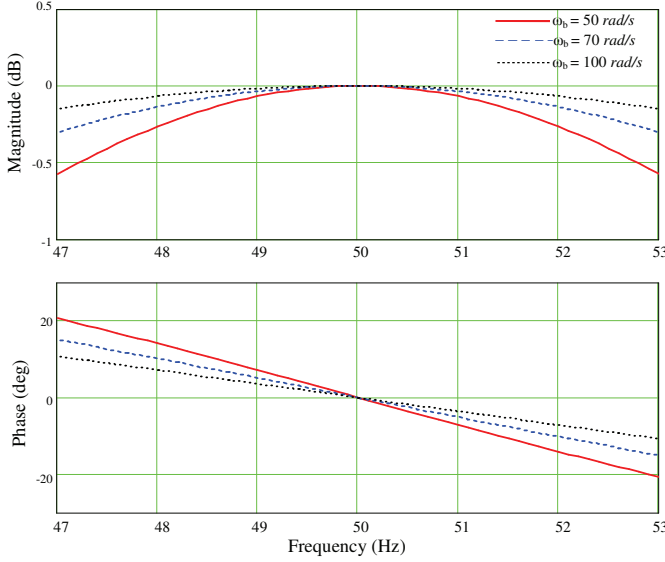
Figure 2.7: Effects of a small frequency variation on the output magnitudes and phases of the filter cell with a fixed central frequency at 50 Hz, where plots for different bandwidths ω_b are compared.
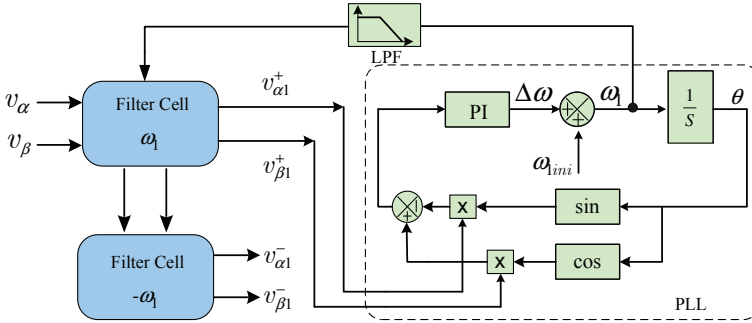
Figure 2.8: Structure diagram of the improved cascaded filter with a fundamental frequency (ω_1) adaptive function.

the bandwidth. In general, frequency tolerance in the grid of 2% is big enough. For higher performance, the robustness of filters can be improved by increasing the bandwidth ω_b slightly.

2.5.2   Adaption to large frequency changes

However, it is illustrated clearly in Fig. 2.7 that a large frequency deviation from the central frequency can lead to a serious phase shift and magnitude damping. Therefore, a frequency updating scheme should be added to the filter cell. A

widely implemented PLL structure is used to update the value of the fundamental frequency ω_1. The implementation structure is shown in Fig. 2.8, where an initial input variable ω_{1ini} should be given as the initial value around the central frequency, and a low pass filter is used to eliminate the ripple on ω_1 introduced by the PLL regulator. Due to the frequency change, the output signals from the filter cell may not be balanced during the transient, thereby resulting in low-order ripple on the output frequency. Several different schemes for the purpose of ripple elimination have been compared in [57], it is not detailed here.

On the other hand, note that the PLL also benefits from the filter because the PLL input signals derived from the filter cell are free, or at least mostly attenuated from noise or harmonics, although their magnitudes and phases are influenced at the moment of frequency change. Therefore, with the frequency and phase variables generated based on the filter in Fig. 2.8, a roubst PLL can be constructed for the control design of grid-interfacing converters in the synchronous reference frame.

2.6 Applicability to single-phase system

The filter cell was introduced in the $\alpha\beta$-frame in Section 2.3 for a three-phase system, but it can also be used for single phase applications. In principle, a single-phase system can be regarded as an extreme case of three-phase unbalanced system, where one of the phases is open and two of the three-phase voltages are zero. Therefore, transforming the single phase signal, denoted by $v_{1\varphi}$, to the $\alpha\beta$ frame as in (2.11) and (2.12), gives

$$\begin{bmatrix} v_\alpha \\ v_\beta \end{bmatrix} = \frac{2}{3} \begin{bmatrix} 1 & -\frac{1}{2} & -\frac{1}{2} \\ 0 & \frac{\sqrt{3}}{2} & -\frac{\sqrt{3}}{2} \end{bmatrix} \begin{bmatrix} v_{1\varphi} \\ 0 \\ 0 \end{bmatrix} = \begin{bmatrix} \frac{2}{3}v_{1\varphi} \\ 0 \end{bmatrix}. \tag{2.38}$$

It means that a set of signals from (2.38) can be used as the input signal of the filter. On the other hand, the single-phase signal can be composed in terms of symmetrical sequences. Similar to (2.4), in phasor notation it can be expressed as

$$\begin{bmatrix} \underline{V}_{1\varphi} \\ 0 \\ 0 \end{bmatrix} = \begin{bmatrix} 1 & 1 & 1 \\ 1 & a^2 & a \\ 1 & a & a^2 \end{bmatrix} \begin{bmatrix} \underline{V}_{1\varphi}^0 \\ \underline{V}_{1\varphi}^+ \\ \underline{V}_{1\varphi}^- \end{bmatrix}. \tag{2.39}$$

After manipulation, the positive- and negative-sequence components can be calculated by

$$\underline{V}_{1\varphi}^+ = \underline{V}_{1\varphi}^- = \frac{1}{3}\underline{V}_{1\varphi}. \tag{2.40}$$

Therefore, if the filter is configured with its fundamental frequency at the central frequency, the two signals derived from the filter will be two signals in the $\alpha\beta$ frame, which represent the positive-sequence component of the extremely unbalanced three-phase signals. One is in phase with the input signal, the other orthogonal, and both have one third the amplitude of the single-phase signal.
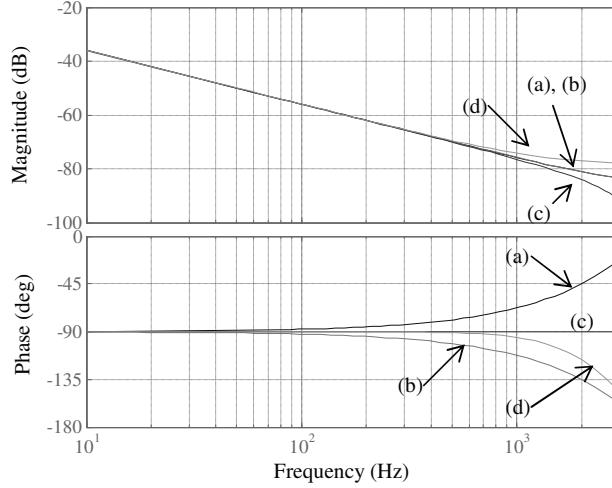
Figure 2.9: Bode plots of the four discrete integrators: (a) forward Euler, (b) backward Euler, (c) trapezoidal, and (d) two-step Adams-Bashforth, for $T_s = 125$ μs.

It is remarked that the bandwidth for this application should be lower than for the application in a three-phase system in order to get good results. This is because the amplitudes of the positive-sequence and the negative-sequence components are equal when the single-phase system is regarded as an extremely unbalanced three-phase one. Note that the zero-sequence component of three-phase system can be similarly applied as a single-phase signal with the sum of the three-phase signals.

2.7 Digital implementation

To implement the filters in a digital way, different methods can be used for the discretization of the integrator ($\frac{1}{s}$) in the filter cell. Several known methods in the z-domain are:

a) Forward Euler

$$\frac{1}{s} \leftrightarrow T_s \frac{z}{z - 1}, \tag{2.41}$$

b) Backward Euler

$$\frac{1}{s} \leftrightarrow T_s \frac{1}{z - 1}, \tag{2.42}$$

c) Trapezoidal(or Tustin)

$$\frac{1}{s} \leftrightarrow \frac{T_s}{2} \frac{z + 1}{z - 1}, \tag{2.43}$$

d) Two-step Adams-Bashforth

$$\frac{1}{s} \leftrightarrow \frac{T_s}{2} \frac{3z - 1}{z^2 - z}, \tag{2.44}$$
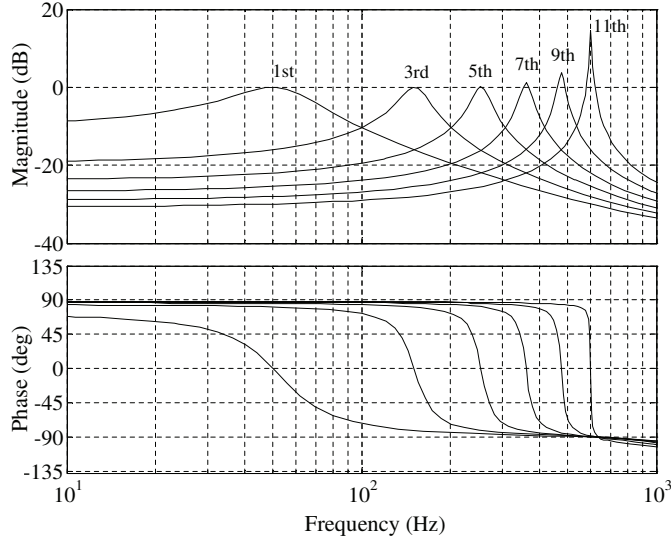
Figure 2.10: Bode plots of the filter cell applied at different central frequencies when using the two-step Adams-Bashforth method.

where T_s denotes the discrete time step.

These methods only approximate an ideal integrator when transforming from the time domain to the discrete domain, so the accuracy of the approximation does influence the effect of the filter. The frequency characteristics of the four methods are shown in Fig. 2.9, where $T_s = 125$ μs. Compared with an ideal integrator, methods (a) and (b) have the worst phase-shift starting at around 100 Hz, (d) is much better, and method (c) is the best one. However, method (c) has an "algebraic-loop" issue due to the implementation structure of the filter cell. A solution for that is to use the closed-loop transfer function of the filter instead, but then the explicit advantage of easy implementation of the filter cell is lost. Certainly, the accuracy of the approximation can also be improved when sampling quicker. In this chapter, method (d) is selected as a compromise.

A further study is carried out to check the limitation on the effect of the filter when using method (d). As an example, a filter cell is investigated, which sets a fundamental frequency of 50 Hz, bandwidth of 100 rad/s, and a sampling frequency 8 kHz. The Bode plots are drawn in Fig. 2.10, where filters applied for positive-sequence components at the fundamental frequency and low-order harmonics are displayed. It is shown that the filters applied for the harmonics above 7th are not correct anymore. A possible improvement is to decrease T_s, but this should be compromised in practice because of other limitations, for example, the minimum computation time for the control loop.
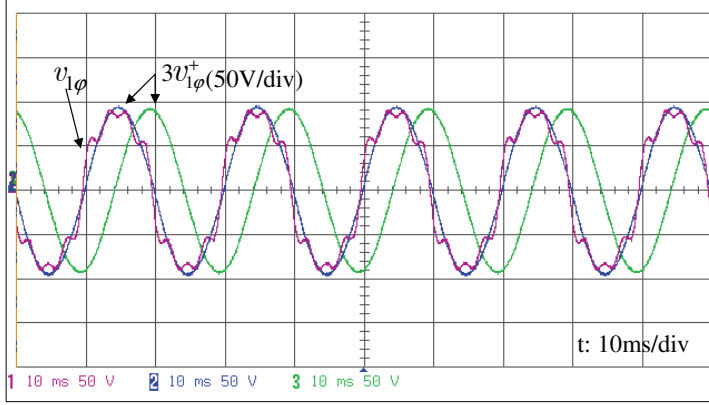
Figure 2.11: Experimental result of the application for a single-phase system, where a distorted voltage $v_{1\varphi}$ consists of a fundamental-frequency component, and 10% of the 3rd, 5th, and 7th harmonic.
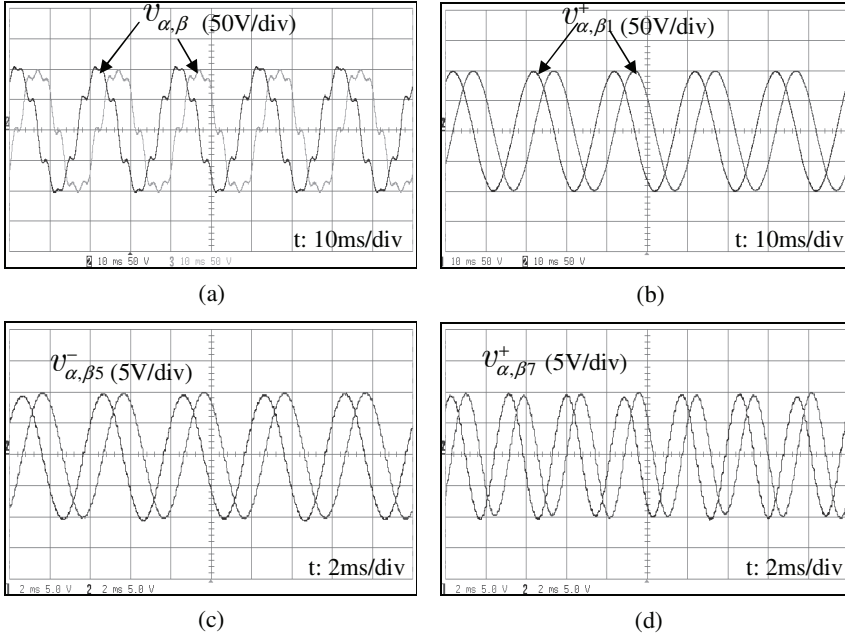
Figure 2.12: Experimental waveforms of the separation from (a) a balanced distorted grid voltage, which involves a 100V fundamental positive-sequence component (shown in (b)), 10% of the 5th negative-sequence (shown in (c)) and 10% of the 7th positive-sequence harmonics (shown in (d)).
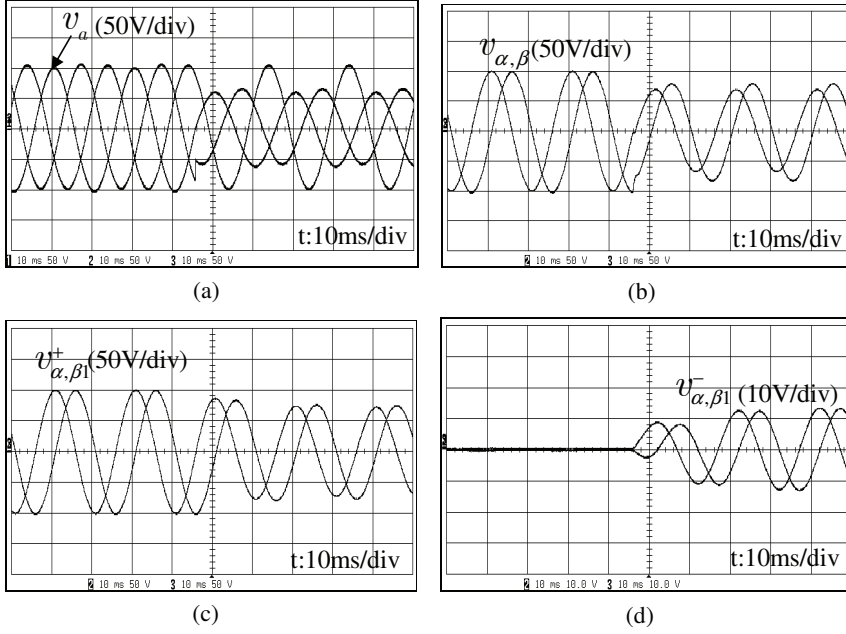
Figure 2.13: Experimental waveforms based on a cascaded filter where the balanced grid voltages dip to 60% of the original magnitude in two phases. The waveforms are (a) grid voltages in the abc-frame, (b) grid voltages in the $\alpha\beta$-frame, (c) fundamental positive-sequence, and (d) negative-sequence voltages.

2.8   Experimental results

Experiments have been carried out for verification purposes. A three-phase programmable ac power source was used to emulate various grid conditions. The controller is built with a dSPACE DS1104 setup. Considering its application for power electronic converters, which usually have 5 kHz to 20 kHz switching frequency, a sampling frequency of 8 kHz was used to implement the digital filters. A two-step Adams-Bashforth discretization method was used.

Figure 2.11 shows the results of the basic filter cell applied in a single-phase system. As presented in Section 2.6, for a single-phase distorted grid voltage $v_{1\varphi}$, two signals ($2v_{1\varphi}/3$ and 0) are used as inputs for the basic filter. The parameter ω_b is set to 60 rad/s. It can be seen that a set of sinusoidal signals at the fundamental frequency (50 Hz) are derived. According to (2.40), the output positive-sequence components, one in phase with the input signal and the other orthogonal, have exactly one third the amplitude of the input single-phase signal.

Next, the filters are verified for the application in a three-phase system. The signals coming out of the filters are shown in the $\alpha\beta$-frame. In the following experiments, ω_b is set to 100 rad/s for the fundamental positive-sequence filter and 80 rad/s for others.

As shown in Fig. 2.12, the harmonic separation from a set of three-phase
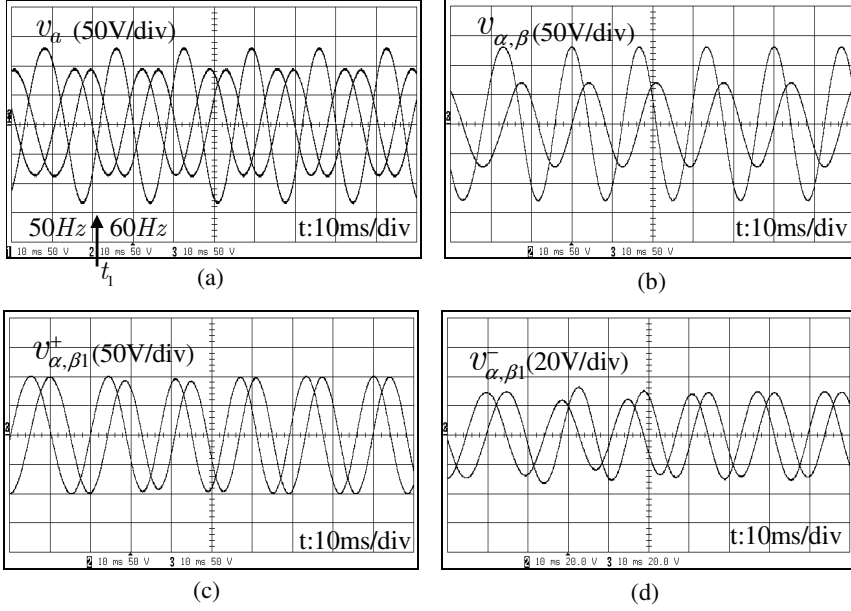
Figure 2.14: Experimental waveforms based on a frequency adaptive filter with the grid frequency changing from 50 Hz to 60 Hz at time t_1. The waveforms are (a) grid voltages in the abc-frame, (b) grid voltages in the $\alpha\beta$-frame, (c) fundamental positive-sequence, and (d) fundamental negative-sequence voltages.

symmetrically distorted signals is achieved based on the cascaded filter given in Fig. 2.5 (b). Figure 2.12 (a) shows the grid voltages in the $\alpha\beta$-frame. Because of the limitation on the filter for high-order harmonics in the case of 8 kHz sampling frequency, only the 5th and 7th harmonics are emulated for the verification. Figure 2.12 (b) to (d) are the output fundamental positive-sequence, 10% of the 5th negative-sequence, and 10% of the 7th positive-sequence components, respectively. Note that the time scales of Fig. 2.12 (c) and (d) are enlarged.

Figure 2.13 shows the behavior of the cascaded filter as in Fig. 2.5 (a) for detecting symmetrical sequences at the fundamental frequency. The balanced grid voltages dip to 60% of the original magnitude in two phases, as shown in the abc-frame and the $\alpha\beta$-frame by Fig. 2.13 (a) and (b), respectively. The output positive-sequence components are shown in Fig. 2.13 (c) with a settling time of 20 ms, while the negative-sequence components shown in Fig. 2.13 (d) are 10 ms slower because of a smaller bandwidth used.

Furthermore, a variable-frequency grid was tested with the frequency adaptive filter shown in Fig. 2.8. As shown in Fig. 2.14 (a), the frequency of an unbalanced grid changes from 50 Hz to 60 Hz at the moment t_1. It can be found that the settling time for both the positive-sequence and the negative-sequence components increases by 10 ms compared with the previous results achieved in the fixed-frequency grid condition. This is caused by the low-pass filtering for the

output frequency variable of the PLL in Fig. 2.8. In addition, note that the α and β quantities of the negative-sequence voltages are slightly unequal in the steady-state amplitudes. To improve the accuracy if necessary, a narrower bandwidth for the negative-sequence filter can be used at the cost of longer response time. In general, the obtained results in Fig. 2.14 (c) and (d) show good performance for symmetrical sequence detection and for the ability of adapting to frequency changes dynamically. Moreover, for a practical grid where the frequency variations are much smaller, the filter parameters can be optimized to get better results.

2.9 Conclusions

This chapter has mathematically described the signal decomposition of disturbed grid voltages and then introduced a group of high performance filters for fundamental positive sequence, negative sequence, and harmonic detection under a variety of grid conditions. The basic filter cell has been demonstrated to be equivalent to a band-pass filter in the stationary frame, and can be easily implemented using a multi-state-variable structure.

Based on the filter cell, cascaded filters have been developed to achieve high performance under unbalanced and distorted grids. It has been shown that the proposed filters are robust to small frequency variations. For large frequency changes (over $\pm 1\%$), frequency-adaptivity of the filter cell has been improved with an extra PLL. By assuming a single-phase system to be an extremely unbalanced three-phase system, the filter has been proved to be effective also for single-phase applications.

In addition, a digital implementation and its limitations has been further considered. It is concluded that the proposed filters are accurate for detecting fundamental and low-order harmonics components, which are essential in the control of grid-interfacing converters. When applying these filters for high-order harmonics, further improvements could be carried out by making the sampling frequency higher or by investigating other digital implementation methods. Finally, the effectiveness of the proposed filters has been verified by experiments, showing high-performance operation in disturbed grids.

Chapter 3

Stationary-frame current regulation

Abstract - Three-phase grid-interfacing converters play an important role in distribution networks where they are used for power flow control, power quality improvement, or distributed power generation. To realize these applications different control strategies are required, that is from control design perspective various external schemes are needed to generate desirable reference signals for controlling active and reactive power, current, or voltage. However, irrespective of the application, controllers used for the inner-loop reference tracking are essential for the system performance and overall control structures. This chapter presents three types of linear controllers, among which stationary frame resonant controllers are selected for specific applications in the next chapters.

Two existing methods are first compared, namely proportional integral (PI) controllers and proportional resonant (PR) controllers. Then, a three-phase four-leg voltage source converter, is modeled in multiple reference frames with the aim of evaluating different current regulators. As a complement to the existing PR controllers, sequence-decoupled resonant (SDR) controllers are proposed for regulating individual symmetric-sequence components in unbalanced grids.

The comparison shows that stationary-frame resonant controllers (PR or SDR) are preferred because of their simplicity and flexible control capability at selected frequencies. The PR controller is suitable for regulating positive- and negative-sequence quantities together and for regulating zero-sequence quantity separately, while the SDR controller is able to achieve independent positive- or negative-sequence control in the stationary frame. Two applications, one is for the current regulation of a parallel grid-connected inverter and another one-for the asymmetric current elimination with a series grid-connected inverter, are presented and experimentally verified.

3.1   Introduction

Three-phase grid-interfacing converters are playing a more and more important role in distributed power generation, power flow control, harmonic compensation, and voltage regulation. In general, all these functions are possible by regulating the converter output voltages, injected currents, or delivered power.

Power control can be classified in direct power control, where the switching states of converters are adjusted directly based on the error between reference power and measured power [58, 59], and indirect power control (eg. voltage-oriented [60] and virtual-flux-oriented [61] power control), which is essentially an internal current control with reference currents derived from external power calculations. Hence, it is not trivial to add auxiliary functions (eg. active power filtering with harmonic current injection) to converters designed for direct power control. For converters with indirect power control, auxiliary functions can easily be achieved by adding extra current references and current compensators.

Considering that in this work auxiliary functions will be needed for voltage quality enhancement, indirect power control is adopted. In this case, internal current regulators essentially determine the system performance and overall control structure. Therefore, this chapter specifies internal current regulation, and includes a comparison of different current controllers. Because voltage control differs from current control only in reference signals and feedback variables, basic compensators and control structures presented in this chapter can also be used for voltage control.

Before proceeding to the selected controllers, several popular controllers will be reviewed. Figure 3.1 shows a simple classification of converter control methods. In the class of nonlinear control, the most frequently used one is a hysteresis controller that simply changes the switching state to enforce a desired output when feedback errors exceed predefined boundaries, leading to fast dynamic responses [62]. The major drawback of hysteresis control is a switching frequency, which changes with operating conditions.

Application of non-linear predictive control brings new possibilities to voltage source converters. The voltage vector that minimizes the errors at the next sampling time is selected by evaluating the predicted values of the variables to be controlled. As this prediction depends on accurate system models it is sensitive to parameter variations [36].

Passivity-based control (PBC), also called Lyapunov-based control, is sometimes applied on pulse-width modulation (PWM) converters. By constructing a Lyapunov function for the system the closed-loop system strictly guarantees a sufficient stability region (independent of the circuit parameters) against large-signal disturbances, while other methods can guarantee system stability against only small perturbations from the operating point [63].

With respect to linear control, the best known principles are predictive deadbeat (DB) [64], proportional integral (PI) [60], and proportional resonant (PR) [49] control. These controllers operate by regulating the low-frequency modulation waveforms of PWM converters to minimize reference tracking errors. Principally, the DB controller is fast becasue it can null the error after only two sampling pe-
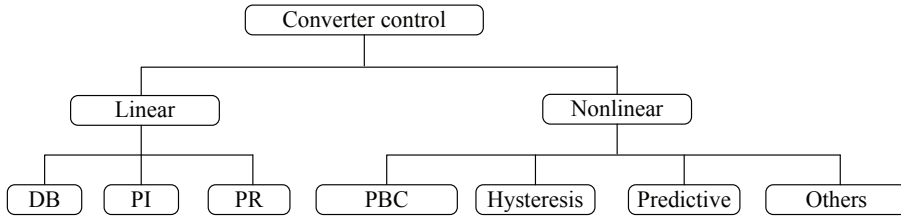
Figure 3.1: A simple classification of converter control methods.

riods, but attention has to be paid to its inherent sensitivity to model parameters and computation delay. This chapter focuses on three types of linear controllers, ie. PI, PR, and an extended resonant controller named sequence-decoupled resonant (SDR). Because of their simplicity and flexible control possibilities at selected frequencies, the resonant-type controllers (PR and SDR) are chosen for specific applications in next chapters .

Concerning only PI or PR controllers, many variations of control design have been proposed due to disturbed grid conditions. In particular, the situation of a unbalanced grid, which may result from asymmetrical source impedances or loads should always be taken into account. In order to improve the performance of grid-connected converters and/or to simplify complex control structures without compromising system performance under unbalanced or distorted grids [24, 25, 27, 49, 50, 65–69], various current control strategies based on PI or PR are therefore proposed.

This chapter first describes PI and PR controllers. Then, a three-phase four-leg voltage source converter, which will be employed in the next chapters to construct flexible systems for dealing with a variety of grid conditions such as three-wire or four-wire unbalanced and/or distorted grids, is modeled in different reference frames. The aim is to compare the design of the current regulators and to evaluate the complexity of the overall control structure.

Furthermore, as a complement to the existing PR controllers, a set of SDR controller [70], which can deal with positive-sequence or negative-sequence components individually, is investigated. This provides another insight into asymmetric current regulation, showing that the *abc* quantities (without zero-sequence components) can be determined by regulating symmetrical positive- and negative-sequence components in the stationary frame, other than regulating α and β quantities. At the end of this chapter, two applications are presented, one-for the current regulation of a parallel grid-connected inverter and another-for asymmetric current elimination by a series grid-connected inverter. Experimental verification and comparison of the PR and SDR controllers is provided.

3.2 Proportional resonant (PR) controllers

3.2.1 PR controllers versus PI controllers

Proportional resonant (PR) control has been recently proposed as an ac signal regulator. In the frequency domain the transfer functions of the PR controllers proposed in [49, 67], and the proportional + generalized integrator presented in [50], are expressed in ideal form as

$$G(s) = K_P + \frac{2K_I s}{s^2 + \omega_c^2}, \tag{3.1}$$

or in practical form, named non-ideal PR controller, as

$$G(s) = K_P + \frac{2\omega_b K_I s}{s^2 + 2\omega_b s + \omega_c^2}, \tag{3.2}$$

where K_P denotes the proportional gain and K_I the gain coefficient of the resonant term; ω_b and ω_c represents the bandwidth and the central frequency of the resonant controller, respectively.

Corresponding bode plots for the ideal and non-ideal PR controllers are shown in Fig. 3.2, where ω_c is chosen to be the fundamental grid frequency. As illustrated, the ideal PR controller has an infinite gain at the fundamental frequency $f_1 = 50$ Hz due to the resonant term, while the non-ideal PR controller has a finite gain but wider bandwidth. It is desirable to have infinite gains at target frequencies with the ideal PR controller. But it should also be realized that the implementation of an ideal PR controller introduces practical problems due to this infinite gain and, consequently, zero bandwidth, such as being sensitive to central frequency variations and to digital implementation errors. Hence, the non-ideal PR controller is more realistic in practical applications.

Note that the bandwidth of non-ideal resonant controllers is determined by ω_b, which also influences the controller gain around the central frequency. Therefore, it is suggested to increase the gain coefficient K_I, thereby reducing the sensitivity to frequency variations, while simultaneously keeping ω_b as small as possible. The magnitude and the phase angle of $G(s)$ in (3.2) are calculated and given by

$$
\begin{aligned}
|G(j\omega)| &= \sqrt{\frac{(2\omega_b\omega)^2(K_P + K_I)^2 + K_P{}^2(\omega_c^2 - \omega^2)^2}{(2\omega_b\omega)^2 + (\omega_c^2 - \omega^2)^2}} \\
&\approx \sqrt{K_P{}^2 + \left\{\frac{2\omega_b(K_P + K_I)}{\omega}\right\}^2}\Bigg|_{\omega \gg \omega_c},
\end{aligned} \tag{3.3}
$$

$$
\begin{aligned}
\angle G(j\omega) &= \tan^{-1}\left\{\frac{2\omega\omega_b(K_P + K_I)}{K_P(\omega_c^2 - \omega^2)}\right\} - \tan^{-1}\left\{\frac{2\omega\omega_b}{(\omega_c^2 - \omega^2)}\right\} \\
&\approx \tan^{-1}\left\{\frac{\omega K_P}{2\omega_b(K_P + K_I)}\right\} - \frac{\pi}{2}\Bigg|_{\omega \gg \omega_c}.
\end{aligned} \tag{3.4}
$$
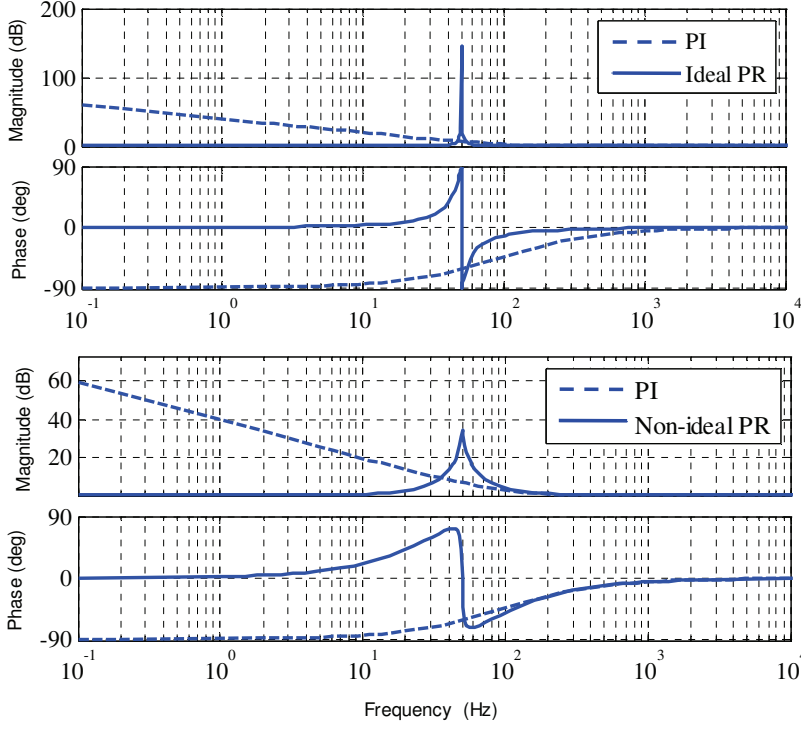
Figure 3.2: Bode plots of ideal and non-ideal proportional resonant (PR) controllers together with PI controller. Here $\omega_c = 2\pi f_1 = 314$ rad/s, $\omega_b = 6$ rad/s, $K_I = 50$, and $K_P = 1$.

To make a comparison between PR and PI controllers, the well-known expression of the PI controller is modified as

$$G(s) = K_P(1 + \frac{1}{s\tau_i}) = K_P + \frac{2\omega_b K_I}{s}, \tag{3.5}$$

where τ_i is the time constant of integrator. With $\tau_i = \frac{K_P}{2\omega_b K_I}$, the resonant term of the non-ideal PR controller and the integrator of the PI controller are determined by the same group of parameters. The magnitude and the phase angle of $G(s)$ in (3.5) are calculated and given by

$$|G(j\omega)| = \sqrt{K_P{}^2 + \left(\frac{2\omega_b K_I}{\omega}\right)^2}, \tag{3.6}$$

$$\angle G(j\omega) = \tan^{-1}\left(\frac{\omega K_P}{2\omega_b K_I}\right) - \frac{\pi}{2}. \tag{3.7}$$

Comparing (3.3) and (3.4) to (3.6) and (3.7), respectively, it can be found that the non-ideal PR and the PI controller have similar frequency responses when ω

is sufficiently larger than ω_c, as shown in Figure 3.2. It implicates that a closed-loop system should be able to achieve the same dynamic response with the PI or PR controllers as compensators given the cross-over frequency (or the control bandwidth) sufficiently larger than ω_c.

However, steady-state errors of closed-loop systems are determined by the gains of controllers at target frequencies. Unfortunately, it can be seen that the PI controller has a very high gain close to the dc frequency and very limited gains around 50 Hz in the magnitude plot. Also, it is noticed that in the phase plot the PI controller introduces phase delay in the low-frequency range, resulting in phase margin[1] reduction within this frequency range. Therefore, PI controllers are more suitable for dc signal regulation, while for the regulation of ac signals PR controllers are more convenient.

3.2.2   Multiple PR controllers at selected frequencies

In the previous section it has been shown that PR controllers only have high gains at central resonant frequencies and almost no influence at other frequencies. This advantage makes it possible to operate multiple PR controllers together without reducing system phase margins to negative values at the cross-over frequency[1]. By adding together more resonant controllers at different central frequencies, multiple PR controllers are expressed by

$$
\begin{aligned}
G(s) = K_P &+ \frac{2\omega_b K_I s}{s^2 + 2\omega_b s + \omega_c^2} \\
&+ \frac{2\omega_{b1} K_{I1} s}{s^2 + 2\omega_{b1} s + \omega_{c1}^2} \\
&+ \frac{2\omega_{b2} K_{I2} s}{s^2 + 2\omega_{b2} s + \omega_{c2}^2} \\
&+ ...,
\end{aligned}
\tag{3.8}
$$

where the parameters for each resonant controller are independent. Figure 3.3 shows a Bode plot of a multiple PR controller with the 1st(50 Hz), 3rd, 5th, 7th, and 9th harmonic frequencies selected.

It can be seen that multiple PR controllers provide high gains at specific frequencies and maintain phase angle zero at high frequencies. However, it should also be noticed that when the selected frequencies of a resonant controller approach the cross-over frequency of an open-loop system, the multiple PR controller will certainly introduce phase delay. For instance, in Fig. 3.3, if the cross-over frequency of a system is around 1 kHz, then there is about 30^0 phase margin reduction by the multiple PR controller. Comparing with Fig. 3.2, there is almost no phase delay at 1 kHz when only the fundamental-frequency resonant controller is used.

Therefore, a combination of PR controllers offers an easy way to regulate ac signals at low-order harmonic frequencies, but one must pay attention to the phase

---

[1]Phase margin, a term in control engineering, is 180^0 plus the phase angle at the cross-over frequency of an open-loop system. It has to be kept positive (conservatively 40^0) when designing control parameters [71].
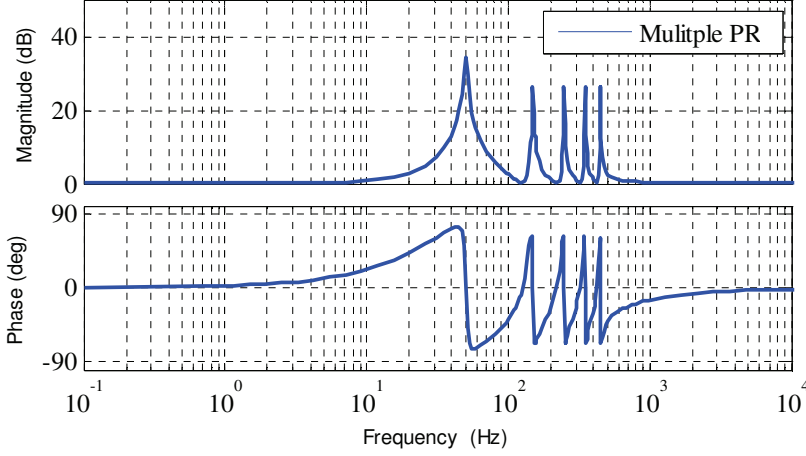
Figure 3.3: Bode plot of multiple non-ideal PR controllers, where the resonant controllers selected for the 3rd, 5th, 7th, and 9th harmonics are assigned the same set of parameters used for the fundamental-frequency resonant controller. Here $\omega_c = 314$ rad/s, $\omega_b = 6$ rad/s, $K_I = 50$, and $K_P = 1$.

margin when using a multiple PR controller for system closed-loop control. More practical considerations have been reported in different applications [72, 73].

3.3 Current regulation in multiple reference frames

This section presents current regulation in different reference frames for grid-connected converters with the previously described linear controllers. For dealing with a variety of grid conditions, such as three-wire or four-wire unbalanced and distorted grid conditions, three-phase four-leg voltage source converters [74, 75] are chosen to investigate generalized applications in the next chapters.

Hence, a four-leg grid-connected system, as shown in Fig. 3.4, is presented here as an example to demonstrate the modeling of three-phase grid-interfacing systems and for comparing current regulators based on PR and PI controllers. A fourth switching leg not only brings one more control degree of freedom than three-wire converters (Fig. 3.4 (b)), but also prevents neutral currents causing voltage ripple on dc capacitors (in other words, reduced number of dc capacitors is needed). This cannot be achieved by four-wire three-leg converters with split dc capacitors (Fig. 3.4 (c)). In the following, the system employed in Fig. 3.4 (a) is modeled in multiple reference frames, namely natural reference frame, stationary reference frame, and synchronous reference frame.

3.3.1 Average model of a four-leg converter system

Average models, as the name indicates, are often used for simplifying the description of PWM converters by averaging the output voltage per switching period

(a)

(b)   (c)
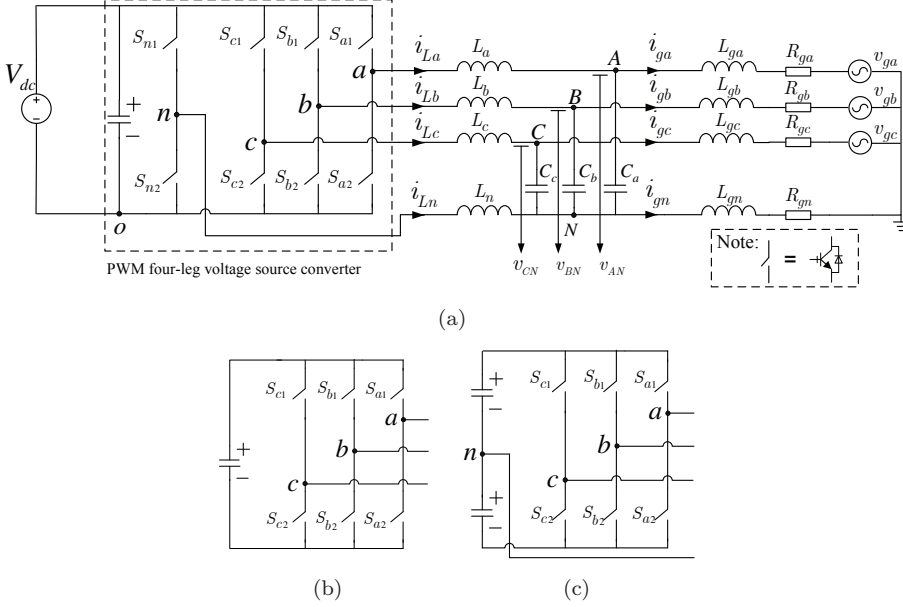
Figure 3.4: Circuit diagrams: (a) three-phase four-leg grid-interfacing converter system, (b) a three-leg converter, and (c) a four-wire three-leg converter with split dc capacitors.

when switching frequencies are much higher than the fundamental frequency of the output voltage.

Figure 3.5 shows the simplification from a switching model to an average model of one switching leg, where the output voltage of the switching leg is represented by a controlled voltage source with the duty cycle d_x (the subscript x represents leg a, b, c, or n) as a gain. In this work, the four-leg converter is controlled with high-frequency PWM and the duty cycle d_x is given by

$$d_x = \frac{1}{2}(1 + \frac{v_{mx}}{V_c}) = \frac{1}{2}(1 + m_x), \tag{3.9}$$

where m_x is called modulation index, and v_{mx} the modulating signal for switching-leg "x"; V_c is the magnitude of carrier waveform. By applying this simplification to the four-leg converter system in Fig. 3.4 (a), an average model is derived, as shown in Fig. 3.6. Consequently, the current and voltage quantities in the average model involve only low-frequency components of those corresponding quantities in the switching model[2].

For further simplification of the mathematical expressions in the following models, $L_{a,b,c}$ are assumed to be an identical value L; $C_{a,b,c}$ are set to the same value C; similarly, $L_{ga,gb,gc}$ are represented by L_g, and $R_{ga,gb,gc}$ are represented by R_g [3].

---

[2]The assumptions are: a) no discontinuous conduction (switches are complementary) and b) filters do not influence signal frequencies.

[3]In case of asymmetric parameters in real systems due to component tolerances, resulting
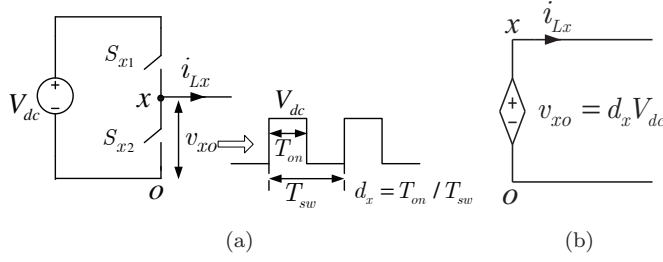
Figure 3.5: Circuit representations: (a) the switching model and (b) the average model of of a switching leg, where x represents a, b, c, or n.
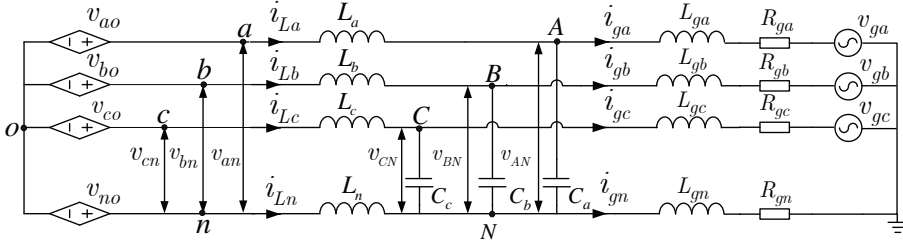
Figure 3.6: Average model of a three-phase four-leg grid-interfacing converter system in natural reference frame.

Note that the neutral-line inductor L_n is selectively used for mitigating switching-frequency ripples at the star point N, and its inductance can be designed smaller than L [76]. Describing the average-model system by differential equations gives

$$\begin{bmatrix} v_{an} \\ v_{bn} \\ v_{cn} \end{bmatrix} = \frac{V_{dc}}{2} \begin{bmatrix} m_a - m_n \\ m_b - m_n \\ m_c - m_n \end{bmatrix} = L\frac{\mathrm{d}}{\mathrm{d}t}\begin{bmatrix} i_{La} \\ i_{Lb} \\ i_{Lc} \end{bmatrix} - L_n\frac{\mathrm{d}}{\mathrm{d}t}\begin{bmatrix} i_{Ln} \\ i_{Ln} \\ i_{Ln} \end{bmatrix} + \begin{bmatrix} v_{AN} \\ v_{BN} \\ v_{CN} \end{bmatrix}, \quad (3.10)$$

$$\begin{bmatrix} v_{AN} \\ v_{BN} \\ v_{CN} \end{bmatrix} = \left(L_g\frac{\mathrm{d}}{\mathrm{d}t} + R_g\right)\begin{bmatrix} i_{ga} \\ i_{gb} \\ i_{gc} \end{bmatrix} - \left(L_{gn}\frac{\mathrm{d}}{\mathrm{d}t} + R_{gn}\right)\begin{bmatrix} i_{gn} \\ i_{gn} \\ i_{gn} \end{bmatrix} + \begin{bmatrix} v_{ga} \\ v_{gb} \\ v_{gc} \end{bmatrix}, \quad (3.11)$$

$$\frac{\mathrm{d}}{\mathrm{d}t}\begin{bmatrix} v_{AN} \\ v_{BN} \\ v_{CN} \end{bmatrix} = \frac{1}{C}\left(\begin{bmatrix} i_{La} \\ i_{Lb} \\ i_{Lc} \end{bmatrix} - \begin{bmatrix} i_{ga} \\ i_{gb} \\ i_{gc} \end{bmatrix}\right). \quad (3.12)$$

It can be seen from (3.10) to (3.12) that three-phase quantities are coupled with each other through neutral currents; the control of modulation indices $m_{a,b,c}$

---

currents and voltages will be unbalanced in an open-loop system even with balanced modulating signals. Nevertheless, with closed-loop control, these influences can be compensated.

is coupled with m_n. Differing from three-leg converter systems, the four-leg converter provides an additional degree of freedom to deal with neutral currents (zero-sequence currents) but, due to the coupling terms, also makes it difficult and complicated to implement controllers direct in the natural abc reference frame. In order to have an explicit design on controllers and to make compensators to operate independently, a decoupling transformation is necessary, as presented in the following.

3.3.2 Stationary-frame current regulation

A matrix for decoupling transformation from phase quantities in the abc-frame to orthogonal quantities in the $\alpha\beta\gamma$-frame was proposed in [77]. In power-invariant form it is given as

$$\boldsymbol{T}_{\alpha\beta\gamma 1} = \sqrt{\frac{2}{3}} \begin{bmatrix} 1 & -1/2 & -1/2 & 0 \\ 0 & \sqrt{3}/2 & -\sqrt{3}/2 & 0 \\ 1/\sqrt{8} & 1/\sqrt{8} & 1/\sqrt{8} & -3/\sqrt{8} \end{bmatrix}. \tag{3.13}$$

Compared to $\boldsymbol{T}_{\alpha\beta\gamma}$ of (2.10), apart from the difference between the coefficient $\sqrt{2/3}$ for power-invariant transformation and $2/3$ for amplitude-invariant transformation, also some of the other coefficients in $\boldsymbol{T}_{\alpha\beta\gamma 1}$ are chosen differently. In order to achieve decoupled three-phase control, the coefficients for the γ-axis quantities in $\boldsymbol{T}_{\alpha\beta\gamma 1}$ are modified, while the matrix parameters for α- and β-axis quantities remain the same as the conventional $\alpha\beta$ transformation (Clarke transformation) matrix. For $\boldsymbol{T}_{\alpha\beta\gamma}$, the transformation from zero-sequence components to γ-axis components is imposed to be amplitude invariant.

A simple derivation of $\boldsymbol{T}_{\alpha\beta\gamma 1}$ and its reduced transforms for phase quantities in practical implementations can be found in Appendix A. With $\boldsymbol{T}_{\alpha\beta\gamma 1}$, the corresponding transformations and notations are given by

$$\begin{bmatrix} v_\alpha \\ v_\beta \\ v_\gamma \end{bmatrix} = \boldsymbol{T}_{\alpha\beta\gamma 1} \begin{bmatrix} v_{an} \\ v_{bn} \\ v_{cn} \\ 0 \end{bmatrix}, \begin{bmatrix} v_{N\alpha} \\ v_{N\beta} \\ v_{N\gamma} \end{bmatrix} = \boldsymbol{T}_{\alpha\beta\gamma 1} \begin{bmatrix} v_{AN} \\ v_{BN} \\ v_{CN} \\ 0 \end{bmatrix}, \begin{bmatrix} v_{g\alpha} \\ v_{g\beta} \\ v_{g\gamma} \end{bmatrix} = \boldsymbol{T}_{\alpha\beta\gamma 1} \begin{bmatrix} v_{ga} \\ v_{gb} \\ v_{gc} \\ 0 \end{bmatrix}, \tag{3.14}$$

$$\begin{bmatrix} i_{L\alpha} \\ i_{L\beta} \\ i_{L\gamma} \end{bmatrix} = \boldsymbol{T}_{\alpha\beta\gamma 1} \begin{bmatrix} i_{La} \\ i_{Lb} \\ i_{Lc} \\ i_{Ln} \end{bmatrix}, \begin{bmatrix} i_{g\alpha} \\ i_{g\beta} \\ i_{g\gamma} \end{bmatrix} = \boldsymbol{T}_{\alpha\beta\gamma 1} \begin{bmatrix} i_{ga} \\ i_{gb} \\ i_{gc} \\ i_{gn} \end{bmatrix}. \tag{3.15}$$

In order to apply the transformations of (3.14) and (3.15) to (3.10), a fourth row with neutral current i_{Ln} is added to the vectors of (3.10), that is

$$\begin{bmatrix} v_{an} \\ v_{bn} \\ v_{cn} \\ 0 \end{bmatrix} = \frac{V_{dc}}{2} \begin{bmatrix} m_a - m_n \\ m_b - m_n \\ m_c - m_n \\ 0 \end{bmatrix} = L\frac{\mathrm{d}}{\mathrm{d}t}\begin{bmatrix} i_{La} \\ i_{Lb} \\ i_{Lc} \\ i_{Ln} \end{bmatrix} - L_n\frac{\mathrm{d}}{\mathrm{d}t}\begin{bmatrix} i_{Ln} \\ i_{Ln} \\ i_{Ln} \\ \frac{L}{L_n}i_{Ln} \end{bmatrix} + \begin{bmatrix} v_{AN} \\ v_{BN} \\ v_{CN} \\ 0 \end{bmatrix}. \tag{3.16}$$
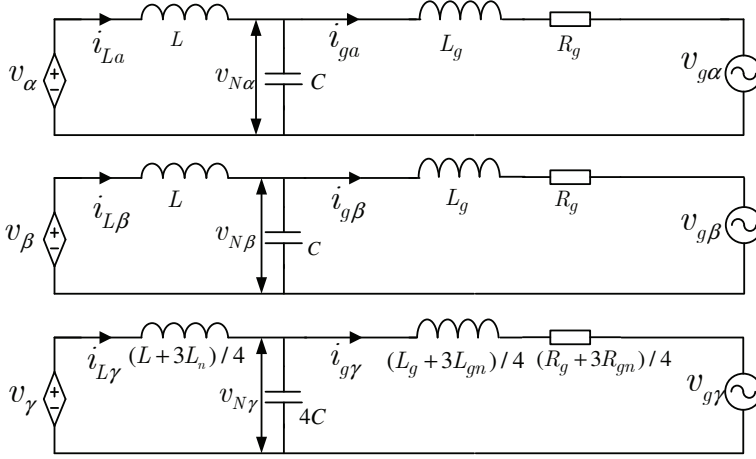
Figure 3.7: Average model of a three-phase four-leg grid-interfacing converter system in stationary reference frame.

Then, by multiplying $\boldsymbol{T}_{\alpha\beta\gamma 1}$ on both sides of (3.16) and after some manipulations with the constraint $i_{La} + i_{Lb} + i_{Lc} + i_{Ln} = 0$, it follows that

$$
\begin{bmatrix} v_\alpha \\ v_\beta \\ v_\gamma \end{bmatrix} = \frac{V_{dc}}{2} \begin{bmatrix} m_\alpha \\ m_\beta \\ m_\gamma \end{bmatrix} = \begin{bmatrix} L & 0 & 0 \\ 0 & L & 0 \\ 0 & 0 & (L+3L_n)/4 \end{bmatrix} \frac{\mathrm{d}}{\mathrm{d}t} \begin{bmatrix} i_{L\alpha} \\ i_{L\beta} \\ i_{L\gamma} \end{bmatrix} + \begin{bmatrix} v_{N\alpha} \\ v_{N\beta} \\ v_{N\gamma} \end{bmatrix}. \quad (3.17)
$$

Similar transformations are applied to (3.11) and (3.12), derived as

$$
\begin{aligned}
\begin{bmatrix} v_{N\alpha} \\ v_{N\beta} \\ v_{N\gamma} \end{bmatrix} &= \begin{bmatrix} L_g & 0 & 0 \\ 0 & L_g & 0 \\ 0 & 0 & (L_g+3L_{gn})/4 \end{bmatrix} \frac{\mathrm{d}}{\mathrm{d}t} \begin{bmatrix} i_{g\alpha} \\ i_{g\beta} \\ i_{g\gamma} \end{bmatrix} \\
&+ \begin{bmatrix} R_g & 0 & 0 \\ 0 & R_g & 0 \\ 0 & 0 & (R_g+3R_{gn})/4 \end{bmatrix} \begin{bmatrix} i_{g\alpha} \\ i_{g\beta} \\ i_{g\gamma} \end{bmatrix} + \begin{bmatrix} v_{g\alpha} \\ v_{g\beta} \\ v_{g\gamma} \end{bmatrix}, \quad (3.18)
\end{aligned}
$$

$$
\frac{\mathrm{d}}{\mathrm{d}t} \begin{bmatrix} v_{N\alpha} \\ v_{N\beta} \\ v_{N\gamma} \end{bmatrix} = \frac{1}{C} \left(\begin{bmatrix} i_{L\alpha} \\ i_{L\beta} \\ i_{L\gamma}/4 \end{bmatrix} - \begin{bmatrix} i_{g\alpha} \\ i_{g\beta} \\ i_{g\gamma}/4 \end{bmatrix} \right). \quad (3.19)
$$

Based on the model described by (3.17) to (3.19), the average model in Fig. 3.6 is transformed to the average model in the stationary frame, as shown in Fig. 3.7. Clearly, the three control inputs $v_{\alpha,\beta,\gamma}$ or $m_{\alpha,\beta,\gamma}$ can independently regulate the grid currents $i_{g\alpha,g\beta,g\gamma}$ or the inductor currents $i_{L\alpha,L\beta,L\gamma}$. As already explained in Section 2.2, α- and β-axis quantities are only composed of positive- and negative-sequence components of unbalanced quantities, and zero-sequence components are only related to γ-axis quantities. For three-wire systems or four-wire systems without zero-sequence components the γ-axis quantities do not exist.

(a)

(b)
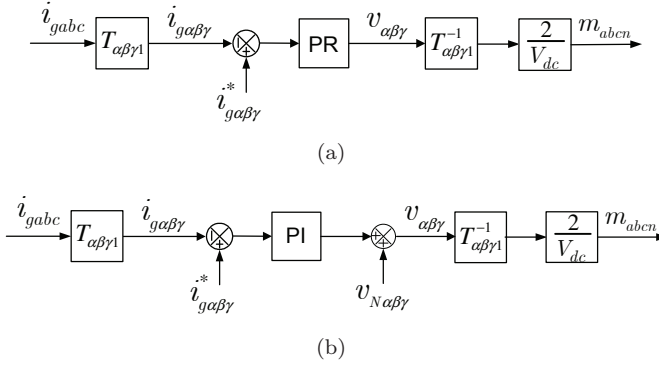
Figure 3.8: Stationary-frame current regulation: (a) with PR controllers and (b) with PI controllers plus voltage feed-forward loop.

Note that the physical parameters of the γ-axis model in Fig. 3.7 are different from the other two axes after the decoupling transformation, thereby causing the plant model to change. For instance, the neutral inductor is designed as $L/3$ in this work, so the cutoff frequency of the output LC filter is lower than the cutoff frequency of the LC filter in α or β quantities. Reflecting on control design with PI or PR controllers as compensators, the proportional gain should be assigned with smaller values than the proportional gains of the α or β quantities.

Figure 3.8 shows the block diagram of grid current regulation with PR or PI controllers, disregarding external current reference calculations and internal control loops for improving system stability. Furthermore, multiple PR controllers can be directly added to the block of PR controllers for eliminating current distortion (e.g. caused by dead-time effects or by polluted grid voltages). Because of low gains of PI controllers at 50 Hz, in Fig. 3.8 (b), an additional output voltage feed-forward loop is added to reduce steady-state error [78]. However, the voltage feed-forward loop can introduce low-order harmonic components when grid voltages are polluted, and this will cause harmonic currents.

With the three outputs $v_{\alpha,\beta,\gamma}$ derived from the stationary frame current regulation, four modulation indices of the four switching legs are calculated by

$$
\begin{bmatrix} m_a \\ m_b \\ m_c \\ m_n \end{bmatrix} = \boldsymbol{T}_{\alpha\beta\gamma 1}^{-1} \begin{bmatrix} m_\alpha \\ m_\beta \\ m_\gamma \end{bmatrix} = \frac{2}{V_{dc}} \boldsymbol{T}_{\alpha\beta\gamma 1}^{-1} \begin{bmatrix} v_\alpha \\ v_\beta \\ v_\gamma \end{bmatrix} \tag{3.20}
$$

with

$$
\boldsymbol{T}_{\alpha\beta\gamma 1}^{-1} = \sqrt{\frac{2}{3}} \begin{bmatrix} 1 & 0 & 1/\sqrt{8} \\ -1/2 & \sqrt{3}/2 & 1/\sqrt{8} \\ -1/2 & -\sqrt{3}/2 & 1/\sqrt{8} \\ 0 & 0 & -3/\sqrt{8} \end{bmatrix}. \tag{3.21}
$$

3.3.3 Synchronous-frame current regulation

Conventionally, output currents of three-phase grid-connected converters are regulated with PI controllers in synchronous reference frame (SRF). By transforming balanced three-phase signals into the SRF, where ac signals become dc quantities, steady-state error can be effectively eliminated with e.g. a PI controller. However, under unbalanced grid conditions conventional SRF current regulation has to be used and the situation becomes more complicated.

In the previous section, three-phase unbalanced quantities were transformed to the stationary frame and represented by α, β, and γ quantities. As presented in Section 2.2, α and β quantities are composed of positive- and negative-sequence components. Taking fundamental-frequency voltage quantities as an example, it is expressed with

$$\underline{v}_{\alpha\beta} = v_\alpha + jv_\beta = \underline{V}_1^+ e^{j\omega_1 t} + \underline{V}_1^- e^{-j\omega_1 t}, \qquad (3.22)$$

where complex numbers are denoted with a bar subscript, the subscripts "+" and "-" denote positive and negative sequences, respectively.

Corresponding quantities in the positive SRF are given by

$$\underline{v}_{dq}^+ = e^{-j\omega_1 t} \underline{v}_{\alpha\beta} = \underline{V}_1^+ + \underline{V}_1^- e^{-j2\omega_1 t} \qquad (3.23)$$

and in the negative SRF,

$$\underline{v}_{dq}^- = e^{j\omega_1 t} \underline{v}_{\alpha\beta} = \underline{V}_1^+ e^{j2\omega_1 t} + \underline{V}_1^- \qquad (3.24)$$

with $\underline{v}_{dq}^{+,-} = v_d^{+,-} + jv_q^{+,-}$. The stationary frame γ quantities, remain unchanged in SRF, i.e.

$$v_o = v_\gamma. \qquad (3.25)$$

Rewriting (3.23) to (3.25) as vectors gives

$$\begin{bmatrix} v_d^+ \\ v_q^+ \\ v_d^- \\ v_q^- \\ v_o \end{bmatrix} = \boldsymbol{T}_r \begin{bmatrix} v_\alpha \\ v_\beta \\ v_\gamma \end{bmatrix}, \qquad (3.26)$$

where

$$\boldsymbol{T}_r = \begin{bmatrix} \cos\omega_1 t & \sin\omega_1 t & 0 \\ -\sin\omega_1 t & \cos\omega_1 t & 0 \\ \cos\omega_1 t & -\sin\omega_1 t & 0 \\ \sin\omega_1 t & \cos\omega_1 t & 0 \\ 0 & 0 & 1 \end{bmatrix}. \qquad (3.27)$$

This rotating transformation can be similarly applied to other quantities. For instance, by multiplying $\boldsymbol{T}_r \boldsymbol{T}_{\alpha\beta\gamma 1}$ on both sides of (3.16), the average model in

the natural frame is transformed to the SRF, as represented by

$$
\begin{bmatrix} v_d^+ \\ v_q^+ \\ v_d^- \\ v_q^- \\ v_o \end{bmatrix} = \frac{V_{dc}}{2} \begin{bmatrix} m_d^+ \\ m_q^+ \\ m_d^- \\ m_q^- \\ m_o \end{bmatrix} = \begin{bmatrix} L & 0 & 0 \\ 0 & L & 0 \\ L & 0 & 0 \\ 0 & L & 0 \\ 0 & 0 & \frac{L+3L_n}{4} \end{bmatrix} \left(\frac{d}{dt} \begin{bmatrix} i_{Ld}^+ \\ i_{Lq}^+ \\ i_{Ld}^- \\ i_{Lq}^- \\ i_{Lo} \end{bmatrix} + \omega_1 \begin{bmatrix} i_{Lq}^+ \\ -i_{Ld}^+ \\ -i_{Lq}^- \\ i_{Ld}^- \\ 0 \end{bmatrix} \right) + \begin{bmatrix} v_{Nd}^+ \\ v_{Nq}^+ \\ v_{Nd}^- \\ v_{Nq}^- \\ v_{No} \end{bmatrix} .
$$
(3.28)

Similarly, (3.11) and (3.12) are transformed to the SRF, i.e.

$$
\begin{bmatrix} v_{Nd}^+ \\ v_{Nq}^+ \\ v_{Nd}^- \\ v_{Nq}^- \\ v_{No} \end{bmatrix} = \begin{bmatrix} L_g & 0 & 0 \\ 0 & L_g & 0 \\ L_g & 0 & 0 \\ 0 & L_g & 0 \\ 0 & 0 & (L_g+3L_{gn})/4 \end{bmatrix} \left(\frac{d}{dt} \begin{bmatrix} i_{gd}^+ \\ i_{gq}^+ \\ i_{gd}^- \\ i_{gq}^- \\ i_{go} \end{bmatrix} + \omega_1 \begin{bmatrix} i_{gq}^+ \\ -i_{gd}^+ \\ -i_{gq}^- \\ i_{gd}^- \\ 0 \end{bmatrix} \right)
$$
$$
+ \begin{bmatrix} R_g & 0 & 0 \\ 0 & R_g & 0 \\ R_g & 0 & 0 \\ 0 & R_g & 0 \\ 0 & 0 & (R_g+3R_{gn})/4 \end{bmatrix} \begin{bmatrix} i_{gd}^+ \\ i_{gq}^+ \\ i_{gd}^- \\ i_{gq}^- \\ i_{go} \end{bmatrix} + \begin{bmatrix} v_{gd}^+ \\ v_{gq}^+ \\ v_{gd}^- \\ v_{gq}^- \\ v_{g0} \end{bmatrix} ,
$$
(3.29)

$$
\frac{d}{dt} \begin{bmatrix} v_{Nd}^+ \\ v_{Nq}^+ \\ v_{Nd}^- \\ v_{Nq}^- \\ v_{No} \end{bmatrix} = \frac{1}{C} \left(\begin{bmatrix} i_{Ld}^+ \\ i_{Lq}^+ \\ i_{Ld}^- \\ i_{Lq}^- \\ i_{Lo}/4 \end{bmatrix} - \begin{bmatrix} i_{gd}^+ \\ i_{gq}^+ \\ i_{gd}^- \\ i_{gq}^- \\ i_{go}/4 \end{bmatrix} \right) + \omega_1 \begin{bmatrix} -v_{Nq}^+ \\ v_{Nd}^+ \\ v_{Nq}^- \\ -v_{Nd}^- \\ 0 \end{bmatrix} .
$$
(3.30)

   Based on (3.28) to (3.30), the average model of the four-leg converter system in the SRF is shown in Fig. 3.9. Strictly speaking, this model is not completely described in the SRF because the o-axis variables contain the same quantities as in the γ-axis model of the stationary frame. Of course, like the methods used in single-phase system applications [79], by making a set of virtual orthogonal quantities with respect to these γ quantities and applying the same rotating transformation used for α, β quantities, the γ-axis model also can be transformed to the SRF. However, this is complicated and also unnecessary since PR controllers are available for γ quantities.

   Figure 3.10 shows the current regulation based on the average model in Fig. 3.9. As illustrated, dual SRF PI current control schemes [24, 25, 66] are used for controlling positive-sequence and negative-sequence components separately, while o-axis quantities (or γ-axis quantities) are regulated by a PR controller. It can be seen that the dual current control scheme is complex and requires double the number of control parts, namely filters (for removing major ac components at twice the fundamental frequency), PI controllers, cross decoupling terms, and reference-frame transformations (represented by $e^{j\omega_1 t}$ and $e^{-j\omega_1 t}$).

   Comparing the overall structures in Fig. (3.8) (a) and Fig. (3.10), the complexity of current regulation with stationary frame PR controllers under unbalanced
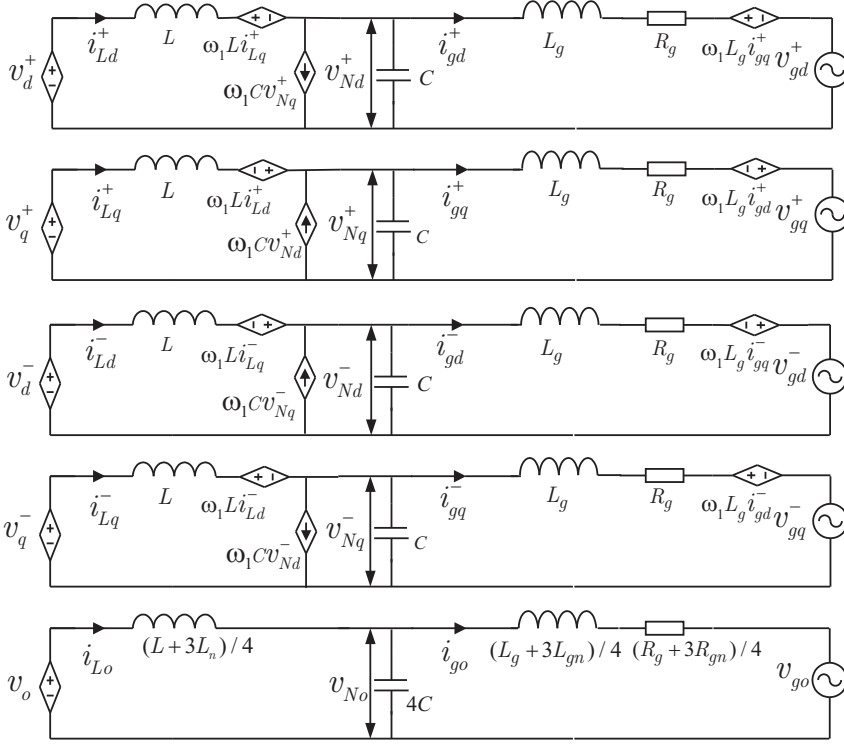
Figure 3.9: Average model of a three-phase four-leg grid-interfacing converter system in the synchronous reference frame.

conditions is considerably reduced. The reason is that the resonant controller part regulates positive-sequence and negative-sequence components jointly in the stationary frame.

However, it is noticed that, the PR controller has the advantages presented above only when both positive-sequence and negative-sequence components are regulated together. There are some situations where only individual sequence quantities need to be regulated. For example, a series connected power quality compensator, which consists of a voltage source inverter in between the upstream grid and the downstream loads or micro-grid through a injection transformer, can be used for the elimination of asymmetrical currents by only regulating negative-sequence currents [41, 42]. Since the PR controller cannot separately control the negative-sequence component of unbalanced feedback currents, the PI control in the negative-sequence SRF (see Fig. 3.10) is again preferred [41]. Another solution is to filter out the target signals with a stationary-frame resonant filter [68], and then to perform current regulation with a PR controller.

As a result, stationary-frame PR controllers are chosen in this work for regulating positive- and negative-sequence quantities together and for regulating zero-sequence quantities independently. To complement the existing PR controllers, an
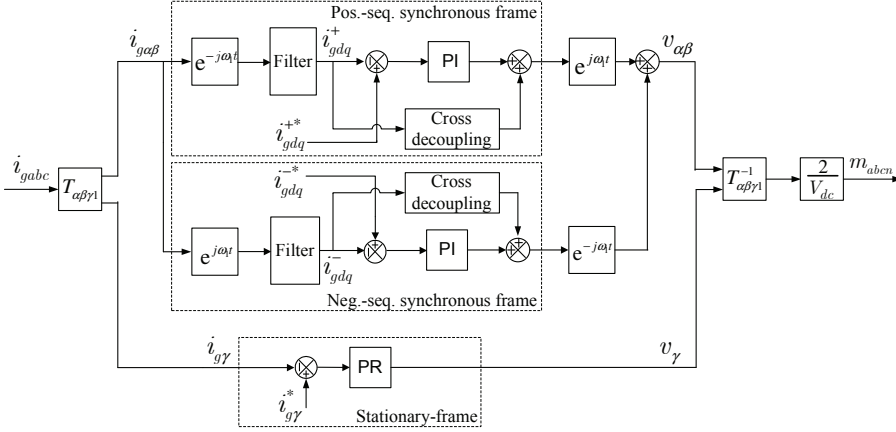
Figure 3.10: Current regulation consists of synchronous frame PI controllers for positive- and negative-sequence components, and stationary frame PR controllers for zero-sequence components (γ-axis quantities).

extended resonant controller, which maintains the advantages of the conventional resonant controller and is able to achieve individual positive- or negative-sequence control, is therefore proposed in the next section.

3.4   Sequence-decoupled resonant (SDR) controllers

Conventional PR controllers were derived from either the stationary-frame integrator directly [50], or by the inverse transformation of the synchronous-frame PI controller to the stationary frame [67, 68]. In a similar manner to the second method, this section presents the derivation of the proposed sequence-decoupled resonant (SDR) controllers, categorized into two types, i.e., ideal and non-ideal SDR controllers. Differing from PR controllers, the derived SDR controllers are given in the form of complex transfer functions [80] and implemented in a multi-state-variable structure, a similar idea as the stationary frame filters in Chapter 2.

3.4.1   Ideal SDR controller

It is well-known that a proportional (P) and a resonant (R) controller can be combined as a PR controller for the control of error feedback, where most of the high frequency or transient response of the regulator is determined by the proportional gain, while the resonant controller gain determines the steady-state error. The proposed SDR controller can also cooperate with a P controller or with other control loops, as will be presented in the application examples in latter sections. Since the P controller has the same function independent of the reference frame, only the SDR controller part is analyzed in the following.
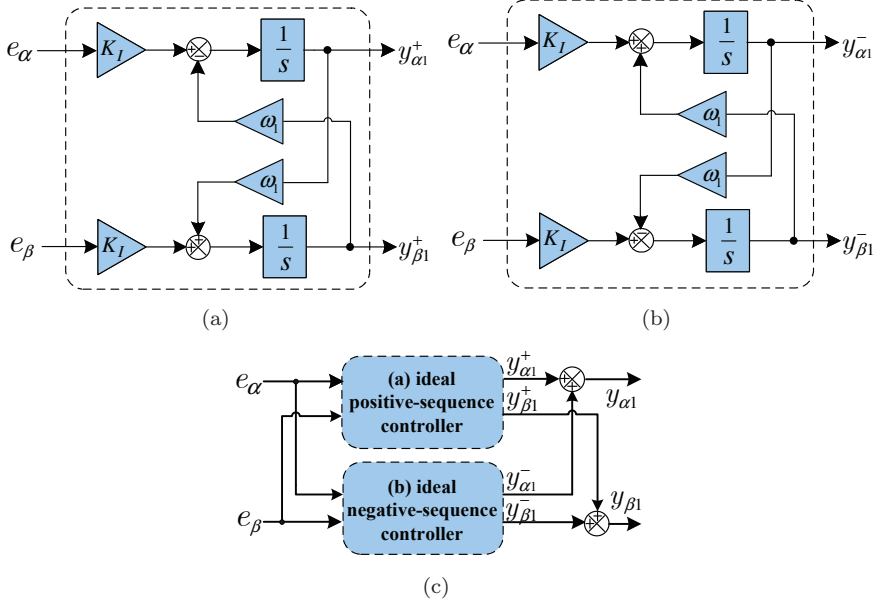
Figure 3.11: Proposed ideal SDR controllers for regulating: (a) fundamental positive-sequence components, (b) fundamental negative-sequence components, and (c) both sequence components.

Disregarding zero-sequence components, three-phase feedback error signals may consist of fundamental positive-sequence, negative-sequence components, and harmonics, as expressed in the stationary $\alpha\beta$ frame and written with complex variables as

$$
\begin{aligned}
\underline{e}_{\alpha\beta}(t) &= e_\alpha(t) + je_\beta(t) \\
&= \sum_{n=1,3\cdots}^{\infty} (\underline{E}_n^+ e^{jn\omega_1 t} + \underline{E}_n^- e^{-jn\omega_1 t}),
\end{aligned}
\tag{3.31}
$$

where n is the harmonic number, ω_1 the fundamental angular frequency; complex numbers are denoted with a bar subscript, and superscript "$+$" and "$-$" denote positive and negative sequences, respectively. Note that zero-sequence components in unbalanced four-wire systems are not discussed because they are independent of positive-sequence and negative-sequence components and can be regulated independently with a PR controller.

The signal $\underline{e}_{\alpha\beta}(t)$ can be transformed to the SRF by multiplying (3.31) with $e^{-j\omega_1 t}$ and $e^{j\omega_1 t}$, which corresponds to the positive and negative SRF, respectively. That is

$$
\begin{aligned}
\underline{e}_{\alpha\beta}(t)e^{-j\omega_1 t} &= \underline{E}_1^+ + \sum_{n=2,4,\cdots}^{\infty} (\underline{E}_n^+ e^{jn\omega_1 t} + \underline{E}_n^- e^{-jn\omega_1 t}), \\
\underline{e}_{\alpha\beta}(t)e^{j\omega_1 t} &= \underline{E}_1^- + \sum_{n=2,4,\cdots}^{\infty} (\underline{E}_n^+ e^{jn\omega_1 t} + \underline{E}_n^- e^{-jn\omega_1 t}).
\end{aligned}
\tag{3.32}
$$

It can be seen that the fundamental positive- and negative-sequence error sig-

nals appear as time-independent complex numbers (with dc quantities for both the real and imaginary parts) in the respective synchronous frames. In order to eliminate the error once the control loop is closed, an ideal integrator can be used to generate an infinite gain for the dc components in (3.32), as expressed in the frequency domain by

$$\underline{y}^+_{\alpha\beta1}(s + j\omega_1) = \underline{e}_{\alpha\beta}(s + j\omega_1)\frac{K_I}{s},$$
$$\underline{y}^-_{\alpha\beta1}(s - j\omega_1) = \underline{e}_{\alpha\beta}(s - j\omega_1)\frac{K_I}{s}, \tag{3.33}$$

where $\underline{y}^+_{\alpha\beta1}(s + j\omega_1)$ and $\underline{y}^-_{\alpha\beta1}(s - j\omega_1)$ are positive- and negative-sequence control output signals, respectively, in the corresponding synchronous frames, and K_I is the integrator gain.

Similar to the derivation of the conventional R controller [68], by making use of an inverse transformation of the integrator back to the stationary frame, $s - j\omega_1 \rightarrow s$ is substituted into the first equation of (3.33), and $s + j\omega_1 \rightarrow s$ into the second one. It follows that

$$\underline{y}^+_{\alpha\beta1}(s) = \underline{e}_{\alpha\beta}(s)\frac{K_I}{s - j\omega_1},$$
$$\underline{y}^-_{\alpha\beta1}(s) = \underline{e}_{\alpha\beta}(s)\frac{K_I}{s + j\omega_1}. \tag{3.34}$$

Therefore, the SDR controllers for positive- and negative-sequence complex variables, written in form of complex transfer functions, are $\underline{G}^+(s) = \frac{K_I}{s - j\omega_1}$, $\underline{G}^-(s) = \frac{K_I}{s + j\omega_1}$, respectively.

By expanding the complex variables in (3.34), the following equations are derived:

$$sy^+_{\alpha1}(s) + \omega_1 y^+_{\beta1}(s) = K_I e_\alpha(s),$$
$$sy^+_{\beta1}(s) - \omega_1 y^+_{\alpha1}(s) = K_I e_\beta(s), \tag{3.35}$$

$$sy^-_{\alpha1}(s) - \omega_1 y^-_{\beta1}(s) = K_I e_\alpha(s),$$
$$sy^-_{\beta1}(s) + \omega_1 y^-_{\alpha1}(s) = K_I e_\beta(s). \tag{3.36}$$

Instead of solving (3.35) and (3.36) directly, they can be represented in a multi-state-variable structure as

$$y^+_{\alpha1}(s) = \frac{1}{s}[K_I e_\alpha(s) - \omega_1 y^+_{\beta1}(s)],$$
$$y^+_{\beta1}(s) = \frac{1}{s}[K_I e_\beta(s) + \omega_1 y^+_{\alpha1}(s)], \tag{3.37}$$

$$y^-_{\alpha1}(s) = \frac{1}{s}[K_I e_\alpha(s) + \omega_1 y^-_{\beta1}(s)],$$
$$y^-_{\beta1}(s) = \frac{1}{s}[K_I e_\beta(s) - \omega_1 y^-_{\alpha1}(s)]. \tag{3.38}$$
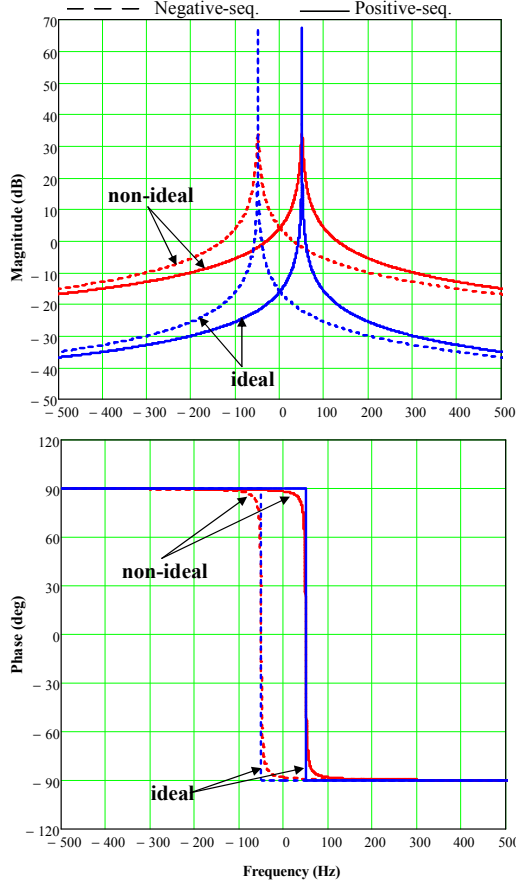
Figure 3.12: Ideal and non-ideal SDR controller plots in the frequency domain, for the fundamental angular frequency $\omega_1 = 314$ rad/s, the bandwidth $\omega_b = 10$ rad/s, and $K_I = 50$.

In this manner, equations (3.37) and (3.38) can be easily implemented in the $\alpha\beta$ frame in the time domain by digital techniques or by analoge circuits. Fig. 3.11 shows the implementation structure diagrams of the controllers for regulating positive-sequence, negative-sequence components or for both sequence components. This controller is called an ideal SDR controller, since it theoretically has an infinite gain at the central frequency ω_1. As shown in Fig. 3.12, the frequency responses of the complex transfer functions ($\underline{G}^+(s)$ and $\underline{G}^-(s)$) in (3.34) are plotted. Note that, since the complex transfer functions are symmetric around the central frequency, both positive and negative frequencies are plotted using a linear frequency scale. As illustrated by Fig. 3.12, the derived ideal SDR controllers can be interpreted as compensators for individual sequence complex variables with a gain for the magnitude regulation and a zero phase-shift at the central frequency. This differs from the conventional resonant controller that compensates independent

(a)   (b)

(c)
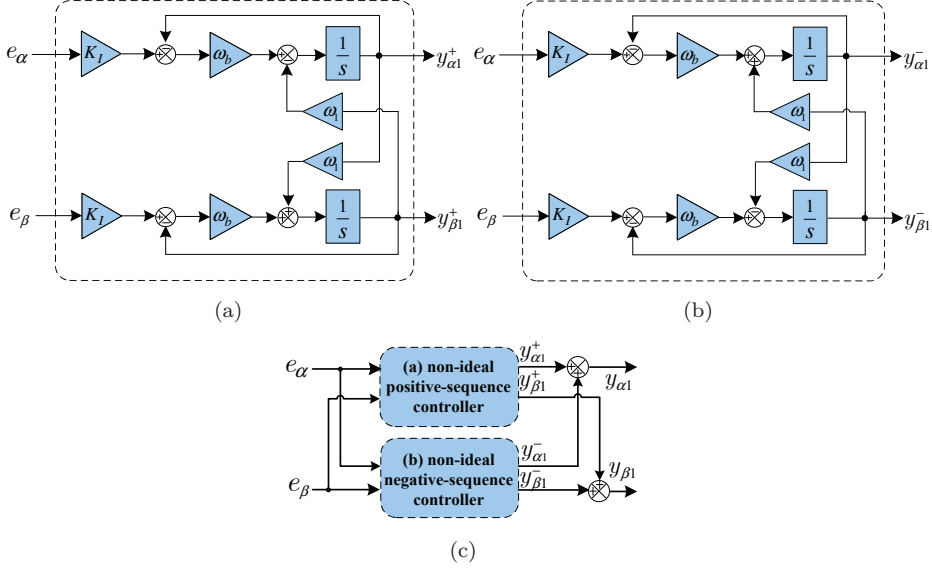
Figure 3.13: Proposed non-ideal SDR controllers for regulating: (a) fundamental positive-sequence components, (b) fundamental negative-sequence components, and (c) both sequence components.

variables along the α and β axes in the stationary frame.

3.4.2   Non-ideal SDR controller

Similar to the conventional ideal PR controllers, due to an infinite gain, there can be practical problems during the implementation of the proposed ideal SDR controller. One such problem is being sensitive to central frequency variations. Therefore, in the following it is proposed corresponding to the conventional non-ideal PR controller, a non-ideal SDR controller suitable for practical applications. Instead of an ideal integrator, a first-order non-ideal integrator is used in (3.33), and by applying the inverse transformation back to the stationary frame it follows that

$$
\begin{aligned}
\underline{y}^{+}_{\alpha\beta1}(s) &= \underline{e}_{\alpha\beta}(s)\frac{K_I \cdot \omega_b}{s - j\omega_1 + \omega_b}, \\
\underline{y}^{-}_{\alpha\beta1}(s) &= \underline{e}_{\alpha\beta}(s)\frac{K_I \cdot \omega_b}{s + j\omega_1 + \omega_b},
\end{aligned}
\tag{3.39}
$$

where ω_b is the cutoff frequency of the non-ideal integrator. Therefore, the non-ideal SDR controllers for positive- and negative-sequence complex variables are $\underline{G}^{+}(s) = \frac{K_I \cdot \omega_b}{s - j\omega_1 + \omega_b}$, $\underline{G}^{-}(s) = \frac{K_I \cdot \omega_b}{s + j\omega_1 + \omega_b}$, respectively.

Likewise, expanding the complex variables, it is derived from (3.39) that

$$sy_{\alpha 1}^+(s) + \omega_b y_{\alpha 1}^+(s) + \omega_1 y_{\beta 1}^+(s) = K_I \omega_b e_\alpha(s),$$
$$sy_{\beta 1}^+(s) + \omega_b y_{\beta 1}^+(s) - \omega_1 y_{\alpha 1}^+(s) = K_I \omega_b e_\beta(s), \tag{3.40}$$

$$sy_{\alpha 1}^-(s) + \omega_b y_{\alpha 1}^-(s) - \omega_1 y_{\beta 1}^-(s) = K_I \omega_b e_\alpha(s),$$
$$sy_{\beta 1}^-(s) + \omega_b y_{\beta 1}^-(s) + \omega_1 y_{\alpha 1}^-(s) = K_I \omega_b e_\beta(s). \tag{3.41}$$

Again, using the multi-state-variable structure, two groups of equations are obtained as

$$y_{\alpha 1}^+(s) = \frac{1}{s}[\omega_b(K_I e_\alpha(s) - y_{\alpha 1}^+(s)) - \omega_1 y_{\beta 1}^+(s)],$$
$$v_{\beta 1}^+(s) = \frac{1}{s}[\omega_b(K_I e_\beta(s) - y_{\beta 1}^+(s)) + \omega_1 y_{\alpha 1}^+(s)], \tag{3.42}$$

$$y_{\alpha 1}^-(s) = \frac{1}{s}[\omega_b(K_I e_\alpha(s) - y_{\alpha 1}^-(s)) + \omega_1 y_{\beta 1}^-(s)],$$
$$y_{\beta 1}^-(s) = \frac{1}{s}[\omega_b(K_I e_\beta(s) - y_{\beta 1}^-(s)) - \omega_1 y_{\alpha 1}^-(s)]. \tag{3.43}$$

The corresponding implementation structures are shown in Fig. 3.13. Because of the finite gain at the central frequency, as shown in the frequency domain plots of Fig. 3.12, the derived practical SDR controller is referred to as a non-ideal SDR controller. With a wider bandwidth around the resonant frequency than the ideal SDR controller, the sensitivity to fundamental frequency variations is therefore decreased.

It is also noticed that unfortunately the off-resonance damping effect of the non-ideal SDR controller is reduced and this can introduce other error signals if they are not well damped. A typical example would be the influence on negative-sequence component regulation introduced by remaining fundamental positive-sequence components when using the negative-sequence SDR controller. This problem will be discussed and improved in Section 3.6 by preprocessing feedback variables.

3.4.3 Discussion

The sequence-decoupled control concept gives other insights into the control of three-phase unbalanced quantities in the stationary frame. As shown in Fig. 3.14, stationary frame three-phase unbalanced quantities $\underline{e}_{\alpha\beta}$, disregarding the zero-sequence components, have two degree-of-freedom control variables. These are independent scalar variables (e_α and e_β) or a combination of independent complex variables ($\underline{e}_{\alpha\beta}^+$ and $\underline{e}_{\alpha\beta}^-$). As presented in section 3.3, conventionally the independent variables e_α and e_β are regulated by compensators such as the stationary-frame PR controller or the synchronous-frame PI controller. With the proposed SDR controllers, it is possible to individually control positive-sequence and negative-sequence components, which is not the case when independently regulating the the two scalar α, β variables.
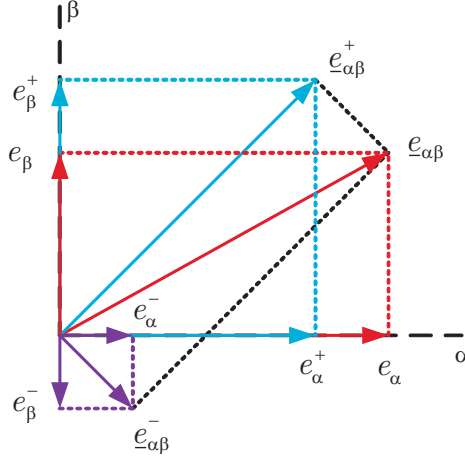
Figure 3.14: Decoupled control variables of unbalanced quantities in the stationary frame.

3.5   Relation between SDR to PR controllers

As derived in the previous sections, SDR controllers make it possible to independently control stationary frame positive-sequence and negative-sequence components. In addition, it is also found that the individual sequence control can be achieved based on conventional resonant controllers. In this section, the relation between the proposed SDR controllers and the conventional resonant controllers is therefore investigated.

Note that (3.40) and (3.41) can be directly solved and the two groups of output variables are found to be

$$
\begin{aligned}
y_{\alpha 1}^{+}(s) &= \frac{K_I \omega_b (s + \omega_b)}{(s + \omega_b)^2 + \omega_1^2} e_\alpha(s) - \frac{K_I \omega_b \omega_1}{(s + \omega_b)^2 + \omega_1^2} e_\beta(s) \\
&\approx \frac{K_I \omega_b s}{s^2 + 2\omega_b s + \omega_1^2} e_\alpha(s) - \frac{K_I \omega_b \omega_1}{s^2 + 2\omega_b s + \omega_1^2} e_\beta(s),
\end{aligned}
\tag{3.44}
$$

$$
\begin{aligned}
y_{\beta 1}^{+}(s) &= \frac{K_I \omega_b \omega_1}{(s + \omega_b)^2 + \omega_1^2} e_\alpha(s) + \frac{K_I \omega_b (s + \omega_b)}{(s + \omega_b)^2 + \omega_1^2} e_\beta(s) \\
&\approx \frac{K_I \omega_b \omega_1}{s^2 + 2\omega_b s + \omega_1^2} e_\alpha(s) + \frac{K_I \omega_b s}{s^2 + 2\omega_b s + \omega_1^2} e_\beta(s),
\end{aligned}
\tag{3.45}
$$

$$
\begin{aligned}
y_{\alpha 1}^{-}(s) &= \frac{K_I \omega_b (s + \omega_b)}{(s + \omega_b)^2 + \omega_1^2} e_\alpha(s) + \frac{K_I \omega_b \omega_1}{(s + \omega_b)^2 + \omega_1^2} e_\beta(s) \\
&\approx \frac{K_I \omega_b s}{s^2 + 2\omega_b s + \omega_1^2} e_\alpha(s) + \frac{K_I \omega_b \omega_1}{s^2 + 2\omega_b s + \omega_1^2} e_\beta(s),
\end{aligned}
\tag{3.46}
$$
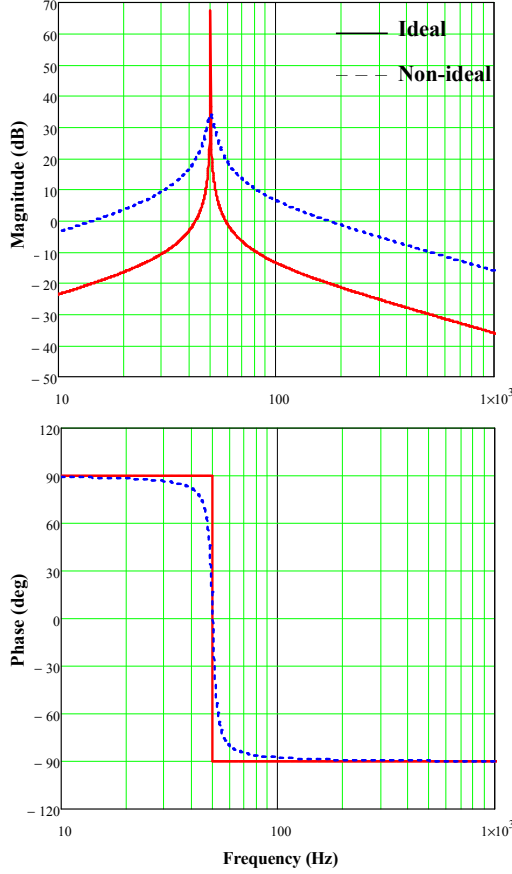
Figure 3.15: Bode plots of ideal and non-ideal resonant controllers, for the fundamental angular frequency $\omega_1 = 314$ rad/s, the bandwidth $\omega_b=10$ rad/s, and $K_I=50$.

$$y_{\beta 1}^-(s) = \frac{-K_I\omega_b\omega_1}{(s+\omega_b)^2+\omega_1^2}e_\alpha(s) + \frac{K_I\omega_b(s+\omega_b)}{(s+\omega_b)^2+\omega_1^2}e_\beta(s) \tag{3.47}$$

$$\approx \frac{-K_I\omega_b\omega_1}{s^2+2\omega_b s+\omega_1^2}e_\alpha(s) + \frac{K_I\omega_b s}{s^2+2\omega_b s+\omega_1^2}e_\beta(s), \tag{3.48}$$

$$\tag{3.49}$$

where the approximations are allowed when $\omega_b \ll \omega_1$. Therefore, another implementation of the non-ideal SDR controller is possible, as shown in Fig. 3.16 (a) and (b).

By combining (3.44) and (3.46), (3.45) and (3.49) it follows that

$$y_{\alpha 1}(s) = y_{\alpha 1}^+(s) + y_{\alpha 1}^-(s) \approx \frac{2K_I\omega_b s}{s^2+2\omega_b s+\omega_1^2}e_\alpha(s), \tag{3.50}$$
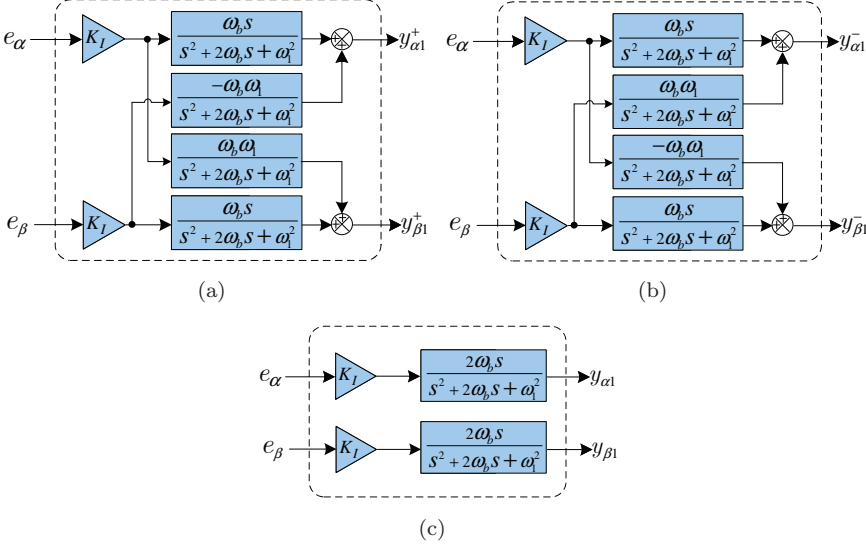
Figure 3.16: Conventional non-ideal resonant controllers for regulating: (a) fundamental positive-sequence components, (b) fundamental negative-sequence components, and (c) both sequence components.

$$y_{\beta 1}(s) = y_{\beta 1}^{+}(s) + y_{\beta 1}^{-}(s) \approx \frac{2K_I \omega_b s}{s^2 + 2\omega_b s + \omega_1^2} e_{\beta}(s). \qquad (3.51)$$

It can be seen that, for regulating both sequence components together, the approximated SDR controllers in (3.50) and (3.51), as shown in Fig. 3.16 (c), are identical to the conventional non-ideal resonant controllers in (3.2).

In the same way, approximated implementation diagrams of ideal SDR controllers are shown in Fig. 3.17. Also, the controllers in Fig. 3.17 (c) are identical to the conventional ideal resonant controllers in (3.1). Now, observe the three controllers in Fig. 3.17. When $K_I = 1$, they are actually the positive-sequence, negative-sequence ideal integrators, and the generalized integrator presented in [50], respectively. So far the derived individual sequence regulators based on conventional resonant controllers are found to be the equivalent implementations of the proposed SDR controllers. Comparing Fig. 3.16 (a)(b) with Fig. 3.13 (a)(b), the SDR-controller-based individual sequence control diagrams are very simple and much easier to be implemented.

3.6 Practical applications of PR and SDR controllers

To illustrate the applicability of PR and SDR controllers in practical situations, and to highlight the controller design, two examples are discussed in detail in this section. Since SDR controllers are proposed only for the regulation of positive- or negative-sequence components, i.e. α- and β-axis quantities in stationary frame, the application examples in this section are based on three-wire systems in order
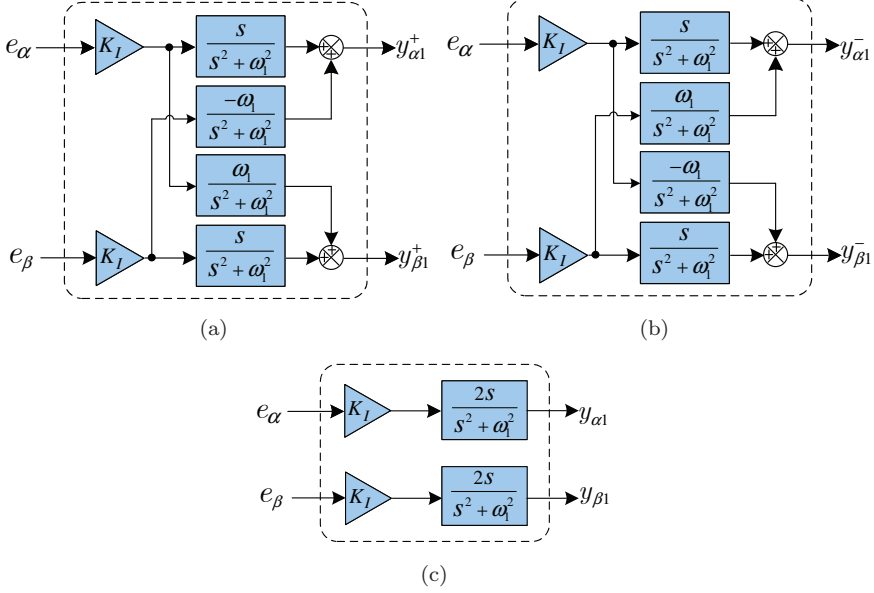
Figure 3.17: Conventional ideal resonant controllers for regulating: (a) fundamental positive-sequence components, (b) fundamental negative-sequence components, and (c) both sequence components.

to compare SDR and PR controllers. Concerning four-wire systems, more applications will be shown in the next chapters, together with specific functions. To ease the description in the following, the SDR controller for positive-sequence regulation is named the PSDR controller, the one for negative-sequence regulation is named the NSDR, and PNSDR denotes SDR controllers for both sequences.

3.6.1 Current regulation of parallel inverters

Most distributed generation systems are coupled to the grid through parallel connected inverters, as shown in the diagram of Fig. 3.18. LC or LCL filtering structures are used for smoothing the output current. The primary source is represented by a dc source V_{dc}, for which the energy is taken from an upstream single-stage or multi-stage power converter system. Note that isolation between the grid and the primary source is normally required either on the grid side or on the dc side, but this requirement is left out on the diagram for simplification.

The control part usually consists of an outer-loop grid current control, a selected inner loop and/or a feedforward loop. As shown in Fig. 3.18, the outer loop is a PR controller or a P+SDR controller, while the inner loop is only shown as a general block with two feedback variables (x_α and x_β) that could be inductor currents, capacitor currents, or capacitor voltages depending on the control strategies adopted [42, 72, 81, 82]. In this work, to improve system stability and dynamics, an inner-loop proportional control for the inductor currents of the inverter is cho-
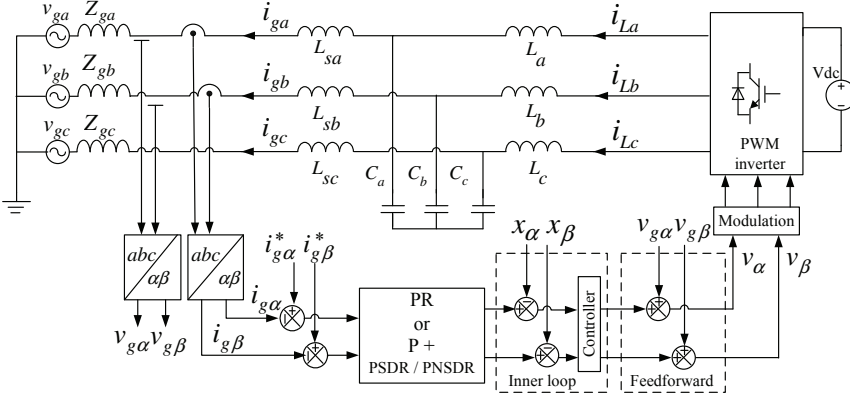
Figure 3.18: Structure diagram of a parallel grid-connected inverter with grid current regulation in the stationary frame.

sen. In the following, two types of structures, one with the PSDR controller and another with the PNSDR controller, are designed by selecting different control blocks from the diagram shown in Fig. 3.18.

a) Tracking symmetric current references:

When symmetric output currents are targeted in a balanced or unbalanced grid, a P + PSDR controller, together with a grid voltage feedforward loop, is employed. Since there are no negative-sequence components, a PSDR controller is sufficient to regulate balanced output currents under a balanced grid. When dealing with unbalanced grids, the PSDR controller performs the control of positive-sequence currents. The grid voltage feedforward loop is able to eliminate most of the negative-sequence currents because almost the same negative-sequence voltage components of the grid are generated by the inverter against the grid voltages. Therefore, it is not necessary to use an extra closed-loop control to further reduce the negative-sequence currents. Experimental results of this system are given in the next section, as well as comparisons with the results obtained by a PR controller or by a PNSDR controller.

b) Tracking asymmetric current references:

If, for instance, asymmetric output currents must be delivered to an unbalanced grid in order to keep constant instantaneous active power [54], then a P + PNSDR controller should be employed, while the feedforward loop is not necessary. When the positive- and negative-sequence parts of the PNSDR controller are given the same parameters, in this situation they are equivalent to a conventional PR controller, but provide an alternative implementation structure, as analyzed in the Section 3.5.

It is interesting to notice that with the proposed control structure it is possible to assign independent gains for the regulation of positive- and negative-sequence components. Since the amplitude of the demanded negative-sequence current is normally much less than that of positive-sequence current, theoretically a much
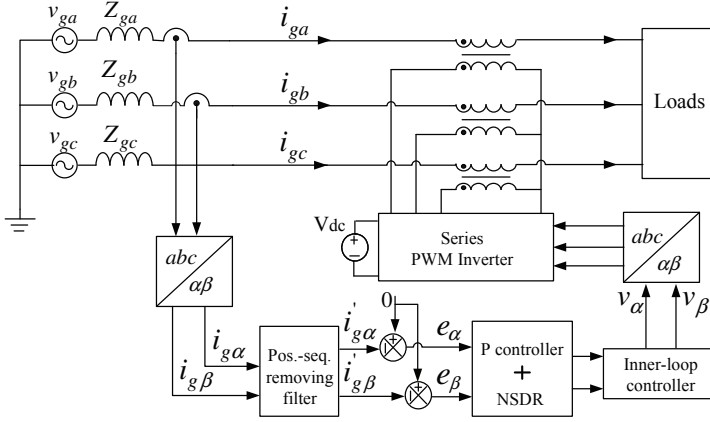
Figure 3.19: Structure diagram of a series grid-connected inverter for eliminating the negative-sequence currents.

higher gain can be assigned to the NSDR controller than to the PSDR controller. This then achieves better reference tracking than conventional PR controllers.

3.6.2 Asymmetrical current elimination with series inverters

The second example is a series grid-connected inverter that eliminates asymmetrical current the grid. As shown in Fig. 3.19, an inverter, including the same output LC filters as in the previous example, is connected in series with the grid and the loads through isolation transformers. It works as an virtual voltage source to eliminate the asymmetrical currents, i.e., the negative-sequence currents in this three-phase three-wire system. Either an unbalanced grid or unbalanced loads may cause asymmetric three-phase grid currents. Therefore, instead of regulating the total grid current, only negative-sequence currents need to be eliminated by the series inverter. As presented in [41, 42], since conventional resonant controllers cannot separately control individual sequences, a SRF PI controller is used to regulate the negative-sequence currents after removing the positive-sequence components.

However, with the SDR controllers, the regulation of negative-sequence currents in the stationary frame is possible and the complexity of the overall control is reduced, as shown in the structure diagram of Fig. 3.19. Note that a filter block is added to preprocess the feedback currents. Because the feedback grid currents contain not only negative-sequence components but also a large amount of positive-sequence components, a non-ideal NSDR controller is not able to damp the positive-sequence components, simply because the gain at 50Hz is not small enough. Consequently, the positive-sequence components of the grid currents will also decrease due to the control of the series inverter, and this is not desirable.

Therefore, the positive-sequence components should be removed from the feedback currents by using a positive-sequence filter [52]. As presented in Chapter 2,

Table 3.1: System parameters

Description	Symbol	Value
Filter inductor	$L_{sa,b,c}$	2 mH
Filter inductor	$L_{a,b,c}$	2 mH
Filter capacitor	$C_{a,b,c}$	5 μF
dc-bus	V_{dc}	750 V
Switching freq.	f_{sw}	16 kHz
Central freq.	ω_1	314 rad/s
Bandwidth	ω_{b1}	100 rad/s
Bandwidth	ω_b	10 rad/s
P gain	K_P	0.1
R or SDR gain	K_I	50
P gain (inner-loop)	K_{Pin}	2.5
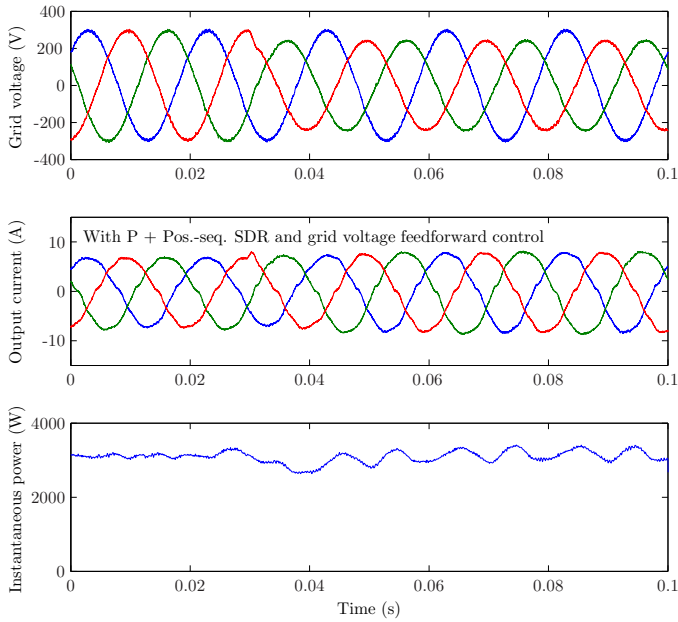
Figure 3.20: Experimental waveforms of the grid voltages, the output currents, and active power. The parallel grid-connected inverter, which is regulated with the P + PSDR controller and has a grid voltage feedforward loop for delivering balanced currents.

this filter operates equivalently to a notch filter for the positive-sequence components. Here the bandwidth (ω_{b1}) of this filter is set to a relatively large value (eg., 100 rad/s) to improve dynamics, and even though a very small amount of positive-sequence components remains, they will be damped further by the non-ideal NSDR controller.
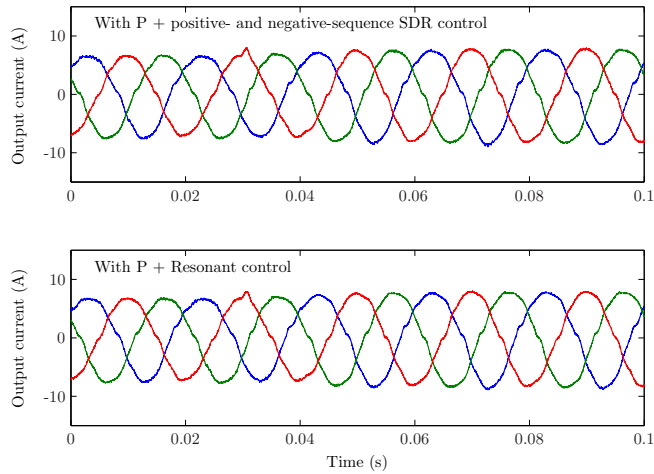
Figure 3.21: Experimental results of the parallel grid-connected inverter delivering balanced currents, regulated by the P + PNSDR controller and by the PR controller, respectively. The grid voltages are the same as in Fig. 3.20.

An inner loop can be applied to improve system dynamic response and stability. Because the same laboratory inverter setup is employed for experimental verification in this work, the same inner-loop control is used in the parallel grid-connected inverter presented previously is kept for easy of implementation. The performance of the outer-loop control by the P + NSDR controller is not influenced.

3.7 Experimental verification

Experiments were carried out to verify the effectiveness of the SDR controllers. The two applications described in the previous section were tested by using the same three-phase grid-connected inverter. The controllers were implemented in a dSPACE DS1104 setup. A programmable power source was used to emulate the grid, and a dc machine was employed as a distributed primary source for the dc bus of the inverter. System parameters are shown in Table 3.1. The grid impedances $Z_{ga,b,c}$ are assumed to be combined with the output inductors. Since the inner-loop inductor current feedback control is always included in this work, only the outer-loop controllers will be mentioned when distinguishing different control schemes. All the SDR controllers used in the experiments are the non-ideal types.

Firstly, the operation of SDR controllers for the current regulation of a parallel grid-connected inverter is verified. To ensure fair evaluation of the control results, the current references for the tests need to be properly generated. Since the related techniques for current reference generation in unbalanced grids have been studied and presented in [54]. This chapter only focuses on the SDR controller part.

Two types of control structures based on the SDR controllers have been pre-
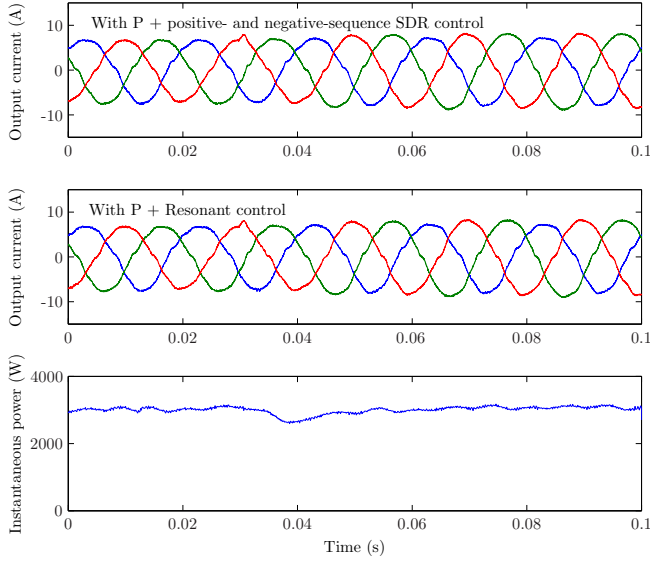
Figure 3.22: Experimental results of the parallel grid-connected inverter, regulated by the P + PNSDR controller or by the PR controller, respectively, when delivering unbalanced currents during voltage dips. The grid voltages are the same as in Fig. 3.20.

sented in the previous section. The first one is based on a P + PSDR controller for positive-sequence current regulation, while a grid voltage feedforward loop is also included for the elimination of asymmetric currents in unbalanced grid situations. Experimental results obtained with this control scheme are shown in Fig. 3.20. When the grid voltages are imposed to be unbalanced due to 20% voltage dips in two phases, output currents are increased to maintain the same amount of average power delivery and the three-phase current outputs are kept well balanced.

Note that the current waveform is slightly distorted. This is because of the dead-time effects of the inverter bridges constructed with IGBTs. Harmonic distortion can be introduced into the output voltage of the inverter when the dead time is large (in this work, more than 4% of the switching period), resulting in distorted currents when the grid impedance is small. Since both the resonant controllers and the SDR controllers only produce a good performance at the fundamental frequency, harmonic components cannot be compensated with the closed-loop control. Although the technique of multiple resonant controllers for selective low-order harmonics compensation can be employed to mitigate dead-time effects [68, 72], this work intends not to use any extra controllers.

For comparison, the same test conditions are repeated on the same inverter system but with two other control schemes, that is the P + PNSDR controller and the conventional PR controller, which are able to regulate both positive- and negative-sequence components. Figure 3.21 shows two groups of output currents obtained under the regulation of these two controllers. It is possible to see from the
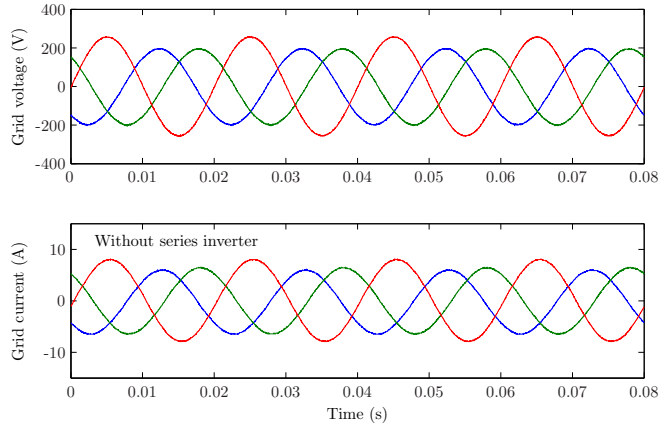
Figure 3.23: Experimental waveforms of the grid voltages and the unbalanced grid currents in steady state, without using the series grid-connected inverter.
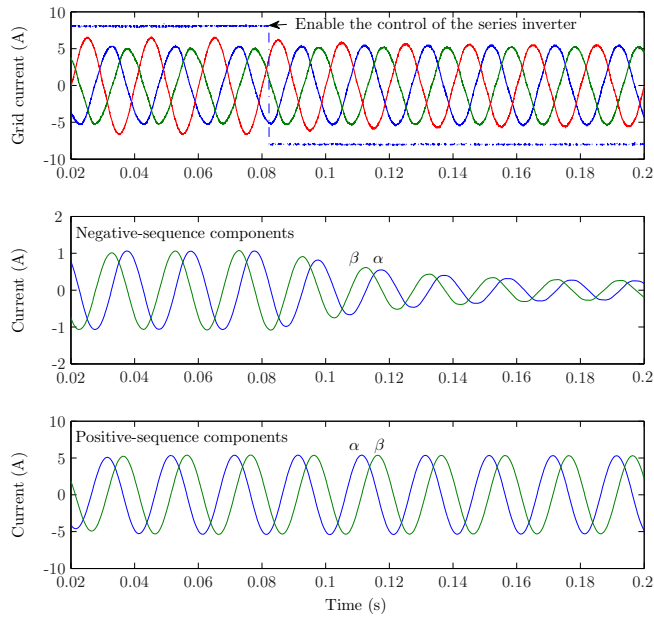
Figure 3.24: Experimental waveforms of the grid currents and corresponding symmetric components when the series grid-connected inverter is connected.

results that the three control schemes achieve the same performance for symmetric current reference tracking.

Other than tracking balanced current references under unbalanced grids, the P + PNSDR controller and the conventional PR controller are also tested with asymmetric current references under the same grid condition, for the purpose of constant instantaneous active power delivery [54]. Figure 3.22 shows the measured current and power outputs obtained with these two controllers. By comparing the current waveforms, it can be seen that the P + PNSDR controller and the PR controller are equivalent under these conditions. Again, it is worth noticing that PNSDR controller used for both sequence components in Fig. 3.13 (c) provides the possibility of assigning different gains for the positive and negative sequences according to practical necessities.

Next, the second application, namely negative-sequence current elimination with a series grid-connected inverter, is verified. For simplicity, the three-phase loads are equipped with three resistors (30Ω). Without connecting the series inverter, the measured waveforms of the grid voltages and the unbalanced grid currents delivered to the loads are shown in Fig. 3.23. After connecting the series inverter, Figure 3.24 shows the grid currents obtained before and after the current control function is activated. It can be seen that the asymmetric currents are eliminated by the NSDR-controller-based control scheme described in Fig. 3.19. By decomposing the currents into symmetric-sequence components with stationary frame filters [52], Figure 3.24 shows that the negative-sequence currents are reduced to a mall amplitude (0.2A), while the positive-sequence currents maintain the same amplitude (5.3A).

3.8   Conclusions

Current regulation, as a low-level control of a grid-interfacing system, has been presented and compared in multiple reference frames in this chapter. Irrespective of external reference derivation for specific applications, internal current regulators determine overall system performance and the complexity of control structures. This chapter has focused on three types of linear controllers, i.e. PI, PR and SDR controllers, of which resonant-type controllers (PR and SDR) are selected for applications in following chapters because of simplicity and flexible control capability at selected frequencies.

To investigate grid-interfacing converters under three-wire or four-wire unbalanced and/or distorted grid conditions, a four-leg converter topology has been selected that will be used to construct a universal platform in this work. The decoupling control of four-leg converters has been detailed by modeling a four-leg grid-connected system in different reference frames.

Differing from conventional three-phase balanced systems, controllers should be able to deal with individual symmetrical sequence components in order to achieve flexible operation of grid-interfacing converters under faulty grids. As shown in this chapter, stationary-frame PR controllers are preferred for regulating positive- and negative-sequence quantities together and for regulating zero-sequence quantities

independently. An extended resonant controller, named the SDR controller, has been proposed that is able to achieve individually positive- or negative-sequence control. Both SDR and PR controllers have been applied and compared in practical systems.

In general, the proposed SDR controllers and related control schemes provide several alternative approaches that complement existing methods. It has been shown that the P + PNSDR controller actually is equivalent to PR controllers but providing the possibility to assign different gains for positive and negative sequences. Besides, the balanced current control scheme based on the P + PSDR controller and the negative-sequence current elimination based on the P + NSDR controller have proven to be simple solutions in the stationary reference frame for individual sequence control.

Part III

Grid interaction of distributed power generation

Chapter 4

Distributed compensation of voltage unbalance

Abstract - Part II has already presented low-level control of grid-interfacing converters, i.e. stationary frame filtering techniques for voltage detection and grid synchronization in disturbed grids, and multiple reference frame current regulation. The presented fundamental control strategies and specific controllers will be applied to grid-interactive control of distributed power generation in Part III, and this chapter starts with distributed compensation of voltage unbalance.

Inverter-based distributed generation used for grid support can offer extra possibilities beyond the primary goal of power delivery. This chapter proposes to ease the responsibility of the grid for voltage unbalance correction with distributed generation systems. Specifically, the functionality to decrease the negative-sequence voltage at the grid connection point is added to the control of distributed generation inverters. In this chapter, two compensation strategies are proposed and analyzed in detail.

The first one is voltage unbalance factor based control. This control scheme mitigates voltage unbalance by regulating negative-sequence currents, which is based on the voltage unbalance factor at the point of connection (PoC) and the positive-sequence currents delivered to the grid by DG inverters. By implementing the method into many distributed generation units present along a same feeder, the unbalanced voltages at the PoC tend to be corrected. However, there are limitations for the first control scheme due to the coupling between the negative- and positive-sequence currents of DG systems. Therefore, a second scheme is presented that can enable DG systems to achieve a co-operative compensation for unbalanced grids by controlling the negative-sequence admittance of DG inverters. Relevant simulation results and experimental verifications are provided.

4.1   Introduction

Voltage unbalance problems are mainly caused by unbalanced distribution of single-phase and nonlinear loads. Together, these loads induce unequal voltage drops across transformers and feeder impedances. The effects of voltage unbalance are quite severe for electrical machines, power electronic converters, etc. [83]. Therefore, many grid-interfacing systems have been studied in how to work properly under unbalanced grid voltages. For example, techniques based on the control of separated symmetrical sequence components have been investigated in order to eliminate dc-bus voltage ripples and distorted line currents [7, 84]. Unfortunately, these techniques only protect local systems from voltage unbalance problems but not supporting the grid with functions like voltage unbalance correction.

On the other hand, there is a cluster of power electronic converters specially designed for voltage regulation, including voltage unbalance compensation. An often used device is called dynamic voltage restorer (DVR) or static series compensator (SSC). The DVR injects compensation voltages through series-connected transformers [85, 86]. The disadvantage of this method is that these grid-interfacing converters are unused or only lightly loaded when there are no voltage unbalance problems. Another existing solution is a static synchronous compensator (STATCOM) that works in parallel with the grid and compensates the ac voltage by regulating reactive power [87, 88]. This approach is not efficient for underground cables where resistance dominates inductance, or for networks where feeder resistance is high, requiring higher ratings and causing more losses. The problem is considered in this chapter for both overhead lines and underground cables.

For dealing with other power quality problems than voltage unbalance, the so-called unified power quality conditioner (UPQC) has been proposed and is continuously improved. The UPQC combines the previous structures in two or more inverters [11, 89], thereby having more control degree of freedoms for voltage and current regulation. Clearly, all these solutions are not designed to cope with distributed generation (DG). Since an inverter-based DG has the same circuit structure as the STATCOM, it can also be controlled for grid voltage regulation. However, the idea of such a kind of grid support with DG systems has received little attention up to now.

Power electronics-based grid-interfacing converters will play an important role in facing the emerging application of distributed generation. In addition to conventional delivery of electricity, auxiliary functionality for reduction of power quality problems is being introduced into grid-interfacing converters [90]. In [28], the capability of an active filter is integrated into an inverter-based DG. A control algorithm is proposed to spread the voltage-control burden over the DG units [29]. To compensate unbalance within microgrids, a reactive power-conductance droop control for regulating negative-sequence currents is distributed among inverters [30]. A similar idea for controlling negative sequence currents is also presented in [31], where the control of a doubly fed induction generator system is concentrated. In this chapter, it is proposed to integrate voltage unbalance correction into the control of grid-interfacing converters. Since the feedback variables for this control are already available, this does not require more hardware. By controlling
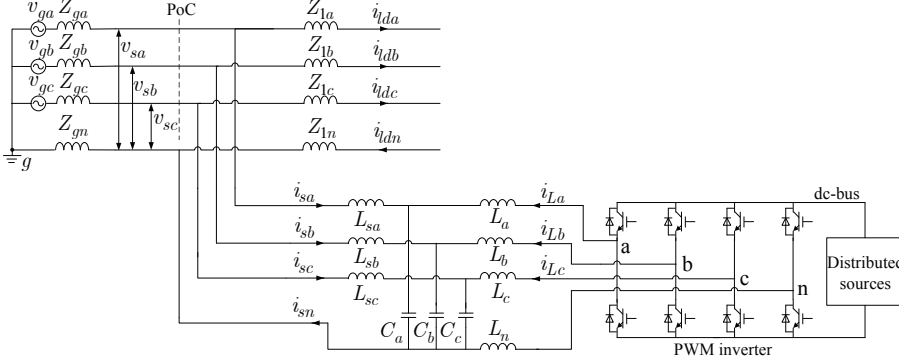
Figure 4.1: A three-phase four-wire grid-interfacing inverter at PoC.

the negative-sequence currents, which induce opposite negative-sequence voltage drops on the feeder impedances, the objective of eliminating negative-sequence voltages at the point of connection (PoC) with the grid can be achieved.

To study the effectiveness of voltage unbalance correction, a three-phase four-wire inverter is used, as shown in Fig. 4.1. It is connected to the utility grid at the PoC through LCL filters and is capable of delivering energy from downstream distributed sources. The currents denoted by $i_{lda,b,c}$ are the collective currents of the loads behind the PoC. Note that, for a general case analysis, this chapter chooses a four-wire system for modeling, while a three-wire system model can be similarly derived. The inverter operates normally when grid voltages are balanced, and performs compensation automatically for negative-sequence voltages when the grid becomes unbalanced. First, the principle of voltage unbalance correction with negative-sequence current control [53] is presented in the following. Finally, two control schemes, one based on the voltage unbalance factor (VUF) [83] and the other using negative-sequence admittance control, are proposed and investigated.

4.2 Principle of voltage unbalance correction

4.2.1 Derivation of the negative-sequence equivalent model

With the theory of symmetric decomposition for three phase systems, unbalanced grid voltages can be divided into three groups, namely positive, negative, and zero sequence voltages. Similarly, current quantities can also be separated. Disregarding the mutual coupling between the grid lines in Fig. 4.1, equivalent circuit models for each group of sequence components can be derived. In the following, the subscripts "+", "-", and "0" denote as usually the positive, negative and zero sequences, respectively. The impedances of each line are given as $\underline{Z}_{ga}$ to $\underline{Z}_{gn}$ (complex numbers are denoted with a bar subscript, matrices are bold), as illustrated in the diagram. For simplification, only fundamental sinusoidal components of all the quantities in Fig. 4.1 are considered. Thus in phasor notation the grid voltages

are expressed as

$$
\begin{bmatrix} \underline{V}_{ga} \\ \underline{V}_{gb} \\ \underline{V}_{gc} \end{bmatrix} = \underline{\boldsymbol{Z}} \begin{bmatrix} \underline{I}_{sa} \\ \underline{I}_{sb} \\ \underline{I}_{sc} \end{bmatrix} + \underline{Z}_{gn} \begin{bmatrix} \underline{I}_{sn} \\ \underline{I}_{sn} \\ \underline{I}_{sn} \end{bmatrix} + \underline{\boldsymbol{Z}} \begin{bmatrix} \underline{I}_{lda} \\ \underline{I}_{ldb} \\ \underline{I}_{ldc} \end{bmatrix} + \underline{Z}_{gn} \begin{bmatrix} \underline{I}_{ldn} \\ \underline{I}_{ldn} \\ \underline{I}_{ldn} \end{bmatrix} + \begin{bmatrix} \underline{V}_{sa} \\ \underline{V}_{sb} \\ \underline{V}_{sc} \end{bmatrix} , \quad (4.1)
$$

where

$$
\underline{\boldsymbol{Z}} = \begin{bmatrix} \underline{Z}_{ga} & 0 & 0 \\ 0 & \underline{Z}_{gb} & 0 \\ 0 & 0 & \underline{Z}_{gc} \end{bmatrix} . \quad (4.2)
$$

Using the transformation from symmetrical sequence components to *abc* components [55] gives

$$
\begin{bmatrix} \underline{V}_{ga} \\ \underline{V}_{gb} \\ \underline{V}_{gc} \end{bmatrix} = \underline{\boldsymbol{A}} \begin{bmatrix} \underline{V}_g^0 \\ \underline{V}_g^+ \\ \underline{V}_g^- \end{bmatrix} , \quad \begin{bmatrix} \underline{V}_{sa} \\ \underline{V}_{sb} \\ \underline{V}_{sc} \end{bmatrix} = \underline{\boldsymbol{A}} \begin{bmatrix} \underline{V}_s^0 \\ \underline{V}_s^+ \\ \underline{V}_s^- \end{bmatrix} , \quad (4.3)
$$

$$
\begin{bmatrix} \underline{I}_{sa} \\ \underline{I}_{sb} \\ \underline{I}_{sc} \end{bmatrix} = \underline{\boldsymbol{A}} \begin{bmatrix} \underline{I}_s^0 \\ \underline{I}_s^+ \\ \underline{I}_s^- \end{bmatrix} , \quad \begin{bmatrix} \underline{I}_{lda} \\ \underline{I}_{ldb} \\ \underline{I}_{ldc} \end{bmatrix} = \underline{\boldsymbol{A}} \begin{bmatrix} \underline{I}_{ld}^0 \\ \underline{I}_{ld}^+ \\ \underline{I}_{ld}^- \end{bmatrix} , \quad (4.4)
$$

where

$$
\underline{\boldsymbol{A}} = \begin{bmatrix} 1 & 1 & 1 \\ 1 & a^2 & a \\ 1 & a & a^2 \end{bmatrix} , \quad a = \mathrm{e}^{j\frac{2\pi}{3}} . \quad (4.5)
$$

Also, neutral currents can be calculated by

$$
\underline{I}_{sn} = \underline{I}_{sa} + \underline{I}_{sb} + \underline{I}_{sc} = \underline{I}_s^0, \quad (4.6)
$$

$$
\underline{I}_{ldn} = \underline{I}_{lda} + \underline{I}_{ldb} + \underline{I}_{ldc} = \underline{I}_{ld}^0. \quad (4.7)
$$

Substituting (4.3) - (4.7) in (4.1) yields

$$
\underline{\boldsymbol{A}} \begin{bmatrix} \underline{V}_g^0 \\ \underline{V}_g^+ \\ \underline{V}_g^- \end{bmatrix} = \underline{\boldsymbol{Z}}\,\underline{\boldsymbol{A}} \begin{bmatrix} \underline{I}_s^0 + \underline{I}_{ld}^0 \\ \underline{I}_s^+ + \underline{I}_{ld}^+ \\ \underline{I}_s^- + \underline{I}_{ld}^- \end{bmatrix} + \underline{Z}_{gn} \begin{bmatrix} \underline{I}_s^0 + \underline{I}_{ld}^0 \\ \underline{I}_s^0 + \underline{I}_{ld}^0 \\ \underline{I}_s^0 + \underline{I}_{ld}^0 \end{bmatrix} + \underline{\boldsymbol{A}} \begin{bmatrix} \underline{V}_s^0 \\ \underline{V}_s^+ \\ \underline{V}_s^- \end{bmatrix} , \quad (4.8)
$$

where it is assumed that the impedances of the grid are the same for each phase, that is $\underline{Z}_{ga} = \underline{Z}_{gb} = \underline{Z}_{gc} = \underline{Z}_g$. By multiplying with $\boldsymbol{A}^{-1}$, (4.8) can be rewritten as

$$
\begin{bmatrix} \underline{V}_g^0 \\ \underline{V}_g^+ \\ \underline{V}_g^- \end{bmatrix} = \underline{Z}_g \begin{bmatrix} \underline{I}_s^0 + \underline{I}_{ld}^0 \\ \underline{I}_s^+ + \underline{I}_{ld}^+ \\ \underline{I}_s^- + \underline{I}_{ld}^- \end{bmatrix} + \underline{Z}_{gn} \begin{bmatrix} \underline{I}_s^0 + \underline{I}_{ld}^0 \\ 0 \\ 0 \end{bmatrix} + \begin{bmatrix} \underline{V}_s^0 \\ \underline{V}_s^+ \\ \underline{V}_s^- \end{bmatrix} . \quad (4.9)
$$

According to (4.9), the equivalent impedances for positive, negative and zero sequences are decoupled. Both positive and negative sequences have the same equivalent impedance $\underline{Z}_g$. Therefore the equivalent circuit models for each symmetric sequence component are derived, as shown in Fig. 4.2. Phasors $\underline{V}_g^{+,-,0}$ and
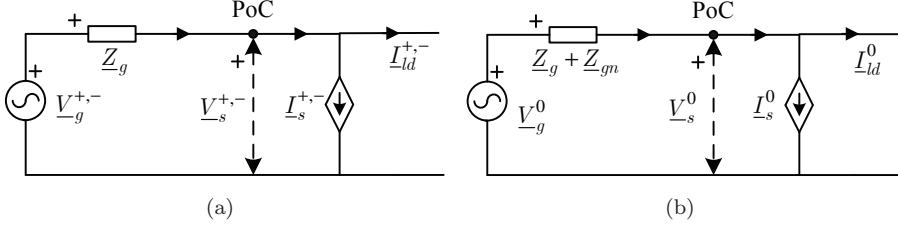
Figure 4.2: Symmetric sequence equivalent models: (a) the positive/negative sequences and (b) the zero sequence.
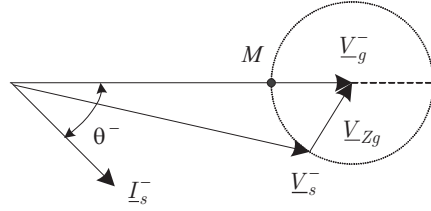
Figure 4.3: Phasor diagram of the negative-sequence model.

$\underline{V}_s^{+,-,0}$ are the respective sequence voltages of the grid and the PoC, respectively. Current $\underline{I}_s^{+,-,0}$ are the positive-sequence, negative-sequence and zero-sequence currents from the inverter, respectively. It should be noticed that the models in Fig. 4.2 only represent a general case for four wire system, because for three-wire system the zero-sequence model does not exist.

4.2.2   Negative-sequence voltage correction

A phasor diagram showing negative-sequence fundamental quantities is drawn in Fig. 4.3. By changing the amplitude and phase of the negative-sequence current $\underline{I}_s^-$, the negative-sequence voltage $\underline{V}_s^-$ can be regulated through the voltage drop across the line impedance, $\underline{V}_{Zg}$. For a given amplitude I_s^-, the voltage changes along the dashed circle and reaches a minimum value at the point M where θ^- (the phase angle between negative-sequence voltage and current) equals the negative impedance angle of $\underline{Z}_g$. The impedance $\underline{Z}_g$ is a combination of inductance X and resistance R. The ratio of R to X for overhead lines, for instance, is around 1 or much less, and is about 4 or higher for underground cables [91].

The conventional reactive power - voltage droop control scheme can be adapted to negative-sequence voltage correction. This is done by controlling the negative-sequence reactive power in the case of small R/X, that is θ^- approximates 90° [30]. The other way around, it is possible to compensate the negative-sequence voltage by consuming negative-sequence active power in the case of high R/X, but this is not efficient. In other words, it all depends on the grid impedance angle how the negative sequence current is going to be controlled. Given the knowledge of R/X,

the negative-sequence currents are forced to lag θ^- behind the negative-sequence voltages.

Similarly, the zero-sequence voltage can also be compensated by regulating zero-sequence currents. Otherwise, it can be isolated by Δ/Y or Y/Y ungrounded transformers. In fact, one should also pay attention to positive-sequence voltages, such as voltage rise due to a large penetration of DG systems. However, other than compensating voltage rise solutions like power flow control and energy storage systems are also possible. This chapter only concentrates on the correction of negative-sequence voltages. According to the described principle in this section, two different control schemes for negative-sequence voltage compensation are proposed to manipulate distributed negative-sequence currents in unbalanced grids.

4.3   Voltage unbalance factor based control

4.3.1   Determination of negative-sequence currents

To eliminate the negative-sequence voltage, a high negative-sequence current and therefore higher rating of the inverters is required. Considering that the power capacity of DG units may be too small to fully achieve the negative-sequence voltage elimination, and because the main function of DG is still power delivery, it is proposed to regulate the negative-sequence current based on the voltage unbalance factor named K_{VUF}. When unbalanced voltages at the PoC are caused by unbalanced loads, the value of K_{VUF} represents the unbalanced distribution of loads. The control scheme effectively compensates for unbalanced local loads with respect to K_{VUF}. By having multiple DG units equipped with the same scheme, elimination of the negative-sequence voltage can be achieved.

The voltage unbalance factor K_{VUF} is defined as the ratio between the amplitude of the negative-sequence voltage V_s^- and the amplitude of the positive-sequence voltage V_s^+. The following constraint equation is proposed to calculate the desired current amplitude I_s^-

$$\frac{I_s^-}{I_s^+} = \frac{V_s^-}{V_s^+} = K_{VUF}, \tag{4.10}$$

where I_s^+ is the amplitude of the positive-sequence current. Note that this is not the only possible way to regulate the desired amplitude of the negative-sequence current. The main purpose of (4.10) is to balance the main function of power delivery with the auxiliary function of unbalanced voltage correction, because the negative-sequence current can cause second order power fluctuation on the dc bus of DG inverters (see section 4.3.5). Furthermore, as additional negative-sequence current injection also causes increased peak current, the proportional coefficient K_{VUF} has to be adjusted to limit the output current.

For voltage unbalance factor based control, the value K_{VUF} is obviously essential to set the amplitude of negative-sequence currents. The detection of symmetric sequence voltages is then important, as well as synchronization with the grid. In
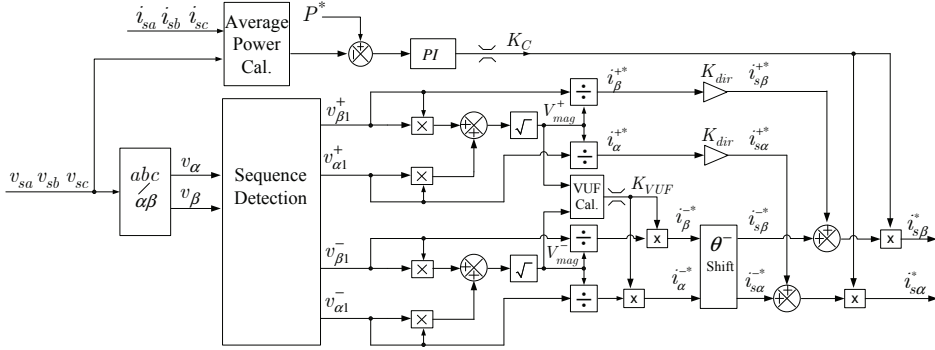
Figure 4.4: Current reference generation for the inverter control.

an unbalanced or distorted grid, the stationary frame filters presented in Chapter 2 are used to measure the positive- and negative-sequence voltages.

4.3.2 Reference signal generation

Figure 4.4 shows the block diagram for current reference generation. It highlights the detection of symmetric sequence voltages with a multi-variable filter, the VUF calculation, average power regulation and the signal synthesis. By utilizing the fundamental positive- and negative-sequence components filtered out by the filter, it follows that

$$
\begin{aligned}
V_{mag}^{+} &= \sqrt{v_{\alpha 1}^{+}{}^{2} + v_{\beta 1}^{+}{}^{2}}, \\
V_{mag}^{-} &= \sqrt{v_{\alpha 1}^{-}{}^{2} + v_{\beta 1}^{-}{}^{2}},
\end{aligned}
\tag{4.11}
$$

where V_{mag}^{+} and V_{mag}^{-} denote the magnitude of the fundamental positive- and negative-sequence voltage, respectively. Consequently, two groups of per-unit reference signals can be derived with (4.11), that is $i_{\alpha}^{+*} + j i_{\beta}^{+*}$ and $i_{\alpha}^{-*} + j i_{\beta}^{-*}$ as shown in Fig. 4.4. According to the principle described in the previous section, negative-sequence currents are designed to keep a phase-shift θ^{-} with the negative-sequence voltage as

$$
i_{s\alpha}^{-*} + j i_{s\beta}^{-*} = (i_{\alpha}^{-*} + j i_{\beta}^{-*}) \mathrm{e}^{j\theta^{-}}.
\tag{4.12}
$$

This phase-shift should equal the negative line impedance angle in order to achieve the maximum correction effect, as shown in Fig. 4.3.

The positive-sequence current references are either in-phase or in anti-phase with the positive-sequence component of the grid voltage, depending on the desired direction for energy delivery. Normally, the gain K_{dir} is set to -1 in order to deliver energy to the utility grid.

In the average power control block of Fig. 4.4, it should be noticed that the power reference P^{*} can be applied according to the application, e.g. as the active power generated by downstream DG or as the power demanded by the upstream utility grid. In order to eliminate the effects of low-order ripple on the measured
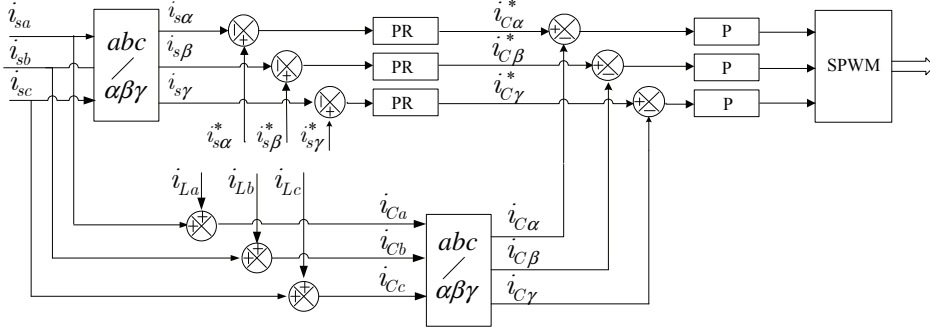
Figure 4.5: Structure of the controller for current regulation in a three-phase four-wire system.

average power, the PI parameters that lead to K_C should have a small proportional gain and a big integration time constant. In this work, the gain is chosen as 0.04 and the time constant is 0.02 s. The output of the PI controller K_C is used to regulate the amplitudes of the desired currents.

All together, it follows that the current references $i_{s\alpha}^*$ and $i_{s\beta}^*$ are derived in the stationary frame. This is beneficial for the controller design, since the controller presented in the next section is also designed in the stationary frame. The mathematical manipulations needed to guarantee optimal implementation of the above digital process are not the subject of this work.

4.3.3 Controller for current regulation

Figure 4.5 shows the controller structure of the grid-interfacing inverter. It is constructed by a dual loop current controller, i.e. an outer control loop with proportional-resonant (PR) controllers for eliminating steady-state error of the delivered currents, and an inner capacitor current control loop with simple proportional control to improve stability. Instead of direct sampling, capacitor currents are calculated from the output currents and the inner filter inductor currents. These currents are measured anyway for over-current protection. To eliminate the zero-sequence currents in four-wire unbalanced grid situations, the current reference $i_{s\gamma}^*$ should be zero.

The control for both positive- and negative-sequence components would be much too complicated and computation-time consuming when conventional PI control with coordinate transformation is used. Therefore, it is preferred to choose a PR or P + SDR controller in the stationary frame, as presented in Chapter 3. For ease of reading, the PR controller with high gain at the fundamental frequency (ω_1) is repeated here, ie.

$$G(s) = K_P + \frac{2\omega_b K_I s}{s^2 + 2\omega_b s + \omega_1^2}, \tag{4.13}$$

where K_P is the proportional gain, K_I the resonant gain, and ω_b the equivalent

bandwidth of the resonant controller. A detailed design for the PR controller has been presented in [67, 82], it is not duplicated here. The parameters used in the simulation and experiments are $K_P = 0.5$, $K_I = 50$, and $\omega_b = 20 \ rad/s$.

4.3.4 Simulation and experimental verifications

Simulation results from PSIM7.0 are provided to enable the verification of the reference signals generation, as shown in Fig. 4.6. System parameters are shown in Table 4.1. In order to easily observe the effects of negative-sequence correction, the values of the line inductances was intentionally exaggerated to the same order as the filter inductors. Therefore, the inductors $L_{sa,b,c}$ are combined with the line impedances. According to the values of the line impedances in Table 4.1, θ^- is obtained and equals -45°. For a straightforward test of the effectiveness of the negative-sequence voltage correction, only fundamental positive- and negative-sequence components are considered in the grid voltages as given in Table 4.1. It should be pointed out that the afore-mentioned control scheme and the multi-variable filter can also be adapted for distorted grid voltages.

To verify the proposed control method with its integrated correction function in a practical set-up, an experiment was carried out with a laboratory prototype that has the same system parameters as the simulation. A 15 KVA three-phase programmable ac power source (SPITZENBERGER+SPIES DM 15000/PAS) was used to emulate the unbalanced utility grid, and a dc machine was connected as the distributed source. The controller was designed on a dSPACE DS1104 setup by using Matlab Simulink.

Figure 4.7 shows the experimental waveforms of the grid-interfacing inverter with integrated negative-sequence voltage correction. Under unbalanced grid voltages, the inverter delivers mainly positive-sequence currents to the utility grid and absorbs 10% of the negative-sequence currents.

The effectiveness of the multi-variable filter in detecting positive- and negative-sequence components from unbalanced voltages is shown in Fig. 4.8. For observation, these experimental waveforms of the practical controller are reproduced through D/A converters. The rms value and phase-shift of the positive- and

Table 4.1: System Parameters

Description	Symbol	Value
	$\underline{V}_{ga}$	$198V \angle 0^o$
Grid voltages	$\underline{V}_{gb}$	$171.71V \angle -125.21^o$
	$\underline{V}_{gc}$	$171.71V \angle 125.21^o$
Line impedance	$Z_{ga,b,c}$	$0.628 + j0.628 \ \Omega$
Neutral impedance	Z_{gn}	$100 \ \mu$H
Filter inductor	$L_{a,b,c}$	2 mH
Filter inductor	L_n	0.67 mH
Filter capacitor	$C_{a,b,c}$	$5 \ \mu$F
dc-bus voltage	V_{dc}	750 V
Switching freq.	f_{sw}	16 kHz
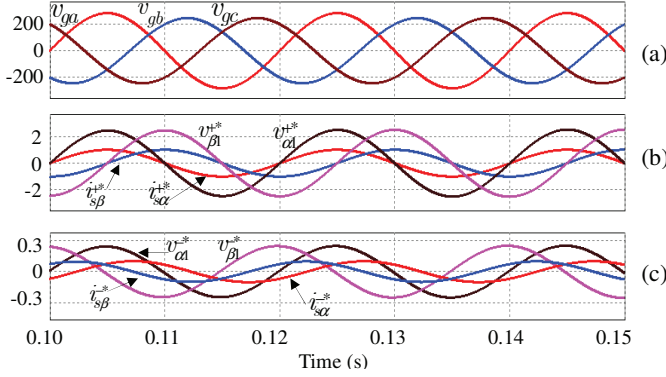
Figure 4.6: Simulation results of the reference currents generation. (a) unbalanced grid voltages in *abc* frame, (b) the per-unit positive-sequence currents $i_{s\alpha}^{+*}$ and $i_{s\beta}^{+*}$ are in-phase with the positive-sequence voltage, and (c) the negative-sequence currents $i_{s\alpha}^{-*}$ and $i_{s\beta}^{-*}$ lag the negative-sequence voltages by 45° in the $\alpha\beta$-frame.
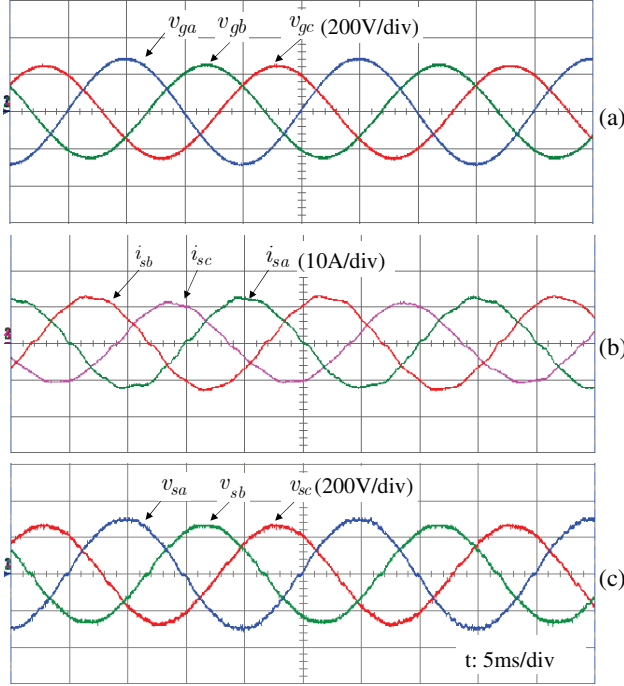
Figure 4.7: Experimental results of the grid-interfacing inverter with integrated voltage unbalance correction (a) unbalanced grid voltages, (b) currents delivered by the inverter, and (c) voltages at the PoC.
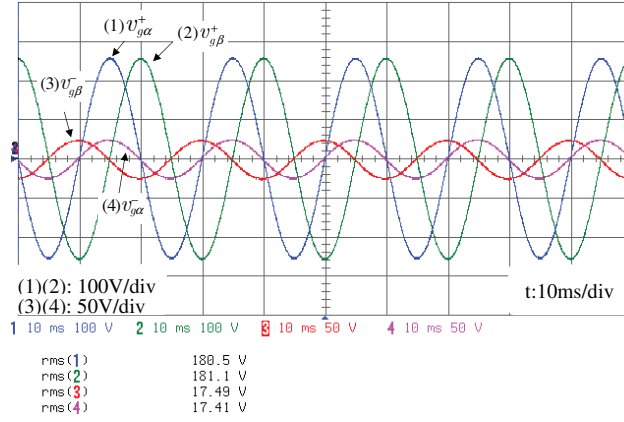
Figure 4.8: Experimental waveforms of positive- and negative-sequence detection, where the extracted fundamental symmetric sequence voltages are derived in the $\alpha\beta$-frame.
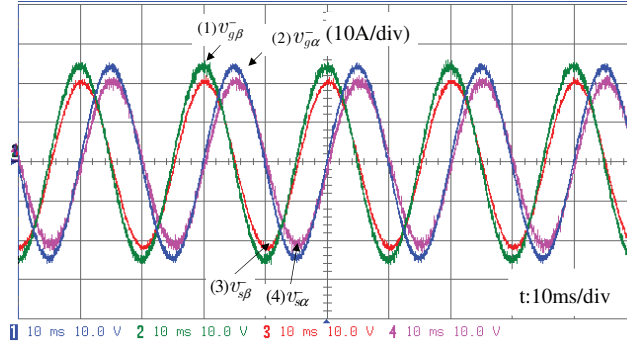
Figure 4.9: Experimental results of the negative-sequence voltage correction. The α, β components of the negative-sequence voltage at the PoC $v_{s\alpha,\beta}^-$ show a 10% amplitude reduction compared with the negative-sequence voltage of the grid $v_{g\alpha,\beta}^-$.

negative-sequence voltages are almost the same as the $\alpha\beta$-frame calculation results as derived from *abc*-coordinates, where symmetrical-sequence voltages are calculated based on equation (4.3).

To observe the negative-sequence voltage correction, the results are illustrated in the $\alpha\beta$-frame by decomposing voltages from the *abc*-frame with the multivariable filter. As seen in Fig. 4.9, the amplitude of the negative-sequence voltage at the PoC is reduced, although the decrease is limited to around 10%. Again note that the line impedance parameters have been exaggerated. In a practical utility grid, for instance 200 μH line impedance is more realistic, and then the decrease would be around 1% for the same conditions. However, when using multiple modules the effect of the negative-sequence voltage correction will be more pronounced.
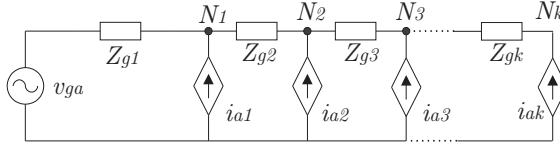
Figure 4.10: Per-phase equivalent circuit with multiple modules.
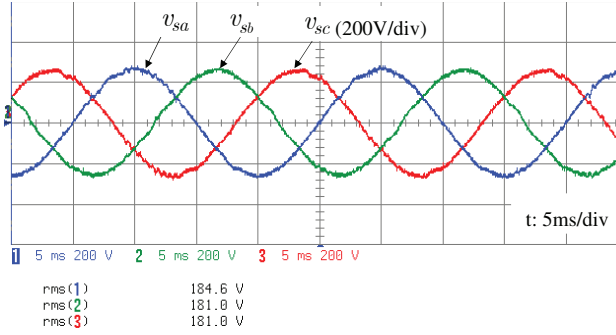
Figure 4.11: Experimental waveforms of the negative-sequence voltage correction. The resulting corrected voltages tend to be balanced.

For investigating the impact of multiple modules, an equivalent circuit is used based on the above described method for a single module. Figure 4.10 shows the per-phase diagram, where many modules-represented by equivalent current sources- are located in different nodes on a feeder. To achieve distributed voltage unbalance mitigation, multiple inverter modules on the same PoC of a feeder, equipped with the same control scheme, should show the same behavior. With the system structure shown, the VUF value at the PoC may be transferred to each module by an information center where measurements are done centrally. Alternatively, the measurements can be done by the inverters locally.

Qualitatively, it is assumed that the regulated negative-sequence currents by the modules in Fig. 4.10 can be lumped into a single module, and therefore should behave identical to the single inverter experiment of Fig. 4.9. Fig. 4.11 shows the corrected voltage at the PoC when simply inject 10 times the negative-sequence current previously delivered by the single module. It can be seen that the three-phase voltages tend to be balanced. This gives an indication of the effectiveness of distributed voltage unbalance correction. However, it must be noted that the proposed method is only an alternative. It is preferable in an unbalanced situation with small voltage deviation, while the conventional methods mentioned in the introduction part are suitable for serious situations with large voltage unbalance that usually appear in another category of voltage quality problems named voltage dips.

4.3.5   Considerations on practical applicability

Under unbalanced situations, the negative-sequence currents do introduce low-order power ripple that reflects on the dc bus of DG inverters, thereby causing dc-bus voltage variation, distorted ac outputs, and even control instability problems. Detailed power analysis and calculation in unbalanced grids are presented in the next chapter. As a result, the low-order active power ripple denoted by $\tilde{p}_{2\omega}$ can be calculated by

$$\tilde{p}_{2\omega} = \frac{3}{2} V_s^+ I_s^- \cos(2\omega t + \theta^{+-} + \theta^-) + \frac{3}{2} V_s^- I_s^+ \cos(2\omega t + \theta^{+-}), \qquad (4.14)$$

where θ^- is the angle between the negative-sequence current and the negative-sequence voltage, that is the negative impedance angle of $\underline{Z}_g$ as defined in section 4.2.1; θ^{+-} is the phase angle between the negative-sequence voltage $\underline{V}_s^-$ and the positive-sequence voltage $\underline{V}_s^+$. Note that here the positive-sequence current is in phase with the positive-sequence voltage only for delivering active power.

Substituting (4.10) in (4.14) obtains

$$\tilde{p}_{2\omega} = \frac{3}{2} V_s^+ I_s^+ K_{VUF}[\cos(2\omega t + \theta^{+-} + \theta^-) + \cos(2\omega t + \theta^{+-})]. \qquad (4.15)$$

It can be seen from (4.15) that $\tilde{p}_{2\omega}$ always exists when DG systems are designed to perform unbalanced voltage compensation, and only when the feeder is a resistive dominated type, i.e. θ^- approximates 180^0, the ripple power $\tilde{p}_{2\omega}$ approximates zero.

On the other hand, it has been shown that the value of I_s^-, which changes with the unbalanced voltage at the PoC as well as with I_s^+, determines the amount of negative-sequence voltage compensation. However, when the amplitude of I_s^+ decreases to a small value for a DG system due to a change of environment (eg., sun shadow effects on a solar panel), or when the active power is designed to decrease according to a certain procedure, the controllable range of I_s^- becomes very limited because of the relationship with I_s^+ that is constrained by (4.10). As a consequence, VUF based control hardly contributes to voltage unbalance compensation in this case.

In summary, the application of the voltage unbalance factor based control for the negative-sequence voltage compensation, as an auxiliary function, is effective only when there is active power delivery. In order to handle the low-order ripple power on the dc bus of DG inverters, either extra dc-bus capacitors are needed or an energy buffer from primary dc source regulation is required [92]. However, in the case of resistive impedance feeders, this control scheme does not introduce the problem of low-order ripple power on the dc side of inverters.

4.4   Negative-sequence admittance control scheme

As shown in the previous section, there is a limitation of the VUF based control scheme because it introduces a coupling between the negative-sequence currents
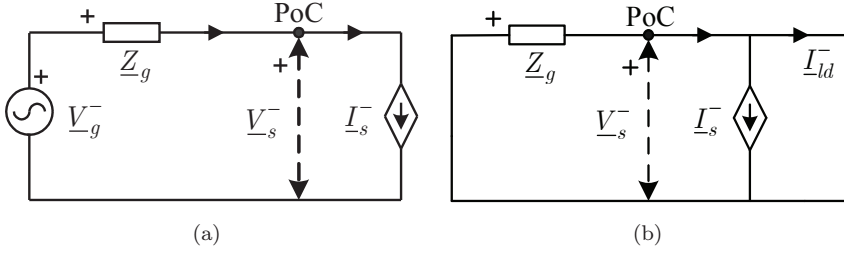
Figure 4.12: Circuit models representing the negative-sequence voltages at the PoC introduced from (a) unbalanced grid voltages or caused by (b) unbalanced loads.

and the positive-sequence currents of DG systems by a proportional coefficient, K_{VUF}. In general, it is desirable that the negative-sequence currents should be independent of the positive-sequence currents during the control action. Thus another optional method, namely negative-sequence admittance control scheme, is proposed in this section.

In Fig. 4.2 (a), the negative-sequence model of a DG system at the PoC is derived. It can be seen that either unbalanced grid voltages or unbalanced loads cause unbalanced voltages at the PoC. For clarity, the unbalanced situation is decomposed into two models representing either unbalanced grid voltages or unbalanced loads, as shown in Fig. 4.12. Based on the two models, in order to compensate for the negative-sequence voltage at the PoC, DG systems need to absorb a certain amount of negative-sequence currents from the grid. This is to introduce a voltage drop across the feeder for mitigating unbalanced grid voltages, and to partially provide unbalanced loads with the negative-sequence currents that are originally supplied by the grid voltage source.

Therefore, if the negative-sequence output admittance of DG systems can be controlled with respect to the negative-sequence voltage at the PoC, it would be possible to regulate the negative-sequence current flow as desired. Note that positive-sequence currents are still controlled separately for active power delivery to the grid.

4.4.1   Admittance droop equations

Regulate the output negative-sequence current of a DG inverter means controlling its output impedance characteristic analogous to a negative-sequence admittance, i.e.

$$\underline{I}^- = \underline{Y}^- \underline{V}^-, \tag{4.16}$$

where $\underline{I}^-$ denotes the compensated negative-sequence current, expressed in the phasor notation; $\underline{Y}^-$ is the controllable negative-sequence admittance, and $\underline{V}^-$ the negative-sequence voltage at the PoC. The subscript 's' of Fig. 4.12 is left out in the following for a general description with simple notation.

The admittance $\underline{Y}^-$ can also be expressed as

$$\underline{Y}^- = G^- + jB^- = Y^- \angle \theta^-, \tag{4.17}$$
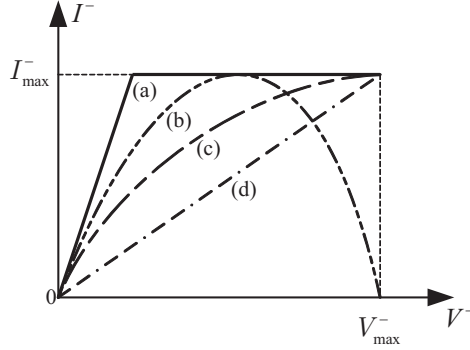
Figure 4.13: Magnitude of the negative-sequence compensating current as a function of V^- with different control schemes for Y^-, where curves (b) and (c) are plotted based on (4.22); curves (a) and (d) are derived from (4.21).

with $Y^- = \sqrt{G^{-2} + B^{-2}}$, and $\theta^- = \tan^{-1}(B^-/G^-)$, where G^- is the conductance part of $\underline{Y}^-$ and B^- the susceptance part. From (4.16), the phase angle between $\underline{I}^-$ and $\underline{V}^-$ is determined by θ^-, and the magnitude of $\underline{I}^-$ can be regulated by changing Y^-.

Like in the previous control scheme, this section discusses a general case of the feeder impedance with the knowledge of R/X, and the θ^- is likewise designed to be the negative of $\tan^{-1}(X/R)$ in order to achieve maximum compensation effect for a certain amount of current. Thus the magnitude of the negative-sequence current should be determined. Rewriting (4.16) in form of magnitudes gives

$$I^- = Y^- V^-, \tag{4.18}$$

where V^- is the measured magnitude of the negative-sequence voltage at the PoC. Apparently, there are infinite schemes that can be proposed to determine Y^-. Considering simple implementations, Y^- can be a constant, i.e.

$$Y^- = Y^{-*}, \tag{4.19}$$

or be controlled as a linear function of V^-. When the negative-sequence voltage V^- decreases because of the compensation, the magnitude of the output negative-sequence admittance Y^- should increase in order to maintain or contribute more current for the compensation according to (4.18). Consequently, it is proposed to introduce a droop control for Y^- like

$$Y^- = Y^{-*} - m(V^- - V^{-*}), \tag{4.20}$$

where the droop coefficient m is a positive scalar number, and Y^{-*} is a set point of the negative-sequence admittance with respect to a set point of negative-sequence voltage V^{-*}. Parameters are designed in the next section.

Substituting (4.19) and (4.20) in (4.18) leads to

$$I^- = Y^{-*} V^-, \tag{4.21}$$

$$I^- = -mV^{-2} + (Y^{-*} + mV^{-*})V^-, \tag{4.22}$$

respectively. Based on (4.21) and (4.22), Figure 4.13 shows the magnitude of the negative-sequence compensating current I^- as a function of V^-, where $I_{\max}^-$ denotes the maximum negative-sequence current applicable for compensation and $V_{\max}^-$ the maximum negative-sequence voltage to be compensated. Four typical curves are shown in the graph, of which curves (b) and (c) are plotted based on (4.22), while curves (a) and (d) are derived from (4.21).

From a control point of view, $I^- - V^-$ curves (c) and (d) are preferred because they have a monotonically increasing characteristic within the operation range of V^-. On the other hand, it can be seen that more current can be contributed to the grid for negative-sequence voltage compensation with the parabola curve (c) than with the curve (d). As a result, the admittance droop control scheme based on (4.20) is adopted; parameters are designed in the following to guarantee a monotonically increasing parabola curve within the operation range of V^-.

4.4.2   Design parameters

First, the magnitude of the negative-sequence admittance Y^- should not be negative. From (4.20), Y^- is always positive when $V^- \leq V^{-*}$, otherwise m is limited by

$$m \leq \frac{Y^{-*}}{V^- - V^{-*}}. \tag{4.23}$$

Consequently, a suitable definition for m would be

$$m = Y^{-*}/V_{\max}^-, \tag{4.24}$$

where $V_{\max}^-$ is a specified maximum negative-sequence voltage considering knowledge of the worst unbalanced situation of the grid where the DG system is connected.

Notice that I^- is a quadratic function of V^- in (4.22), and hence it reaches the maximum point at the axis of symmetry of the parabola. According to curve (c) in Fig. 4.13, the parameters are imposed to meet the following equations:

$$\frac{Y^{-*} + mV^{-*}}{2m} = V_{\max}^-, \tag{4.25}$$

$$\frac{(Y^{-*} + mV^{-*})^2}{4m} = I_{\max}^-, \tag{4.26}$$

where $I_{\max}^-$ is the maximum current available for the voltage unbalance compensation. Hence, from (4.24) to (4.26) the solution is derived as

$$Y^{-*} = \frac{I_{\max}^-}{V_{\max}^-}, \ m = \frac{I_{\max}^-}{V_{\max}^{-2}}, \ V^{-*} = V_{\max}^-. \tag{4.27}$$

Note that (4.20) can be simplified by combining the derived parameters Y^{-*} and V^{-*}, but it is preferred to keep the expression as (4.20) since the two parameters calculated from (4.27) represent the boundary of the negative-sequence admittance droop control. Figure 4.14 shows the static droop characteristics of Y^-.
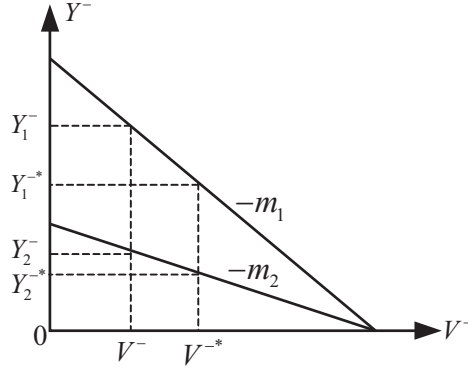
Figure 4.14: Static droop characteristics.

4.4.3 Negative-sequence current sharing

Taking into account the operation of multiple DG modules connected together at the same PoC or located separately along the same feeder, it is expected that the negative-sequence compensating currents can be shared by DG systems in proportion to their negative-sequence current rating. To look at the situation of multiple co-operative DG modules, define

$$I_n^- = Y_n^- V_n^-, \tag{4.28}$$

$$Y_n^- = Y_n^{-*} - m_n(V_n^- - V_n^{-*}), \tag{4.29}$$

where the subscript n denotes the nth module.

Comparing the negative-sequence currents between module n and $n + 1$ gives

$$\frac{I_n^-}{I_{n+1}^-} = \frac{Y_n^- V_n^-}{Y_{n+1}^- V_{n+1}^-}. \tag{4.30}$$

When DG modules equipped with the same control scheme are connected close to the same PoC, the negative-sequence voltages of each module are equal. Based on (4.27) to (4.30), it can be derived that these modules share the negative-sequence compensating current with respect to their maximum negative-sequence currents, as represented by

$$\frac{I_n^-}{I_{n+1}^-} = \frac{Y_n^-}{Y_{n+1}^-} = \frac{I_{\max\_n}^-}{I_{\max\_n+1}^-}. \tag{4.31}$$

Figure 4.14 also shows the relationship between the negative-sequence admittances of two DG modules as a function of V^-.

It should be noticed that the negative-sequence voltages of DG modules will be slightly different, when DG modules with droop compensation are located separately from each other along the feeder, or are coupled into a same connection point of the grid but with different length of feeders.
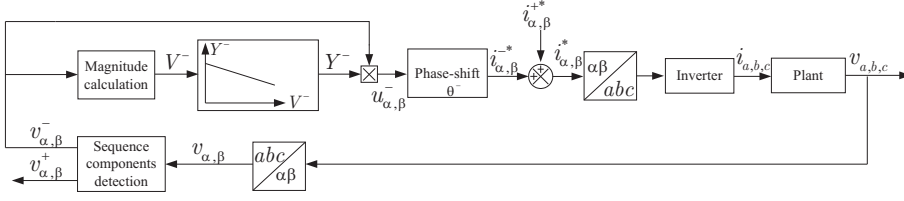
Figure 4.15: Block diagram of the negative-sequence voltage – admittance droop scheme.

(a)

(b)
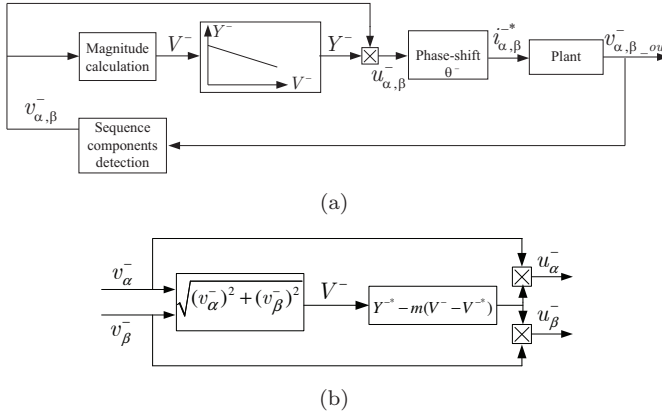
Figure 4.16: Block diagrams: (a) the equivalent part of the system control for negative-sequence components, and (b) the derivation of $u_{\alpha,\beta}^-$.

4.4.4   Small-signal modeling

Figure 4.15 shows the block diagram of a DG inverter control with the negative-sequence voltage - admittance droop scheme, while the reference currents $i_{\alpha,\beta}^{+*}$ generated for active power delivery are not detailed. As already mentioned, the control for positive-sequence and negative-sequence components can be separated. An equivalent part of the control for negative-sequence components is presented in Fig. 4.16. The block diagram is described in the $\alpha\beta$-reference frame, where the transformations between the abc- and $\alpha\beta$-reference frames are left out. Because the closed-loop bandwidth of the inverter is much higher than the bandwidth of the external negative-sequence current reference generation, the inverter part is also simplified as a unity gain block. In the following, a small-signal model of Fig. 4.16 (a) is derived, and the system stability with the proposed control scheme is analyzed.

Figure 4.16 (b) illustrates the derivation of $u_{\alpha,\beta}^-$ from the feedback quantities $v_{\alpha,\beta}^-$, showing a strongly nonlinear transformation from the inputs to the outputs, and also indicating coupling between the α and β variables. It is rather complicated to try to derive a small-signal model directly from the scheme in Fig. 4.16.

To facilitate the small-signal modeling, the magnitudes of the negative-sequence
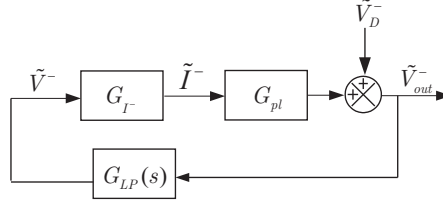
Figure 4.17: Small-signal model of the negative-sequence voltage – admittance droop control.

Table 4.2: Parameters for admittance droop control

Description	Symbol	Value
droop coefficient	m	0.08 S/V
droop control set-points	Y^{-*}	1.2 S
	V^{-*}	15 V
Max. neg.-seq. current	$I_{\max}^-$	18 A
Max. neg.-seq. voltage	$V_{\max}^-$	15 V
Pre-compensated voltage	V^-	5 V
Feeder impedance	R_g	0.206 Ω
per km	L_g	0.248 mH
Filter bandwidth	ω_{cut}	15 rad/s

control variables in Fig. 4.16 (a) are extracted for analysis. This is possible because the phase shift θ^- between the negative-sequence currents and voltages is fixed and the closed loop only leads to magnitude change of negative-sequence currents. With the high performance stationary frame filter (see (2.37) in Chapter 2) for sequence components detection, it is assumed that the measured quantities v_α^- and v_β^- are equal in magnitude and phase orthogonal. Therefore the magnitude of $i_{\alpha,\beta}^{-*}$, denoted by I^-, is given by

$$I^- = [Y^{-*} - m(V^- - V^{-*})]V^-, \tag{4.32}$$

with V^- the amplitude of $v_{\alpha,\beta}^-$. Writing in small-signal format gives

$$\tilde{I}^- = (Y^{-*} + mV^{-*} - 2mV_0^-)\tilde{V}^- = G_{I^-}\tilde{V}^-, \tag{4.33}$$

where V_0^- is the operating point, and G_{I^-} represents the gain.

Through the system plant, the small signal of the magnitude of v_{α,β_out}^- can be expressed as

$$\tilde{V}_{out}^- = -Z_g\tilde{I}^- = G_{pl}\tilde{I}^-, \tag{4.34}$$

where the minus sign is due to the definition of the current direction.

Because the detection block of sequence components is a stationary frame bandpass filter for ac quantities, it is equivalent to a low-pass filter for dc quantities in the synchronous frame. In other words, when considering the magnitude response
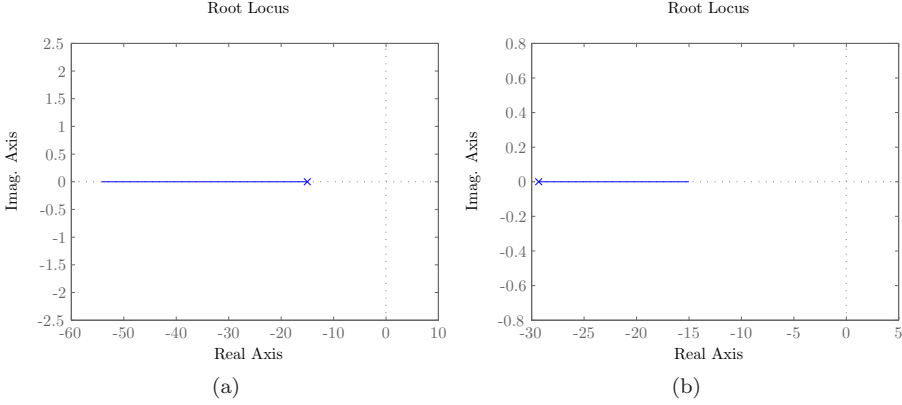
Figure 4.18: Root locus diagrams: (a) for a varied feeder length from $0 \le l_{fd} \le 2$ km, with $V_0^- = 2.67$ V and (b) for the operating point $0 \le V_0^- \le 15$ V, with $l_{fd} = 0.6$ km.
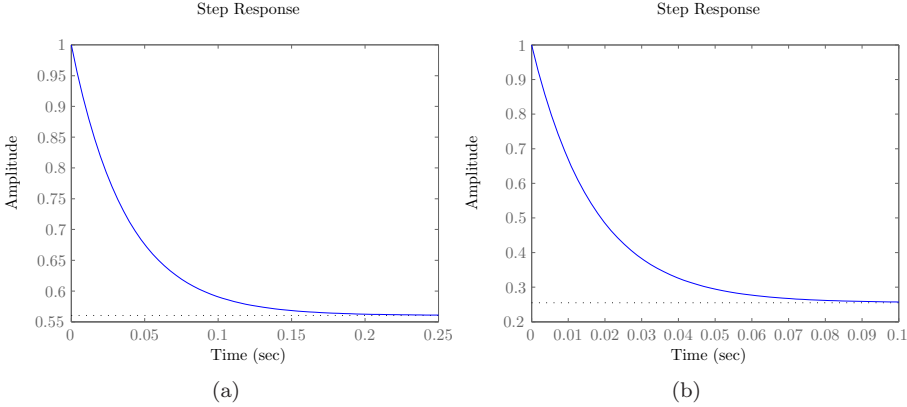
Figure 4.19: System step responses to the negative-sequence voltage: (a) when $l_{fd} = 0.6$ km, $I_{\max}^- = 18$ A, and (b) when $l_{fd} = 0.6$ km, $I_{\max}^- = 60$ A.

from v_{α,β_out}^- to $v_{\alpha,\beta}^-$, a low-pass filter can be used to simplify the transfer function in between, i.e.

$$\tilde{V}^- = \frac{\omega_{cut}}{s + \omega_{cut}} \tilde{V}_{out}^- = G_{LP}(s) \tilde{V}_{out}^-, \qquad (4.35)$$

where ω_{cut} is the cut-off angular frequency of the low-pass filter and should be designed below one tenth of the grid frequency.

Figure 4.17 is the block diagram of the derived small-signal model, where the disturbance signal $\tilde{V}_D^-$ from the grid is also included. Thus the closed-loop system is simplified as a first-order system, which is found to be always stable with a variation of the feeder length or the operating point V_0^-. The root-locus diagrams are depicted in Fig. 4.18, and other parameters are listed in Table. 4.2.

Grid disturbance signal $\tilde{V}_D^-$ is introduced from the unbalanced grid voltages or

from the voltage drop on the grid impedance caused by unbalanced load currents. The closed-loop control can be regarded as a damping of the negative-sequence voltage with a certain gain, which is derived as

$$G_{cl}(s) = \frac{1}{1 - G_{LP}(s)G_{pl}G_{I-}}. \tag{4.36}$$

The amplitude of $G_{cl}(s)$, that is the gain, varies with feeder impedances and the droop control parameters (determined by $I_{\max}^-$). Two step-response plots are drawn in Fig. 4.19, showing different gains and response time.

4.4.5 Steady-state analysis

As already described, the negative-sequence voltage compensation at the PoC can be represented by two separate models, as shown in Fig. 4.12 (a) and (b). To analyze the steady-state results of the negative-sequence admittance control scheme, the results can be derived separately based on these two models, and then superimpose the results. Firstly, the steady-state results are derived based on the model in Fig. 4.12 (a). According to the control scheme and the circuit model,

$$\underline{V}^- = \underline{V}_g^- - \underline{Z}_g\underline{I}^-, \tag{4.37}$$

$$\underline{I}^- = (Y^-\angle{-\theta^-})\underline{V}^-. \tag{4.38}$$

Again, note that the subscript 's' in the model is left out. It follows that the steady-state current is calculated by

$$\underline{I}^- = (\frac{Y^-}{1 + Z_gY^-}\angle - \theta^-)\underline{V}_g^-. \tag{4.39}$$

It can be seen from (4.38) and (4.39) that DG systems have to absorb negative-sequence currents from the grid in order to compensate the part of negative-sequence voltage from the upstream grid voltage. The farther the DG system is located from the voltage source, the bigger will be Z_g, and the less the compensating current is needed. Also, it can be seen from (4.38) and (4.39) that when Y^- increases to high values, the amplitude of the compensating current tends to be a constant and the negative-sequence voltage tends to be zero.

On the other hand, in most cases the unbalanced voltages are caused by the asymmetrical distribution of loads. The model in Fig. 4.12 (b) is expressed by

$$\underline{V}^- = -(\underline{I}_{ld}^- + \underline{I}^-)\underline{Z}_g. \tag{4.40}$$

Substituting (4.40) to (4.38), the steady-state current is found to be

$$\underline{I}^- = -\frac{Y^-}{1 + Z_gY^-}Z_g\underline{I}_{ld}^-. \tag{4.41}$$

It can be seen from (4.40) and (4.41) that DG systems actually provide negative-sequence current to the loads in order to decrease the negative-sequence voltage at the PoC. In other words, the controllable negative-sequence admittance of the DG system can be viewed as part of the loads, and tries to make the loads behind the PoC more symmetrically distributed.
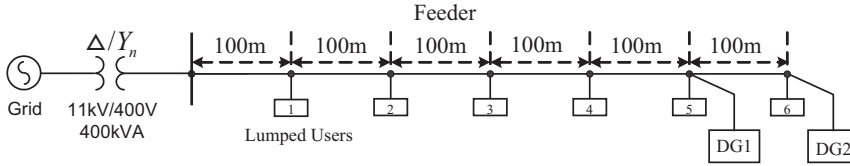
Figure 4.20: Single-line configuration of the system used for simulation verification.

4.4.6   Simulation results

Simulations are carried out in Matlab/simulink to verify the proposed control scheme. Figure 4.20 shows the single-line system configuration, where two DG modules, DG1 and DG2 both equipped with the negative-sequence voltage compensation function are connected at the node 5 and 6. Loads located along the feeder are lumped together every 100 meters, as denoted by the block 1 to 6. Each lumped user is connected with 10 KVA inductive loads (power factor is set to 0.7) per phase. Simulation parameters of DG1 are the same as shown in Table 4.2; DG2 is specified with three times the maximum negative-sequence current of DG1, and other control parameters of DG2 can be correspondingly derived from (4.27).

Single DG Unit

Firstly, a single DG is simulated to verify the operation of DG1 with combined functions of active power delivery and negative-sequence voltage compensation. As shown in Fig. 4.21, the system became unbalanced at $t = 0.3$ s due to unbalanced distribution of loads (intentional switching to very light loads in one phase), and DG1 is activated at $t = 0.5$ s with active power delivery (30 kW) to the grid and negative-sequence voltage compensation. Note that the slow responses of the measured symmetric sequence components in Fig. 4.21 (a) are due to the low bandwidth of the sequence detection filter. It can be seen that the negative-sequence voltage is decreased from 9.5 V to 8.5 V even with a limited compensation capability from a single DG unit, and the positive-sequence voltage is increased because of the active power support to the grid.

Dual DG units

To observe only the compensation for the negative-sequence voltages with multiple DG units, DG1 and DG2 are activated at $t = 0.5$ s and $t = 0.7$ s, respectively, but without delivering active power. The results are shown in Fig. 4.22. It can be found that the negative-sequence voltage at the PoC of the two DGs are almost the same, and decrease from 9.5 V to 5.5 V, while in terms of voltage unbalance factor, they decrease to 1.7% from 3.1%. In Fig. 4.22 (b), it can be seen that the steady-state negative-sequence compensating currents of DG1 and DG2 are proportional to their assigned maximum currents. Figure 4.23 shows the active power and reactive power measured at the node 4. As analyzed in the previous
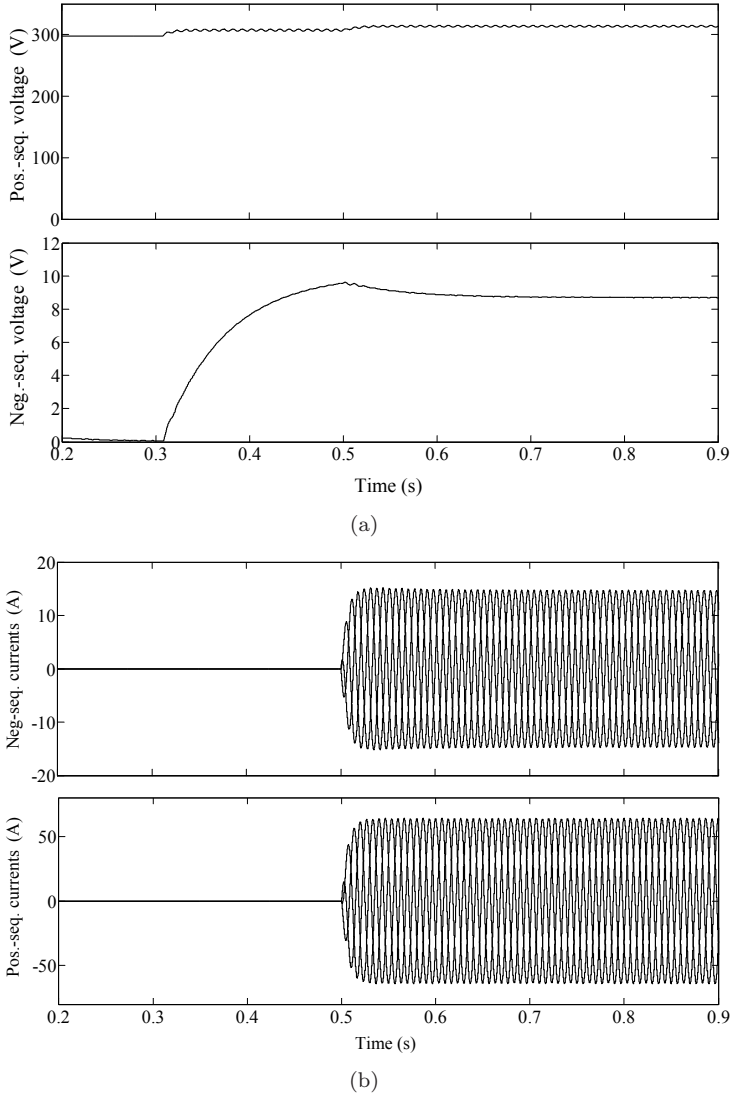
Figure 4.21: Simulation results with single DG unit (DG1): (a) the magnitudes of positive-sequence voltages and negative-sequence voltages at the node 5, and (b) the positive and negative sequence components of the currents from DG1.
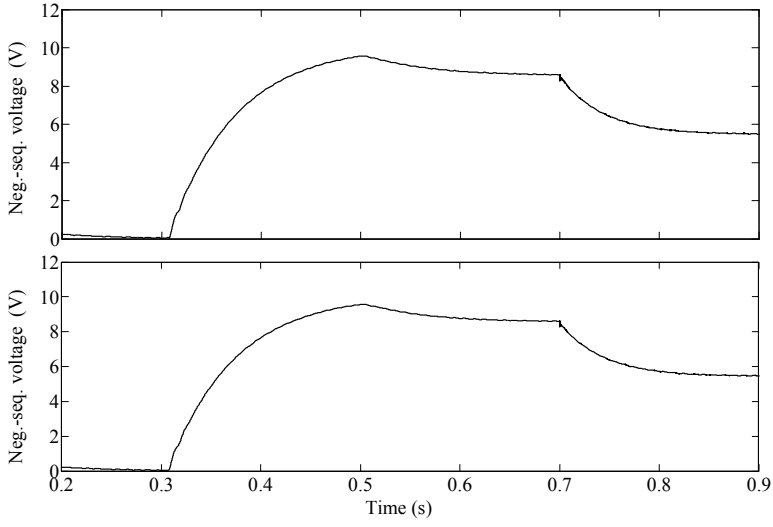
(a)
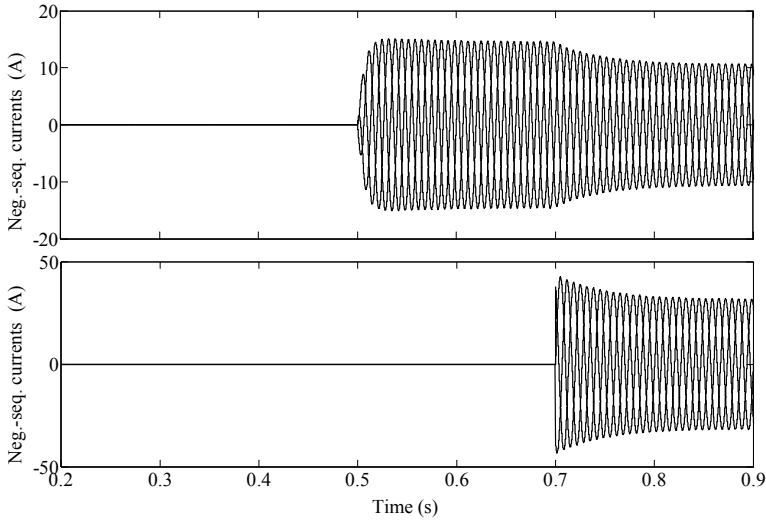
(b)

Figure 4.22: Simulation results with dual DG units: (a) the magnitudes of negative-sequence voltages and (b) the compensated negative-sequence currents, where the waveforms (from top to bottom) correspond with DG1 and DG2, respectively.
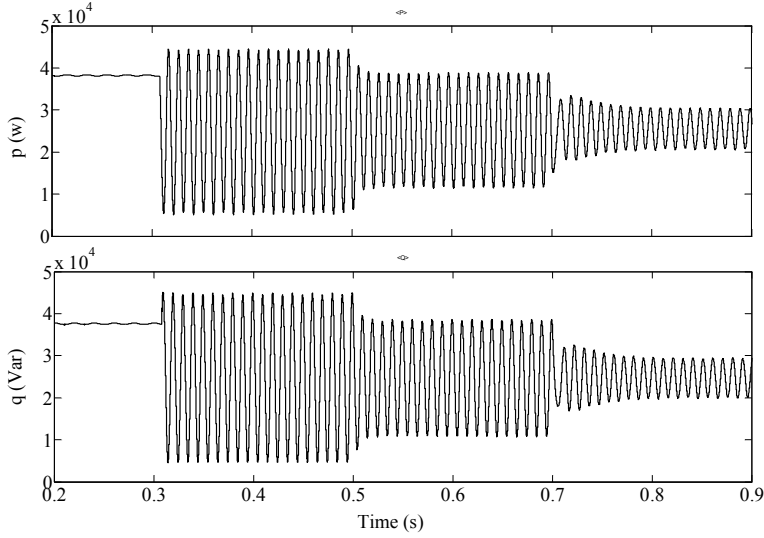
Figure 4.23: Simulation results with dual DG units, where the active power and reactive power at the node 4 are measured.

section, the oscillating power is reduced because the equivalent loads behind node 4 become more symmetrical after the compensation.

4.5   Conclusions

This chapter has presented the basic principles for the compensation of voltage unbalance that rely on inverter-based distributed power generation. Two control schemes have been proposed. Specifically, the negative-sequence voltages at the point of connection to the grid are compensated and mitigated by regulating the negative-sequence currents flowing between grid-interfacing inverters and the grid.

The first control scheme is based on the voltage unbalance factor and on the positive-sequence current that is delivered by DG inverters to the grid in normal conditions. When the grid is unbalanced due to voltage propagation from upstream faulty grids or asymmetrical distribution of downstream loads, the DG inverters absorb a small amount of negative-sequence currents from the grid based on the voltage unbalance factor at the PoC, thereby correcting the negative-sequence voltages. The unbalanced voltages at the PoC tend to be corrected by the collective action of multiple DG modules equipped with the same compensation schemes. Simulation and experimental results have shown the effects of this control scheme.

However, there are limitations for the first control scheme, due to the coupling between the negative-sequence currents and the positive-sequence currents of DG systems. Therefore, a second scheme has been presented. By controlling the negative-sequence admittance of the DG inverters, the negative-sequence compensating currents can be regulated independently. Modeling, analysis and

simulations have shown the effectiveness of the second control scheme. With this scheme, distributed DG systems can automatically achieve a co-operative compensation for the unbalanced grid voltages or unbalanced loads in proportion to specified current rating.

Chapter 5

Grid-fault ride through control of DG inverters

Abstract - Chapter 4 has investigated the compensation of voltage unbalance by means of DG grid-interactive inverters, where voltage unbalance is considered as a steady situation indicating slight asymmetry among three phases. However, another category of unbalance grid situation, namely voltage dips, which is typically caused by a temporary fault somewhere on the power system, appears as severe voltage variations and phase asymmetry with short duration times. It is well known that in this case most end users are obliged to disconnect from the grid, but in a future scenario with large penetration of DG systems it is expected to have those DG systems riding through this severe voltage disturbance.

Being the grid interface of distributed energy sources, DG inverters are therefore addressed in this chapter with regard to their grid-fault ride through control, i.e. uninterrupted active power delivery for grid support. In addition, reactive power support from DG systems with large power capacity is also expected by the grid, and this issue will be presented in the next chapter.

Aiming to provide DG inverters with the flexibility to adapt to the coming change of grid requirements, an optimized active power control strategy is proposed that facilitates the ride-through control of DG inverters under grid faults. Specifically, through an adjustable parameter it is possible to change the relative amplitudes of oscillating active and reactive power smoothly, while simultaneously eliminating the second-order active or reactive power ripple at the two extremes of the parameter range. The steering possibility of the proposed strategy enables DG inverters to be optimally designed from the perspectives of both the power-electronic converters and the power system. The proposed strategy is proved through simulation and further validated by experimental results. Furthermore, the contribution of zero-sequence currents to active power control is also studied; it is shown that the use of zero-sequence components is technically effective but may lead to badly unbalanced currents.

5.1 Introduction

Voltage dips, usually caused by remote grid faults in the power system, are short-duration decreases in rms voltage. Most voltage dips are due to unbalanced faults, while balanced voltage dips are relatively rare in practice [93, 94]. Conventionally, a distributed generation (DG) system, as shown in Fig. 5.1, would be required to disconnect from the grid when voltage dips occur and to reconnect to the grid when faults are cleared. However, this requirement is changing. With the increasing application of renewable energy sources, more and more DG systems actively deliver electricity into the grid. In particular, wind power generation is becoming an important electricity source in many countries. Consequently, in order to maintain active power delivery and reactive power support to the grid, grid codes now require wind energy systems to ride through voltage dips without interruption [32, 33, 95].

As shown in Fig. 5.2, a guideline is given for a type-2 generating plant (all other plants but the ones connected to the network through synchronous generators) connected to the medium-voltage network. The DG systems must maintain stable operation when voltage dips are above the borderline 1, and must coordinate with the network operator when voltage dips at values in between borderline 1 and 2, while immediate disconnection is permitted for DG system when voltage dips are below the borderline 2 [95]. For the future scenario of a grid with significant DG penetration, it is necessary to investigate the ride-through control of wind turbine systems and other DG systems as well. Disregarding various upstream distributed sources and their controls, this chapter will focus on the grid-side DG inverters.

Concerning the control of DG inverters under grid faults, two aspects should be noticed. First, fast system dynamics and good reference tracking are necessary. Note that inverters use the same converter topologies as PWM rectifiers. Hence, techniques which have been developed to control PWM rectifiers [34, 96] can also be adapted to DG inverters. It has been shown that, because conventional controllers cannot effectively handle the negative-sequence voltages, systems during unbalanced voltage dips can have unbalanced and distorted grid currents as well as voltage variations in the dc bus [96]. This problem is discussed in [24], where dual PI current controllers in dual synchronous reference frames (SRF) are proposed to control positive-sequence and negative-sequence components separately. Unfortunately, the symmetric sequences of the feedback quantities have to be extracted in dc form by filtering out the components oscillating at twice the grid frequency. The system dynamics are considerably limited due to the notch filter used for this purpose.

As an alternative, a delayed signal cancellation (DSC) method with 1/4 fundamental period delay can be used to improve the sequence detection, but due to the time delay this method still influences the system dynamics [97, 98]. In order to leave out the sequence detection of feedback currents and further improve system dynamics, two extra resonant controllers working at twice the grid frequency are added to dual SRFs, eliminating the oscillation parts by means of compensation [34]. Alternatively, stationary frame resonant controllers are found to be suitable to control all the sequences (including the zero sequence which has been disre-
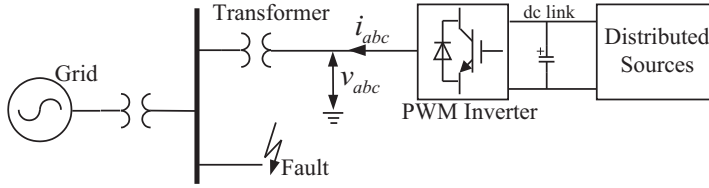
Figure 5.1: A distributed generation inverter operating under grid faults.
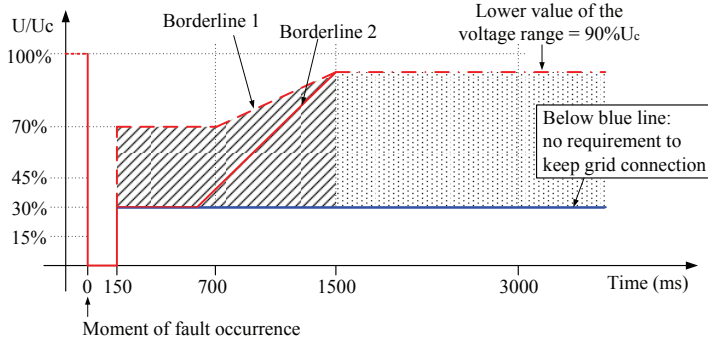
Figure 5.2: Borderlines of the voltage profile of a type-2 generating plant at the network connection point[95].

garded in many studies). This can simplify dual SRFs to a single stationary frame and achieve zero steady-state error [50, 68]. Also, symmetric sequence detection in feedback currents becomes unnecessary when using the resonant controllers, e.g. the scalar resonant control structure presented in [99]. In summary, in order to improve system dynamics and reference tracking, controllers must be able to deal with all the symmetric-sequence components and have direct feedback signals for closed-loop control. This is achieved by the controller employed in this chapter.

Secondly, the generation of reference currents in case of unbalanced voltage dips is important. Assuming that controllers are fast enough when the voltage dips, then the only difference before and after a grid fault is a change in demanded current. Depending on practical applications, current reference generation is objective oriented. Considering the power-electronics converter constraints, a constant dc-link voltage is usually desirable, as in the objective set of [34] and [35]. In other words, the instantaneous power at the output terminal of the inverter bridge is expected to be a constant. For simplification, only the instantaneous power at the grid connection point is considered by neglecting the part of oscillating power on account of the output filters [24]. However, a constant dc bus is achieved at the cost of unbalanced grid currents, and this results in a decrease of maximum deliverable power. In [100], a power reducing scheme is used to confine the current during a grid fault.

On the other hand, the effects of the grid currents on the power system side

should also be taken into account when designing reference currents for DG invert-
ers. As presented in [37], in terms of instantaneous power oscillation and current
distortion, several individual strategies are possible to obtain different power qual-
ity at the grid connection point. One of the methods in [37] based on instantaneous
power theory [101] obtains zero instantaneous power oscillation but generates dis-
torted grid currents due to asymmetry of grid voltages. From power quality point
of view, this method may not be desirable for the grid even during voltage dips.
Alternatively, another three strategies in [37] can obtain sinusoidal output currents
based on symmetric-sequence components. These strategies show flexible control
possibilities of DG systems under grid faults. However, they only cope with spe-
cific cases. This chapter aims to provide DG inverters with a generalized strategy
to adapt to the coming change of grid requirements and to improve ride-through
capability of DG inverters during voltage dips.

    This chapter proposes a generalized active power control strategy under unbal-
anced grid faults based on symmetric-sequence components, and shows explicitly
the contributions of symmetrical sequences to instantaneous power [102]. The
steering possibility of the proposed strategy enables DG inverters to be optimally
designed from the perspective of both the power-electronics converter and the
grid. Thus, a further discussion on objective-oriented optimization of the proposed
strategy is presented. Simulations and experiments are carried out to validate the
proposed strategy. Furthermore, to date hardly any work has been done to analyze
active power control of a four-wire system by taking into account zero sequence
components of unbalanced voltages. To this purpose, the chapter also investigates
the contribution of zero-sequence components to current reference generation.

5.2   Instantaneous power calculation

In this section, instantaneous power theory [101, 103] is revisited. Then instan-
taneous power calculation based on symmetric sequences is developed, and the
notation for the reference current design in the next sections is defined.

5.2.1   Instantaneous power theory

For a three-phase DG system shown in Fig. 5.1, instantaneous active power and
reactive power at the grid connection point are given by, respectively,

$$p = \mathbf{v} \cdot \mathbf{i} = v_a i_a + v_b i_b + v_c i_c \tag{5.1}$$

$$q = \mathbf{v}_\perp \cdot \mathbf{i} = \tfrac{1}{\sqrt{3}}[(v_a - v_b)i_c + (v_b - v_c)i_a + (v_c - v_a)i_b] \tag{5.2}$$

with $\mathbf{v}_\perp = \frac{1}{\sqrt{3}} \begin{bmatrix} 0 & 1 & -1 \\ -1 & 0 & 1 \\ 1 & -1 & 0 \end{bmatrix} \mathbf{v}$

where $\mathbf{v} = \begin{bmatrix} v_a & v_b & v_c \end{bmatrix}^T$, $\mathbf{i} = \begin{bmatrix} i_a & i_b & i_c \end{bmatrix}^T$, bold symbols represent vectors, and
the operator "·" denotes the dot product of vectors. Note that the subscript "⊥"
is used to represent a vector derived from the matrix transformation in (5.2),
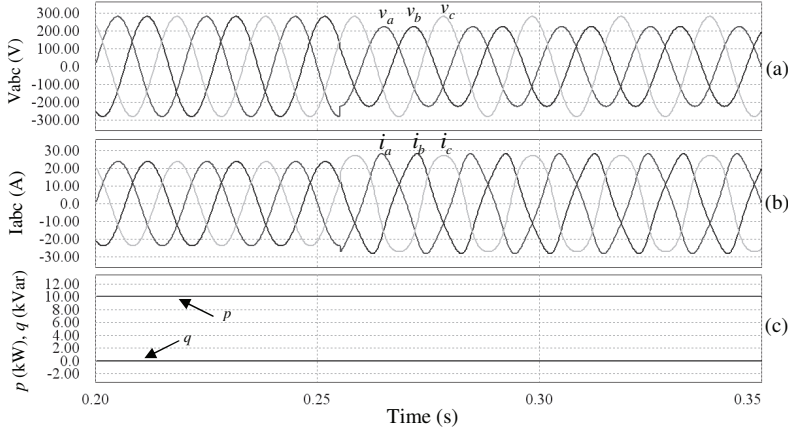
Figure 5.3: Simulation results obtained based on instantaneous power theory: (a) phase voltages, where voltages of phase a and b dip to 80% at t=0.255 s, (b) injected currents, and (c) instantaneous p, q.

although vectors $\mathbf{v}_\perp$ and $\mathbf{v}$ are orthogonal only when the three-phase components in vector $\mathbf{v}$ are balanced.

To deliver a given constant instantaneous active power ($p = P$) and zero reactive power, the corresponding currents can be calculated based on the instantaneous power theory. The derived currents, denoted by $\mathbf{i}_p$, are expressed by

$$\mathbf{i}_p = \frac{P}{\|\mathbf{v}\|^2}\mathbf{v}, \tag{5.3}$$

where $\|\mathbf{v}\|^2 = \mathbf{v}\cdot\mathbf{v} = v_a^2 + v_b^2 + v_c^2$, operator "$\|\cdot\|$" means the norm of a vector, and subscript "p" represents active power related quantities. Since $\mathbf{i}_p$ is in phase with $\mathbf{v}$, the resulting instantaneous reactive power q in (5.2) equals zero. Because $\|\mathbf{v}\|$ is constant when the voltages are balanced and sinusoidal, the derived currents are also balanced and sinusoidal waveforms. However, when the voltages become unbalanced or distorted, $\|\mathbf{v}\|$ is not a constant but varies with twice the fundamental frequency. Consequently, reference current $\mathbf{i}_p$ becomes distorted and unbalanced, as illustrated in Fig. 5.3.

Although the method of instantaneous power control achieves constant active and reactive power at the cost of current distortion, it may not be acceptable to inject low quality currents into the grid even during voltage dips. It is conceivable to employ only balanced fundamental quantities for sinusoidal current generation. Therefore, instantaneous power calculations based on symmetric-sequence components are derived in the following.

5.2.2 Symmetric-sequence based instantaneous power

Phasor notation is a proven and convenient way to describe sinusoidal quantities. For instance, where harmonics are negligible, voltages in the *abc* frame can be

expressed by

$$\mathbf{v} = \begin{bmatrix} v_a \\ v_b \\ v_c \end{bmatrix} = \Re \left(e^{j\omega t} \begin{bmatrix} \underline{V}_a \\ \underline{V}_b \\ \underline{V}_c \end{bmatrix} \right), \tag{5.4}$$

where phasors are denoted with a bar subscript, and $\Re(\cdot)$ represents the real part of a complex number. Applying symmetric-component transformation [55] to voltage phasors yields symmetric-sequence phasors as

$$\begin{bmatrix} \underline{V}^0 \\ \underline{V}^+ \\ \underline{V}^- \end{bmatrix} = \frac{1}{3} \begin{bmatrix} 1 & 1 & 1 \\ 1 & a & a^2 \\ 1 & a^2 & a \end{bmatrix} \begin{bmatrix} \underline{V}_a \\ \underline{V}_b \\ \underline{V}_c \end{bmatrix}, \text{with } a = e^{j\frac{2\pi}{3}}, \tag{5.5}$$

where subscripts "+", "-", and "0" denote positive, negative, and zero sequences, respectively. The inverse transformation of (5.5) is found to be

$$\begin{bmatrix} \underline{V}_a \\ \underline{V}_b \\ \underline{V}_c \end{bmatrix} = \begin{bmatrix} 1 & 1 & 1 \\ 1 & a^2 & a \\ 1 & a & a^2 \end{bmatrix} \begin{bmatrix} \underline{V}^0 \\ \underline{V}^+ \\ \underline{V}^- \end{bmatrix}. \tag{5.6}$$

Correspondingly, instantaneous values can be derived from the symmetric-component phasors given by (5.6). Otherwise stated, the following expressions for the abc voltages are applicable:

$$\mathbf{v} = \mathbf{v}^+ + \mathbf{v}^- + \mathbf{v}^0, \tag{5.7}$$

where $\mathbf{v}^+ = \begin{bmatrix} v_a^+ \\ v_b^+ \\ v_c^+ \end{bmatrix} = \Re \left(\underline{V}^+ e^{j\omega t} \begin{bmatrix} 1 \\ a^2 \\ a \end{bmatrix} \right),$

$\mathbf{v}^- = \begin{bmatrix} v_a^- \\ v_b^- \\ v_c^- \end{bmatrix} = \Re \left(\underline{V}^- e^{j\omega t} \begin{bmatrix} 1 \\ a \\ a^2 \end{bmatrix} \right), \text{ and}$

$\mathbf{v}^0 = \begin{bmatrix} v_a^0 \\ v_b^0 \\ v_c^0 \end{bmatrix} = \Re \left(\underline{V}^0 e^{j\omega t} \begin{bmatrix} 1 \\ 1 \\ 1 \end{bmatrix} \right).$

Similarly, current quantities can also be represented in terms of symmetric sequences, i.e.

$$\mathbf{i} = \mathbf{i}^+ + \mathbf{i}^- + \mathbf{i}^0, \tag{5.8}$$

where $\mathbf{i}^{+,-,0} = \begin{bmatrix} i_a^{+,-,0} & i_b^{+,-,0} & i_c^{+,-,0} \end{bmatrix}^T$. As a result, the calculation of instantaneous power in (5.1) and (5.2) can be rewritten as

$$p = \mathbf{v} \cdot \mathbf{i} = (\mathbf{v}^+ + \mathbf{v}^- + \mathbf{v}^0) \cdot (\mathbf{i}^+ + \mathbf{i}^- + \mathbf{i}^0), \tag{5.9}$$

$$q = \mathbf{v}_\perp \cdot \mathbf{i} = (\mathbf{v}_\perp^+ + \mathbf{v}_\perp^- + \mathbf{v}_\perp^0) \cdot (\mathbf{i}^+ + \mathbf{i}^- + \mathbf{i}^0). \tag{5.10}$$

With respect to the definitions of the symmetric-sequence vector in (5.7), corresponding orthogonal vectors in (5.10) can be derived by using the matrix transformation in (5.2). Note that $\mathbf{v}_\perp^+$ lags $\mathbf{v}^+$ by 90°, $\mathbf{v}_\perp^-$ leads $\mathbf{v}^-$ by 90°, and $\mathbf{v}_\perp^0$ is

always equal to zero. Because the dot products between $\mathbf{i}^0$ and positive-sequence or negative-sequence voltage vectors are also always zero (due to symmetry of the components in $\mathbf{v}^+$ and $\mathbf{v}^-$), equation (5.9) and (5.10) can be simplified by

$$p = \mathbf{v} \cdot \mathbf{i} = (\mathbf{v}^+ + \mathbf{v}^-) \cdot (\mathbf{i}^+ + \mathbf{i}^-) + \mathbf{v}^0 \cdot \mathbf{i}^0, \tag{5.11}$$

$$q = \mathbf{v}_\perp \cdot \mathbf{i} = (\mathbf{v}_\perp^+ + \mathbf{v}_\perp^-) \cdot (\mathbf{i}^+ + \mathbf{i}^-). \tag{5.12}$$

Because the calculation of instantaneous power and current references is carried out in terms of vectors, it can also be used in other reference frames, simply by substituting the vectors in the abc-frame with vectors derived in other frames. For example, an alternative expression in the stationary $\alpha\beta\gamma$-frame for the instantaneous power calculation can be derived, i.e.

$$p = \mathbf{v} \cdot \mathbf{i} = (\mathbf{v}_{\alpha\beta}^+ + \mathbf{v}_{\alpha\beta}^-) \cdot (\mathbf{i}_{\alpha\beta}^+ + \mathbf{i}_{\alpha\beta}^-) + v_\gamma \cdot i_\gamma, \tag{5.13}$$

$$q = \mathbf{v}_\perp \cdot \mathbf{i} = (\mathbf{v}_{\alpha\beta\perp}^+ + \mathbf{v}_{\alpha\beta\perp}^-) \cdot (\mathbf{i}_{\alpha\beta}^+ + \mathbf{i}_{\alpha\beta}^-), \tag{5.14}$$

with $v_\gamma = \sqrt{3}v_a^0$, $i_\gamma = \sqrt{3}i_a^0$, $\mathbf{v}_{\alpha\beta}^{+,-} = T_{\alpha\beta}\mathbf{v}^{+,-}$ and $\mathbf{i}_{\alpha\beta}^{+,-} = T_{\alpha\beta}\mathbf{i}^{+,-}$, where

$$T_{\alpha\beta} = \sqrt{\frac{2}{3}} \begin{bmatrix} 1 & -\frac{1}{2} & -\frac{1}{2} \\ 0 & \frac{\sqrt{3}}{2} & -\frac{\sqrt{3}}{2} \end{bmatrix}.$$

The orthogonal matrix transformation of α, β quantities is

$$\mathbf{v}_{\alpha\beta\perp}^{+,-} = \begin{bmatrix} 0 & 1 \\ -1 & 0 \end{bmatrix} \mathbf{v}_{\alpha\beta}^{+,-}. \tag{5.15}$$

Note that in the experiment these symmetric-sequence components are detected in the time domain. Based on this symmetric-sequence-based power definition, a comprehensive investigation on how to generate sinusoidal current references for DG inverters is presented in the next section.

5.3 Current reference generation design

In this section, current control based only on positive-sequence and negative-sequence components is investigated. Because zero-sequence voltages of unbalanced voltage dips do not exist in three-wire systems, nor can they propagate to the secondary side of star-ungrounded or delta connected transformers in four-wire systems, most case-studies only consider positive and negative sequences. Even for unbalanced systems with zero-sequence voltage, four-leg inverter topologies can eliminate zero-sequence current with appropriate control, as tested in the experiments, and no power introduced by zero-sequence components exists.

Simplifying assumptions to be used:

- Only positive-sequence and negative-sequence currents are present;

- Only fundamental components exist, the power introduced by harmonics is vanishingly small;

- The amplitude of the positive-sequence voltage is higher than the negative sequence, that is $\|\mathbf{v}^+\| > \|\mathbf{v}^-\|$.

Since no zero-sequence currents are involved, $\mathbf{i}_p$ can be separated into $\mathbf{i}_p^+$ and $\mathbf{i}_p^-$, which will be defined in phase with $\mathbf{v}^+$ and $\mathbf{v}^-$, respectively, in order to yield active power only. Rewriting (5.11) and (5.12) in terms of $\mathbf{i}_p^+$ and $\mathbf{i}_p^-$ obtains

$$p = \underbrace{\mathbf{v}^+ \cdot \mathbf{i}_p^+}_{P^+} + \underbrace{\mathbf{v}^- \cdot \mathbf{i}_p^-}_{P^-} + \underbrace{\mathbf{v}^+ \cdot \mathbf{i}_p^- + \mathbf{v}^- \cdot \mathbf{i}_p^+}_{\tilde{p}_{2\omega}}, \qquad (5.16)$$

$$q = \underbrace{\mathbf{v}_\perp^- \cdot \mathbf{i}_p^+ + \mathbf{v}_\perp^+ \cdot \mathbf{i}_p^-}_{\tilde{q}_{2\omega}}, \qquad (5.17)$$

where P^+ and P^- denote the constant active power introduced by positive and negative sequences, respectively, $\tilde{p}_{2\omega}$ is oscillating active power, and $\tilde{q}_{2\omega}$ oscillating reactive power. It can be found that the two terms of $\tilde{p}_{2\omega}$ are in-phase quantities oscillating at twice the fundamental frequency. A similar property can be found for the two terms of $\tilde{q}_{2\omega}$.

Proof

The dot product of a positive-sequence voltage vector $\mathbf{v}^+$ and a negative-sequence vector $\mathbf{i}^-$ can be calculated in the *abc* reference frame as

$$\mathbf{v}^+ \cdot \mathbf{i}^- = v_a^+ i_a^- + v_b^+ i_b^- + v_c^+ i_c^- \qquad (5.18)$$

$$= V^+ \cos(\omega t + \varphi_1) I^- \cos(\omega t + \varphi_2)$$

$$+ V^+ \cos(\omega t + \varphi_1 - \frac{2}{3}\pi) I^- \cos(\omega t + \varphi_2 + \frac{2}{3}\pi)$$

$$+ V^+ \cos(\omega t + \varphi_1 + \frac{2}{3}\pi) I^- \cos(\omega t + \varphi_2 - \frac{2}{3}\pi)$$

$$= \frac{3}{2} V^+ I^- \cos(2\omega t + \varphi_1 + \varphi_2), \qquad (5.19)$$

where symbols φ_1 and φ_2 are the phase angle of v_a^+ and i_a^-, respectively. It can be seen that the dot product of $\mathbf{v}^+$ and $\mathbf{i}^-$ leads to an instantaneous power oscillation at twice the fundamental frequency.

As defined, $\mathbf{i}_p^+$ and $\mathbf{i}_p^-$ are in phase with $\mathbf{v}^+$ and $\mathbf{v}^-$, respectively. Thus $\mathbf{i}_p^+ = k_1 \mathbf{v}^+$, $\mathbf{i}_p^- = k_2 \mathbf{v}^-$, where k_1 and k_2 are scalars. Hence, it can be obtained that

$$\mathbf{v}^- \cdot \mathbf{i}_p^+ = \frac{1}{k_2} \mathbf{i}_p^- \cdot k_1 \mathbf{v}^+ = \frac{k_1}{k_2} (\mathbf{v}^+ \cdot \mathbf{i}_p^-). \qquad (5.20)$$

Likewise, it can also be found that the dot products of $\mathbf{v}_\perp^- \cdot \mathbf{i}_p^+$ and $\mathbf{v}_\perp^+ \cdot \mathbf{i}_p^-$ have a similar relationship.

Because oscillating active power can result in a variation of the dc-link voltage, and high dc voltage variation may cause over-voltage problems, output distortion, or even control instability, it is desirable to eliminate $\tilde{p}_{2\omega}$. On the other hand, the oscillating reactive power $\tilde{q}_{2\omega}$ also causes power losses and operating current increase, and therefore it is advantageous to mitigate $\tilde{q}_{2\omega}$ as well. A trade-off between $\tilde{p}_{2\omega}$ and $\tilde{q}_{2\omega}$ is not straightforward and depends on practical requirements. In the following, strategies to achieve controllable oscillating active and reactive power are derived from two considerations.

5.3.1 Controllable oscillating active power

For a given level of active power P injection into the grid, determined by the power availability of the DG source and the converter ratings, the first two terms of (5.16) are designed to meet

$$P = \mathbf{v}^+ \cdot \mathbf{i}_p^+ + \mathbf{v}^- \cdot \mathbf{i}_p^- . \tag{5.21}$$

Since the two terms of $\tilde{p}_{2\omega}$ in (5.16) are in-phase quantities, it is convenient that these two terms can easily compensate each other. Therefore, intentionally set

$$\mathbf{v}^+ \cdot \mathbf{i}_p^- = -k_p \mathbf{v}^- \cdot \mathbf{i}_p^+, \quad 0 \le k_p \le 1, \tag{5.22}$$

where k_p is a scalar coefficient used as a weighting factor for the elimination of oscillating active power; the subscript "p" is related to active power (P) control. After some manipulations the negative-sequence current $\mathbf{i}_p^-$ is derived from (5.22) as

$$\mathbf{i}_p^- = \frac{-k_p \mathbf{v}^+ \cdot \mathbf{i}_p^+}{\|\mathbf{v}^+\|^2} \mathbf{v}^- . \tag{5.23}$$

Substituting (5.23) into (5.21) obtains

$$P \|\mathbf{v}^+\|^2 = \left(\|\mathbf{v}^+\|^2 - k_p \|\mathbf{v}^-\|^2 \right) \left(\mathbf{v}^+ \cdot \mathbf{i}_p^+ \right) . \tag{5.24}$$

Then, based on (5.23) and (5.24), currents $\mathbf{i}_p^+$ and $\mathbf{i}_p^-$ can be calculated as

$$\mathbf{i}_p^+ = \frac{P}{\|\mathbf{v}^+\|^2 - k_p \|\mathbf{v}^-\|^2} \mathbf{v}^+ , \tag{5.25}$$

$$\mathbf{i}_p^- = \frac{-k_p P}{\|\mathbf{v}^+\|^2 - k_p \|\mathbf{v}^-\|^2} \mathbf{v}^- . \tag{5.26}$$

Finally, the total current reference is the sum of $\mathbf{i}_p^+$ and $\mathbf{i}_p^-$, that is

$$\mathbf{i}_p^* = \frac{P}{\|\mathbf{v}^+\|^2 - k_p \|\mathbf{v}^-\|^2} (\mathbf{v}^+ - k_p \mathbf{v}^-), \quad 0 \le k_p \le 1. \tag{5.27}$$

5.3.2 Controllable oscillating reactive power

Instead of compensating the oscillating active power in (5.16), the oscillating reactive power $\tilde{q}_{2\omega}$ in (5.17) can be similarly shaped. For this purpose negative-sequence currents are imposed to meet

$$\mathbf{v}_\perp^+ \cdot \mathbf{i}_p^- = -k_p \mathbf{v}_\perp^- \cdot \mathbf{i}_p^+, \quad 0 \le k_p \le 1. \tag{5.28}$$

where the scalar coefficient k_p is now a weighting factor for the elimination of $\tilde{q}_{2\omega}$. Note that the subscript "p" in k_p remains consistent as used in (5.22), representing active power (P) control.
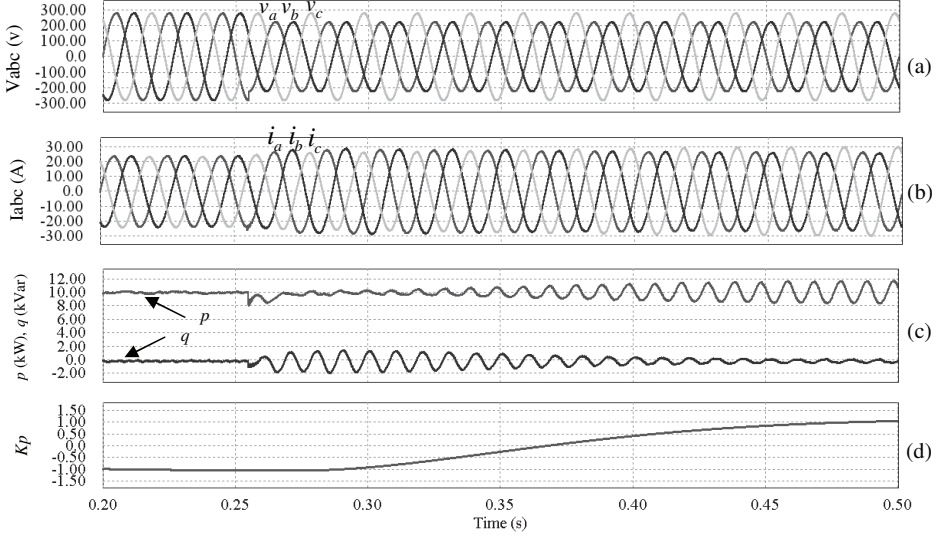
Figure 5.4: Simulation results of the proposed control strategy: (a) phase voltages, where voltages of phase a and b dip to 80% at t=0.255 s, (b) injected currents, (c) instantaneous p, q, and (d) controllable coefficient k_p sweeping from -1 to 1.

By considering equation $\mathbf{v}_\perp^+ \cdot \mathbf{i}^- = -\mathbf{v}^+ \cdot \mathbf{i}_\perp^-$ (because $\mathbf{v}_\perp^+$ lags $\mathbf{v}^+$ by 90° and $\mathbf{i}_\perp^-$ leads $\mathbf{i}^-$ by 90°), the left side of (5.28) can be rewritten as

$$\mathbf{v}_\perp^+ \cdot \mathbf{i}_p^- = -\mathbf{v}^+ \cdot \mathbf{i}_{p\perp}^- = -k_p \mathbf{v}_\perp^- \cdot \mathbf{i}_p^+, \tag{5.29}$$

where $\mathbf{i}_{p\perp}^-$ denotes the orthogonal vector of $\mathbf{i}_p^-$ according to (5.2). Then, it follows that

$$\mathbf{i}_{p\perp}^- = \frac{k_p \mathbf{v}^+ \cdot \mathbf{i}_p^+}{\|\mathbf{v}^+\|^2} \mathbf{v}_\perp^-. \tag{5.30}$$

Hence the negative-sequence current $\mathbf{i}_p^-$ follows directly from (5.30) as

$$\mathbf{i}_p^- = \frac{k_p \mathbf{v}^+ \cdot \mathbf{i}_p^+}{\|\mathbf{v}^+\|^2} \mathbf{v}^-. \tag{5.31}$$

Solving (5.21) and (5.31), the positive-sequence currents and negative-sequence currents are derived as

$$\mathbf{i}_p^+ = \frac{P}{\|\mathbf{v}^+\|^2 + k_p \|\mathbf{v}^-\|^2} \mathbf{v}^+, \tag{5.32}$$

$$\mathbf{i}_p^- = \frac{k_p P}{\|\mathbf{v}^+\|^2 + k_p \|\mathbf{v}^-\|^2} \mathbf{v}^-. \tag{5.33}$$

Again, the total current reference is the sum of $\mathbf{i}_p^+$ and $\mathbf{i}_p^-$, i.e.

$$\mathbf{i}_p^* = \frac{P}{\|\mathbf{v}^+\|^2 + k_p \|\mathbf{v}^-\|^2} (\mathbf{v}^+ + k_p \mathbf{v}^-), \quad 0 \le k_p \le 1. \tag{5.34}$$

(a)   (b)
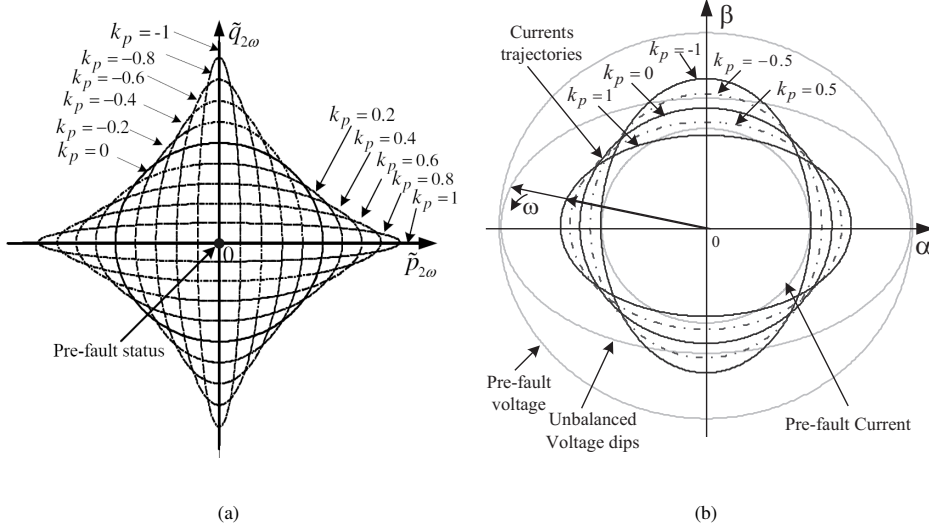
Figure 5.5: Graphic representation of (a) relationship between oscillating active power $\tilde{p}_{2\omega}$ and oscillating reactive power $\tilde{q}_{2\omega}$, and (b) grid voltage and current trajectories before and after unbalanced voltage dips in the stationary frame, with k_p as a changing parameter.

5.3.3 Combining the strategies

Simple analysis reveals that (5.27) and (5.34) can be combined and represented by

$$\mathbf{i}_p^* = \frac{P}{\|\mathbf{v}^+\|^2 + k_p \|\mathbf{v}^-\|^2}(\mathbf{v}^+ + k_p\mathbf{v}^-), \quad -1 \le k_p \le 1. \tag{5.35}$$

In order to analyze the variation of the power, substituting (5.35) into (5.16) and (5.17) gives

$$p = P + \frac{P(1 + k_p)(\mathbf{v}^- \cdot \mathbf{v}^+)}{\|\mathbf{v}^+\|^2 + k_p \|\mathbf{v}^-\|^2}, \tag{5.36}$$

$$q = \frac{P(1 - k_p)(\mathbf{v}_\perp^- \cdot \mathbf{v}^+)}{\|\mathbf{v}^+\|^2 + k_p \|\mathbf{v}^-\|^2}. \tag{5.37}$$

It can be seen that the variant terms of (5.36) and (5.37), i.e. oscillating active power and reactive power, are controlled by the coefficient k_p. These two parts of oscillating power are orthogonal and equal in maximum amplitude.

Simulation results are obtained in Fig. 5.4 by sweeping the parameter k_p. Related circuit structure and controller parameters are given in the experimental part. It can be seen that the amount of oscillating active power or oscillating reactive power can be controlled and even can be eliminated at the two extremes of the k_p curve. In other words, a constant dc-link voltage can be achieved by the elimination of oscillating active power when $k_p = -1$; symmetric currents can be

derived when $k_p = 0$; and unity power factor can be achieved when $k_p = 1$ where the three-phase current follows the grid voltage.

Therefore, with the proposed method, there is a wide choice of possibilities for k_p in between -1 and 1, allowing an optimum control of the currents in order to achieve different objectives. For instance, within a certain range of dc-voltage variation, the currents can be optimized to get maximum power output by changing the k_p with respect to the grid voltage. A graphic representation of the relationship between these two instantaneous oscillating powers is plotted in Fig. 5.5 (a). It illustrates clearly that the two oscillating powers shift from one to another with the increase or decrease of k_p under the proposed strategy. This controllable characteristic allows to enhance system control flexibility and facilitates system optimization. Further discussion on objective-oriented optimization of this generalized strategy is presented in the next section.

5.4   Analysis of objective-oriented optimization

As can be observed, the proposed current reference generation strategy provides DG inverters with control flexibility, i.e. the coefficient k_p can be optimally determined based on optimization objectives and be adaptively changed in case of voltage dips. Therefore, applications of the proposed strategy are discussed for different requirements.

5.4.1   Constraints of DG inverters

Considering the power-electronic converter constraints, a serious problem for the inverters is the second-order ripple on the dc bus, which reflects to the ac side and creates distorted grid currents during unbalanced voltage dips. Either for facilitating dc-bus voltage control or for minimizing the dc bus capacitors, it is preferred to make k_p in (5.35) close to -1 so that the dc-link voltage variations can be kept very small. However, the maximum deliverable power has to decrease because unbalanced phase currents reduce the operating margin of inverters. Therefore, for a maximum power-tracking system it is preferable to shift k_p towards zero to get balanced currents as long as the variation on the dc-link is acceptable. Note that the inverter losses and oscillating power on account of output filters are not considered. The effect of output filters will be commented on later.

To help understanding, a vector diagram that represents current trajectories changing with k_p during an unbalanced voltage dip is drawn in Fig. 5.5 (b). For a desired power P, unbalanced currents are generated that achieve zero $\tilde{p}_{2\omega}$ when k_p equals -1. When the asymmetry of voltage dips becomes more pronounced, the generated currents will finally cross overcurrent levels if the system tries to maintain the same power delivery as during the pre-fault status and keeps zero $\tilde{p}_{2\omega}$ simultaneously. Therefore, k_p has to be adapted toward zero, as shown in Fig. 5.5 (b), i.e. the current trajectory starts from the flattest ellipse and reshapes to a circle. Hence, k_p will be somewhere in between 0 and 1 as long as $\tilde{p}_{2\omega}$ is smaller

than the allowed maximum value $\tilde{p}_{2\omega\_pk}$, which can be calculated by

$$\tilde{p}_{2\omega\_pk} = 2\pi f_1 V_{dc} C_{dc} \Delta V_{dc}, \qquad (5.38)$$

where f_1 is the grid frequency, V_{dc} is the average dc voltage, C_{dc} is the dc-link capacitance and ΔV_{dc} the specified peak-peak dc voltage variation. Note that when k_p reaches zero and the amplitudes of balanced currents are still out of the maximum current range, the delivered power has to be decreased. As a consequence, the upstream distributed sources should also take actions to guarantee the power balance on the dc-link.

5.4.2   Effects on the grid

On the other hand, the effects of the proposed strategy on the power system side could also impose constraints on the control design, especially for large scale DG systems. Because the oscillating reactive power causes extra power losses in the grid, it is preferred to make k_p close to 1 in order to eliminate $\tilde{q}_{2\omega}$. Because the amplitude of $\tilde{p}_{2\omega}$ is increasing when k_p shifts to 1, the dc-bus voltage variation again becomes a constraint. Therefore, similar comparison between the oscillating power either estimated by (5.36) or actually measured, and the maximum ripple power $\tilde{p}_{2\omega\_pk}$ given by (5.38) should be carried out. As long as the active power oscillation is acceptable, k_p can move toward 1 as close as possible. Otherwise, delivered power downgrades in quantity.

However, the objective becomes different from a voltage quality point of view. As shown in the results of Fig. 5.4, when k_p is getting close to 1, less current is delivered into the phases in which grid voltage is relatively low. Also, it can be seen in Fig. 5.5 (b) that the current vector tends to synchronize with the grid voltage vector, that is the reference currents tend to follow the asymmetry of the grid voltages. Consequently, the unbalanced voltage will be worsened due to unbalanced voltage rise across grid impedances, introduced by the injected grid currents (if the grid impedance is resistive and the injected currents are large enough). On the contrary, when k_p is close to -1, higher current is delivered into the phases in which grid voltage is relatively low, thereby compensating the voltage imbalance at the grid connection point. As is revealed in the analysis above, the objectives of improving the effects on the grid side could conflict with each other. Fortunately, the proposed strategy can be easily adapted according to practical objectives.

5.4.3   Effects of output inductors

The effects of output inductors are well-known and therefore are only briefly presented here. The instantaneous power control discussed so far has been treated at the grid connection point. When the objective is aimed at optimizing dc voltage variations, and the oscillating power on account of the output inductors cannot be neglected (in case of large and unbalanced currents or small dc capacitance), instead of the grid voltages, the fundamental components of the inverter-bridge output voltages should be used in the proposed strategy for calculation. Indirect
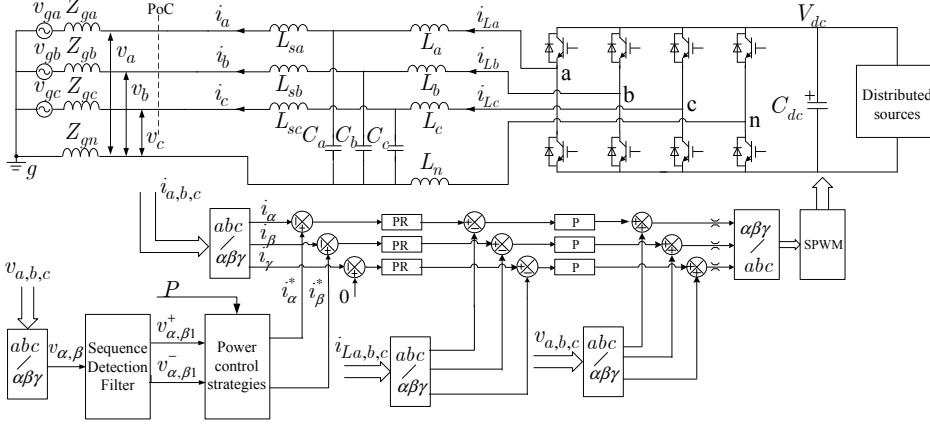
Figure 5.6: Circuit diagram and control structure of experimental four-leg inverter system.

Table 5.1: System Parameters

Description	Symbol	Value
Output filtering inductor	$L_{sa,b,c}$	2 mH
Output filtering capacitor	$C_{a,b,c}$	5 μF
Output filtering inductor	$L_{a,b,c}$	2 mH
Neutral filtering inductor	L_n	0.67 mH
dc-link voltage	V_{dc}	750 V
dc-link capacitors	C_{dc}	4400 μF
Switching frequency	f_{sw}	16 kHz
System rated power	S	15 kVA
Tested power	P	2500 W

derivation based on grid voltages and currents or direct measurement on the output of the inverter bridge can be used to get the voltages as presented in [34] and [35].

5.5   Experimental verifications

To verify the proposed strategy, experiments are carried out on a laboratory experimental system constructed from a four-leg inverter that is connected to the grid through LCL filters, as shown in Fig. 5.6. The system parameters are listed in Table 5.1. By using a four-leg inverter, zero-sequence currents can be eliminated when the grid has zero-sequence voltages. For the cases where the zero-sequence voltage of unbalanced grid dips is isolated by transformers, a three-leg inverter can be applied. A 15 kVA three-phase programmable ac power source is used to emulate the unbalanced utility grid, and the distributed source is implemented by
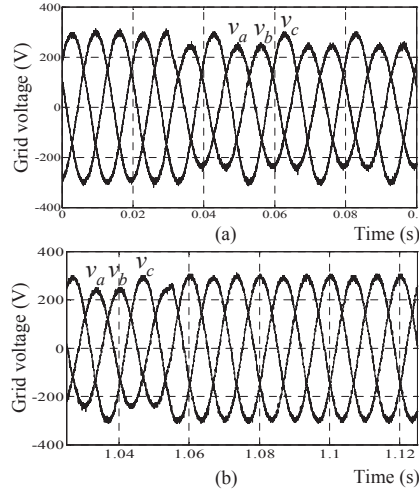
Figure 5.7: Emulated grid voltages: (a) to be faulty at $t = 0.03$ s, where phases a and b dip to 80%, (b) to be recovered at $t = 1.055$ s.

a dc power supply.

5.5.1 Control realization

The controller is realized with a double-loop current controller, which consists of an outer control loop with proportional-resonant (PR) controllers for compensating the steady-state error of the fundamental-frequency currents, and an inner inductor current control loop with simple proportional gain to improve stability. In addition, a feed-forward loop from the grid voltages is used to improve the system response to voltage disturbances.

Furthermore, the direct feedback of currents in the stationary frame is achieved, which is desirable as stated in the introduction. Also, the control for dual sequence components is simple without transformations between reference frames. A non-ideal proportional-resonant (PR) controller or sequence-decoupled resonant (SDR) controllers with high gain at the fundamental frequency can be employed, with the parameters used in the experiment: $K_P = 2$, $K_I = 100$, and $\omega_b = 10$ rad/s (see Chapter 3).

The symmetric-sequence components are detected in the time domain with a stationary frame filter in the $\alpha\beta$ frame [52], as has been presented in Chapter 2. The basic filter cell is equivalent to a band-pass filter in the stationary frame, and can be easily implemented using a multi-state-variable structure. Since the power supply only emulates the magnitude drop of the grid voltage in this experiment, disregarding large grid frequency variations, a phase locked loop (PLL) is not needed because of the robustness of the filter for small frequency variations. Otherwise, a PLL should be added to the filter for adapting to large frequency changes [52].
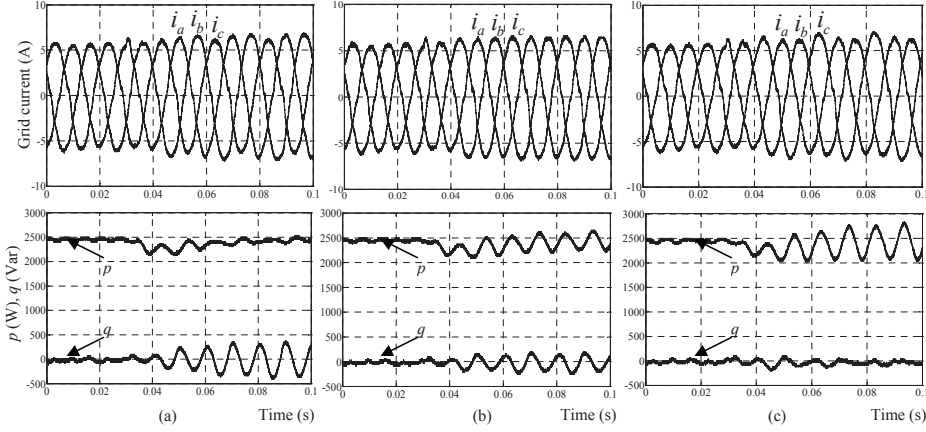
Figure 5.8: Experimental results during unbalanced voltage dips with (a) k_p = -1, (b) k_p = 0 and (c) k_p = 1, where the waveforms from top to bottom are injected grid currents and instantaneous power.

Note that dc-link voltage control is not added here. Usually, a dc-link voltage control loop is included in the control structure, for instance, in a rectifier system [35] or for a wind turbine inverter [100]. The dc bus in the experimental system is only controlled by the dc power supply with a quite low bandwidth to maintain a stable dc bus in an average sense. Since the experiment intends to investigate the effects of the proposed strategy when choosing different k_p, it is better to leave out the dc voltage control in order to only observe the performance of the proposed strategy.

5.5.2   Experimental results

By shifting the controllable parameter k_p, the system is tested during unbalanced voltage dips with the proposed strategy. In order to capture the transient reaction of the system, three situations are intentionally tested for comparison at the start moment and finish moment of voltage dips.

During voltage dips

As shown in Fig. 5.7 (a), grid voltages are emulated to be faulty at t = 0.03 s where phases a and b dip to 80%. In case of $k_p = -1$, the injected grid currents and instantaneous power are shown in Fig. 5.8 (a). It can be seen that in order to get a constant active power the currents on phases with lower voltage are higher than the phase with higher voltage.

As analyzed in Section 5.3, negative-sequence current opposite to the negative-sequence voltage is injected to compensate part of the oscillating active power introduced by negative-sequence voltage and positive-sequence current. Also, it can be seen that the instantaneous reactive power has a large ripple oscillating
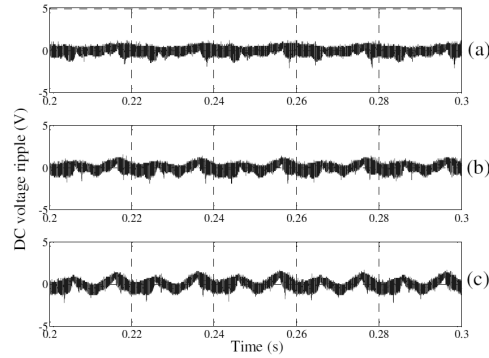
Figure 5.9: Experimental results of dc-link ripple during unbalanced voltage dips with (a) k_p = -1, (b) $k_p = 0$, and (c) $k_p = 1$.

at twice the grid frequency. The worst case is when $k_p = -1$ due to an extra part of oscillating reactive power generated by the negative-sequence currents and positive-sequence voltages.

In Fig. 5.8 (b), results with $k_p = 0$ are shown. As illustrated, the currents are kept balanced before and after grid faults. Hence, the oscillating part of the instantaneous active and reactive power are equal in amplitude and have a 90° phase shift, as only positive-sequence currents exist. The results when $k_p = 1$ are given in Fig. 5.8 (c), it can be seen that the three-phase currents are in phase with the corresponding voltages. This means that unity power factor can be achieved. In addition, dc-link voltage ripple during voltage dips is also observed as shown in Fig. 5.9, where the ripple reflected by the ac-side oscillating active power are clearly illustrated. Note that the dc voltage variations are not large, even when $k_p = 1$, because of the big dc-link capacitance used in the system and a relatively low tested power.

After voltage dips

Experimental results are also available when grid voltages recover after voltage dips. As shown in Fig. 5.7 (b), the unbalanced grid voltages become balanced at t = 1.055 s. With respect to different values of k_p, corresponding results of injected grid currents and instantaneous power are shown in Fig. 5.10. It can be seen that, when the grid voltages become balanced, current waveforms and instantaneous power waveforms, which were controlled by k_p during voltage dips, are the same as originally.

5.6 Contribution of zero-sequence currents to active power control

It was assumed previously that zero-sequence components are either not present or eliminated in the above control strategy. In the literature, hardly any work has
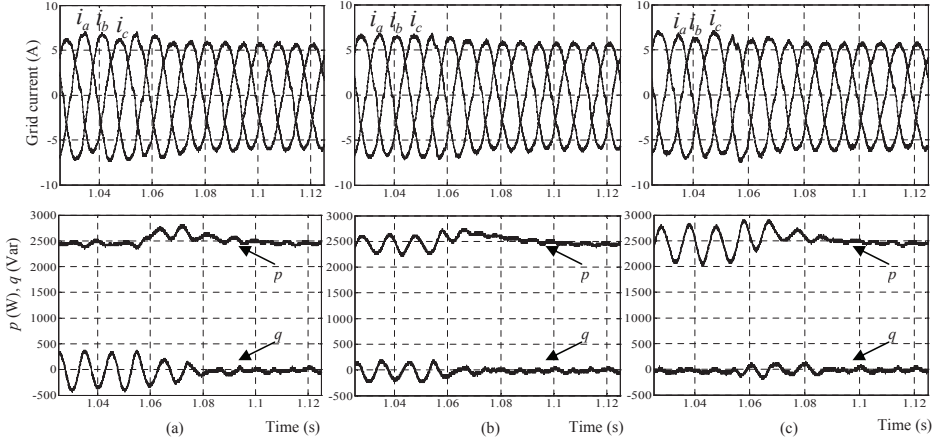
Figure 5.10: Experimental results when the voltage recovers at $t = 1.055$ s with (a) k_p $= -1$, (b) $k_p = 0$ and (c) $k_p = 1$, where the waveforms from top to bottom are injected grid currents and instantaneous power.

been done to analyze active power control of a four-wire system that take into account zero sequence components of unbalanced voltages. Although zero-sequence currents are not expected to enter the grid from DG systems, it is still interesting to understand the contribution of zero-sequence currents when delivering active power. Due to the extra degree of freedom of generating zero-sequence components, the current reference generation of a four-wire DG inverter can become more flexible. Note that a four-leg inverter topology is required in order to fully control zero-sequence currents.

As presented in (5.11), active power caused by zero-sequence quantities, p^0, can only exist if there are both zero-sequence current $\mathbf{i}^0$ and voltage $\mathbf{v}^0$, that is $p^0 = \mathbf{v}^0 \cdot \mathbf{i}^0$. Since p^0 is not related to reactive power, it can only be used to compensate the oscillating active power. Negative-sequence current is utilized to cancel the oscillating reactive power, and this has already been derived in Section 5.3. From (5.9), it is obtained that

$$p = \underbrace{\mathbf{v}^+ \cdot \mathbf{i}_p^+}_{P^+} + \underbrace{\mathbf{v}^- \cdot \mathbf{i}_p^-}_{P^-} + \underbrace{\mathbf{v}^+ \cdot \mathbf{i}_p^- + \mathbf{v}^- \cdot \mathbf{i}_p^+}_{\tilde{p}_{2\omega}} + \underbrace{\mathbf{v}^0 \cdot \mathbf{i}_p^0}_{P^0 + \tilde{p}_{2\omega}^0}, \tag{5.39}$$

where P^0 and $\tilde{p}_{2\omega}^0$ represent the average power and oscillating power produced by the zero-sequence components. Separating (5.39) into two parts, that is constant power and oscillating power, yields

$$P = \underbrace{\mathbf{v}^+ \cdot \mathbf{i}_p^+}_{P^+} + \underbrace{\mathbf{v}^- \cdot \mathbf{i}_p^-}_{P^-} + P^0, \tag{5.40}$$

$$\tilde{p} = \underbrace{\mathbf{v}^+ \cdot \mathbf{i}_p^- + \mathbf{v}^- \cdot \mathbf{i}_p^+}_{\tilde{p}_{2\omega}} + \tilde{p}_{2\omega}^0. \tag{5.41}$$
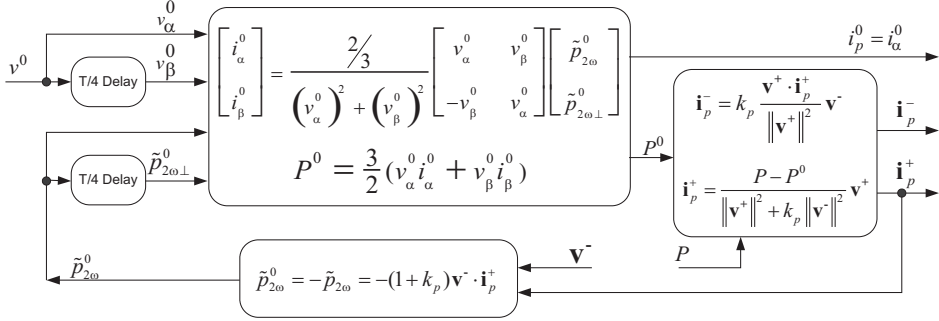
Figure 5.11: Structure diagram for generating controllable reference currents based on symmetric sequences.
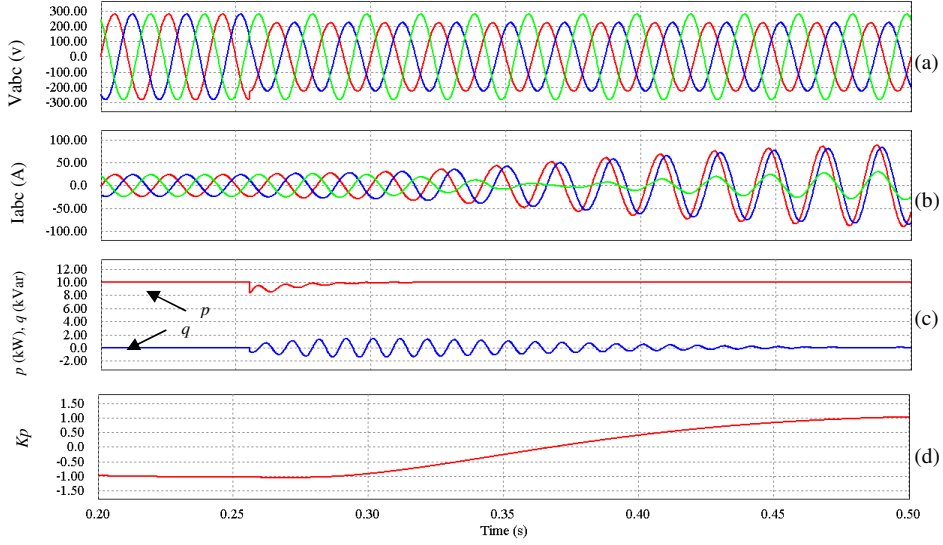
Figure 5.12: Simulation results of of the proposed active power control including all symmetric sequences: (a) grid voltages of phase a and b dip to 80% at $t = 0.255$ s, (b) injected currents, (c) instantaneous p, q, and (d) controllable coefficient k_p sweeping from -1 to 1.

Substituting (5.31) into (5.40) and (5.41) obtains

$$\mathbf{i}_p^+ = \frac{P - P^0}{\|\mathbf{v}^+\|^2 + k_p \|\mathbf{v}^-\|^2} \mathbf{v}^+, \tag{5.42}$$

$$\tilde{p} = \underbrace{(1 + k_p)\mathbf{v}^- \cdot \mathbf{i}_p^+}_{\tilde{p}_{2\omega}} + \tilde{p}_{2\omega}^0. \tag{5.43}$$

It is expected that $\tilde{p}_{2\omega}^0$ can compensate $\tilde{p}_{2\omega}$, hence appropriate zero-sequence cur-

rents should meet

$$\tilde{p}_{2\omega}^0 = -\tilde{p}_{2\omega} = -(1 + k_p)\mathbf{v}^- \cdot \mathbf{i}_p^+. \tag{5.44}$$

For a certain $\tilde{p}_{2\omega}^0$ given by (5.44), the corresponding zero-sequence currents can therefore be calculated. In the stationary frame it is found to be

$$\begin{bmatrix} i_\alpha^0 \\ i_\beta^0 \end{bmatrix} = \frac{2/3}{(v_\alpha^0)^2 + (v_\beta^0)^2} \begin{bmatrix} v_\alpha^0 & v_\beta^0 \\ -v_\beta^0 & v_\alpha^0 \end{bmatrix} \begin{bmatrix} \tilde{p}_{2\omega}^0 \\ \tilde{p}_{2\omega\perp}^0 \end{bmatrix}, \tag{5.45}$$

where $\tilde{p}_{2\omega\perp}^0$ denotes a 90° lagging signal of $\tilde{p}_{2\omega}$, v_α^0 the zero-sequence grid voltage; v_β^0 denotes 90° lagging signal of v_α^0, i_α^0 the zero-sequence current and i_β^0 represents the 90° lagging signal of i_α^0 (see the derivation of (5.45) in Appendix B).

With (5.42) to (5.45), the derived current reference generation based on positive, negative, and zero sequences is shown in Fig. 5.11. Note that when P^0 equals zero, the block diagram of Fig. 5.11 for the calculation of $\mathbf{i}_p^-$ and $\mathbf{i}_p^+$ is the same as the previously presented strategy based on positive and negative sequence components.

Next, numerical simulations were carried out to observe the contribution of zero-sequence currents. Under the same grid dip condition as in Fig. 5.4, simulation results are illustrated in Fig. 5.12. As shown in Fig. 5.12 (c), because of the contribution of zero-sequence components, constant active power is achieved. However, when the parameter k_p is getting close to 1, the output currents become severely unbalanced with a large amplitude increase in the phase currents. Because the zero-sequence voltage is much smaller than the positive-sequence voltage, a large proportion of zero-sequence components is then needed to compensate the oscillating active power introduced by positive and negative sequence currents.

Therefore, this section provides a clear view on the contribution of zero-sequence components to active power control. It shows that the strategy utilizing zero-sequence currents is not practical when the zero-sequence voltage of grid is too small. Unbalanced phase currents would increase sharply, seriously reducing the operation margin of the inverter and causing large unbalanced voltage drop across line impedances.

5.7   Conclusions

This chapter has proposed a generalized active power control strategy for distributed generation inverters operating under unbalanced grid faults. The strategy facilitates on-line performance optimization of the inverters during voltage dips, i.e., improving grid-fault ride-through capabilities.

Based on derived formulas and graphic representations, the contribution of symmetric-sequence components to the instantaneous power and the interaction between symmetric sequences has been explained in detail.

By intentionally introducing an adjustable parameter in between the reference currents and the grid voltages, the proposed strategy has been found able to control the dc-link ripple, and to impact the symmetry of currents or the power factor in terms of controllable oscillating active and reactive powers.

The analysis of different strategies has been discussed from the perspective of both the power-electronic converter and the power system sides. The flexible adaptivity of the proposed strategy allows it to cope with multiple constraints in practical applications. Finally, the proposed control strategy has been experimentally verified, achieving satisfying results.

Furthermore, because hardly any work had been carried out in the literature, the contribution of zero-sequence currents to active power control has also been studied. A technically effective control method has been proposed for eliminating second-order power ripple by including fundamental zero-sequence components. However, it is worth noticing that a serious phase unbalance and a large amplitude increase appear in the currents when using zero-sequence components.

Chapter 6

Pliant active and reactive power control for grid support

Abstract - A voltage dip ride-through control of DG inverters, which enables uninterrupted supply of active power from the DG system to the grid, has been presented in Chapter 5. On the other hand, reactive power injection is also desirable at the grid side for voltage support under voltage dips, especially for large scale DG systems such as wind farms. By extending the active power control strategies presented in Chapter 5 and by including reactive power control, this chapter further addresses flexible control strategies of DG inverters under voltage dips.

It is shown that active power and reactive power can be independently controlled with two individually adaptable parameters. By changing these parameters, the relative amplitudes of oscillating power, as well as the peak values of three-phase grid currents, can be smoothly regulated. As a result, the power control of grid-interactive inverters becomes quite flexible and adaptable to various grid requirements or design constraints. Furthermore, two strategies for simultaneous active and reactive power control are proposed that preserve flexible controllability. An application example is given to illustrate the simplicity and adaptability of the proposed strategies for on-line optimization control. Finally, experimental results are provided that verify the proposed power control.

6.1   Introduction

In Chapter 5, a ride-through control of DG inverters for uninterrupted delivery of active power to the grid during voltage dips has been presented. Going one step further, this chapter specifies the simultaneous control of both active and reactive power of DG inverters for grid voltage support.

Reactive power injection is desirable at the grid side. Based on a prior agreements with grid operators, DG systems should also be able to support the grid voltage with additional reactive current during a voltage dip [32, 33]. For example, as shown in Fig. 6.1 that is reproduced from the grid code of E.ON Netz GmbH [32], a certain amount of reactive current/power has to be fed into the grid in the event of a voltage dip of more than 10% of the nominal voltage. The ratio between the additional reactive power to the system rated power depends on the percentage of voltage dip. If necessary, a reactive power of 100% the rated current must be able to be delivered to the grid for voltage support.

Since voltage dips are as diverse as grid faults, there will be always multiple objectives with constraints imposed by the converters or by the grid requirements in case of ride-through control; and these objectives have to be compromised and adapted under different grid faults so as to optimize the system overall performance. Therefore, a generalized power control strategy, which can be easily adapted to fulfill different objectives under voltage dips, is of interest.

Starting from the ideas in [37] and [104], this chapter proposes generalized active and reactive power control strategies that enable DG inverters to be optimally designed under voltage dips [54]. This chapter is organized as follows. The derivation of the proposed strategies for independent active and reactive power control is described in Section 6.2. Then, two strategies for simultaneous active and reactive power control, which preserve the adaptive controllability, are derived and compared in Section 6.3. In Section 6.4, an application example illustrates the simplicity and adaptability of the proposed strategies for on-line optimization control. Finally, experimental verifications of the proposed power control strategies and conclusions are presented.

6.2   Strategies for independent active and reactive power control

In the previous chapter, the instantaneous active and reactive power of three-phase systems has been derived in form of symmetric sequence components, repeated here as

$$p = \mathbf{v} \cdot \mathbf{i} = (\mathbf{v}^+ + \mathbf{v}^-) \cdot (\mathbf{i}^+ + \mathbf{i}^-) + \mathbf{v}^0 \cdot \mathbf{i}^0, \qquad (6.1)$$

$$q = \mathbf{v}_\perp \cdot \mathbf{i} = (\mathbf{v}_\perp^+ + \mathbf{v}_\perp^-) \cdot (\mathbf{i}^+ + \mathbf{i}^-). \qquad (6.2)$$

where subscripts "+", "-", and "0" denote as usually positive, negative, and zero sequences, respectively. For the notations of current/voltage vectors and the principle of instantaneous power calculation based on symmetric sequences, please
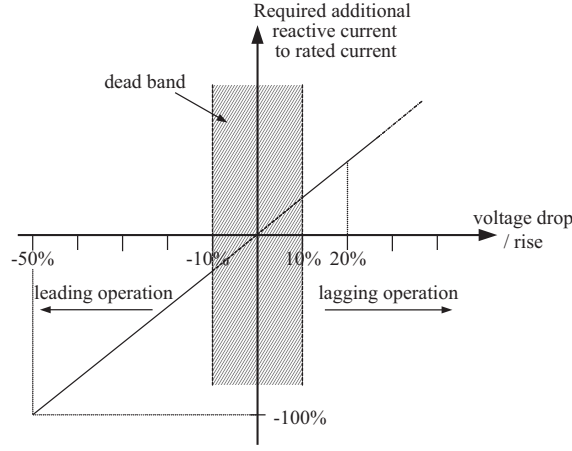
Figure 6.1: Reactive currents required for voltage support in the event of grid faults [32].
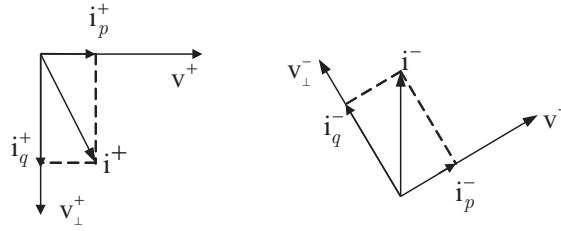
Figure 6.2: Decoupling of currents for independent active and reactive control.

refer to Sections 5.2 and 5.3. Similar as in the previous chapter, assumptions that will be used are:

- Only positive-sequence and negative-sequence currents are present;
- Only fundamental voltages exist, in practice they can be extracted out;
- The amplitude of the positive-sequence voltage is higher than the negative sequence one.

In order to separately analyze the contribution of currents to independent active and reactive power control, sequence currents $\mathbf{i}^{+,-}$ can be decoupled into two orthogonal quantities, i.e. $\mathbf{i}_p^{+,-}$ and $\mathbf{i}_q^{+,-}$, as depicted in Fig. 6.2. The subscript "p" is related to active power control, and "q" is related to reactive power control.

6.2.1 Reactive power control

For reactive power control, only $\mathbf{i}_q^+$ and $\mathbf{i}_q^-$ are present, which are defined in phase with $\mathbf{v}_\perp^+$ and $\mathbf{v}_\perp^-$, respectively, in order to generate only reactive power. Rewriting

(6.1) and (6.2) in terms of $\mathbf{i}_q^+$ and $\mathbf{i}_q^-$ obtains

$$p = \underbrace{\mathbf{v}^+ \cdot \mathbf{i}_q^- + \mathbf{v}^- \cdot \mathbf{i}_q^+}_{\tilde{p}_{2\omega}}, \tag{6.3}$$

$$q = \underbrace{\mathbf{v}_\perp^+ \cdot \mathbf{i}_q^+}_{Q^+} + \underbrace{\mathbf{v}_\perp^- \cdot \mathbf{i}_q^-}_{Q^-} + \underbrace{\mathbf{v}_\perp^- \cdot \mathbf{i}_q^+ + \mathbf{v}_\perp^+ \cdot \mathbf{i}_q^-}_{\tilde{q}_{2\omega}}, \tag{6.4}$$

where Q^+ and Q^- denote the constant reactive power introduced by positive and negative sequences, respectively, $\tilde{p}_{2\omega}$ represents oscillating active power, and $\tilde{q}_{2\omega}$-oscillating reactive power. It can be found that the two terms of $\tilde{p}_{2\omega}$ are in-phase-quantities oscillating at twice the fundamental frequency. A similar property can be found for the two terms of $\tilde{q}_{2\omega}$.

Because oscillating active power can reflect a variation on the dc-bus voltage, and high dc voltage variation may cause over-voltage problems, output distortion, or even control instability, it is desirable to eliminate $\tilde{p}_{2\omega}$. On the other hand, the oscillating reactive power $\tilde{q}_{2\omega}$ also causes power losses and increased operating current, and therefore it is advantageous to mitigate $\tilde{q}_{2\omega}$ as well. A trade-off between $\tilde{p}_{2\omega}$ and $\tilde{q}_{2\omega}$ is not straightforward and depends on practical requirements. In the following, strategies to achieve controllable oscillating active and reactive power are derived from two considerations.

1) Controllable oscillating reactive power

For a desired level of injection into the grid of reactive power Q, which, for the DG system under consideration, should be determined in advance in agreement with the grid operator by taking also into account the inverter power ratings, the first two terms of (6.4) are designed to meet

$$Q = \mathbf{v}_\perp^+ \cdot \mathbf{i}_q^+ + \mathbf{v}_\perp^- \cdot \mathbf{i}_q^-. \tag{6.5}$$

Since the other two terms of $\tilde{q}_{2\omega}$ in (6.4) are in-phase quantities, these two terms can easily compensate each other. Therefore, intentionally set

$$\mathbf{v}_\perp^+ \cdot \mathbf{i}_q^- = -k_q \mathbf{v}_\perp^- \cdot \mathbf{i}_q^+, \quad 0 \le k_q \le 1, \tag{6.6}$$

where k_q is a scalar coefficient used as a weighting factor for the elimination of $\tilde{q}_{2\omega}$; and the subscript "q" is related to reactive power (Q) control. Derived from (6.6), the negative-sequence current $\mathbf{i}_q^-$ is expressed by

$$\mathbf{i}_q^- = \frac{-k_q \mathbf{v}_\perp^+ \cdot \mathbf{i}_q^+}{\left\| \mathbf{v}_\perp^+ \right\|^2} \mathbf{v}_\perp^-, \tag{6.7}$$

where $\left\| \mathbf{v}_\perp^+ \right\|^2 = \left\| \mathbf{v}^+ \right\|^2 = \mathbf{v}^+ \cdot \mathbf{v}^+$, operator "$\| \cdot \|$" means the norm of a vector.

Substituting (6.7) into (6.5), and using $\left\| \mathbf{v}_\perp^{+,-} \right\|^2 = \left\| \mathbf{v}^{+,-} \right\|^2$, it follows that

$$Q \left\| \mathbf{v}^+ \right\|^2 = \left(\left\| \mathbf{v}^+ \right\|^2 - k_q \left\| \mathbf{v}^- \right\|^2 \right) \left(\mathbf{v}_\perp^+ \cdot \mathbf{i}_q^+ \right). \tag{6.8}$$

Then, based on (6.7) and (6.8), currents $\mathbf{i}_q^+$ and $\mathbf{i}_q^-$ can be calculated as

$$\mathbf{i}_q^+ = \frac{Q}{\|\mathbf{v}^+\|^2 - k_q \|\mathbf{v}^-\|^2} \mathbf{v}_\perp^+, \tag{6.9}$$

$$\mathbf{i}_q^- = \frac{-k_q Q}{\|\mathbf{v}^+\|^2 - k_q \|\mathbf{v}^-\|^2} \mathbf{v}_\perp^-. \tag{6.10}$$

Finally, the total current reference is the sum of $\mathbf{i}_q^+$ and $\mathbf{i}_q^-$, that is

$$\mathbf{i}_q^* = \frac{Q}{\|\mathbf{v}^+\|^2 - k_q \|\mathbf{v}^-\|^2} (\mathbf{v}_\perp^+ - k_q \mathbf{v}_\perp^-), \quad 0 \le k_q \le 1. \tag{6.11}$$

2) Controllable oscillating active power

Instead of compensating the oscillating reactive power in (6.4), the oscillating active power in (6.3) can be similarly controlled. For this purpose negative-sequence currents are imposed to meet

$$\mathbf{v}^+ \cdot \mathbf{i}_q^- = -k_q \mathbf{v}^- \cdot \mathbf{i}_q^+, \quad 0 \le k_q \le 1. \tag{6.12}$$

where the scalar coefficient k_q is now a weighting factor for the elimination of $\tilde{p}_{2\omega}$. Note that the subscript "q" in k_q remains consistent as used in (6.6), representing reactive power (Q) control.

By considering that $\mathbf{v}^+ \cdot \mathbf{i}^- = \mathbf{v}^+{}_\perp \cdot \mathbf{i}^-{}_\perp$ (because $\mathbf{v}_\perp^+$ lags $\mathbf{v}^+$ by 90° and $\mathbf{i}_\perp^-$ leads $\mathbf{i}^-$ by 90°), the left side of (6.12) can be rewritten as

$$\mathbf{v}^+ \cdot \mathbf{i}_q^- = \mathbf{v}_\perp^+ \cdot \mathbf{i}_{q\perp}^- = -k_q \mathbf{v}^- \cdot \mathbf{i}_q^+, \tag{6.13}$$

where $\mathbf{i}_{q\perp}^-$ denotes the orthogonal vector of $\mathbf{i}_q^-$ according to (5.2). Then, it follows that

$$\mathbf{i}_{q\perp}^- = \frac{-k_q \mathbf{v}_\perp^+ \cdot \mathbf{i}_q^+}{\|\mathbf{v}^+\|^2} \mathbf{v}^-. \tag{6.14}$$

Hence, the negative-sequence current $\mathbf{i}_q^-$ follows directly from (6.14) as

$$\mathbf{i}_q^- = \frac{k_q \mathbf{v}_\perp^+ \cdot \mathbf{i}_q^+}{\|\mathbf{v}^+\|^2} \mathbf{v}_\perp^-. \tag{6.15}$$

Solving (6.15) and (6.5), the positive-sequence current and negative-sequence current are derived as

$$\mathbf{i}_q^+ = \frac{Q}{\|\mathbf{v}^+\|^2 + k_q \|\mathbf{v}^-\|^2} \mathbf{v}_\perp^+, \tag{6.16}$$

$$\mathbf{i}_q^- = \frac{k_q Q}{\|\mathbf{v}^+\|^2 + k_q \|\mathbf{v}^-\|^2} \mathbf{v}_\perp^-. \tag{6.17}$$

Again, the total current reference is the sum of $\mathbf{i}_q^+$ and $\mathbf{i}_q^-$, that is,

$$\mathbf{i}_q^* = \frac{Q}{\|\mathbf{v}^+\|^2 + k_q \|\mathbf{v}^-\|^2} (\mathbf{v}_\perp^+ + k_q \mathbf{v}_\perp^-), \quad 0 \le k_q \le 1. \tag{6.18}$$
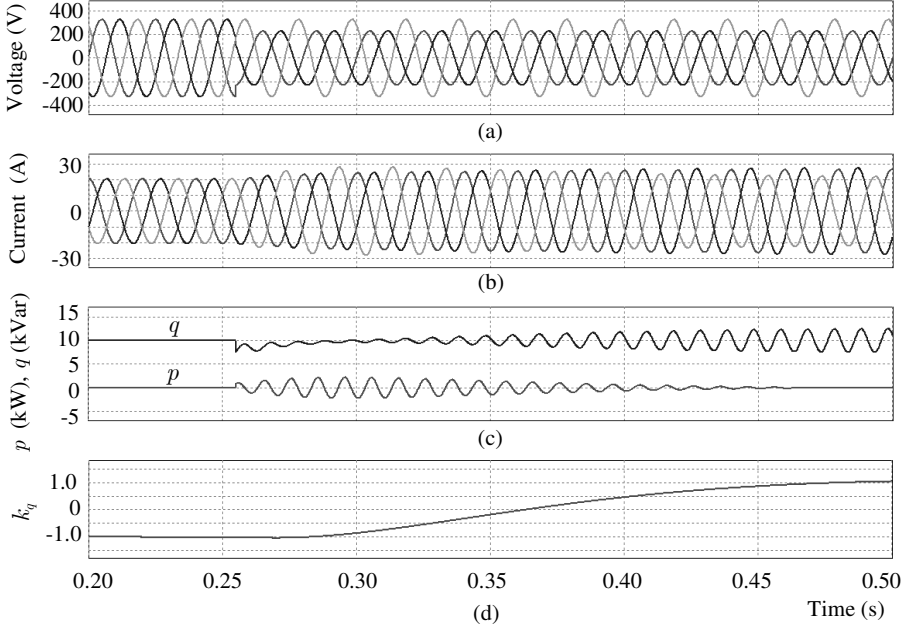
Figure 6.3: Simulation results of the proposed reactive power control strategy for 10kVar power delivery, (a) phase voltages, where two phases dip to 70% at t = 0.255 s, (b) generated current references, (c) instantaneous active power p and reactive power q, and (d) adjustable coefficient k_q sweeping from -1 to 1.

3) Merging strategies 1) and 2)

Simple analysis reveals that (6.11) and (6.18) can be put together as

$$\mathbf{i}_q^* = \frac{Q}{\|\mathbf{v}^+\|^2 + k_q \|\mathbf{v}^-\|^2}(\mathbf{v}_\perp^+ + k_q\mathbf{v}_\perp^-), \quad -1 \leq k_q \leq 1. \tag{6.19}$$

Further, by substituting (6.19) into (6.3) and (6.4), it follows that

$$p = \frac{Q(1 - k_q)\left(\mathbf{v}_\perp^+ \cdot \mathbf{v}^-\right)}{\|\mathbf{v}^+\|^2 + k_q \|\mathbf{v}^-\|^2}, \tag{6.20}$$

$$q = Q + \frac{Q(1 + k_q)\left(\mathbf{v}_\perp^+ \cdot \mathbf{v}_\perp^-\right)}{\|\mathbf{v}^+\|^2 + k_q \|\mathbf{v}^-\|^2}. \tag{6.21}$$

It can be seen that the variant terms of (6.20) and (6.21), i.e. oscillating active power and reactive power, are controlled by the coefficient k_q. These two parts of oscillating power are orthogonal and their amplitudes are equal.

To observe the controllability of the strategy represented by (6.19), simulation results are shown in Fig. 6.3 by sweeping parameter k_q from -1 to 1, where the un-

balanced voltage dips are assumed to persist. It is illustrated that either the oscillating active power or the oscillating reactive power can be controlled smoothly and even can be eliminated at the two extremes of the k_q curve. It is pointed out that the strategies presented in [104], namely positive-negative-sequence compensation (PNSC), average active-reactive control (AARC), and balanced positive-sequence (BPS) are equivalent to the results of the proposed strategy when k_q equals to -1, 1, and 0, respectively. Other than only three specific points, there is a wide choice of possibilities in between with the proposed method, and moreover, strategies from one to another operation point can be simply shifted with the value of the coefficient k_q. This controllable and smooth characteristic allows to enhance system control flexibility and facilitates system optimization. An application example will be presented in Section 6.4.

6.2.2 Active power control

For a given level of injection into the grid of active power P, which is determined by the power availability of the DG source and the converter ratings, the current reference for active power control has been derived in Chapter 5, i.e.

$$\mathbf{i}_p^* = \frac{P}{\|\mathbf{v}^+\|^2 + k_p \|\mathbf{v}^-\|^2}(\mathbf{v}^+ + k_p\mathbf{v}^-), \quad -1 \le k_p \le 1, \tag{6.22}$$

where k_p is a similar adjustable coefficient as k_q, but denotes a weighting factor for the elimination of oscillating active power or reactive power related to the active power (P) control. Hence, the subscript "p" in k_p denotes active power control.

6.3 Strategies for combined active and reactive power control

As already mentioned, some grid codes also require DG systems to contribute with reactive power [32] [33]. For example, with respect to the amplitude drop of voltages, DG systems having agreements with grid operators are expected to deliver both active power and reactive power during grid faults. Hence the reference currents for this case, named $\mathbf{i}_{pq}^*$, can be derived by adding (6.19) and (6.22), as expressed by

$$\mathbf{i}_{pq}^* = \mathbf{i}_p^* + \mathbf{i}_q^* = \frac{P}{\|\mathbf{v}^+\|^2 + k_p \|\mathbf{v}^-\|^2}(\mathbf{v}^+ + k_p\mathbf{v}^-) + \frac{Q}{\|\mathbf{v}^+\|^2 + k_q \|\mathbf{v}^-\|^2}(\mathbf{v}_\perp^+ + k_q\mathbf{v}_\perp^-),$$
$$\tag{6.23}$$

with $-1 \le k_p \le 1, -1 \le k_q \le 1$.

It can be seen that there are infinite combinations for (6.23) with independent coefficients k_p and k_q. This also implicates that the linear controllability benefit from previous independent power control strategies does not really exist. In order to preserve the controllability, two joint strategies are proposed to simplify (6.23) by linking the two coefficients. Hence, differing from k_p and k_q in (6.23), a new symbol k_{pq} is created to denote the coefficient for combined active and reactive power control.
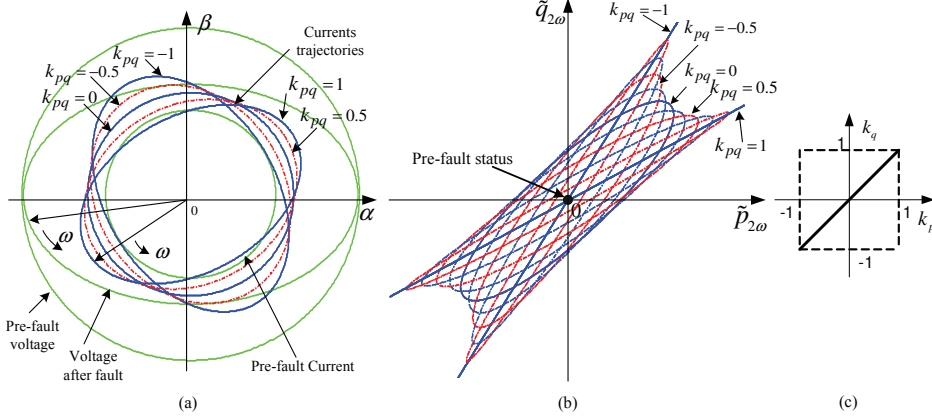
Figure 6.4: Graphic representation of (a) grid voltage and current trajectories under unbalanced voltage dips in the stationary frame, and (b) relationship between oscillating active power $\tilde{p}_{2\omega}$ and reactive power $\tilde{q}_{2\omega}$. Here k_{pq} is an adjustable parameter under the joint strategy of (c), where $k_p = k_q = k_{pq}$.

6.3.1   Joint strategy A: same-sign coefficients

By setting $k_p = k_q = k_{pq}$ in (6.23), reference current calculation is simplified and rewritten as

$$\mathbf{i}_{pq}^* = \frac{S}{\left\| \mathbf{v}^+ \right\|^2 + k_{pq} \left\| \mathbf{v}^- \right\|^2} \mathbf{R}(\varphi)(\mathbf{v}^+ + k_{pq}\mathbf{v}^-), \tag{6.24}$$

where $S = \sqrt{P^2 + Q^2}$ is the apparent power and φ the power factor angle, with

$$\varphi = \cos^{-1}\left(\frac{P}{\sqrt{P^2 + Q^2}} \right). \tag{6.25}$$

Since the $\alpha\beta$ reference frame is used in the experiment, it can be derived that

$$\mathbf{R}(\varphi) = \begin{bmatrix} \cos\varphi & \sin\varphi \\ -\sin\varphi & \cos\varphi \end{bmatrix}. \tag{6.26}$$

Note that $\mathbf{R}(\varphi)$ will be different in the *abc* reference frame.

On the basis of (6.24), the resulting currents and oscillating powers can now be adjusted by k_{pq}. A vector diagram representing the grid voltage and current trajectories, and the relationship between oscillating powers are plotted with k_{pq} as an adjustable parameter and the power factor angle φ set to 30° under an unbalanced voltage dip.

As shown in Fig. 6.4(a), when k_{pq} changes from 1 to -1, the length of current vectors changes and reaches a minimum value at $k_{pq} = 0$. In other words, the reference currents given by (6.24) become balanced when $k_{pq} = 0$. In Fig. 6.4 (b), the amplitudes of the oscillating powers, which are calculated by substituting (6.24) into (6.1) and (6.2), also vary with the change of k_{pq}. Because φ is not
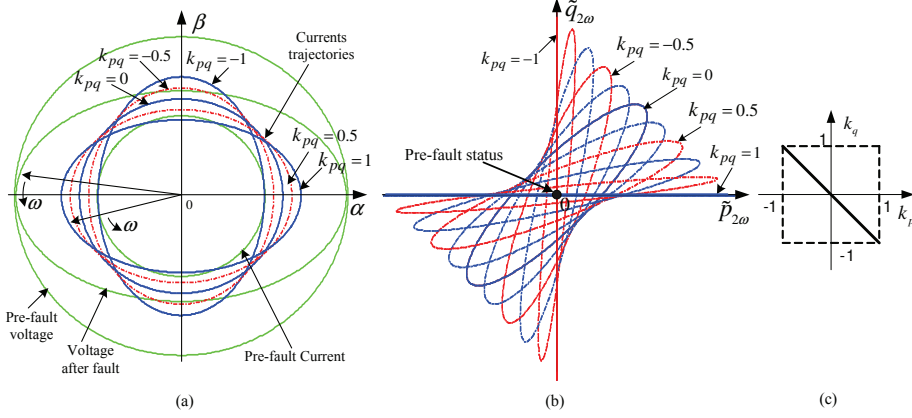
Figure 6.5: Graphic representation of (a) grid voltage and current trajectories under unbalanced voltage dips in the stationary frame, and (b) relationship between oscillating active power $\tilde{p}_{2\omega}$ and reactive power $\tilde{q}_{2\omega}$. Here k_{pq} is an adjustable parameter under the joint strategy of (c), where $k_p = -k_q = k_{pq}$.

Table 6.1: Controllability of Joint Strategies

Description	Strategy A	Strategy B
Active power control	yes	yes
Reactive power control	yes	yes
Current symmetry control	yes	yes
Null $\tilde{q}_{2\omega}$ control	no[1]	yes
Null $\tilde{p}_{2\omega}$ control	no[1]	yes

1) only possible when $\varphi = 0°$ or $90°$.

equal to $0°$ or $90°$, i.e., active power or reactive power is not zero, $\tilde{p}_{2\omega}$ and $\tilde{q}_{2\omega}$ cannot be eliminated since either active power or reactive power delivery always introduces oscillating power at the two extremes of k_{pq}.

6.3.2 Joint strategy B: opposing-sign coefficients

By setting $k_p = -k_q = k_{pq}$ in (6.23), the reference current is represented by

$$\mathbf{i}_{pq}^* = \frac{S\cos\varphi}{\|\mathbf{v}^+\|^2 + k_{pq}\|\mathbf{v}^-\|^2}(\mathbf{v}^+ + k_{pq}\mathbf{v}^-) + \frac{S\sin\varphi}{\|\mathbf{v}^+\|^2 - k_{pq}\|\mathbf{v}^-\|^2}(\mathbf{v}_\perp^+ - k_{pq}\mathbf{v}_\perp^-). \quad (6.27)$$

Illustrative plots are drawn in Fig. 6.5. It can be seen from (6.27) that this joint strategy requires almost twice the computation time of joint strategy A. Fortunately, zero $\tilde{p}_{2\omega}$ or $\tilde{q}_{2\omega}$ can be achieved at the two extremes of k_{pq}, as shown in Fig. 6.5 (b). Similar to joint strategy A, when shifting k_{pq} towards zero it implies that the length of the current vectors decreases and reaches a minimum
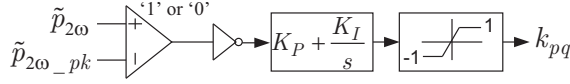
Figure 6.6: Control scheme of k_{pq} for confining oscillating active power.

value at $k_{pq} = 0$, achieving in this way balanced grid currents. For this value, the current trajectory becomes a circle, as shown in Fig. 6.5 (a).

The main aspects of the two joint strategies are tabulated in Table 6.1. Strategy A can only remove oscillating power when $\varphi = 0°$ or $90°$, whereas strategy B allows a more flexible controllability. In summary, the simple adaptive controllability of independent power control strategies is preserved in the joint strategies above. This enables DG systems to be optimized under unbalanced voltage dips and makes them flexible to meet the upcoming grid codes which might allow
- Constant active / reactive power (strategy B)
- Balanced grid currents (strategy A or B)
- Unbalanced currents with limited unbalanced factor [83] (strategy A or B)
- Average power delivery with limited oscillating power (strategy A or B).

6.4   Application case: confined oscillating active power

To illustrate the simplicity and adaptability of the proposed methods for on-line optimization control, an application case concerning confined oscillating active power is given in this section. Because the joint strategy B can fully eliminate the oscillating power, it is chosen to confine the oscillating active power of DG inverters that deliver active power in normal grid conditions and support the grid with reactive power under voltage dips.

To implement the joint strategy B, the control range and regulating directions of k_{pq} should be determined. Considering the power-electronics converter constraints, a serious problem for the inverters is the second-order ripple on the dc bus, which reflects to the ac side and creates distorted grid currents during unbalanced voltage dips [66]. Either for facilitating dc-bus voltage control or for minimizing the dc-bus capacitors, it is preferred to make k_{pq} in (6.27) close to -1 so that the dc voltage variations can be kept very small. However, the maximum deliverable power has to decrease because unbalanced phase currents reduce the operating margin of the inverters. Therefore, for a maximum power-tracking system it is preferable to shift k_{pq} towards zero to get balanced currents as long as the oscillating active power is within a certain limit. It is concluded that the k_{pq} should start from 0, and be shifted towards -1 when the amplitude of the oscillating active power is more than a maximum threshold, denoted as $\tilde{p}_{2\omega\_pk}$.

For a DG inverter, the maximum oscillating active power can be expressed as a function of dc-bus capacitance and dc voltage variations, as presented in (5.38), that is

$$\tilde{p}_{2\omega\_pk} = 2\pi f_1 V_{dc} C_{dc} \Delta V_{dc}, \tag{6.28}$$

where f_1 is the grid fundamental frequency, V_{dc} is the average dc voltage, C_{dc} is the dc-bus capacitance and ΔV_{dc} the peak-peak value of the specified dc-bus voltage variation.

According to (6.1), the oscillating active power is expressed by

$$\tilde{p}_{2\omega} = \mathbf{v}^+ \cdot \mathbf{i}^- + \mathbf{v}^- \cdot \mathbf{i}^+. \tag{6.29}$$

Following that, Fig. 6.6 shows a simple control scheme for regulating k_{pq}. When the oscillating active power is bigger than the $\tilde{p}_{2\omega\_pk}$, a proportional plus integral controller ramps up the value of k_{pq} towards -1. It is noticed that the integrator should be reset when the grid gets back to normal conditions. Therefore, the oscillating active power will be limited by the adaptive control of k_{pq}, while the grid currents are controlled to be as more balanced as possible.

In similar manners, the proposed strategies can be adapted for optimizing other control objectives as discussed in Section 5.4. It is pointed out that the oscillating power generated on the output filters is disregarded, because the instantaneous power control discussed so far has been treated at the grid connection point. Considerations on the effect of output inductors have been discussed in Section 5.4.

6.5 Experimental verifications

To verify the proposed strategy, experiments are carried out on a laboratory experimental system constructed from a four-leg inverter that is connected to the grid through LCL filters, as shown in Fig. 6.7. The system parameters are listed in Table 6.2, and the grid impedances are assumed to be combined with the output inductors. By using a four-leg inverter, zero-sequence currents can be eliminated when the grid has zero-sequence voltages. For the cases where the zero-sequence voltage of unbalanced grid dips is isolated by transformers, a three-leg inverter can be applied. A 15 kVA three-phase programmable ac power source is used to emulate the unbalanced utility grid, and the distributed source is implemented by a dc-power supply. The controller is designed on a dSPACE DS1104 setup by using Matlab / Simulink.

6.5.1 Control realization

As shown in Fig. 6.7, the proposed current controller is realized with a double-loop current controller, which consists of an outer control loop with proportional resonant (PR) controllers for eliminating the steady-state error of the fundamental-frequency currents, and an inner inductor current control loop with simple proportional gain to improve system dynamics and stability. In addition, a feed-forward loop from the grid voltages is used to improve system response to voltage disturbances. Because the controller in Fig. 6.7 is the same as the one presented in Chapter 5 except for the block labeled "power control strategies", the figure is not duplicated here. Note that the current control is used only for the laboratory test,
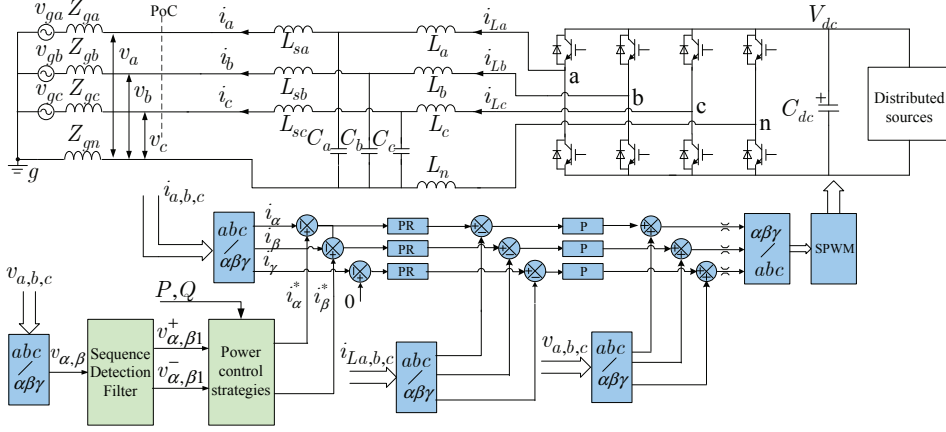
Figure 6.7: Circuit diagram and control structure of experimental four-leg inverter system.

Table 6.2: System parameters

Description	Symbol	Value
Output filtering inductor	$L_{sa,b,c}$	2 mH
Output filtering capacitor	$C_{a,b,c}$	5 μF
Output filtering inductor	$L_{a,b,c}$	2 mH
Neutral filtering inductor	L_n	0.67 mH
dc-bus voltage	V_{dc}	750 V
dc-bus capacitors	C_{dc}	4400 μF
Switching frequency	f_{sw}	16 kHz
System rated power	S_{rat}	15 kVA
Tested apparent power	S	2500 VA

but it is not the key point of this chapter; other current controllers can also be applied [65, 82, 105].

Concerning the power factor angle φ, defined in (6.25), two values are tested in the experiment. Firstly, a slightly modified approach is used to calculate the angle φ according to the grid code in [32]. Specifically, the DG system should inject at least 2% of the rated current as reactive current for each percent of the fundamental-sequence voltage dip. Therefore, if the desired angle φ is calculated from

$$\varphi = \sin^{-1}\left(2\frac{|V^+ - V_N|}{V_N}\right), \tag{6.30}$$

where V_N is nominal voltage amplitude, and $V^+ = \sqrt{(v_{\alpha 1}^+)^2 + (v_{\beta 1}^+)^2}$ is the positive-sequence voltage amplitude, then the requirements in [32] will be satisfied. Furthermore, it is also required in [32] that a reactive power output of at least 100% of the rated current should be possible when necessary. Hence also $\varphi = 90°$ will
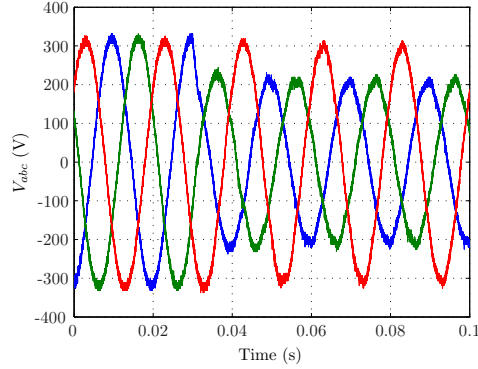
Figure 6.8: Emulated grid voltages to be faulty at t = 0.03 s, where two phases dip to 70%.

be assigned directly to test a complete range from active power to reactive power.

It is noticed that dc-bus voltage control is not added here. Usually, a dc-bus voltage control loop is included in the control structure, for instance, in a rectifier system [35] or for a wind turbine inverter [100]. The dc bus in the experimental system is only controlled by the dc power supply with a quite low bandwidth to maintain a stable dc bus in an average sense. Since the experiment intends to investigate the effects of the proposed strategies when choosing different k_{pq}, it is convenient to leave out the dc-voltage control in order to only observe the performance of the power control strategies.

6.5.2 Tests of the joint strategies at specific operating points

By shifting the controllable parameter k_{pq} to specific values, the system is tested under unbalanced voltage dips with the joint strategies. In order to capture the transient reaction of the system, three situations are intentionally tested under equivalent voltage dips.

As shown in Fig. 6.8, grid voltages are emulated to be faulty at t = 0.03 s where two phases dip to 70%. Consequently, the power factor angle φ derived in the control by (6.30) is 23° and the corresponding results of joint strategy A are shown in Fig. 6.9. In order to allow clear observation of the low-order oscillating power, high-order components are filtered out. It can be seen that the reactive power support starts within half a cycle after voltage dips. As analyzed in Section IV, the instantaneous active power and reactive power always have ripple, and the injected grid currents get balanced only when k_{pq} is near to zero. In case φ equals 90° (intentionally imposed), the joint strategy A turns out to be a reactive power control strategy as expressed by (6.19). Comparing with the simulation results in Fig. 6.3 at the point of k_q = -1, 0 and 1, it can be seen that the results in Fig. 6.10 show the same effects on the regulation of oscillating power and reference currents.

Further, it is noticed that the delivered active power and reactive power have a certain ramp slope when changing from one average value to the other, and
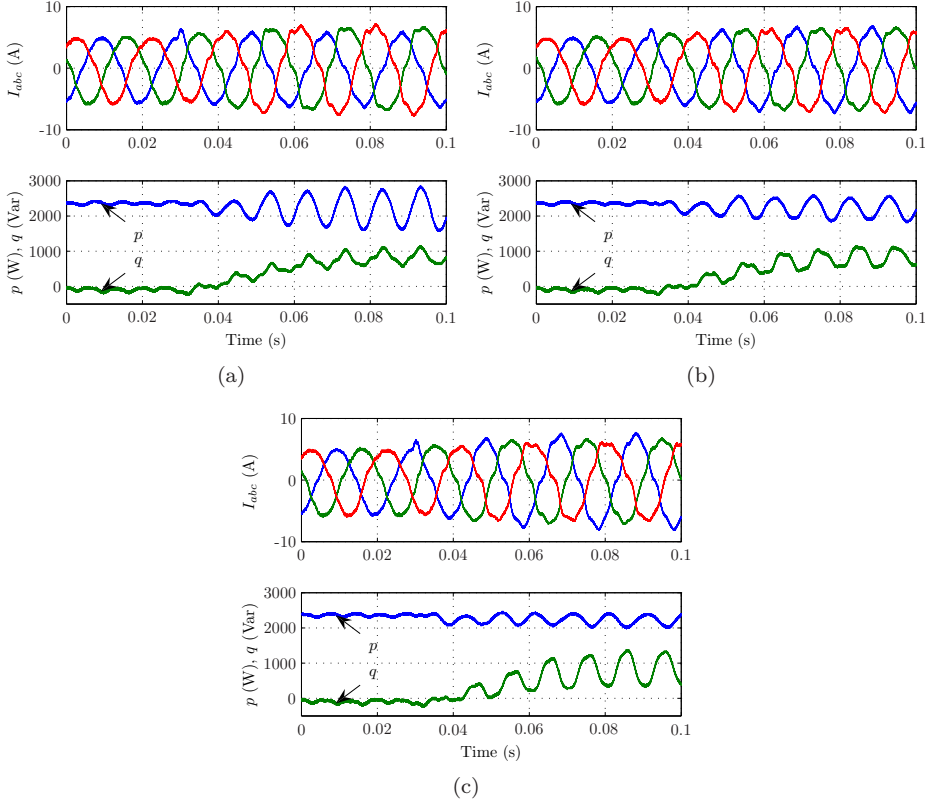
Figure 6.9: Experimental results of the joint strategy A with (a) $k_{pq} = 1$, (b) $k_{pq} = 0$, and (c) $k_{pq} = -1$. The waveforms from the top down are: injected currents, instantaneous active power p and reactive power q when $\varphi = 23°$.

this is because a low-pass filter is used to smooth the output of the power factor angle φ as calculated in (6.30). To detect accurate symmetric-sequence voltages under unbalanced and/or distorted voltage dips, the sequence detection filter used in Fig. 6.7 was designed with a settling time of 20ms, which copes well with a test condition up to 40% voltage dip. As a result, the outputs from the sequence detection filter after the moment of voltage dips will cause low-frequency ripple on the magnitude value of V^+ in (6.30), due to unequal amplitudes of $v_{\alpha 1}^+$ and $v_{\beta 1}^+$ at the transient. An extra low-pass filter, also with a settling time of 20 ms, was used to further smooth the ripple effect on the power factor angle. For other unbalance conditions, the settling time of the sequence detection filter and the low-pass filter should be optimized. Other fast detection techniques [23] can also be used, thereby improving the design.

Under the same test conditions, experimental results are also measured for joint strategy B. As shown in Fig. 6.11, nearly zero oscillating reactive power and active power are achieved at $k_{pq} = 1$ and $k_{pq} = -1$, respectively. When $k_{pq} =$

(a)

(b)

(c)
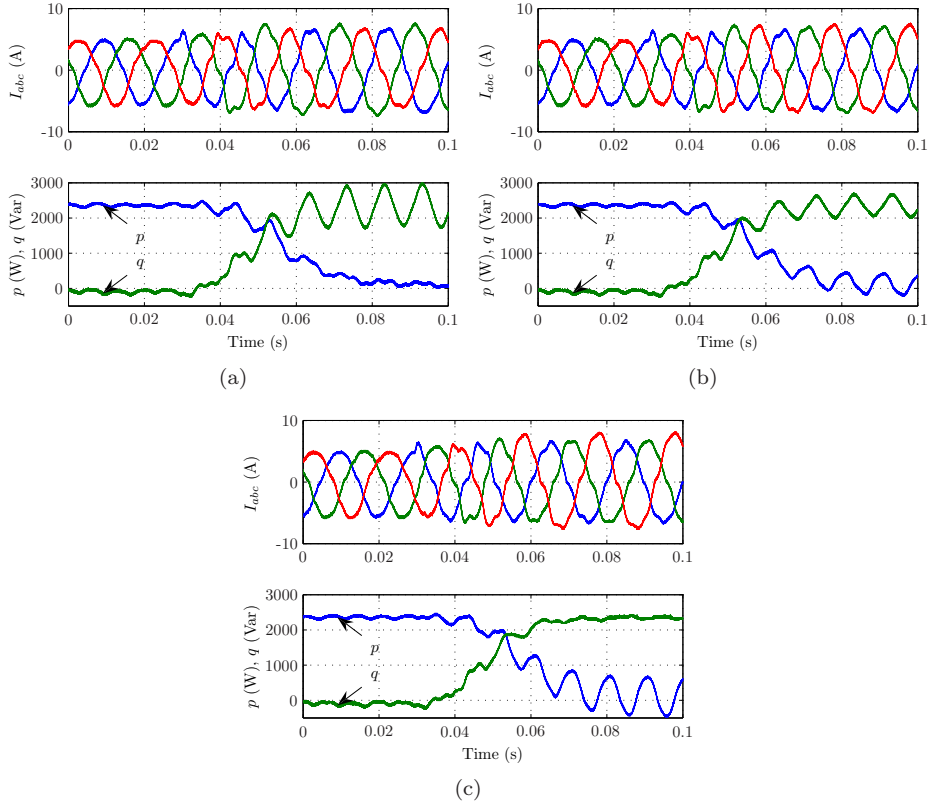
Figure 6.10: Experimental results of the joint strategy A with (a) $k_{pq} = 1$, (b) $k_{pq} = 0$, and (c) $k_{pq} = $ -1. The waveforms from the top down are: injected currents, instantaneous active power p and reactive power q when $\varphi = 90°$.

0, the results of joint strategy B are the same as the results of joint strategy A, since both joint strategies only depend on positive-sequence components in this case. The experimental results with $\varphi = 90°$ are given in Fig. 6.12. Comparing them with the results in Fig. 6.10 of joint strategies A, it is clear that the joint strategies with opposite signs of k_{pq} turn out to produce the same results.

It is noticed that the grid currents are slightly distorted especially after a grid fault. There are two reasons that cause the low frequency harmonic currents. The first one is the dead-time effect of the IGBT inverter bridges used in the lab system. In this work, a fixed dead time reaches 4% of the switching period, thereby leading to significant voltage harmonics on the output of the inverter. These voltage harmonics then cause distorted grid currents through small grid impedances. However, the current distortion will be less when increasing the fundamental currents. The second reason is the dc-bus voltage variations. In the experimental verifications, a dc-bus voltage control was not implemented in order to allow observing the behavior of the power control strategies. In this case,

(a)

(b)

(c)
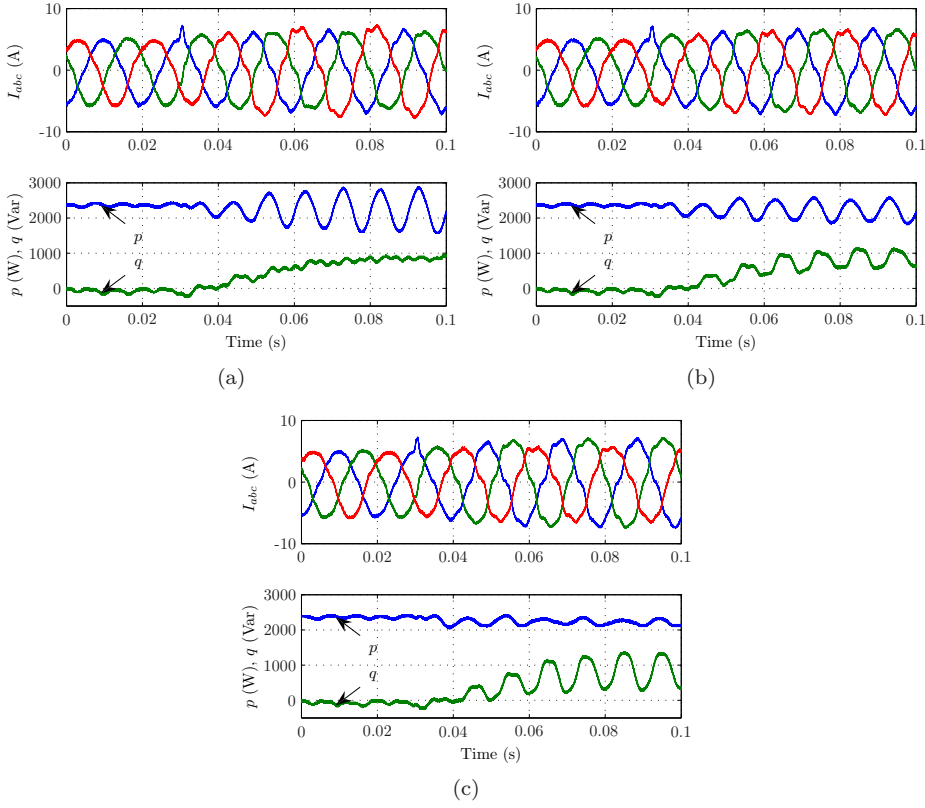
Figure 6.11: Experimental results of the joint strategy B with (a) $k_{pq} = 1$, (b) $k_{pq} = 0$, and (c) k_{pq} = -1. The waveforms from the top down are: injected currents, instantaneous active power p and reactive power q when $\varphi = 23°$.

variations are present in the dc voltage when changing the delivered power after grid faults and/or when oscillating active power exists. Therefore, the voltage variations reflect to the grid side, leading to low frequency current harmonics.

6.5.3   Test of adaptive control

Next, the joint strategy B is applied to confine the oscillating active power of the inverter under unbalanced voltage dips with the control scheme presented in Section 6.4. The proportional gain K_P and the integral gain K_I of the PI parameters in Fig. 6.6 are 0.1 and 50 s^{-1}, respectively. Because the tested power level is around 2.5 kW, a value of 200 W is assigned to $\tilde{p}_{2\omega\_pk}$ as the peak limit of oscillating active power, instead of calculating it from (6.28).

Under the same test conditions as for Fig. 6.12, with $\varphi = 90°$ and the same phase voltage dip shown in Fig. 6.8, two levels of voltage dips (30% and 40%) are emulated to test the adaptive control of k_{pq}. Measured waveforms are shown in
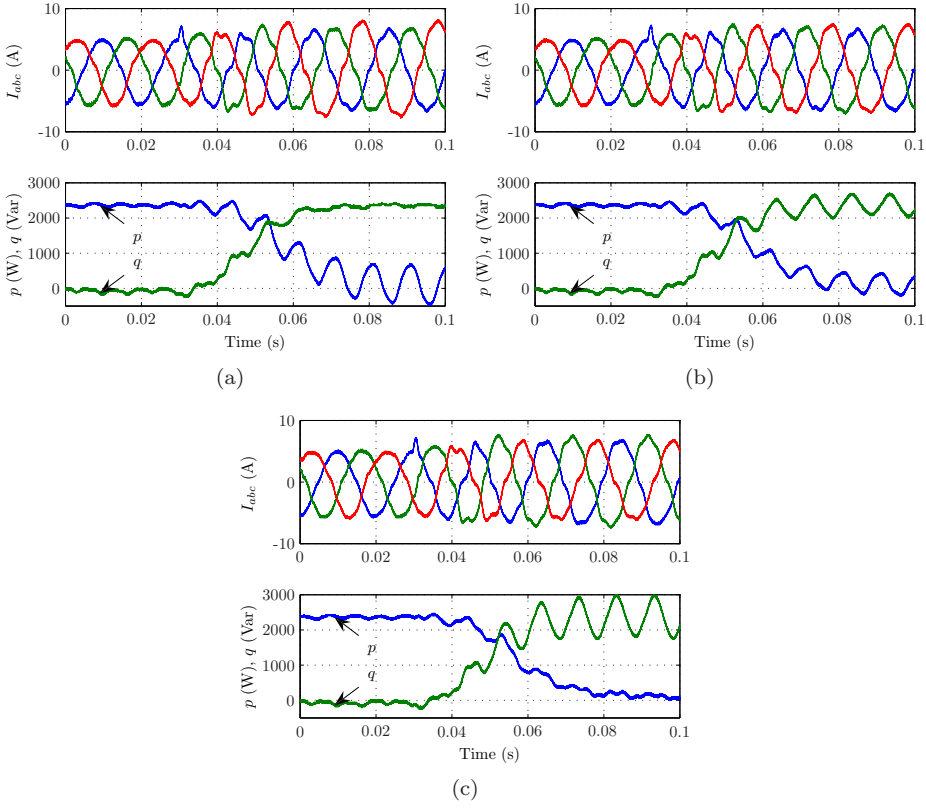
Figure 6.12: Experimental results of the joint strategy B with (a) $k_{pq} = 1$, (b) $k_{pq} = 0$, and (c) $k_{pq} = -1$. The waveforms from the top down are: injected currents, instantaneous active power p and reactive power q when $\varphi = 90°$.

Fig. 6.13, where the coefficient k_{pq} shifts towards -1 so as to confine the oscillating active power. The deeper the voltage dips, the smaller the k_{pq}. It can be seen that the oscillating components of the active power under the voltage dips are limited below the set point. As a result, the oscillating reactive power under 40% voltage dip is larger than the one under 30% voltage dip.

6.6 Conclusions

This chapter has proposed methods for independent active and reactive power control of distributed generation inverters operating under unbalanced voltage dips. By changing two adaptable parameters used as weighting factors for the compensation of oscillating power and for the regulation of three-phase grid currents, the proposed strategies enable DG systems to be optimally controlled and flexibly adapted to all possible requirements for grid voltage support.

Furthermore, for simultaneous control of active and reactive power, two joint
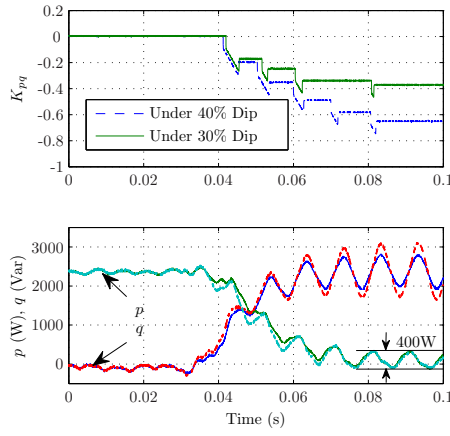
Figure 6.13: Measured waveforms of regulated coefficient k_{pq}, instantaneous active power p and reactive power q.

strategies have been proposed, yielding adaptive controllability that can cope with multiple constraints in practical applications. Application examples together with experimental results have been given, verifying the simplicity and adaptivity of the proposed ideas.

Chapter 7

Modeling and analysis of harmonic interaction

Abstract - In the previous chapters of Part III, a concept of grid support with auxiliary functions offered by DG systems has been presented. Clearly, either for auxiliary grid support or for conventional power delivery, a significant contribution to the grid side will require a collective action of many DG systems equipped with the same functionality. However, a large number of DG inverters coupled to the grid, may cause harmonic interactions. As a result, the DG systems may collectively aggravate grid voltage distortion and even lead to abnormal operation of grid-connected users. This chapter therefore proposes an impedance-based analytical method for modeling and analysis of harmonic interactions between a polluted grid and DG inverters.

The key cause of harmonic interaction/resonance problems is introduced. It is found to be the impedance-network quasi-resonance between the effective output impedance of the inverter and the equivalent grid impedance at the connection point. Starting with the output impedance modeling of an inverter, which is simply controlled by a PI regulator, a Norton model of the inverter is derived. Comparing with the switching model and the average model of the inverter, simulation results show the effectiveness of the Norton model for analyzing the harmonic current caused by a distorted grid. As a consequence, in order to minimize the harmonic distortion impact on grids, this chapter proposes that impedance limits should be specified and used as an extra design constraint for DG inverters. Moreover, an inverter based on multiple PR controllers is designed and modeled to examine the idea of output impedance limits. Assuming the impedance models of individual inverters and local loads within a distributed grid are known, especially in the case of new grids under construction, harmonic interactions between the grid and a certain number of DG inverters can be estimated in advance, as detailed later in this chapter.

7.1   Introduction

Harmonic interactions are potential problems for grid-connected inverters in a distributed grid. When the supply voltage of a distributed grid is polluted by nonlinear loads, poorly-designed grid connected inverters easily can have distorted output currents. In return, the resulting distorted currents aggravate voltage harmonics in the grid. Consequently, a high penetration of grid connected inverters in a distorted grid may lead to high harmonic current or voltage oscillation. As already presented in [38], such phenomena had been observed and investigated in an existing residential grid where a large number of distributed photovoltaic (PV) inverters were installed. Because the resonance frequency was found outside of any inverter control bandwidth, for harmonic analysis, the output impedance of PV inverters was simply modeled as the capacitance of the output filter, while the inverter control was excluded [38].

However, previous work in [39] and [40] has already shown that inverter topologies together with control certainly influence harmonic interactions in distorted grids. Depending on the penetration levels of DG inverters and practical grid parameters, harmonic resonances can also appear at frequencies within the inverter control bandwidth. This is the frequency range of interest for which harmonic interactions of DG inverters will be studied in this chapter.

To minimize harmonic interactions between DG inverters and polluted grids, first of all, in order to mitigate its current distortion impact in a distorted grid, each individual inverter should have a good current control design. The existing approaches are to increase the control bandwidth and to reduce the sensitivity of the inverter to grid harmonic voltages by applying different controllers and control loop design [82, 106]. However, the control parameters of the inverter are usually tuned by trial and error so as to ensure the output current complying with current distortion limits [107, 108]. It is not a systematic approach to design controllers in such a way because there is no guidance to impose restriction in the inverter design. Therefore, approaching from another point of view, this chapter proposes to introduce output impedance constraints to facilitate inverter control design. To clarify this proposal, the output impedance modeling of the inverter and detailed analysis are presented.

On the other hand, even when each individual inverter is designed to comply with current distortion limits, aggregated DG inverters can have harmonic resonance problems on a grid scale. It is noticed that, at the power system side, studies such as harmonic propagation and resonances, modeling and simulation of various loads, and benchmark test systems have been presented in [109–112]. However, specific modeling and analysis of the harmonic interactions between DG inverters and polluted grids have not been fully explored. This issue will be addressed later in this paper, where an impedance-model based analytical approach is presented.

The remaining parts of this chapter are organized as follows. In Section 7.2, the harmonic interaction problems are introduced. Starting with a simple example on the output impedance modeling of inverters in Section 7.3, it is then proposed in Section 7.4 to specify output impedance limits for DG inverters as a design constraint. Based on the proposed impedance limits, Section 7.5 shows the inverter
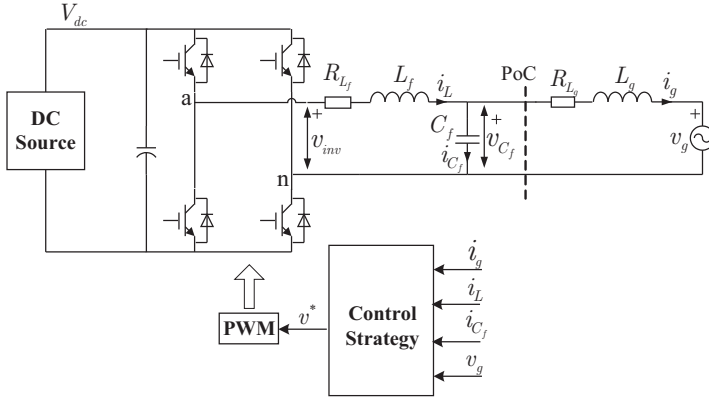
Figure 7.1: Single-phase grid-connected inverter system.
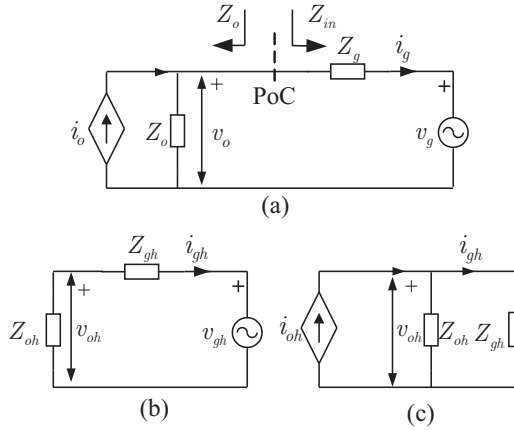
Figure 7.2: Impedance representations of (a) Norton equivalent model of a grid connected inverter, (b) series quasi-resonance, and (c) parallel quasi-resonance with respect to the harmonic component of order h.

impedance design and the harmonic distortion impact of one single inverter. Finally, an impedance-based model is derived to illustrate the harmonic interactions in a power electronics based distributed grid.

7.2 Harmonic interactions

A single-phase grid connected inverter system is used to interpret harmonic interaction problems, but it also represents typically one phase of the three-phase inverter. Therefore, in this chapter, the explored work based on the single-phase inverter has broad applicability and can be used for the study of three-phase in-

verters. As shown in Fig. 7.1, the inverter is coupled to the grid through a LC filter at the point of connection (PoC). To describe a general case, all the currents at the ac side and the grid voltage are assumed to be measured, although only the necessary control-variables are needed depending on the control strategy. Considering that the control of the dc bus can be achieved by an upstream power conversion stage, or that the dc-bus control has a large time constant with respect to inverter current regulation, only the inverter-side control is included in Fig. 7.1. The influence of low-frequency voltage variations on the dc bus is investigated in a later section.

Since the grid connected inverter is controlled to inject currents into the grid, the inverter is expected to be represented by a Norton model (i.e., a current source i_o and a parallel output impedance Z_o)[1], as shown in Fig. 7.2 (a). Independently on modeling, the output impedance Z_o is always a function of the frequency. Generally speaking, the output impedance of an inverter will lead to output harmonic currents due to the interaction with the corresponding background grid voltage harmonics.

Furthermore, impedance-network quasi-resonance (the harmonic frequency is near to the resonant frequency of impedance networks) between the output impedance of an inverter and the input impedance at the PoC should be considered. Figure 7.2 (b) shows a possible series quasi-resonance at a particular frequency where the grid voltage harmonic v_{gh} can result in a high current harmonic. Figure 7.2 (c) shows a parallel quasi-resonance at the same frequency where the distortion on i_{oh} generated by the inverter can lead to a high voltage harmonic at the output of the inverter. The subscript "h" denotes the harmonic order. It is noticed that both the equivalent input impedance Z_{in} and the resonant frequencies change because of the various feeder impedances in different grids and varying loads connected at the PoC.

It is qualitatively explained above that harmonic interaction can be present between grid connected inverters and a distributed grid. In the following, a more quantitative analysis, based on the output impedance of the inverter, will be presented.

7.3   Output impedance modeling

It is desirable to derive a model that is accurate enough for the analysis of harmonic interaction up to the 40th-line harmonic. To describe an inverter, an average circuit model [113] is accurate enough to achieve the same results as a switching circuit model when the switching frequency is much higher than the frequency of interest.
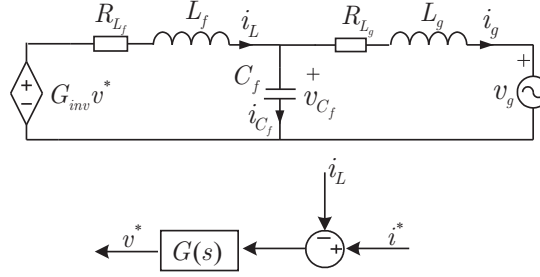
Figure 7.3: Average circuit model of a single phase inverter as in Fig. 7.1.

7.3.1 Average circuit model and small-signal model

Again, the single phase inverter in Fig. 7.1 is used as an example for modeling. The method presented in the following section can be directly used for a three-phase inverter in balanced grids or should be slightly adapted for unbalanced grid situations by modeling symmetric-sequence components separately.

The average circuit model of the inverter is shown in Fig. 7.3, where a description for the dynamics of the dc bus is not included. To make the modeling less complex, a simple control scheme is used. The output inductor current of the inverter is controlled by a single-loop inductor current feedback with a PI compensator, that is,

$$G(s) = K_P + K_I \frac{1}{s}, \tag{7.1}$$

which is widely used in existing designs because of its simplicity. The switching frequency of the inverter bridge is assigned much higher than the 40th-line frequency, so each switching period can be averaged and the PWM inverter bridge can be represented by a gain

$$G_{inv} = \frac{V_{dc}}{V_{cm}}, \tag{7.2}$$

where V_{dc} is the dc-bus voltage and V_{cm} the magnitude of the carrier waveform [114].

The variations of V_{dc} can introduce nonlinearities to the product $G_{inv}v^*$ in Fig. 7.3. By supposing the dc-bus voltage constant, which is assumed in the previous section, the derived reduced-order model is typically valid above the fundamental frequency [115, 116]. The control structure diagram of the inverter in Fig. 7.3 is drawn in Fig. 7.4 (a). Consequently, a Norton model like that in Fig. 7.2 (a) can be obtained from Fig. 7.4 (a) based on the small-signal analysis around an operation point, as shown in Fig. 7.4 (b). In the block diagram of Fig. 7.4 (b), the resulting inverter output impedance $Z_o(s)$ is found from Fig. 7.4 (a) with

$$Z_o(s) = \left. \frac{v_{C_f}(s)}{-i_g(s)} \right|_{i^*=0}, \tag{7.3}$$

---

[1]Symbols of all the impedances in this chapter represent phasors; a bar subscript, which has been used to denote phasor notation, is left out for the simplification of notation in this chapter.

(a)

(b)
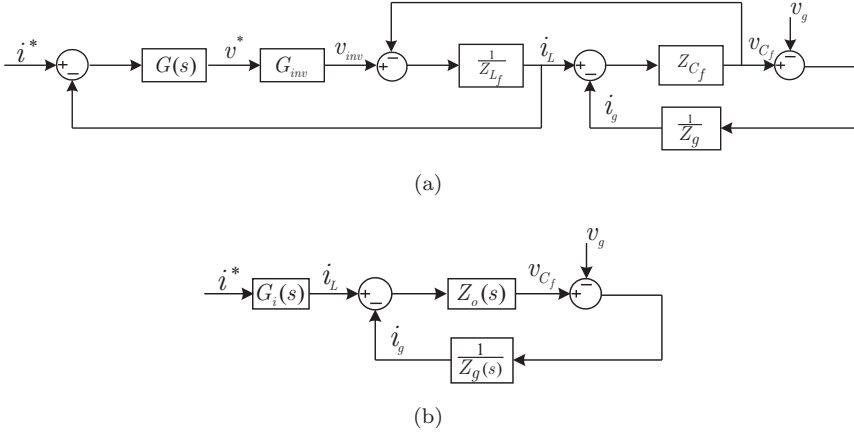
Figure 7.4: Block diagrams: (a) control structure of a single phase inverter with inductor current feedback as given in Fig. 7.3 and (b) the Norton equivalent model for analyzing harmonic interactions.

which gives

$$Z_o(s) = \frac{Z_{C_f} Z_{L_f} + Z_{C_f} G_{inv} G(s)}{Z_{C_f} + Z_{L_f} + G_{inv} G(s)}, \tag{7.4}$$

where $Z_{C_f} = 1/(sC_f)$, $Z_{L_f} = R_{L_f} + sL_f$, and the inverter output current is a function of the reference current as represented by

$$G_i(s) = \left. \frac{i_L(s)}{i^*(s)} \right|_{v_{C_f} = 0}, \tag{7.5}$$

yielding

$$G_i(s) = \frac{G(s)G_{inv}}{Z_{L_f} + G(s)G_{inv}}. \tag{7.6}$$

It should be noticed that in general $Z_o(s)$ and $G_i(s)$ do depend on the structure of the applied controller.

7.3.2   Validation of the Norton model

Comparisons among the switching model, the average circuit model and the Norton model are carried out to check correctness and effectiveness. System parameters are listed in Table. 7.1. It is noticed that the transfer function $G_i(s)$ in Fig. 7.4 (b) can be simplified as a unity gain since the target frequency of i^* is very low with respect to the switching frequency.

First, as shown in Fig. 7.5 and Fig. 7.6, the frequency responses of the output impedance are determined through small ac perturbations in the average circuit model of Fig. 7.3 and through ac sweep frequency in (7.3), respectively. The results at low frequencies are found to be virtually the same for both cases. The

Table 7.1: System Parameters

Description	Symbol	Value
Utility grid voltage	V_g	230 V
Line resistance	R_g	0.4 Ω
Line inductance	L_g	0.8 mH
dc-bus voltage	V_{dc}	400 V
Filter capacitance	C_f	5 uF
Filter inductance	L_f	2 mH
	R_{Lf}	0.1 Ω
Switching frequency	f_{sw}	16 kHz
Carrier wave magnitude	V_{cm}	7.5 V
PI parameters	K_P	1
	K_I	$10000 \ s^{-1}$
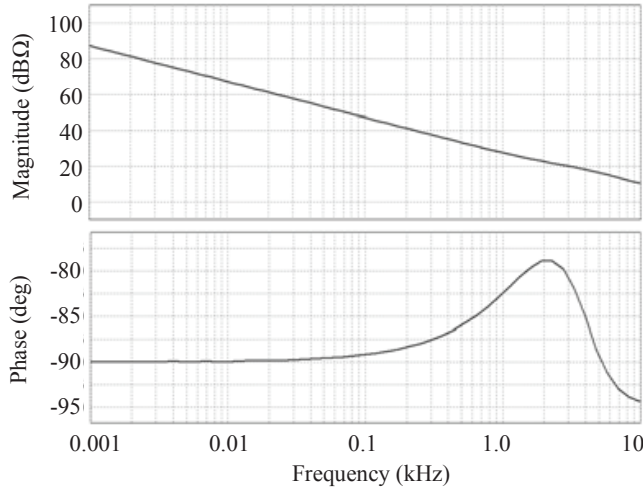
Figure 7.5: Magnitude and phase response of the output impedance $Z_o(s)$ as obtained by small ac perturbations in the average model in Fig. 7.3.

ac perturbation-based approach is a way to check the correctness of the output impedance derived with the average model. Alternatively, this can also be used to obtain the output impedance of an existing product from measurements without requiring knowledge of the control methods and design parameters.

To test the effectiveness of the derived Norton model, a strongly distorted grid voltage can be easily programmed in simulations so as to exaggerate the differences between the Norton model and the other two models. Therefore, a voltage with 28% of total harmonic distortion (THD), including 20% 5th, 10% 7th, 11th, 17th and 19th harmonics, is used as grid voltage, although the recommended THD values of the grid voltage in electrical power systems are intended to be low enough (maximum 8%) according to the IEEE Std 519-1992 [108] and EN 50160 [56]. The
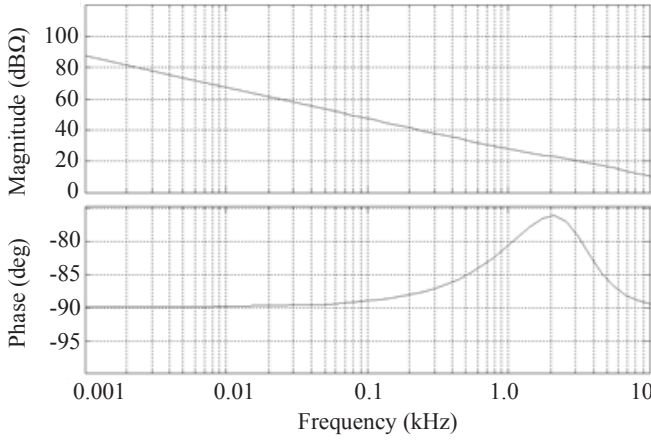
Figure 7.6: Bode plots of the output impedance $Z_o(s)$ as derived from Eq. (7.4).

derived output currents of the three models are compared in the time domain and the frequency domain, as shown in Fig. 7.7. It can be seen that the results of the three models in the frequency range of interest are in perfect agreement, in spite of being tested under an extreme grid situation.

7.3.3   Influence of dc-bus voltage variations

For the linearization of the average circuit model in Fig. 7.3, the dc-bus voltage was assumed to be constant. In practice, single-phase systems or three-phase unbalanced systems may have voltage variations on the dc bus depending on the control schemes and circuit topologies. Figure 7.8 shows the influence of small dc-bus voltage variations (e.g. by imposing $\pm$ $10\%V_{dc}$, 100Hz) on the ac output currents. Apparently, the Norton model is different from the switching model and the average model; no harmonic currents resulting from the dc-bus voltage variations can be reproduced by the Norton model since this model is created with the assumption of constant dc-bus voltage. However, it can be seen in Fig. 7.8 that the resulting harmonics generated by dc-bus voltage variations are quite small with respect to the fundamental current amplitude. The Norton model, therefore, is accurate enough to forecast the harmonic currents caused by a distorted grid.

Similarly, for simplification, it is assumed that the influence on the inverter output currents that may be caused by switching dead-time effects and the physical asymmetry of semiconductors in practical inverters are negligible.

7.4   Design constraints on the output impedance

Since power electronic converters are the grid interface of DG systems, the design of an inverter is driven by the need to satisfy the current harmonic limits allowed by the IEEE standards [107, 108]. To make the output current compliant with
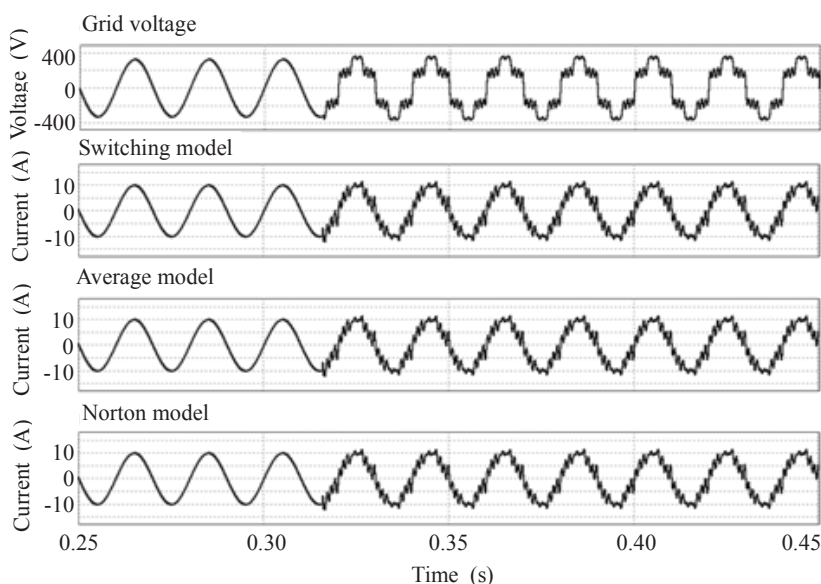
(a)
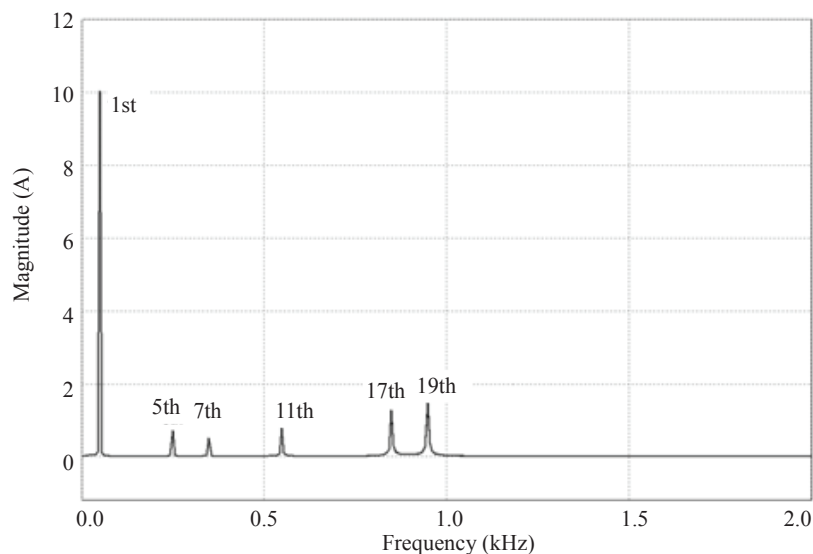
(b)

Figure 7.7: Output current waveforms are found to be the same in (a) time domain and (b) frequency domain. The waveforms are measured in a grid with 28% of THD, including 20% 5th, 10% 7th, 11th, 17th and 19th voltage harmonics.
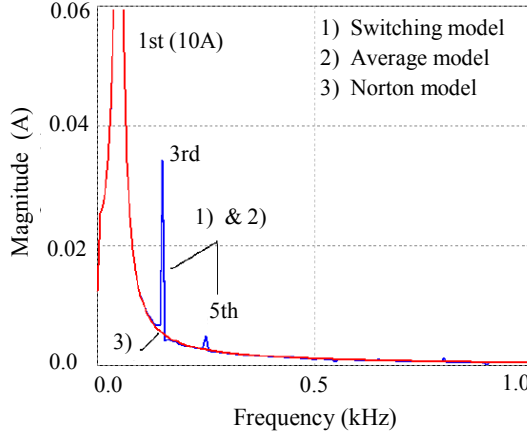
Figure 7.8: Output current harmonics caused by dc-bus voltage variations.

the standards in distorted grids, control parameters are usually tuned by trial and error, based on simulations or measurements. It is not a systematic approach to design controllers in such a way because up to now there is no guidance to impose restrictions on the inverter design. To get acceptable results, this chapter proposes to introduce output impedance as constraints for inverter control design or analysis.

7.4.1   Output impedance limits

Table 7.2 lists the current distortion limits of grid-connected PV systems, for instance, as required by the standard IEEE Std. 929-2000 [107]. It is desirable that the output currents of PV inverters can comply with the current distortion limits even when connecting to a practical grid with harmonic voltages. Conservatively, the limits of the grid harmonic voltages given in EN 50160 are used here as an example, which are shown in Table 7.3 [56]. Therefore, it is proposed to specify the lower magnitude limit of an inverter's output impedance within the frequency of interest, as expressed by

$$|Z_{\%h}| = \frac{U_1 \, U_{\%h}}{I_1 \, I_{\%h}}, \tag{7.7}$$

where $U_{\%h}$ is the relative voltage as given in Table 7.3 and $I_{\%h}$-the relative current as given in Table 7.2; U_1 is the fundamental grid voltage and I_1-the rated fundamental current of the grid connected inverter system under consideration; $|Z_\%|$ is the minimum desirable value for the inverter's output impedance at the harmonic of order h.

With $U_1 = 230$ V and $I_{1rms} = 7$ A as an example, the obtained harmonic impedance $Z_\%$ is plotted in Fig. 7.9, where the output impedance Z_o of the inverter as derived in (7.4) is also plotted. Comparing the two curves, it can

Table 7.2: Current harmonic limits

Odd harmonics	Distortion limit
3rd - 9th	<4.0%
11th - 15th	<2.0%
17th - 21st	<1.5%
23rd - 33rd	<0.6%
Above the 33rd	<0.3%

Note: even harmonics are limited to 25% of the odd harmonics above.

Table 7.3: Voltage harmonic limits

Odd harmonics				Even harmonics	
Not multiples of 3		Multiples of 3			
Order h	Relative voltage (%)	Order h	Relative voltage (%)	Order h	Relative voltage (%)
5	6	3	5	2	2
7	5	9	1.5	4	1
11	3.5	15	0.5	6 - 24	0.5
13	3	21	0.5		
17	2				
19 - 25	1.5				

be seen that the magnitude of the output impedance $|Z_o|$ is lower than $|Z_\%|$ at frequencies beyond the 11th harmonic.

By assuming a grid voltage with odd harmonics from 5th to 19th according to Table 7.3 (no multiples of 3), simulations were carried out based on the average circuit model. Figure 7.10 shows the output current harmonic spectrum of the inverter, where, as expected, the current harmonics at 11th, 13th, 17th, and 19th order are all slightly over the current harmonic limits of Table 7.2, as indicated by the curve comparison from Fig. 7.9.

The concept of the output impedance limits, therefore, can be used for control parameter selection when designing an inverter used in a distorted grid or for evaluating an existing inverter on the basis of output impedance measurements without knowing the internal design.

7.4.2 Intersection point of input and output impedances

As already sketched in Fig. 7.2, network resonance is one of the conditions for potential harmonic quasi-resonance problems. In Fig. 7.2 (b), the voltage harmonic v_{oh} across the output impedance can be expressed as a function of the grid voltage harmonic v_{gh} by

$$v_{oh} = \frac{1}{1 + Z_{gh}/Z_{oh}} v_{gh}. \tag{7.8}$$
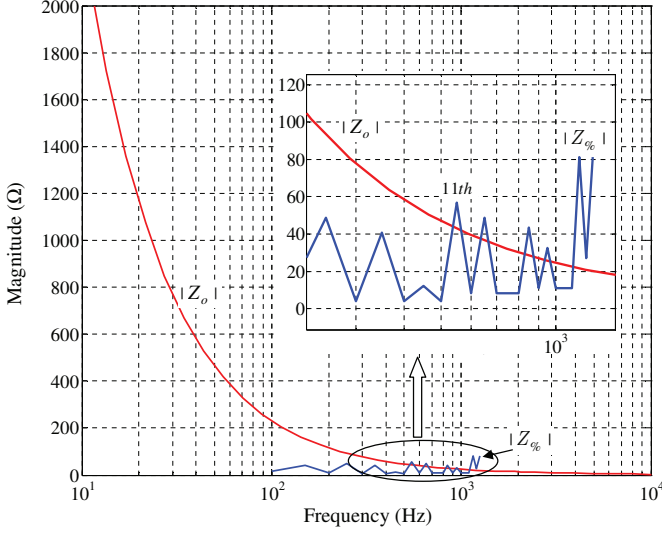
Figure 7.9: Magnitude of the output impedance $|Z_o|$ and the output harmonic impedance limit $|Z_\%|$ as a function of frequency.
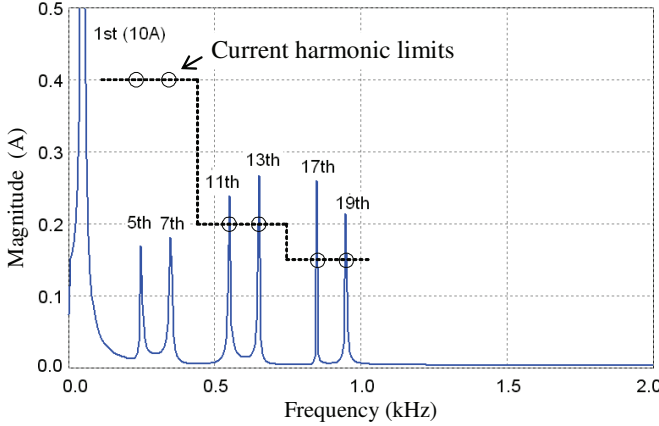
Figure 7.10: Current harmonic spectrum of the inverter in a distorted grid programmed with odd harmonic voltages from 5th to 19th according to Table 7.3 (no multiples of 3), showing that harmonics at 11th, 13th, 17th, and 19th are over the standard limits.

When Z_{oh} and Z_{gh} are equal in amplitude and opposite in sign, the denominator of (7.8) is zero, thereby giving rise to a high voltage harmonic v_{oh} even with a small perturbation input of v_{gh}. Similarly, quasi-resonance in Fig. 7.2 (c) will result in a high current harmonic i_{gh} driven by a small output current harmonic output from the inverter. As a consequence, the inverter can trigger instability problems.
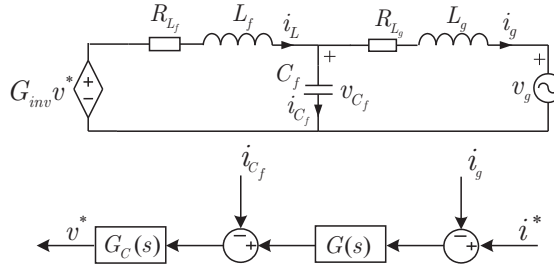
Figure 7.11: Average circuit model of a single phase inverter with dual loop control.

By looking at the magnitude and phase responses of the output impedance in Fig. 7.6, it can be noticed that the output impedance of an inverter turns to behave as a capacitance at high frequencies. Moreover, the control design of the inverter can only change the output impedance characteristics within the control bandwidth; this will be further illustrated in the next section.

Therefore, the magnitude response of an inverter's output impedance will unavoidably have an intersection with the grid impedance, and this probably will introduce resonance problems. To avoid or minimize possible harmonic resonances, the intersection point (the resonant frequency) should be located at a frequency higher than the 40th harmonic (e.g. above 2.5 kHz), because the harmonic sources are then expected to be with significantly low amplitudes.

In the next section, a design example illustrates the way to introduce the output impedance limits as a design constraint and to examine the intersection point of input and output impedances.

7.5 Minimizing harmonic distortion impact of a single inverter

7.5.1 Selective harmonic impedance enhancement

Considerations on closed-loop system stability and dynamics are important when designing a controller. In addition, the output impedance can help tune control parameters for mitigating harmonic interaction problems. Hence we can adjust the output impedance of the inverter investigated in the previous section by increasing the gain and control bandwidth, by applying more control loops, or other types of controllers.

This section focuses on selective harmonic impedance enhancement as an example to explicitly clarify design aspects related to shaping of the output impedance. Instead of single-loop inductor current feedback control, a dual-loop control, that is, an outer-loop grid current regulator and an inner-loop capacitor current feedback, is used [82]. Figure 7.11 shows the average model of the dual loop control and Fig. 7.12 details the corresponding control structure diagram. The advantage of this method is that it achieves a direct grid current control and stabilizes the
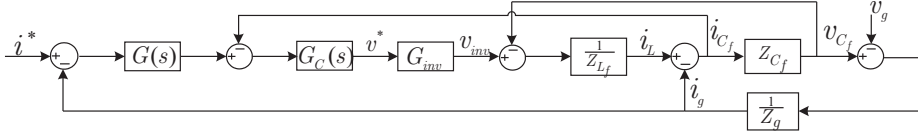
Figure 7.12: Control structure diagram of a single phase inverter with dual loop control as given in 7.11.

control system in a weak grid with a large inductive feeder impedance. Specifically, a multiple proportional resonant (PR) controller (see Section 3.2) expressed as

$$
\begin{aligned}
G(s) = K_P &+ \frac{2K_I\omega_b s}{s^2 + 2\omega_b s + \omega_1^2} \\
&+ \frac{2K_{I5}\omega_b s}{s^2 + 2\omega_b s + (5\omega_1)^2} \\
&+ \frac{2K_{I7}\omega_b s}{s^2 + 2\omega_b s + (7\omega_1)^2} \\
&+ \frac{2K_{I11}\omega_b s}{s^2 + 2\omega_b s + (11\omega_1)^2}
\end{aligned}
\tag{7.9}
$$

is employed for the outer-loop grid current regulation.

In (7.9), resonant controllers at the 5th, 7th, and 11th harmonic are added to achieve selective harmonic impedance enhancement. With high gains at their individual central frequencies, the resonant controllers can realize high output impedances at the selected frequencies. The inner-loop compensator, $G_c(s)$ in Fig. 7.12, is only a simple proportional gain represented by $K_{Pc} = 1$. Setting in (7.9) the parameters $K_P = 1$, $K_I = 50$ rad/s, $K_{I5} = K_{I7} = K_{I11} = 25$ rad/s, $\omega_b = 10$ rad/s, and $\omega_1 = 314$ rad/s, the enhanced output impedance can be calculated according to (7.3).

Figure 7.13 shows the magnitude of the enhanced output impedance Z_o; as expected, the magnitudes at several particular frequencies are sharply increased. It is noticed that the output impedance at frequencies that have not been explicitly enhanced are also almost above the lower limits for the 13th, 17th, and 19th harmonic. Tested with the same grid voltage as used in Fig. 7.10, the output current harmonics at frequencies with enhanced impedances are significantly mitigated, and most other current harmonics are also below the standard limits, as shown in Fig. 7.14.

It should be mentioned that another reason to choose the dual-loop control scheme with multiple PR controllers is to confirm again the validity of the output impedance based model under different control strategies. In the same manner, comparisons of the three models based on the above designed multiple PR controllers are repeated for the same grid situation as in Fig. 7.7. Again the results shown in Fig. 7.15 validate the effectiveness of the impedance based model.
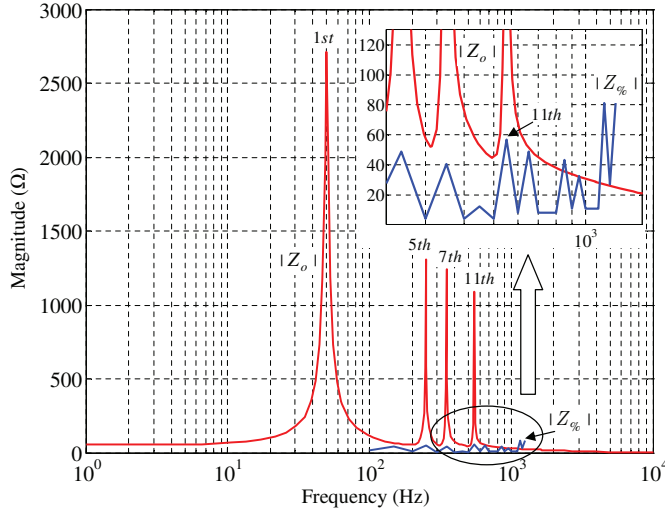
Figure 7.13: Magnitude of the output impedance $|Z_o|$ of the inverter with enhanced harmonic impedances and the output harmonic impedance limit $|Z_\%|$ as a function of frequency.
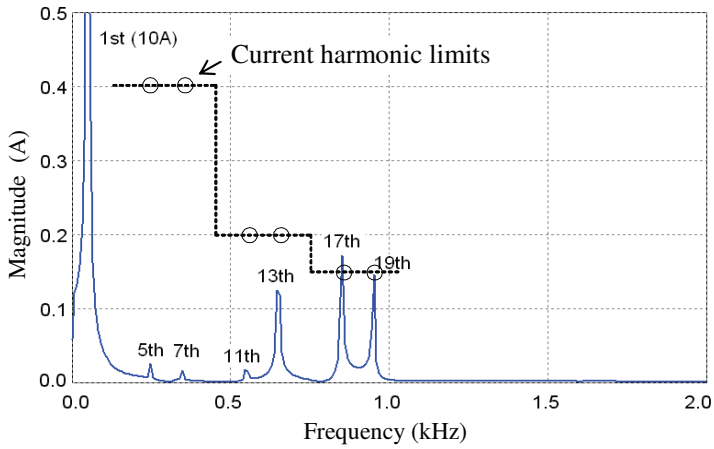
Figure 7.14: Current harmonic spectrum of the inverter with enhanced output impedance in the same distorted grid as tested in Fig. 7.10.

7.5.2   Impedance intersection point

As presented in Section 7.4.2, to analyze possible network resonance when connecting an inverter to the grid, one can examine the intersection point of the output impedance Z_o of the inverter with the input impedance Z_{in} at the PoC as in Fig. 7.2, where the input impedance Z_{in} is for now only the grid impedance Z_g. Figure 7.16 shows that the intersection point of the output and input impedances is beyond the harmonic frequency of interest (up to 2 kHz) for the parameters in Table 7.1. Therefore, harmonic quasi-resonance due to voltage/current harmonics can be avoided.

Concerning grid impedances, it is difficult to have an exact model for a distributed grid connected with multiple inverters and other loads. It is suggested to either choose the worst case grid impedance with the knowledge of a target grid, or measure the grid impedance by injecting perturbation voltages. It should be kept in mind that, when doing impedance measurements with perturbation voltages, the measured grid impedances may not be accurate at low-order harmonic frequencies due to the presence of varying nonlinear loads in the grid. Magnitude and phase information of the measured impedance at high-order harmonics (eg. above 2 kHz) can represent the grid impedance quite accurately since the influence of nonlinearities on high-order harmonics are negligible [115].

7.5.3   Summary and discussion

In order to mitigate harmonic interactions in a distorted grid, the previous considerations on output impedance limits and the impedance intersection point provide useful design constraints for DG inverters. Two extra aspects to be considered on the proposed concept are summarized in the following.

It is noticed in Fig. 7.13 that the lower limits of output impedance are still above the enhanced output impedance of the inverter at the 21st, 23rd and 25th harmonics. Due to the finite control bandwidth, designed to be at 2.5 kHz, the decrease of the output impedance at high frequencies is inevitable. Much more effort is needed if one wants to improve further the control bandwidth, the system loop gain and the switching frequency. Alternatively, the proposed output impedance limits are too conservative and should be reevaluated at high-order harmonics based on practical grid distortions.

Assuming the impedance models of individual inverters and local loads within a distributed grid are known, it is possible to analyze the harmonic interactions in a DG inverter based grid. This is the subject of the next section.

7.6   Harmonic interaction analysis of aggregated inverters

7.6.1   Impedance calculation based on bus admittance matrix

According to a benchmark test for a distribution system in [110], a simplified grid with multiple DG inverters is shown in Fig. 7.17, where capacitance of the short
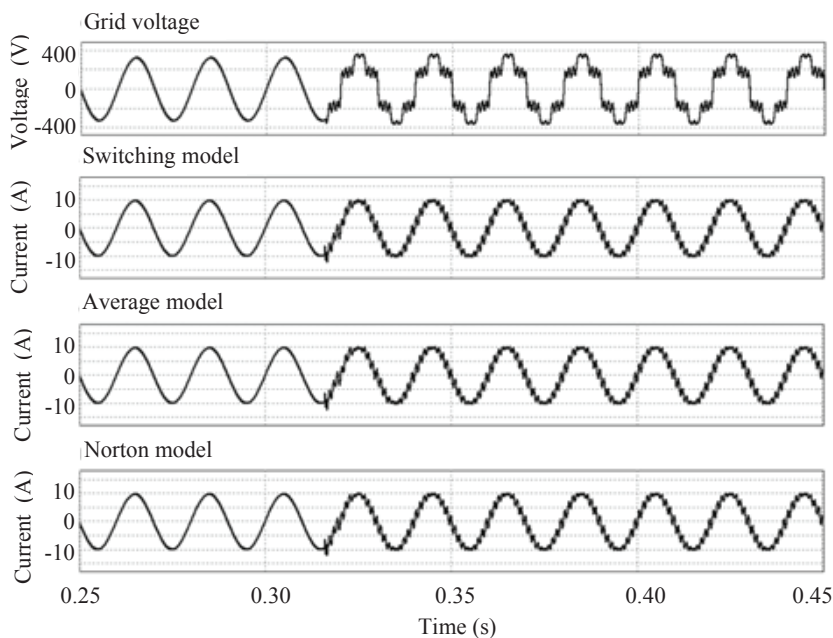
(a)
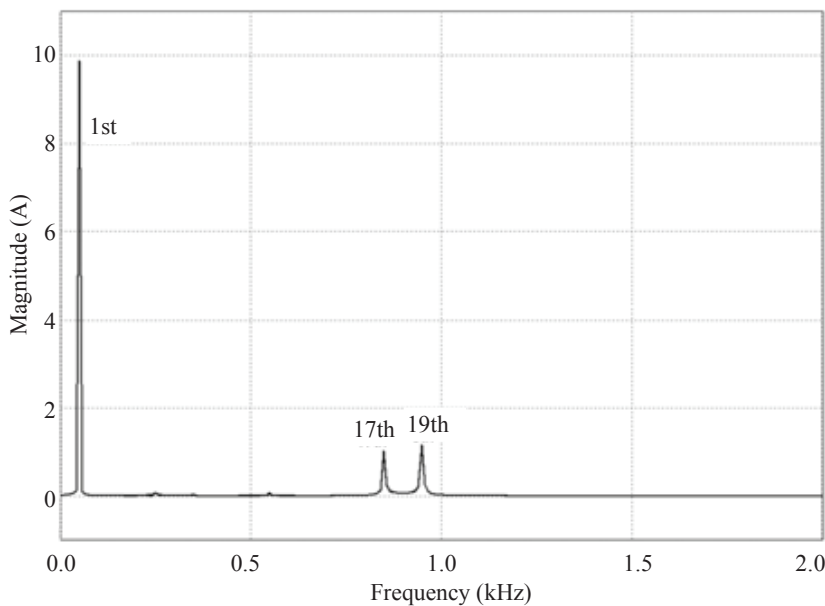
(b)

Figure 7.15: Output current waveforms are found to be the same in (a) time domain and (b) frequency domain. The waveforms are measured with the same grid voltage as in Fig. 7.7, including 20% 5th, 10% 7th, 11th, 17th and 19th voltage harmonics.
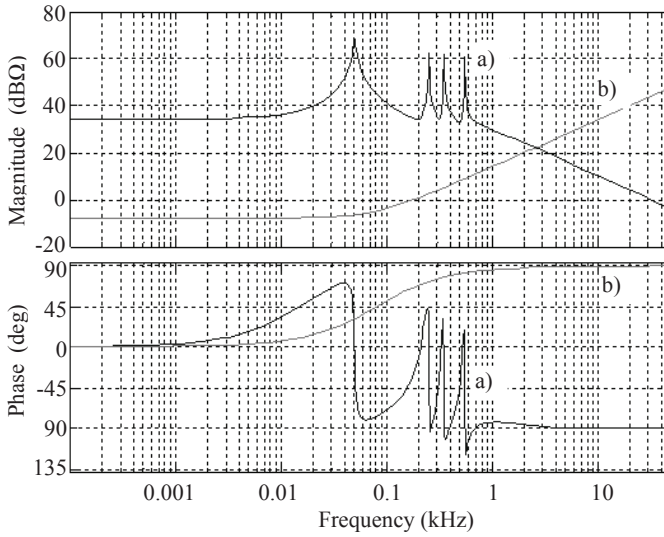
Figure 7.16: Bode plots of a) the enhanced output impedance Z_o and b) the input impedance Z_{in} or the grid impedance in Fig. 7.2.
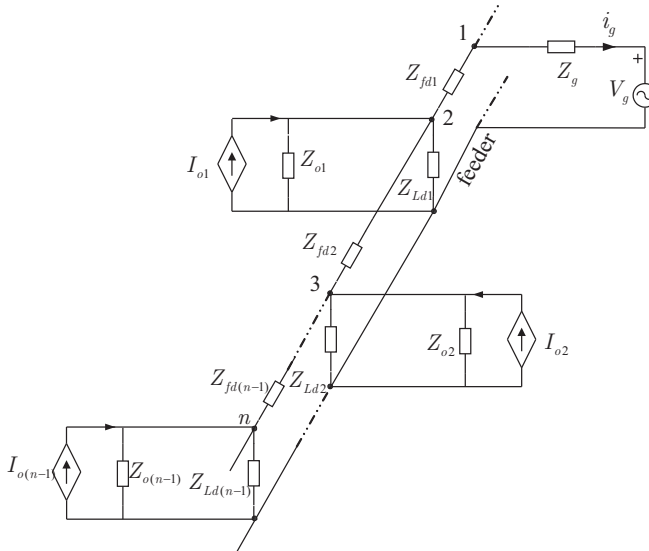
Figure 7.17: Impedance-model representation of a distributed grid with multiple inverter systems connected.
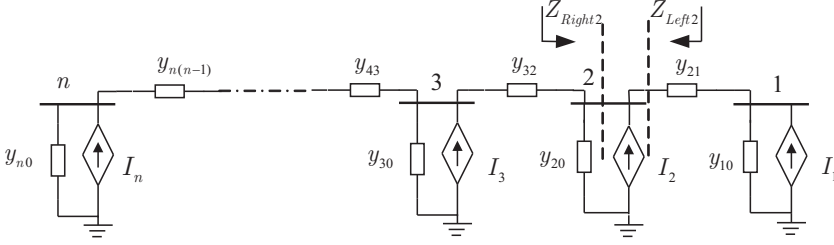
Figure 7.18: Single-line admittance model of the system in Fig. 7.17.

overhead line and all cables are neglected. The connected converter systems are represented by impedance models as in Fig. 7.2. Assuming in Fig. 7.17 a LV-feeder for powering domestic appliances, electricity loads are partially lumped together, namely Z_{Ldn}, while feeder impedances between lumped regions are represented by Z_{fdn}. It is known that household loads cannot simply be modeled as linear network components due to nonlinearities, but they are nevertheless represented by dominant capacitances here (the household capacitance varies from 0.6 to 6 μF [38]) for preliminary estimation of harmonic interactions and also for simplifying the example. The presented method is applicable for more complex grids with impedance models of other loads. [111, 116] specifies the modeling of harmonic sources with nonlinear voltage-current characteristics.

To calculate the output and input impedances at each node of the feeder, the network of Fig. 7.17 can be redrawn as a single-line admittance model as shown in Fig. 7.18. In terms of a bus bar structure, each node is now marked with bus number from 1 to n, and all the impedances under a same bus are combined and renamed for applying standard description algorithms based on bus admittance matrices [117]. As a result, the correspondence between Fig. 7.17 and 7.18 follows from

$$I_2 = I_{o1}, I_3 = I_{o2}, \ldots I_n = I_{o(n-1)},$$
$$y_{20} = 1/(Z_{o1}//Z_{Ld1}), \ldots y_{n0} = 1/(Z_{o(n-1)}//Z_{Ld(n-1)}),$$
$$y_{21} = 1/Z_{fd1}, \ldots y_{n(n-1)} = 1/Z_{fd(n-1)}. \tag{7.10}$$

Besides, the grid supply source (V_g and Z_g) are represented by a Norton equivalent as

$$I_1 = V_g/Z_g, y_{10} = 1/Z_g. \tag{7.11}$$

Applying Kirchhoff's current law (KCL) to each bus obtains

$$I_1 = (y_{10} + y_{21})V_1 - y_{21}V_2, \tag{7.12}$$
$$I_2 = -y_{21}V_1 + (y_{20} + y_{21} + y_{32})V_2 - y_{32}V_3, \tag{7.13}$$
$$I_3 = -y_{32}V_2 + (y_{30} + y_{32} + y_{43})V_3 - y_{43}V_4, \tag{7.14}$$

$$\vdots$$

$$I_n = -y_{n(n-1)}V_{n-1} + (y_{n0} + y_{n(n-1)})V_n. \tag{7.15}$$
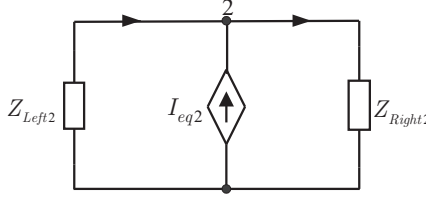
Figure 7.19: Equivalent circuit model at the bus bar 2 of Fig. 7.18.
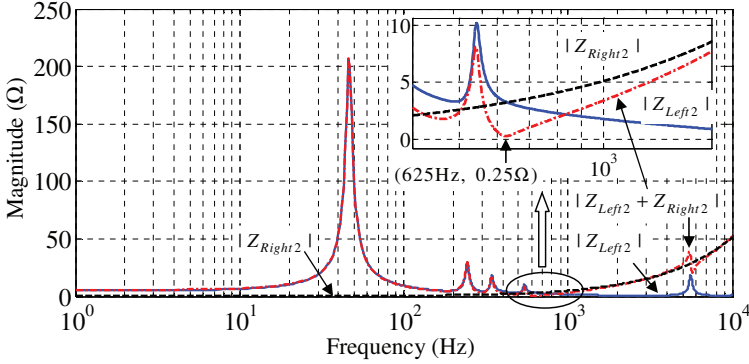
Figure 7.20: Frequency responses of the impedance Z_{Left2}, Z_{Right2}, and the sum of both impedances at bus 2 of Fig. 7.18, when 10 inverter modules are connected.

Writing (7.12) - (7.15) in matrix form gives

$$
\begin{bmatrix} I_1 \\ I_2 \\ I_3 \\ \vdots \\ I_n \end{bmatrix} = \begin{bmatrix} Y_{11} & Y_{12} & Y_{13} & \cdots & Y_{1n} \\ Y_{21} & Y_{22} & Y_{23} & \cdots & Y_{2n} \\ Y_{31} & Y_{32} & Y_{33} & \cdots & Y_{3n} \\ \vdots & \vdots & \vdots & \ddots & \vdots \\ Y_{n1} & Y_{n2} & Y_{n3} & \cdots & Y_{nn} \end{bmatrix} \begin{bmatrix} V_1 \\ V_2 \\ V_3 \\ \vdots \\ V_n \end{bmatrix},
\tag{7.16}
$$

where $V_1 \ldots V_n$ are the node voltages from bus 1 to n, and

$$
\begin{aligned}
Y_{nn} &= \sum_{i=0}^{n+1} y_{ni}, \\
Y_{(n-1)n} &= Y_{n(n-1)} = -y_{n(n-1)},
\end{aligned}
\tag{7.17}
$$

with $y_{ni} = y_{in}$, $y_{nn} = 0$. It is noticed that (7.16) is a general admittance matrix, and it can also be applied to a system with many branches in a bus. In the model of Fig. 7.18, since there are no connections between bus 1 and 3, 4 $\ldots n$, it follows that $Y_{13} = Y_{31} = \ldots Y_{1n} = Y_{n1} = 0$; similar results apply for other nodes.

Based on (7.16), the output and input impedances at any node can be derived. Taking bus 2 as an example, the following illustrates the calculation of Z_{Left2} and Z_{Right2} in Fig. 7.18. By separating the network in Fig. 7.18 into two parts, as
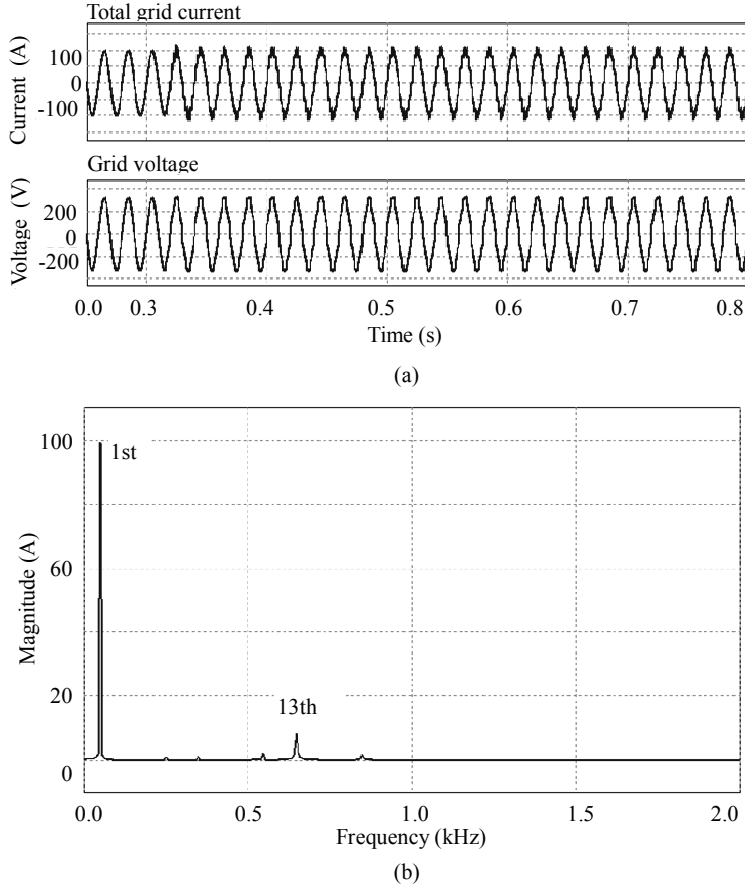
Figure 7.21: Simulation results of the system in Fig. 7.18 with 10 inverter modules: (a) total grid current and the grid voltage, and (b) harmonic spectrum of the total grid current at the period of 0.7s to 0.8s.

shown with the two dashed lines at bus 2, the admittance matrix (7.16) should be also separated as

$$\begin{bmatrix} I_1 \\ I_2 \end{bmatrix} = \begin{bmatrix} Y_{11} & Y_{12} \\ Y_{21} & Y_{22} \end{bmatrix} \begin{bmatrix} V_1 \\ V_2 \end{bmatrix}, \tag{7.18}$$

or

$$\boldsymbol{I}_{1,2} = \boldsymbol{Y}_{1,2} \boldsymbol{V}_{1,2} \tag{7.19}$$

and

$$\begin{bmatrix} I_2 \\ I_3 \\ \vdots \\ I_n \end{bmatrix} = \begin{bmatrix} Y_{22} & Y_{23} & \cdots & Y_{2n} \\ Y_{32} & Y_{33} & \cdots & \vdots \\ \vdots & \vdots & \ddots & \vdots \\ Y_{n2} & Y_{n3} & \cdots & Y_{nn} \end{bmatrix} \begin{bmatrix} V_2 \\ V_3 \\ \vdots \\ V_n \end{bmatrix}, \tag{7.20}$$
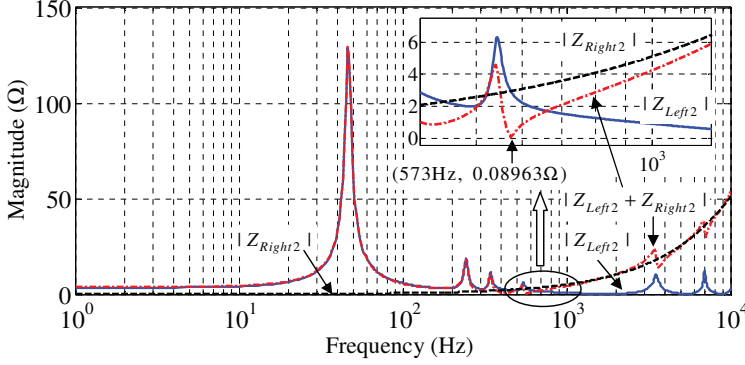
Figure 7.22: Frequency responses of the impedance Z_{Left2}, Z_{Right2}, and the sum of both impedances at bus 2 of Fig. 7.18, when 16 inverter modules are connected.

or

$$\boldsymbol{I}_{2,n} = \boldsymbol{Y}_{2,n}\,\boldsymbol{V}_{2,n}. \tag{7.21}$$

Because the connections at bus 2 in this new representation have been changed, the value of Y_{22} should be updated with $Y_{22} = y_{21}$ for (7.18) and $Y_{22} = y_{20} + y_{32}$ for (7.20).

From (7.19) and (7.21) the bus voltages can be solved as

$$\boldsymbol{V}_{1,2} = \boldsymbol{Z}_{1,2}\boldsymbol{I}_{1,2}, \tag{7.22}$$

$$\boldsymbol{V}_{2,n} = \boldsymbol{Z}_{2,n}\boldsymbol{I}_{2,n}, \tag{7.23}$$

where $\boldsymbol{Z}_{1,2} = \boldsymbol{Y}_{1,2}^{-1}$, $\boldsymbol{Z}_{2,n} = \boldsymbol{Y}_{2,n}^{-1}$. As a consequence, the values of the impedances at bus 2 are now found to be

$$Z_{Right2} = [\boldsymbol{Z}_{1,2}]_{(2,2)}, \tag{7.24}$$

$$Z_{Left2} = [\boldsymbol{Z}_{2,n}]_{(1,1)}, \tag{7.25}$$

leading to the equivalent circuit model in Fig. 7.19, where I_{eq2} represents the contribution of all the sources. For the study of harmonic quasi-resonances, only the values of Z_{Left2} and Z_{Right2} are essential, as shown in the next section.

7.6.2   Resonance analysis and simulation results

With the above method, the input and output impedance at bus 2 is calculated in order to observe possible quasi-resonance in the system of Fig. 7.18, when connecting different numbers of inverters to the grid. For simplification, feeder impedances between each pair of adjoining buses are set to the same values (R = 0.01 Ω and L = 0.01 mH); each lumped load is configured with 3 μF equivalent capacitance; and all the inverter related parameters are the same as presented in the previous section. For simulations, the grid voltage is programmed with odd harmonics (no multiples of 3) from 5 to 25 according to Table 7.3.
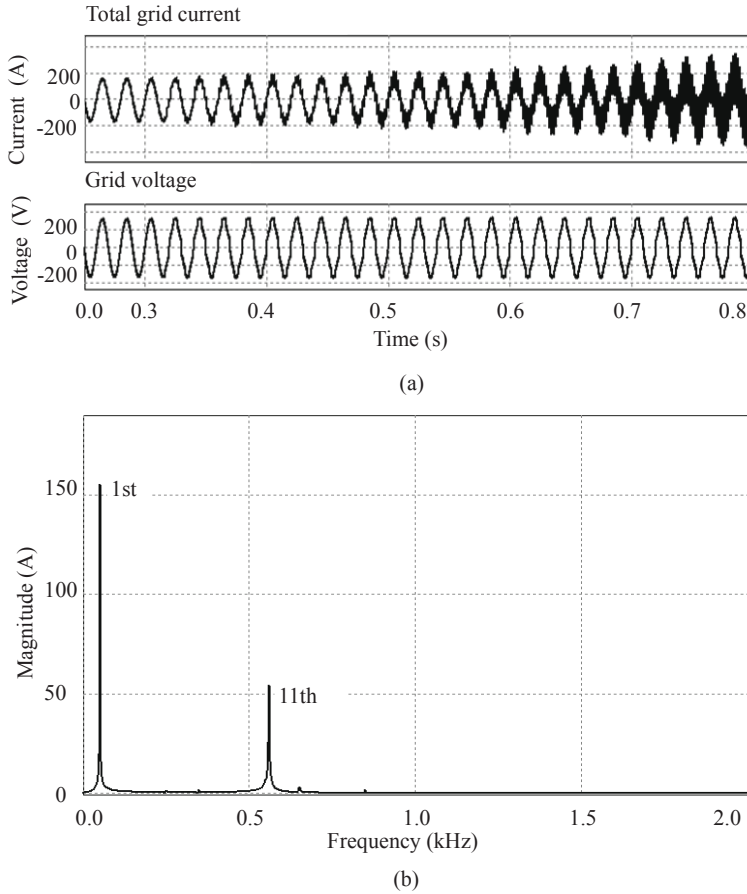
Figure 7.23: Simulation results of the system in Fig. 7.18 with 16 inverter modules: (a) total grid current and the grid voltage, and (b) harmonic spectrum of the total grid current at the period of 0.7s to 0.8s.

Connecting 10 inverter modules to the grid results in a bus number $n = 11$ in Fig. 7.18. The resulting characteristics of Z_{Left2} and Z_{Right2} are shown in Fig. 7.20, as well as the sum of both impedances. It can be seen that the lowest magnitude of $Z_{Left2} + Z_{Right2}$ is 0.25Ω at 625Hz, that is near to 13th harmonic. According to Section 7.4.2, the current harmonic introduced by the background voltage harmonic at this frequency will be amplified. Based on the average circuit model, simulation results for the 10 modules together are presented in Fig. 7.21, showing that the grid current is amplified around the 13th harmonic, when the grid voltage is programmed to start being distorted at 0.32 s.

Furthermore, by connecting more and more modules to the grid, the impedance analysis forecasts that with 16 modules or higher, series quasi-resonance may occur. Indeed, Figure 7.22 shows that a quasi-resonance appears at 573Hz close to the

11th harmonic. Corresponding results are found in simulations. As shown in Fig. 7.23 (a), the current starts resonating when the programmed grid voltage becomes distorted at 0.32 s. The harmonic spectrum in Fig. 7.23 (b) also shows a large current increase around the 11th harmonic.

7.7   Conclusions

This chapter has introduced an analytical approach for the analysis of harmonic interaction/resonance problems of DG inverters in polluted grids.

To analyze the harmonic distortion impact of an individual inverter in a distorted grid, a method based on inverter output impedance has been proposed. By modeling the output impedance of two inverters, one with single-loop PI control and another with dual-loop multiple PR controllers, their harmonic interactions with a distorted grid have been effectively analyzed. Consequently, in order to mitigate harmonic interaction in a distorted grid, the concept of output impedance limits has been proposed as a design constraint for grid-connected inverters.

Furthermore, the output impedance based method has been extended from the case of a single inverter, to a microgrid connected to multiple inverters for analyzing potential resonant problems. Results obtained from modeling, analysis and simulations show that the proposed method is a simple and effective way for estimating harmonic resonance problems.

Finally, it is suggested that experiments could be carried out to further examine the effectiveness and accuracy of the proposed method. Besides, as the output impedance modeling has only been investigated based on inverters with linear controllers, further study on nonlinear control based inverters could be done by using the analytical approach proposed in this chapter.

Part IV

System-level concepts and implementation

Chapter 8

Converter systems with enhanced voltage quality

Abstract - Part III has presented grid interactions of distributed power generation, with the focus placed mainly on the effects at the grid side. In this chapter, system-level studies on voltage quality enhancement at both the user side and the grid side are carried out. Therefore, issues about system configuration, functionalities, and realization are the main points to be addressed.

First, by adapting the conventional series-parallel structure, a couple of grid-interfacing system topologies are proposed for the purpose of DG applications, voltage quality enhancement, and flexible power transfer. As a consequence, the functionality of the proposed systems is also reconfigured in order to ease the control design and to improve overall system performance, differing from existing series-parallel structure based systems. Simple comparison shows that the proposed systems in this chapter are more preferable to the shunt-connected systems.

Next, experiments with a concrete laboratory system are given to detail the proposed concepts and to demonstrate the practical implementation. Two three-phase four-leg inverters, together with dc micro-sources and nonlinear loads, are employed to construct a general series-parallel grid-interfacing system module. Through the introduction of multi-level control objectives, it is illustrated that the proposed system could ride through voltage disturbances and continue the power transfer to/from the grid, while a high quality voltage is maintained for the local loads within the system module. In addition, the system also shows the possibility to achieve auxiliary functions such as grid unbalance correction and harmonic current compensation at the grid connection point.

To achieve these objectives, the control of the series-parallel converter is essential. Hence, the main design aspects of the two controllers are specified later on. The entire system control is effectively validated on the laboratory setup.

8.1   Introduction

Concern for power quality problems is urgently growing. High power quality service from the utility grid is demanded by sensitive loads. Stricter standards are required for end-user equipment, especially for power electronic devices [118], and many solutions are required for power quality improvement either from the utility side or the customer side [14].

Facing the emerging application of distributed generation (DG), that is the generation of electricity dispersed throughout the power system, power electronic-based grid-interfacing converters play an important role between the DG and the utility grid. Usually grid-interfacing converters only manage to deliver electrical energy to the utility grid and controls the power transfer in a normal grid condition, but they are not ready for enduring various voltage quality problems. In turn, a number of important power quality issues may be induced.

In order to deal with disturbed grid conditions in a future scenario with high penetration of DG systems, additional techniques should be taken into account. It has been implicated that power electronics-based converters not only can service as interfaces with the utility grid, but also have the potential for handling power quality problems [90]. Some auxiliary functions such as active filtering have been reported [28]. Other works such as voltage unbalance compensation, grid support, and ride-through control under voltage dips have been presented in Part III.

This chapter focuses on system-level implementation of voltage quality enhancement at both the user side and the grid side. From a future application point of view, aggregated DG units or systems should be flexibly and smartly controlled. Specifically, in addition to the function of delivering energy between DG systems and the utility grid, additional auxiliary functions can be integrated into the proposed distributed grid-interfacing system modules. These functions could be voltage unbalance correction, harmonic current compensation at the grid connection point, protection of local systems from grid disturbances, etc.

Starting with the possibilities of future grid-interfacing systems, this chapter adopts the conventional series-parallel structure to construct a grid-interfacing converter system. By reconfiguring the system functionalities, a versatile power electronics-based interface is derived for DG applications, voltage quality enhancement, and flexible power transfer [44].

8.2   System structure and functionalities

This section presents a possible system configuration based on the conventional series-parallel structure and, moreover, retailors the functionality of the adopted system. The features of the proposed system are discussed in terms of system structure, control objectives, and micro-grid applications.

8.2.1   Series-parallel grid-interfacing systems

A general structure consisting of two converters, one in series and the other one in parallel with the grid, has conventionally been used for power quality regulation or
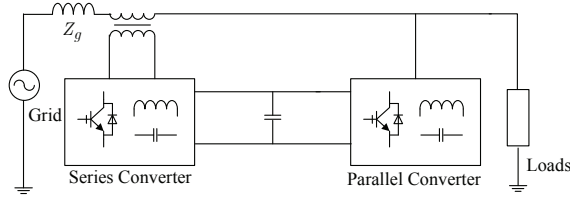
Figure 8.1: Single-line diagram of a conventional series-parallel structure.

power flow control in transimission and distribution systems [10, 11, 119]. Figure 8.1 shows the single-line diagram of the conventional series-parallel structure. The capacitor between the series and parallel converters serves as a common dc bus.

Normally, three-phase three-wire or four-wire inverters with output filters are used as the converters. Because the parallel converter and the series converter are coupled at the dc side, for the series converter, isolation transformers are required to connect with the grid. The function of the transformer for voltage step up is not considered, because the parallel converter would then also need one. The same series-parallel structure can be found in single-phase applications; this work focuses on three-phase systems.

Based on the conventional structure in Fig. 8.1, the system structure can be reconfigured by combining distributed sources and energy storage. As shown in Fig. 8.2 (a), a simple adaption for DG systems is derived by powering the dc bus with distributed sources. Again, the isolation transformers are needed for the series converter. A similar structure was studied in a line-interactive UPS system [12] and a combined operation of unified power quality conditioner (UPQC) with rectified dc bus [13].

Furthermore, by implementing isolated dc/dc conversion techniques such as multi-port converters [92], the series and parallel converters can be isolated at the dc side, as shown in Fig. 8.2 (b). As a result, those expensive and bulky isolation transformers can be left out. Alternatively, as illustrated in Fig. 8.2 (c), the series and the parallel converters can be supplied by independent primary sources and energy storage.

It is noticed that the series-parallel topology is a right-shunt structure, which enables multiple converters to be paralleled and therefore to construct a micro-grid. Hence the series inverter can be regarded as an interface/solid-state switch to connect the micro-grid into the grid or to couple two micro-grids, performing as a power flow controller and a fault protection device. Figure 8.2 (d) shows an example of the series-parallel system applied for interfacing a micro-grid to the utility grid.

8.2.2 Flexible control objectives

Systems based on the series-parallel structure can offer different functionalities because of the degrees of freedom brought by the series and parallel converters. One example is the well-known UPQC that regulates the ac-bus voltage of critical
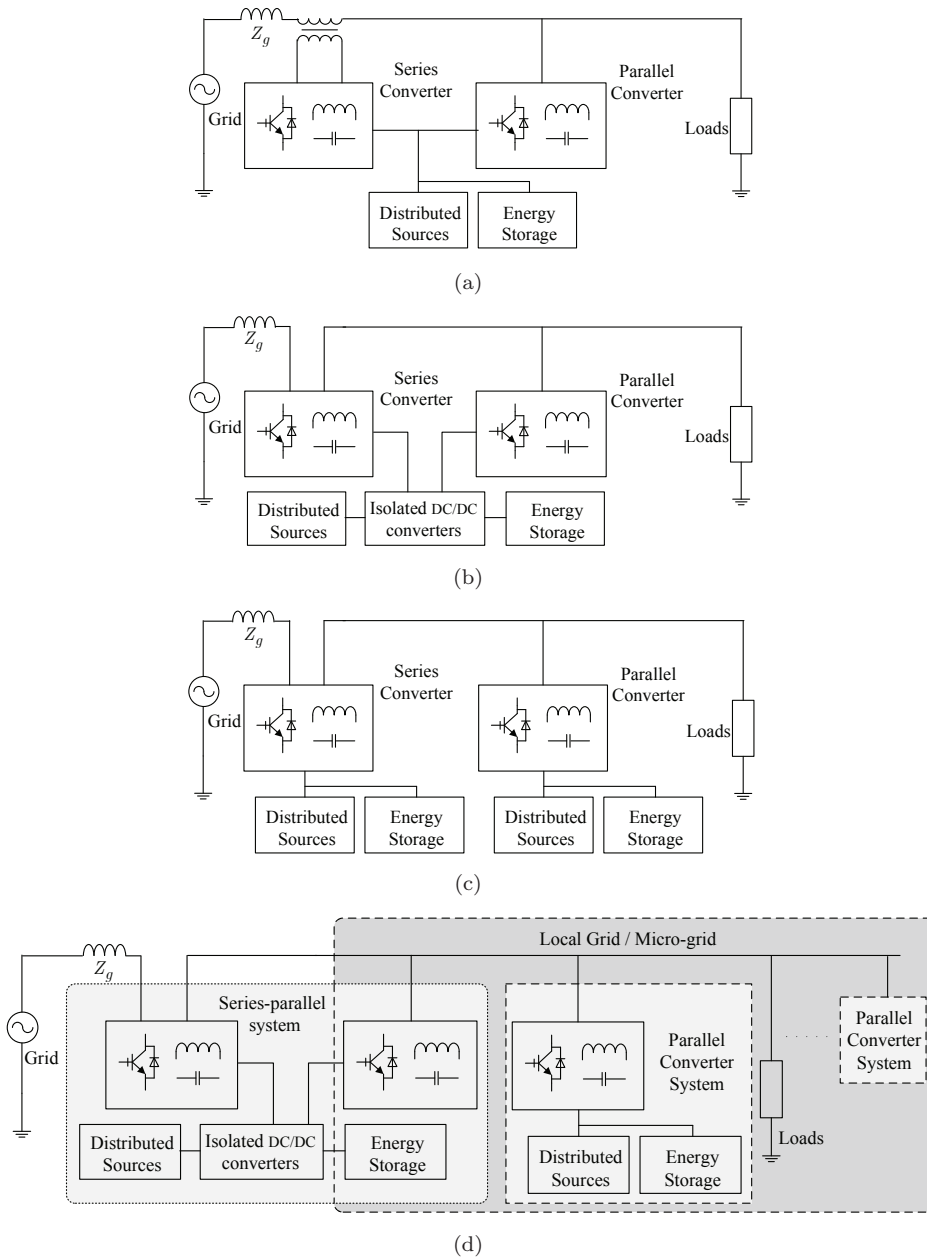
Figure 8.2: Single-line diagrams of the adapted series-parallel structure: (a) common distributed sources powered dc bus, (b) common distributed sources powered dc bus with isolation techniques, (c) independent distributed sources powered dc bus, and (d) an example of the the series-parallel structure applied for coupling the utility grid and a local grid/micro-grid.

loads against voltage unbalance, harmonics, and other disturbances occurring in a distribution network [10, 11, 89]. Technically, the series converter is controlled as a voltage source to compensate voltage disturbances from the grid so as to maintain voltage of good quality at the load side. The parallel converter is designed as a current source mainly for the compensation of the negative-sequence, zero-sequence, and harmonic current components drawn by the loads, thereby achieving balanced and sinusoidal current that flows into the grid.

However, when the voltage of the grid collapses to a low value, the UPQC system may fail to draw the required amount of power to maintain the dc bus. To deal with larger grid voltage dips or even interruptions, the dc capacitor must be replaced by an energy storage (e.g., supercapacitor, battery, etc.). As an alternative, in [13] a distributed source was used to power the dc bus of the UPQC, and that is the structure shown in Fig. 8.2 (a). The series and parallel converters operate exactly the same as the conventional UPQC in the grid-connected mode. When the grid voltage interrupts, the series converter disconnects from the grid, and the parallel converter behaves as a voltage source to power the local loads in islanding mode, providing an uninterruptible service.

It can be seen that the system in [13] is suitable for improving the power quality at the grid connection point of an independent customer system. Moreover, assuming that the customer system is a micro-grid (e.g., the topology in Fig. 8.2 (c)), the parallel converters have to work cooperatively for the power sharing among multiple DG systems in islanding mode.

To facilitate the power sharing between the parallelled converters in the micro-grid and to smooth the switching between grid-connected mode and islanding mode, the authors in [41, 42] proposed a unique control strategy to enhance the power quality of a micro-grid. The parallelled converters maintain balanced voltage for the local loads and dispatch power to the utility grid or within the micro-grid. The series converter is responsible for keeping balanced grid currents by injecting negative- and zero-sequence voltages to compensate grid voltage unbalance, and to limit fault current when grid voltage dips. The entire system control requires complicated changing sequence of control functions [41, 42]; and the output voltage of the parallel converter is disturbed during the voltage dip transient, which could still be a problem for some critical loads.

8.2.3   Reconfiguring system functionalities

Clearly, flexible control objectives depend on various system functionalities. Differing from the solutions in the previous subsection, the next intends to decouple the roles of the series and parallel converter so as to optimize their control performance. Figure 8.3 shows a circuit representation of the proposed system, where the subscript '1' denotes fundamental components, 'h'-harmonic components, 'g'-grid, 's'-series converter, 'p'-parallel converter and 'ld'-loads; the superscript '+' represents positive-sequence components and '-' the negative-sequence components [1]. The series converter performs current control for regulating harmonic, fundamental positive- and negative-sequence currents; the parallel converter performs

---

[1]Zero-sequence components may also exist in four-wire systems, but are not indicated here.
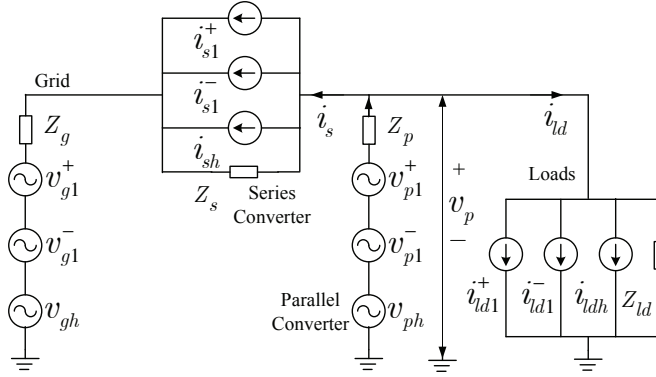
Figure 8.3: A circuit representation of the proposed series-parallel converter system in terms of voltage and current sources.

voltage control for maintaining sinusoidal and balanced voltage v_p under nonlinear/unbalanced load conditions. Supposing the series inverter is well controlled, the utility grid can also be regarded as a load for the local micro-grid, but the power flow is bidirectional.

Power transfer between the grid and the local grid relies on the control of the series converter, while the reference/demanding power has to be determined based on the capacity of the local system and the power demand from the distribution grid. Data communication therefore is important for the series inverter to get realtime demands from the user or supplier. However, the network-scale communication and computation of realtime reference commands are out of the scope of this work, and this chapter mainly addresses the realization of the base-level power electronic system [2].

Certain aspects concerning inverter parallel operation within the micro-grid have been recently studied in [121–123]. Because the main task of this work is the series-parallel grid-interfacing concept, the study of power sharing among multiple parallel converters is not considered.

Therefore, in the lab system, only one parallel converter is used and for simplicity the dc bus is shared by the series and the parallel converters, resulting the system topology shown in Fig. 8.2 (a).

8.2.4   Comparison with shunt-connected systems

At first glance, the series-parallel structure in Fig. 8.2 is much more complicated and expensive than the shunt-connected system in Fig. 8.4 when the parallel-converter number n=1. Therefore, it is necessary to make a fair comparison based on system functionality.

---

[2]As a kind of future structure for the smart grid, the data communication between the distribution grid, the local micro-grid and the series converter can be done by "networked intelligence" that is also the concept in smart-grid [120].
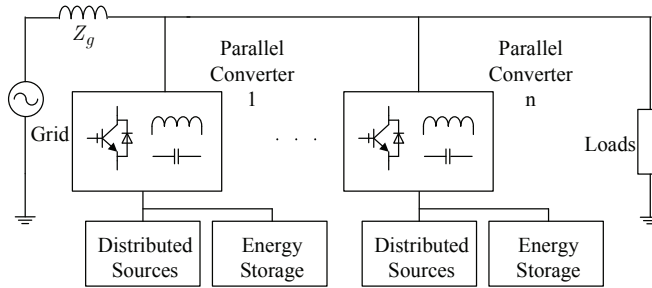
Figure 8.4: Single-line diagram of shunt-connected systems.

First, assuming that the parallel converters in all the strucutres of Fig. 8.2 and the shunt converters in Fig. 8.4 have the same ratings, a comparison can be made between the two systems in term of the required amount of converters.

Therefore, in order to maintain voltage of good quality for the local loads, at least two shunt converters are required for the shunt-connected system in Fig. 8.4. One is the same as the parallel converter in the series-parallel system for supplying the local loads or the grid with a certain amount of power based on the distributed sources; the second one must be used for regulating the voltage under disturbed grid conditions. Considering that the feeder could be inductive over-head lines or resistive underground cables, all the converters used for compensation are installed with primary sources so as to inject active or reactive power for voltage regulation. Although the two shunt converters can be combined into one larger-power converter in practice, the hardware cost can roughly be considered twice the cost of one low-power converter.

Also, it should be realized that, due to the low feeder impedance, the voltage regulation of the shunt converter by means of power/current injection could require higher current rating for the converter and generate more power losses than the method of voltage injection by the series converter. Concerning the isolation transformers used by the series converter, as mentioned earlier, the proposed structures in Fig. 8.2 provide alternatives to avoid these expensive and bulky transformers. This is a significant difference from the conventional series-parallel structure used by systems like UPQC.

Moreover, the series converter normally works with low output voltage (around the voltage difference between two synchronized grids, i.e., the utility grid and the local system), so its power capacity could be smaller than the shunt converter. It could be expected that when the series-parallel system is applied for interfacing micro-grids, the cost of the series converter, even with the isolation transformers, would still be reasonable compared to the total cost of a micro-grid.

As already discussed in the previous subsections, the proposed series-parallel system can achieve very flexible control objectives because of the independently controllable voltage and current sources. The shunt-connected system, however, can only easily improve current quality by controlling the injected currents. For voltage regulation, it has to deliver a large amount of active or reactive power and
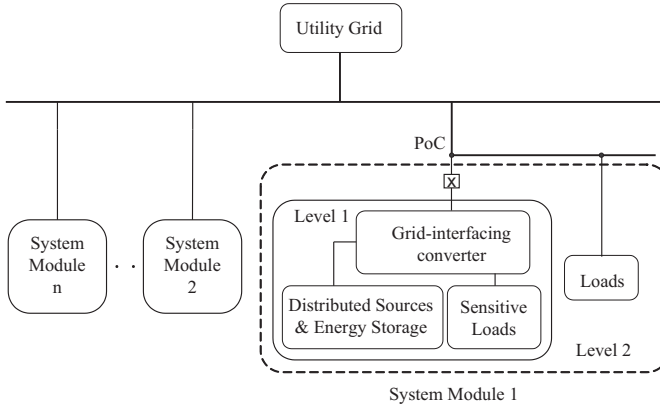
Figure 8.5: Proposed modular system structure.

could even be ineffective if the feeder impedance is too low.

Therefore, as a solution applicable for DG applications, voltage quality enhancement, and interfacing micro-grids, the proposed series-parallel grid-interfacing system is more preferable to the shunt-connected system.

8.3   System module

Looking at a large scale network, it is desirable that distributed grids or micro-grids including the series-parallel grid-interfacing systems can be integrated as a system module in order to facilitate network-scale management. A concept for this purpose is presented in this section.

Modular system

Figure 8.5 shows the proposed modular system structure. The modules are divided into two levels. The fundamental unit of the first level, consisting of series-parallel grid-interfacing converters, distributed sources, energy storage, and so-called sensitive loads, is connected to the utility grid at the point of connection (PoC). The reason to point out sensitive loads within the unit is to emphasize the demand for a continuous and balanced sinusoidal voltage.

Above this first level, some loads could be present at the PoC. These loads are not sensitive to power quality problems and do not require uninterruptible power. The configuration of the system module 1 in Fig. 8.5 could be, for example, a DG-backed office building or community, where computer systems are regarded as the sensitive loads. Other loads, possibly nonlinear, are put on the second level.

PWM converter

To configure the system module for more general applications, a four-leg converter is used as the basic PWM converter unit for a case study on three-phase four-wire
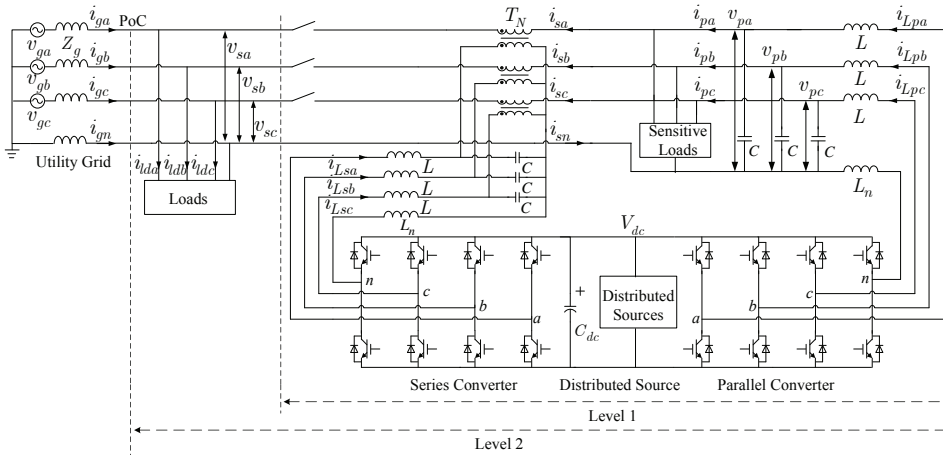
Figure 8.6: Employed configuration of the system module.

systems. Because of the extra degree of freedom brought by the fourth-leg of the structure, the outputs of the three phases become independent. As a result, a balanced output voltage can be achieved for unbalanced loads, and the neutral current in an unbalanced or distorted utility situation can be handled.

Module configuration

With the four-leg converter as the basic unit, the whole module configuration is illustrated in Fig. 8.6. Two levels of the system module are correspondingly identified according to Fig. 8.5.

8.4 Multi-level control objectives

Based on the system structure in Fig. 8.6, it is desirable to maintain good voltage quality for the sensitive loads and to improve the power quality at the grid side. Starting from the base level, through the second level, and then reaching the modular system level, different control objectives are specified as follows.

Level 1

The aim of the first level in Fig. 8.6 is mainly voltage quality enhancement for the sensitive loads within the system module, and bidirectional energy transfer under disturbed grid conditions. Appropriate separation of the series and parallel converter roles can ease the control design of the two converters and optimize the system overall performance.

Specifically, the parallel converter works as a voltage source so as to provide balanced and sinusoidal voltage under asymmetrical and nonlinear load conditions. As a benefit, it can easily switch to the islanding mode and offers uninterruptible
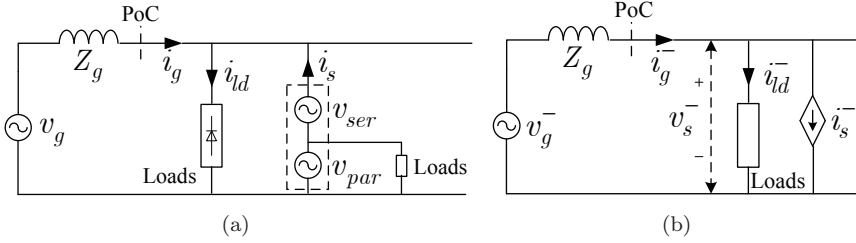
Figure 8.7: Per-phase equivalent diagrams of system auxiliary functions: (a) active filter function and (b) grid unbalance compensation (the superscript '-' denotes negative-sequence components).

service when the grid voltage interrupts. Besides, the output voltage of the parallel converter is synchronized with the fundamental positive-sequence component of the grid voltage in order to minimize the voltage across the series converter, especially when the grid voltage is disturbed.

Power flow control is achieved by the series converter. When disturbances appear in the grid voltage, the module can still deliver power between the grid and the local system. For instance, with the proposed power control strategies in Chapter 5 and 6, the system can ride through unbalanced voltage dips. In other words, the series converter also protects the local system from disturbed grid voltage problems.

Level 2

Coming to the second level, some loads, which are not sensitive or critical but may produce current harmonics, can be located behind the PoC, as shown in Fig. 8.6. By detecting the harmonic components of the load current $i_{lda,b,c}$, the series-parallel system can act as an active filter to prevent low-order current harmonics from flowing through the utility grid, while high-order harmonic currents can be easily removed by adding passive filters if necessary.

In this situation, the grid-interfacing converter resembles a current source connected in parallel with the loads. As illustrated in Fig. 8.7 (a), v_{par} denotes the output voltage of the parallel converter, and the series converter controls the current flow i_s by injecting the series voltage v_{ser}. It should be noticed that this extra active filter function requires a higher rating for the converters since the harmonic currents increase the rms value of the total current.

System Level

Furthermore, it is possible to integrate voltage unbalance correction on the system level. Each of the system modules in Fig. 8.5 can help decrease the negative-sequence voltage at the PoC if the grid appears unbalanced. In Chapter 4, it has already been discussed that how to correct voltage unbalance by using multiple modules working together in a coordinated manner. For the sake of clarity, the principle of the proposed control methods is briefly repeated here.

With the theory of symmetric decomposition for three-phase systems, an equivalent circuit model for sequence voltages can be derived. The diagram for negative-sequence components is shown in Fig. 8.7 (b). Voltage v_g^- and v_s^- are the negative-sequence voltages of the utility grid and PoC, respectively. Current i_s^- is the negative-sequence current from the grid-interfacing system. By controlling the amplitude and phase of the negative-sequence current i_s^-, the negative-sequence voltage v_s^- can be compensated through the voltage drop across the line impedance.

8.5   System control design

Figure 8.8 shows the overall control structure of the series-parallel system, which consists of reference signal generation and two individual controllers. A basic block, the symmetric-sequence voltage detection and synchronization (see Chapter 2), is essential to determine the fundamental positive- and negative-sequence voltage, as well as the grid frequency. This information is important for both converters in order to synchronize with the grid and to design control reference signals.

8.5.1   Overall control structure

As shown in Fig. 8.8 (a), based on the fundamental positive-sequence grid voltages $(v_{\alpha 1}^+, v_{\beta 1}^+)$ derived in the stationary frame, the amplitude conversion block first shapes the signals to per-unit quantities and then generates a set of reference signals $(v_{p\alpha}^*, v_{p\beta}^*)$ with a specified amplitude for the parallel converter.

The series converter, as mentioned in the previous section, is applicable for achieving multi-level control objectives. Hence, the block "function selection and combination" in Fig. 8.8 (b) indicates that different objectives can be integrated into the system by choosing appropriate reference signals $i_{s\alpha}^*, i_{s\beta}^*, i_{s\gamma}^*$. Details about the unbalance correction scheme, which is used to generate current reference for negative-sequence voltage compensation, have been presented in Chapter 4. For the power control strategy, which are used to obtain desired currents for active/reactive power transfer, please refer to Chapters 5 and 6.

The active filter function is represented by the block "low-order harmonics filter". With the filtering techniques presented in Chapter 2, references of low-order current harmonics, denoted by $i_{s\alpha h, s\beta h, s\gamma h}^*$, can be obtained.

In order to track the desired reference signals, the rest of this section presents the main design aspects of the series and parallel converter control.

8.5.2   Control of the parallel converter

The control diagram of the parallel-converter is shown in Fig. 8.9, where the sampling and transfer delay of the control is considered and represented by e^{-sT_d}. System parameters are provided in the section of experimental results. Simplifying the inverter to have a unity gain, the average model of the α-quantities in the proposed control scheme is shown in Fig. 8.10. In the stationary frame, the α, β, and γ quantities are decoupled and their control designs are similar. For details on
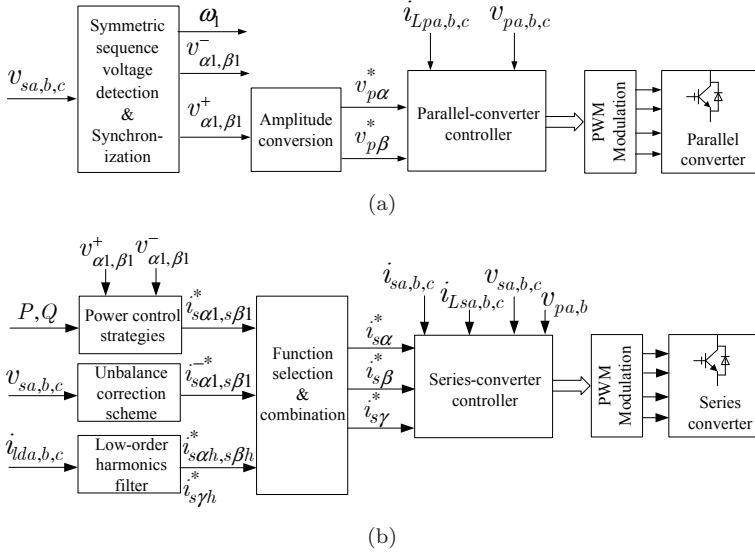
Figure 8.8: Block diagrams of the overall control structure: (a) the parallel converter and (b) the series converter.

the modeling of four-leg converters in the stationary-frame and the reference-frame transformations, please refer to Chapter 3.

System instability improvement

A voltage feedforward loop can usually be used to improve system dynamics. It is shown in this section that this loop can also eliminate the instability of parallel converters under no-load conditions.

When the parallel converter is not connected to local loads and also does not deliver power to the grid, the output current $i_{p\alpha}$ in Fig. 8.10 equals to zero. The transfer function of the physical plant (from the inverter output v_α to the filter output $v_{p\alpha}$) in Fig. 8.10 can be expressed as

$$G_{pl}(s) = \frac{v_{p\alpha}}{v_\alpha} = \frac{Z_C}{Z_L + Z_C}, \tag{8.1}$$

with $Z_L = sL + R_L$ and $Z_C = R_C + \frac{1}{sC}$, where R_L and R_C are the equivalent series resistors (ESR) of L and C, respectively.

Taking into account the sampling and transfer delay in the feedforward loop, it follows that

$$F_{v\alpha}(s) = K_{ff}\mathrm{e}^{-sT_d} \approx K_{ff}\frac{1 - sT_d/2}{1 + sT_d/2}, \tag{8.2}$$

where K_{ff} is the forward gain, and the time delay e^{-sT_d} is rewritten based on the Pade approximation with T_d set to one sampling period.
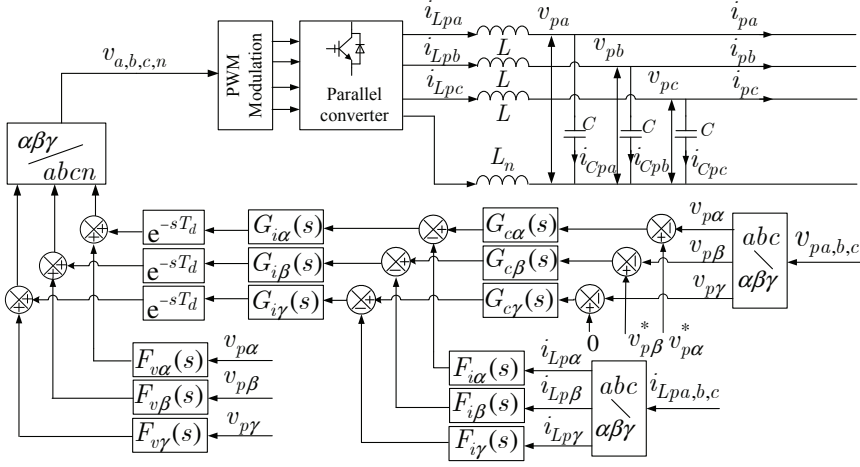
Figure 8.9: Control diagram of the parallel converter.
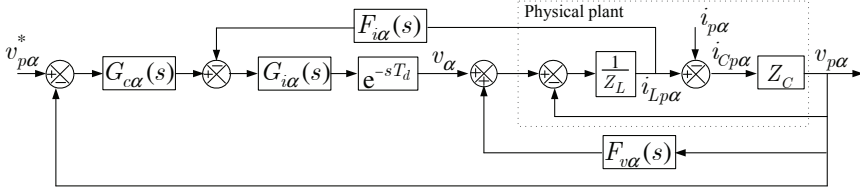
Figure 8.10: Block diagram representation of the α-quantities in Fig. 8.9.

In order to observe the effect of the feedforward loop on the physical plant, the inductor current control-loop is excluded by setting $F_{i\alpha}(s) = 0$ in Fig. 8.10. Therefore, after including the voltage feedforward loop, the transfer function from v_α to $v_{p\alpha}$ is obtained as

$$G_{pl-ff}(s) = \frac{v_{p\alpha}}{v_\alpha} = \frac{G_{pl}(s)}{1 - G_{pl}(s)}. \tag{8.3}$$

Frequency responses of $G_{pl-ff}(s)$ are plotted with different K_{ff} in Fig. 8.11. It can be seen that when $K_{ff} = 0$, that is $G_{pl-ff}(s) = G_{pl}(s)$, a sharp increase of the amplitude and a $180°$ phase-shift appear at the resonance frequency of the LC filter tank. This limits the control bandwidth and also makes the controller design difficult. If the parallel converter is designed with a bandwidth beyond or closed to this resonance frequency, it may have instability problems at no-load conditions.

When $0 < K_{ff} \leq 1$ the resonance is damped because of the feedforward loop, as shown in Fig. 8.11. It should be noticed that when K_{ff} approaches 1 the feedforward loop introduces more and more phase delay at low-order harmonic frequencies and this reduces the system phase margin. Thus, a compromise should be made, as will be presented in the next paragraph.
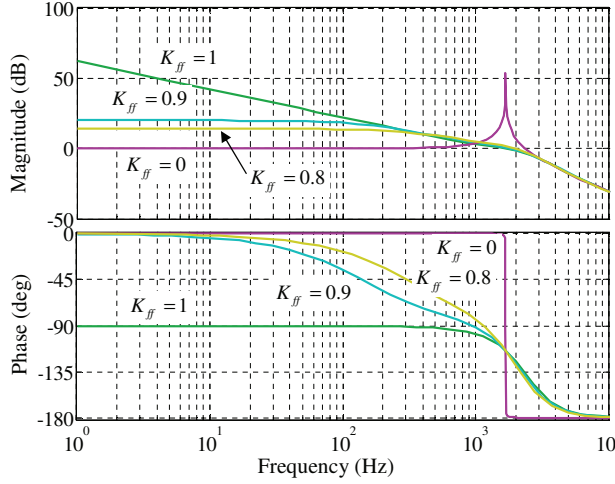
Figure 8.11: Bode plots of the plant transfer function with feedforward loop.

Selective harmonic regulation

Before studying the inner current-loop, the external voltage control-loop is first designed. In order to prevent the output voltage from being distorted under non-linear load conditions, multiple PR controllers (see Section 3.2.2) are employed as compensators for voltage regulation at selected harmonic frequencies, expressed as by

$$G_{c\alpha}(s) = K_P + \sum_{n=1,3,5,7}^{9} \frac{2\omega_{bn}K_{In}s}{s^2 + 2\omega_{bn}s + (n\omega_c)^2}, \tag{8.4}$$

where the resonant terms at 1st, 3rd, 5th, 7th, and 9th harmonics are selected, with $K_P = 0.55, K_{I1} = 50, K_{I3,5,7,9} = 20, \omega_{b1} = 10$ rad/s, $\omega_{b3,5,7,9} = 6$ rad/s, and $\omega_c = 314$ rad/s.

Figure 8.12 shows the bode plots of the open-loop transfer function of the system in Fig. 8.10. By setting $F_{i\alpha}(s) = 0$ and $G_{i\alpha}(s) = 1$, the current loop is still not included. It can be seen that the open-loop gains at selected frequencies are enhanced so as to fully compensate the voltage harmonics at these frequencies. The influences of the feedforward gain K_{ff} on the system open-loop transfer function are also illustrated in Fig. 8.12. It is found that the feedforward loop changes the frequency responses at low-order frequencies. As a compromise, in order to damp the resonance and also to keep the system enough phase margin, K_{ff} is chosen to be 0.8 in this chapter. As shown in Fig. 8.12, the system has a bandwidth of 1.2 kHz and the phase margin is about 20°.

Disturbance sensitivity improvement

The inner current-loop is used to improve system sensitivity to the disturbances on the output current $i_{p\alpha}$. Since the voltage regulation loop plus the feedforward
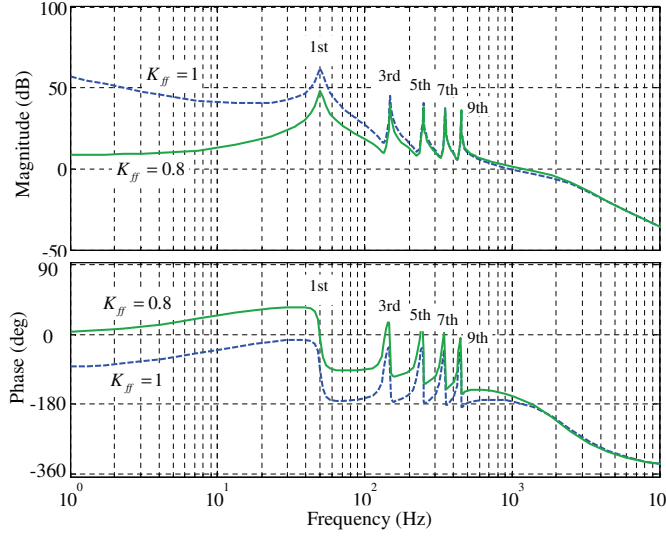
Figure 8.12: Bode plots of the open-loop transfer function of the system in Fig. 8.10, excluding the inner current loop.

loop have already pushed the system bandwidth to 1.2 kHz with a phase margin of 20°, the inner current compensator $G_{i\alpha}(s)$ can hardly increase the bandwidth. In order to maintain the characteristics of the system control at low-order harmonic frequencies, a unity gain is assigned to the inner current regulator, that is $G_{i\alpha}(s) = 1$, and only high-frequency components of the inductor current are sampled. Thus, current feedback loop is expressed as

$$F_{i\alpha}(s) = K_{fI}\frac{s}{s + 2\pi f_{hp}}, \tag{8.5}$$

where K_{fI} is the current feedback coefficient and f_{hp} the high-pass bandwidth.

Hence, based on the block diagram in Fig. 8.10, the system sensitivity to current disturbances can be obtained, i.e.

$$G_d(s) = \left.\frac{v_{p\alpha}(s)}{i_{p\alpha}}\right|_{v_{p\alpha}^*=0}, \tag{8.6}$$

which indicates the response of the output voltage with respect to the change of load current. In Fig. 8.13, the amplitude response of $G_d(s)$ as a function of frequency is plotted, with $f_{hp} = 1$ kHz and different K_{fI}. It can be seen that when the inner current-loop is not included (that is $K_{fI} = 0$) $G_d(s)$ has a very high magnitude at the resonance frequency of the LC filter tank, implying any current disturbance at this frequency will cause large output voltage oscillation. By adding the current loop, the resonance is well damped with different K_{fI} but the magnitudes at low-order frequencies are slightly increased. In the experiment, the current feedback coefficient K_{fI} is set to 4.
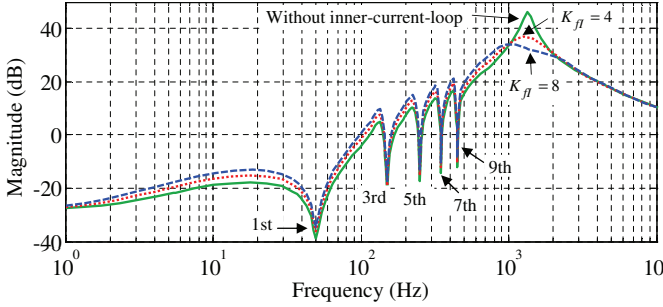
Figure 8.13: System sensitivity to current disturbances.

8.5.3   Control of the series converter

Assuming the parallel converter is an ideal voltage source, the series-parallel structure in Fig. 8.6 can be simplified as a shunt system connected to an equivalent grid, as shown in Fig. 8.14. The voltages of this equivalent grid, v_{spx}, are equal to $v_{sx} - v_{px}$ with x denoting phase a, b, and c. The feeder impedance and the leakage inductance of the transformer in Fig. 8.6 are lumped together as the equivalent grid impedance L_g.

Based on the sensitivity analysis in Fig. 8.13, the parallel converter behaves as a voltage source with a very small internal impedance at the grid frequency and the low-order harmonic frequencies. Therefore, for easing the control design of the series converter within the frequency up to 1 kHz or so, it is reasonable to assume the parallel converter is an ideal voltage source. The control of the series converter is also shown in Fig. 8.14 and the corresponding average model of the α quantities is derived in Fig. 8.15 (a) [3].

It can be seen that a LCL filter structure is formed in between the grid and the series converter. As a third-order system, the LCL-filter can bring instability problems to the control design of the series converter due to its resonance feature. To deal with this problem of system instability, the dual-current-loop control scheme have been implemented in Chapter 2 and 6 for the experiments of shunt-connected inverters. Many other control methods have also been studied in [73, 82, 124–126]. These usually damp the resonances by including an additional control loop or other active damping schemes.

As illustrated in Fig. 8.8 (b), the series converter is designed to achieve multiple control objectives by tracking various current references. In order to improve the system stability and to facilitate the compensator design at low-order frequencies, this chapter adopts a unique method proposed in [126]. This method uses combination of the filtering-inductor current and the grid-side current as the feedback-control variable, in this way degrading the third-order system to first-order.

---

[3]It is noticed that the transfer function of the control loop are denoted by the same symbols used in the control of the parallel converter. However, they are used solely for the presentation in respective subsections.
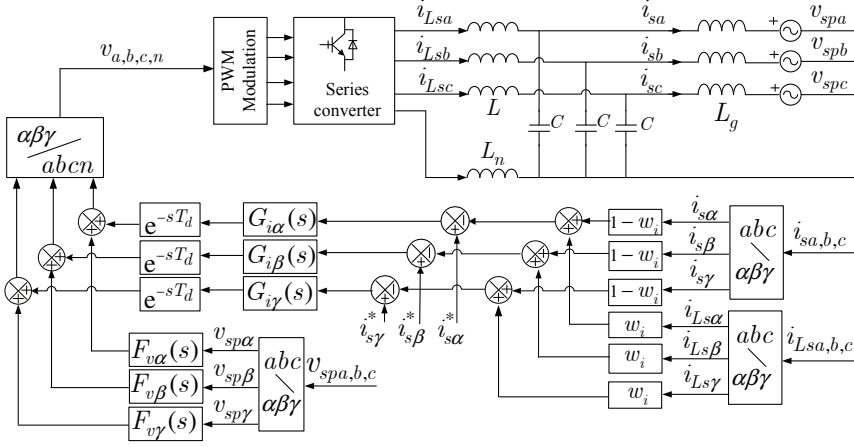
Figure 8.14: Control diagram of the series converter.
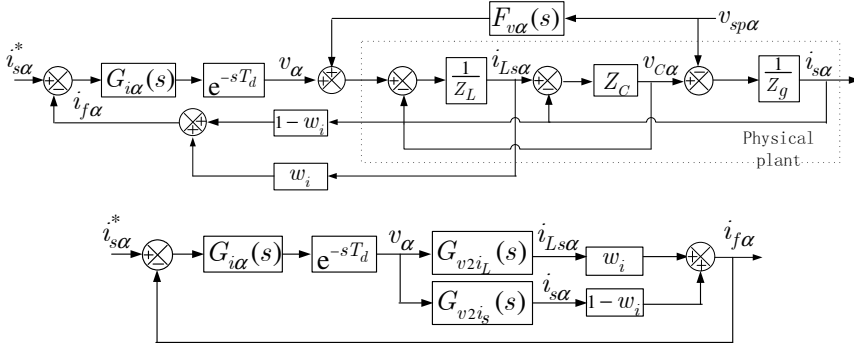
Figure 8.15: Block diagram representation of (a) the average model of the α-quantities in Fig. 8.14 and (b) the small-signal model.

Again, taking the model of the α-quantities in Fig. 8.15 (a) as an example, the control consists of a voltage feedforward loop and a current feedback-control loop. As an additional voltage feedforward loop, it is used to decouple the influence of grid voltage disturbances on the output current $i_{s\alpha}$, thereby improving system dynamics. In this chapter, $F_{v\alpha}(s)$ is simply a unity gain. In the rest of this subsection, only the current feedback-control loop is specified.

Based on small-signal analysis, the model in Fig. 8.15 (b) is derived. Disregarding the ESRs of the inductor and the grid impedance, the transfer function from the inverter output voltage to the inductor current and the grid current are expressed, respectively, as

$$G_{v2i_L}(s) = \frac{i_{Ls\alpha}}{v_\alpha} = \frac{L_g C s^2 + 1}{L L_g C s^3 + (L + L_g)s}, \tag{8.7}$$
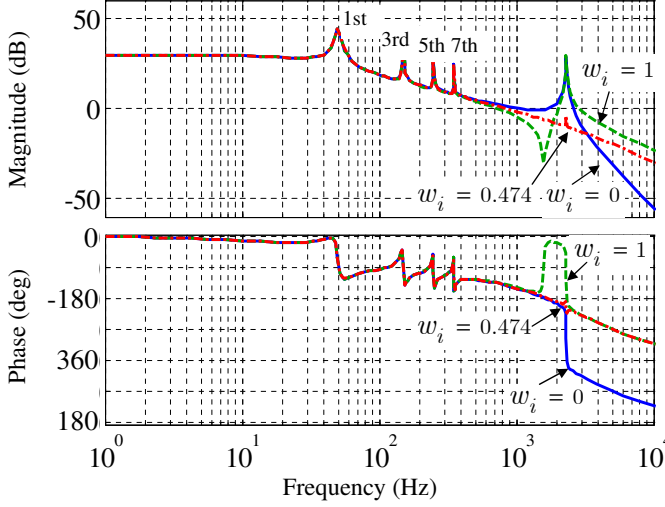
Figure 8.16: Bode plots of the open-loop transfer function of the system in Fig. 8.15.

and

$$G_{v2i_s}(s) = \frac{i_{s\alpha}}{v_\alpha} = \frac{1}{LL_gCs^3 + (L + L_g)s}. \tag{8.8}$$

By introducing a weighting factor w_i for the two currents, as shown in Fig. 8.15, the modified system transfer function from the inverter output voltage v_α to feedback current $i_{f\alpha}$ is obtained, i.e.

$$G_{v2i_f}(s) = w_i \frac{L_gCs^2 + 1}{LL_gCs^3 + (L + L_g)s} + (1 - w_i)\frac{1}{LL_gCs^3 + (L + L_g)s}. \tag{8.9}$$

When $w_i = 0$, the control model in Fig. 8.15 (b) represents grid current feedback control, and when $w_i = 1$, it represents inductor current feedback control.

Defining $L_{sum} = L + L_g$, $w_i = L/L_{sum}$ and substituting them into (8.9) gives

$$G_{v2i_f}(s) = \frac{1}{sL_{sum}}. \tag{8.10}$$

Therefore, the third-order system is turned into a first-order system, implying that the resonance problem is eliminated.

For the purpose of suppressing harmonic currents, the current compensator $G_{i\alpha}(s)$ is designed with the multiple PR controller as in (8.4). In the experiment, the resonant terms are only selected at the 1st, 3rd, 5th, and 7th harmonic frequencies. Corresponding parameters are $K_P = 10$, $K_{I1} = 200$, $K_{I3} = 150$, $K_{I5} = 120$, $K_{I7} = 120$. The other parameters of the PR controllers are the same as in (8.4).

With the system parameters shown in the experimental section, the Bode plots of the system open-loop transfer function are drawn in Fig. 8.16 with different w_i. It is seen that when $w_i = 0$ or 1 high peak amplitudes appear at the resonance

frequency. However, when $w_i = 0.474$ the resonance is almost fully suppressed. Although because of the mismatched ESRs of the inductors it is difficult to achieve a complete elimination of the resonance, the control scheme is still quite effective and can well mitigate the resonance problem caused by the LCL filter.

8.6   Laboratory setup

Figure 8.17 shows the entire laboratory system, which consists of, from left to right, a dc source (representing the distributed source), three-phase ac loads (emulating various load conditions), the parallel converter, the series converter, the grid emulator, and two independent controllers.

The system control platform is shown in Fig. 8.18, and is based on Matlab Simulink and dSpace control interfaces. The entire system has been tested successfully, as proved by the experimental results in the next section.

Concerning the main components of the lab system, specific technical data are given as follows:

Four-leg IGBT module
- Type: SEMIX202GB128D
- IGBT: 1200 V, 190 A (max) @ 25 ^{0}C and 135 A (max) @ 80 ^{0}C
- Typical switching frequency: 10 kHz to 15 kHz (Gate resistor Rg = 6.8 Ω)
- Inverse diode: forward voltage and current (2 V, 150 A) @ 25 ^{0}C

IGBT driver
- Type: SKYPER32
- Gate resistor (min): 2 Ω
- Switching frequency (max): 50 kHz
- Supply and input voltage: 15 V
- Output gate voltage: $V_{gon} = +15$ V and $V_{goff} = $ -7 V

Grid emulator
- Three-phase four-quadrant ac power supply
- Type: SPITZENBERGER+SPIES DM 15000/PAS, 5 kVA/phase

DC source
- Regatron/Topcon power supply, 1000 VDC (max) and 10 kW (max)

Three-phase ac loads
- Type: California Instruments, 3091LD-230 model - Power capacity: 3 kVA/phase

Controller development environment
- dSpace: DS1104 + control-desk/real-time workshop
- Matlab-Simulink
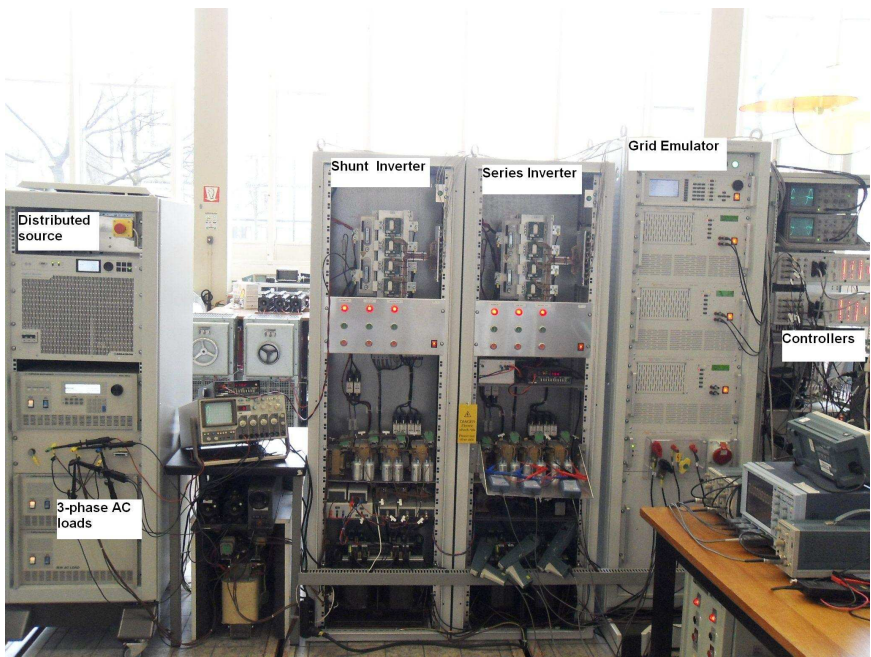
Figure 8.17: Photograph of the laboratory system.

Figure 8.18: Photograph of the developed system control platform.

Table 8.1: System parameters

Description	Symbol	Value
Rated grid voltage	$V_{ga,b,c}$	230V/50Hz
Grid impedance	Z_g	2 mH (ESR 0.628 Ω)
Output inductor	L	1.8 mH (ESR 0.03 Ω)
Output capacitor	C	5 μF
Neutral inductor	L_n	0.67 mH (ESR 0.02 Ω)
Series transformer	T_N	$1:1$
dc-link voltage	V_{dc}	750 V
dc-link capacitors	C_{dc}	4400 μF
Switching frequency	f_{sw}	16 kHz
Sampling frequency	f_{sp}	8 kHz

8.7   Experimental results

The system parameters of the laboratory set-up are listed in Table 8.1, and all the symbols are given with respect to the circuit diagram in Fig. 8.6. The grid impedance includes the leakage inductance of the transformer. The series and parallel converters have identical four-leg IGBT modules and output filters.

Voltage quality improvement under unbalanced/nonlinear loads

First of all, the parallel converter should be able to guarantee the voltage quality for the local loads within the system module, either in the grid-connected mode or in the islanding mode. Therefore, in order to observe the performance of the parallel converter, it is loaded with a single-phase nonlinear load (crest factor 1.8) when the whole system works in the grid-connected mode. Figure 8.19 shows the measured results. The output voltages of the parallel converter are balanced but also distorted when the low-order harmonic compensation is disabled, as shown in Fig. 8.19 (a), and turns out to be of good quality when the selective low-order harmonic compensation (at 3rd, 5th, 7th, and 9th line frequencies) is activated, as shown in Fig. 8.19 (b). Corresponding frequency spectra and the total harmonic distortion (THD) of the phase voltage, which powers the nonlinear load, are shown in Fig. 8.20 (a) and (b).

In addition, the effect of the feedforward gain was also observed. As shown in Fig. 8.21, the parallel voltages appear unstable/oscilating when the feedforward loop gain K_{ff} in (8.2) is set to 1 at the no-load condition. This is because the system phase margin almost reaches zero when $K_{ff} = 1$, as illustrated in Fig. 8.12.

Active filter function

As described in Section 8.4, the system could also offer auxiliary functions such as voltage unbalance correction and active filtering, that is, low-order harmonic current compensation. Since Chapter 4 has already presented the idea and the experimental results of the voltage unbalance correction, only active filter func-
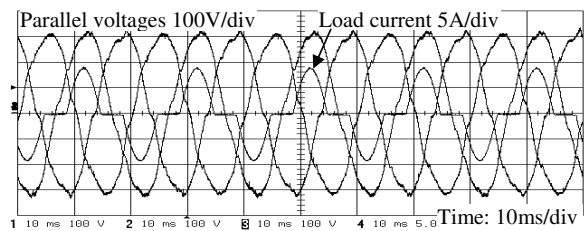
(a)
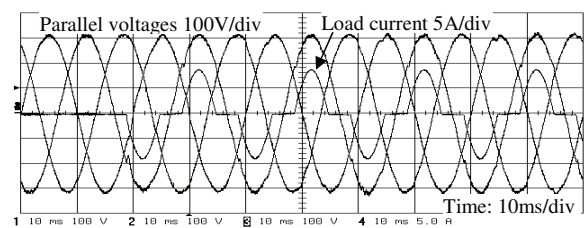
(b)

Figure 8.19: Output voltages of the parallel converter tested under a single-phase nonlinear load: (a) without low-order harmonic compensation and (b) with selective low-order harmonic compensation at 3rd, 5th, 7th, and 9th line frequencies.
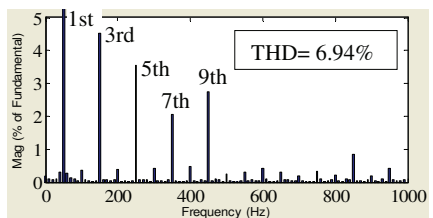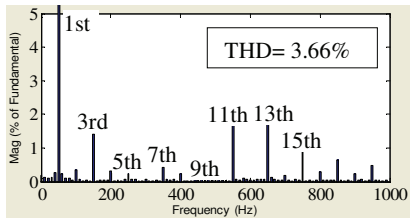
(a)   (b)

Figure 8.20: Frequency spectrums and the total harmonic distortion of the parallel voltage in Fig. 8.19: (a) without low-order harmonic compensation and (b) with selective low-order harmonic compensation at 3rd, 5th, 7th, and 9th line frequencies.
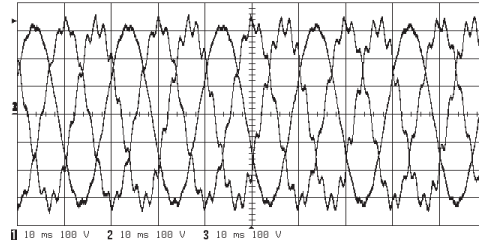
Figure 8.21: The parallel voltages become unstable/oscilating when the feedforward gain is set to 1 at the no-load condition.
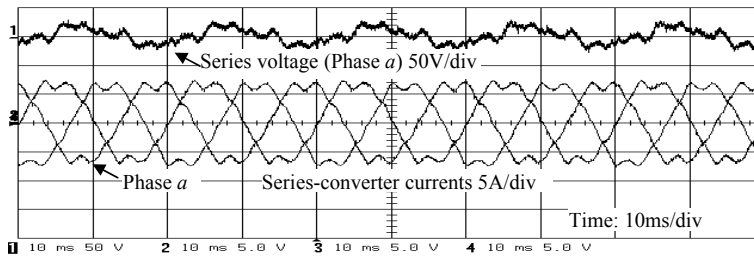
(a)
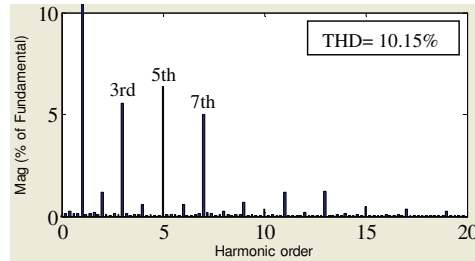
(b)

Figure 8.22: Emulation of the active filter function with low-order harmonic current injection: (a) time-domain measurements and (b) the frequency spectra of the phase current.

tion is intended to be tested here. Therefore, the control objective for the series converter is to enable the system to inject low-order harmonic currents so as to compensate the measured low-order harmonic components of the load currents at the PoC (see Fig. 8.7 (a)).

Due to the limitation of available A/D channels in the dSpace controller, the system was tested by directly imposing certain amplitudes of low-order harmonic current references to the series converter, assuming that the load currents are already known. Figure 8.22 (a) shows the results of the low-order harmonic current injection done by the series converter, emulating the active filter function at selected harmonic frequencies. It can be seen that the series output voltage gets

distorted so as to generate desired harmonic currents at 3rd, 5th, and 7th line frequencies; and Figure 8.22 (b) shows the frequency-domain components according to one of the three-phase currents.

System test under distorted grid conditions

Next, the entire system was tested with a distorted grid having a voltage THD around 6.7%. As shown in Fig. 8.23 (a), the distorted voltage involves 5% of 3rd harmonic, 4% of 5th harmonic, and 2% of 7th harmonic. The output voltages of the parallel converter together with one phase current of the local loads are given in Fig. 8.23 (b), showing good voltage quality. The series converter therefore injects quite distorted voltages, as shown in Fig. 8.23 (c), in order to deliver balanced and sinusoidal grid currents. The resulting grid currents are shown in Fig. 8.23 (d), with a THD about 3.5%.

System test under unbalanced voltage dips

Finally, the entire system was tested with unbalanced voltage dips. As shown in Fig. 8.24 (a), starting from a balanced grid condition, the voltages of phase a and b dip to 80%. In Fig. 8.24 (b), it is shown that the output voltages of the parallel converter are very stable and are kept balanced and sinusoidal. The series converter therefore immediately injects unbalanced voltages after voltage dips, as shown in Fig. 8.24 (c), so as to protect the local system from the grid distrubances and to maintain constant active power delivery to the grid (Fig. 8.24 (d)).

It is noticed that the grid currents are reasonable in quality but still have slight distortion after the transient voltage dips. As also explained in Chapter 6, balanced currents together with unbalanced voltages will generate low-order power ripple on the dc side; and the resulting dc-voltage variations then reflect to the ac side and introduce low-order harmonics on the grid currents. The grid current can be improved by applying the proposed power control strategies in Chapter 6 so as to eliminate the power ripple or by adding a conventional dc-link control loop to the system, but this will not be further discussed here.

8.8   Conclusions

This chapter has introduced system-level concepts and implementation aspects aiming at voltage quality enhancement at both the grid side and the user side. A group of series-parallel grid-interfacing system topologies have been proposed. They are suitable for DG applications, voltage quality improvement, and power transfer. With the reconfigurable functionalities, the proposed systems have been compared with conventional series-parallel systems and shunt-connected systems, showing flexible applicability.

To specify the proposed concepts and system control, a laboratory set-up, which consists of two three-phase four-leg converters, a distributed source, a set of nonlinear loads, and a grid emulator, has been designed. By defining multi-level
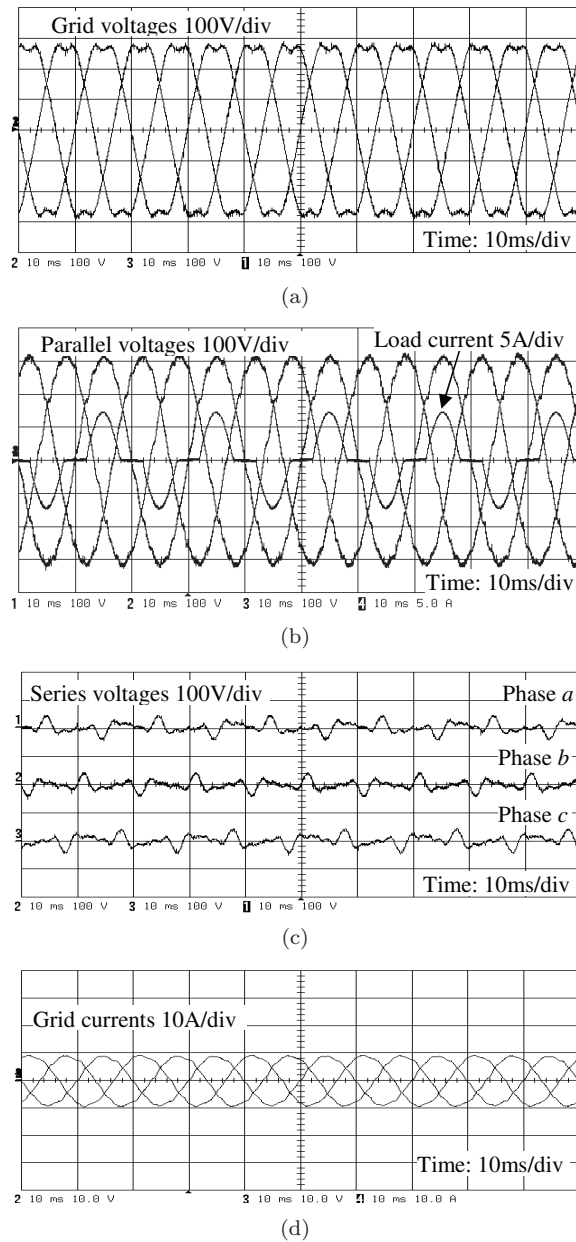
Figure 8.23: Experimental results of the series-parallel system under a distorted grid: (a) grid voltages, (b) output voltages of the parallel converter and one phase of the load currents, (c) output voltages of the series converter, and (d) currents delivered from the system to the grid.
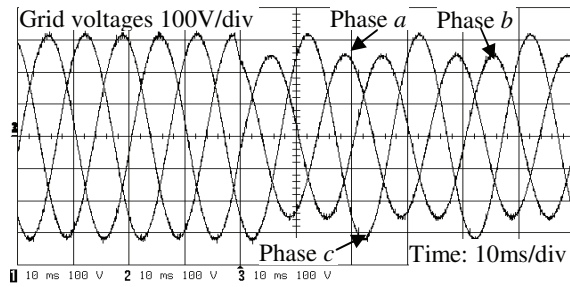
(a)
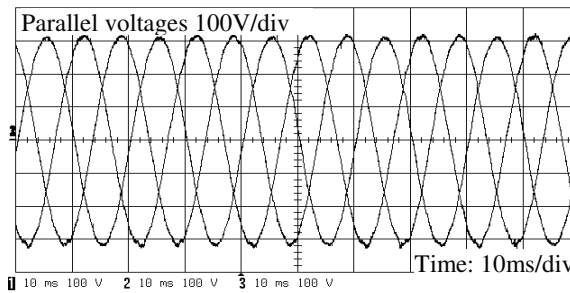
(b)
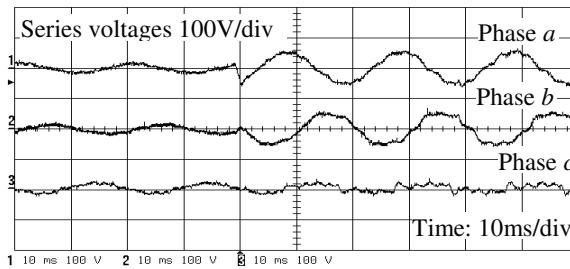
(c)
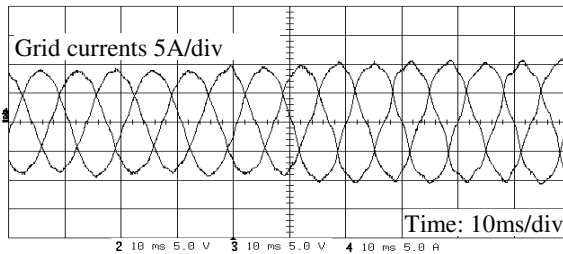
(d)

Figure 8.24: Experimental results of the series-parallel system under unbalanced voltage dips: (a) grid voltages, (b) output voltages of the parallel converter, (c) output voltages of the series converter, and (d) currents delivered from the system to the grid.

control objectives for the system module, it has been shown that the proposed system can ride through grid disturbances, maintain good-quality voltage and achieve flexible power control. Also, the possibilities to integrate auxiliary functions like grid unbalance correction and harmonic current compensation into the system have been detailed.

Finally, the entire control design of the series and parallel converters have been presented, where the main design aspects of the controllers have been highlighted. The proposed methods have been verified by comprehensive experimental tests on the laboratory setup.

Considering both the system concepts and practical implementation and either large-scale networks or distributed micro-grids, this chapter has shown the applicability and feasibility of the proposed system for voltage quality enhancement and DG applications. As bottom-up solutions they are becoming promising tools to facilitate the integration of distributed generation into the future distribution network.

Part V

Closing

Chapter 9

Conclusions and recommendations

This thesis has investigated the flexible operation of grid-interfacing converters in distribution networks, ending up with a grid-interfacing system that optimally combines the functions of voltage quality enhancement and fitting in of distributed generation. From the low-level power electronics control, through the realization of individual system functionality, and arriving at system-level concepts and implementation, the research has been carried out in a bottom-up fashion.

Being essential for the control of grid-interfacing converters, both stationary-frame filtering techniques for voltage detection and synchronization in disturbed grids, and multiple reference frame current regulation have been explored and experimentally verified. These fundamental control methods facilitate the control design of grid-interfacing converters under various grid conditions.

Grid-interactive control of distributed generation systems, i.e. distributed voltage unbalance compensation, grid-fault ride-through control and flexible power delivery, as well as the modeling of harmonic interaction has been investigated. The in-depth study and analysis of these grid interactions have shown the grid-support possibilities and potential negative impact on the grid of inverter-based distributed generation units, beyond their primary goal of power delivery.

Through integrating these proposed control strategies, a couple of grid-interfacing system topologies have been proposed for the purpose of DG application, voltage quality enhancement, and flexible power transfer. A dual-converter laboratory setup has been built, with which the proposed concepts and practical implementation therefore have been fully demonstrated.

The conclusions are grouped according to objectives formulated in Chapter 1. Finally, thesis contributions as well as the recommendations for future development are given.

9.1   Low-level control of grid-interfacing converters

Voltage detection and synchronization in disturbed grids

A group of high performance filters for the detection of fundamental positive sequence, negative sequence, and harmonics under a variety of grid conditions have been proposed. The basic filter cell has been demonstrated to be equivalent to a band-pass filter in the stationary frame, which can be easily implemented based on a multi-state-variable structure. The signal decomposition theory of unbalanced/distorted grid voltages has also been detailed. Experimental results have shown the high-performance operation of the filters in disturbed grids.

On the basis of the filter cell, a couple of cascaded filters have been developed to achieve high performance under unbalanced and distorted grids. Detailed analysis has shown the robustness of the proposed filters to small grid-frequency variations. For large grid-frequency changes, an extra phase-locked loop has been added to improve the frequency adaptivity of the filter cell. Considering a single-phase system to be an extremely unbalanced three-phase system, obviously the filter is also effective for single-phase application.

Investigations of the digital implementation have shown that the proposed filters are accurate for detecting fundamental and low-order harmonics components, which are essential in the control of grid-interfacing converters. However, applying these filters for high-order harmonics, further improvements could be carried out by raising the sampling frequency appropriately or by investigating other digital implementation methods.

Stationary-frame current regulation

Different from conventional three-phase balanced systems, in order to achieve flexible operation of grid-interfacing converters in disturbed grids, their controllers should be able to deal with individual symmetrical sequence components. Based on the modeling of a four-leg grid-connected system in different reference frames, three types of linear controllers, i.e. PI, proportional resonant (PR) and sequence-decoupled resonant (SDR) controllers, have been compared.

The comparison has shown that resonant-type controllers (PR and SDR) are preferred because of their simplicity and flexible control capability. Specifically, stationary-frame PR controllers are suitable for regulating positive- and negative-sequence quantities together but independently for regulating zero-sequence quantities. The proposed SDR controller is able to achieve individual positive- or negative-sequence control. Both SDR and PR controllers have been applied and compared in practical systems. It has been shown that the proportional plus positive-negative sequence-decoupled resonant (PNSDR) controller actually is equivalent to PR control but provides the possibility to assign different gains for positive and negative sequences. The balanced current control scheme based on the proportional plus positive sequence-decoupled resonant (PSDR) controller, and the negative-sequence current elimination based on the proportional plus negative sequence-decoupled resonant (NSDR) controller, proved to be simple solutions in the stationary frame for individual sequence control.

9.2 Grid interaction of distributed power generation

Distributed compensation of voltage unbalance

Two control schemes that rely on inverter-based distributed generation, namely voltage unbalance factor based control and negative-sequence admittance control, have been proposed for the compensation of grid voltage unbalance. The principles of both control schemes are the same, i.e, the negative-sequence voltages at the grid connection point are compensated and mitigated by regulating the negative-sequence currents flowing between grid-interfacing converters and the grid.

The first control scheme is dependent on the voltage unbalance factor and the positive-sequence current delivered by DG inverters to the grid in the normal condition. When the grid is unbalanced, the DG inverters draw a small amount of negative-sequence currents from the grid based on the voltage unbalance factor at the PoC, thereby correcting the negative-sequence voltages. The unbalanced voltages at the PoC tend to be eliminated by the collective action of multiple DG modules equipped with the same compensation schemes. The effect of this control scheme has been verified by simulations and experimental results.

However, due to the coupling between the negative-sequence and the positive-sequence currents of DG systems, there are limitations for the first control scheme. To overcome this drawback, the negative-sequence compensating currents can be regulated independently by controlling the negative-sequence admittance of the DG inverter. Modeling, analysis and simulations have shown the effectiveness of the second control scheme. With this scheme, distributed DG systems can automatically achieve a co-operative compensation for the unbalanced grid voltages or unbalanced loads in proportion to their specified current rating.

Flexible power control under grid faults

Independent active and reactive power control of grid-interfacing converters operating under unbalanced voltage dips has been proposed. By changing adaptable weighting factors for the compensation of oscillating power and for the regulation of three-phase grid currents, the proposed strategies enable DG systems to be optimally controlled and flexibly adapted to all possible requirements for grid voltage support. Furthermore, for simultaneous control of active and reactive power, two joint strategies have been proposed, yielding adaptive controllability that can cope with multiple constraints in practical applications. An application case showed the simplicity and adaptivity of the proposed ideas.

Based on derived formulas and graphic representations, the contribution of symmetric-sequence components to the instantaneous power and the interaction between symmetric sequences has been explained in detail. By intentionally introducing an adjustable parameter in between the reference currents and the grid voltages, the proposed strategy has been found able to control the dc-link ripple, and to impact the symmetry of currents or the power factor in terms of controllable oscillating active and reactive powers.

The contribution of zero-sequence currents to active power control, which has not yet received attention in the literature, has also been studied. A technically

effective control method has been proposed for eliminating second-order power ripple by including fundamental zero-sequence components. However, it is worth noticing that a serious phase unbalance and a large amplitude increase appear in the currents while using zero-sequence components.

Modeling and analysis of harmonic interaction

An analytical approach for the analysis of harmonic interaction between aggregated DG inverters and the grid has been introduced. To analyze the harmonic distortion impact of an individual inverter in a distorted grid, a method based on the inverter output impedance has been proposed. By modeling the output impedance of two inverters, one with single-loop PI control and another with dual-loop multiple PR controllers, their harmonic interactions with a distorted grid could be analyzed. In order to mitigate the harmonic distortion in a polluted grid, the concept of output impedance limits has been proposed as a constraint on the design of grid-interfacing converters.

The aforementioned output impedance based method has been extended to analyze aggregated inverters. Results obtained from modeling, analysis and simulations have shown that the proposed method is a simple and effective way for estimating harmonic quasi-resonance problems.

It is suggested that experiments are carried out to further examine the effectiveness and accuracy of the proposed method. Besides, as the output impedance modeling has only been investigated based on inverters with linear controllers, further study on nonlinear control based inverters could be done by using the proposed analytical approach.

9.3   System modules with enhanced voltage quality

Aiming for voltage quality enhancement at both the grid and user sides, system-level concepts and implementation aspects have been studied. A group of series-parallel grid-interfacing system topologies have been proposed by adapting the conventional series-parallel structure, which is suitable for DG applications, voltage quality improvement, and power transfer. With this reconfigurable functionality, the proposed systems have been compared with conventional series-parallel systems and shunt-connected systems.

Experiments with a concrete laboratory system have been given to detail the proposed concepts and to demonstrate the practical implementation. The introduction of multi-level control objectives has illustrated that the proposed system can ride through voltage disturbances and continue the power transfer to/from the grid, while a high quality voltage is maintained for the local loads within the system module. In addition, auxiliary functions such as grid unbalance correction and harmonic current compensation at the grid connection point have also been investigated.

The achieved results shows the applicability and feasibility of the proposed systems for voltage quality enhancement and DG applications. They are promising

tools to facilitate the integration of distributed generation into the future distribution networks.

9.4   Realization of a laboratory set-up

To specify the proposed concepts and system control, a laboratory set-up, which consists of two three-phase four-leg converters, a distributed source, a set of nonlinear loads, and a grid emulator, has been designed. The proposed voltage detection and synchronization technique has been used for the series- and parallel converters to determine the fundamental positive-, negative-sequence voltages and the grid frequency. A voltage unbalance correction scheme and power control strategies, as well as an active filter function have been integrated into the series converter.

System stability improvement at no-load conditions, selective harmonic regulation, and disturbance sensitivity improvement have been considered for improving the performance of the parallel converter. For the series converter, the LCL-filter, a third-order system, can bring instability problems due to its resonance behavior. In order to improve the system stability and to facilitate the compensator design at low-order harmonic frequencies, a unique method has been adopted that uses the combination of the filtering-inductor current and the grid-side current as the feedback-control variable so as to degrade the third-order system to a first-order one.

All the proposed concepts and methods have been successfully verified by experimental tests on the laboratory system.

9.5   Thesis contributions

The major contributions of this thesis can be summarized as follows:

- *High performance stationary-frame filters for the detection of symmetrical sequences and harmonics under various grid conditions.* Most of previously presented approaches are either not suitable for various grid conditions or can not be implemented in the stationary frame, or require intensive calculations. A group of methods proposed in this thesis gives an alternative and improved solution in the stationary frame, and is essential for the control of grid-interfacing converters in disturbed grids.

- *Sequence-decoupled resonant controllers for regulating individual positive- or negative-sequence components in the stationary frame.* Conventional linear controllers cannot separately regulate symmetrical sequences in the stationary frame. The proposed controllers offer grid-interfacing converters the possibility to regulate individual symmetrical sequences in the stationary frame.

- *Control schemes for distributed voltage unbalance compensation.* Grid support with DG systems has not yet received enough attention up to now, and most existing solutions are not designed to cope with DG systems. Two

strategies, a voltage unbalance factor based control scheme and an unbalanced current sharing scheme, are proposed in this thesis. They achieve voltage unbalance compensation while relying on inverter-based DG.

- *Flexible active and reactive power control strategies for grid-interfacing converters during voltage dips.* Many power control strategies proposed for power converters under unbalanced grid conditions mainly focus on eliminating dc-bus voltage ripple or specific optimal objectives. In this thesis, the proposed strategies enable DG systems to be optimally controlled and flexibly adapted to all possible requirements for grid voltage support.

- *The modeling and analysis of harmonic interactions between the grid and aggregated DG inverters.* Specific modeling and analysis of harmonic interaction has not been fully explored in the literature. The proposed analytical approach in this thesis helps understand how to mitigate the harmonic distortion impact of an individual inverter in a distorted grid, and can also be used to estimate harmonic quasi-resonance problems in a grid connected to multiple DG inverters.

- *Experimental verification of a series-parallel grid-interfacing system with enhanced voltage quality.* A laboratory set-up has been developed to demonstrate the system-level concept, i.e. a grid-interfacing system cooperating with DGs to achieve voltage quality enhancement at both the grid side and the user side, and to manage flexible power transfer under various grid conditions.

9.6   Recommendations

Based on the results that have been presented in this thesis, the following recommendations for future development can be given.

- **Grid-impedance adaptive control**

  In the thesis, both the control schemes for voltage unbalance compensation and the control of the series converter in the final laboratory system needed the information of grid impedance, which was assumed to be known. Therefore, a mechanism to update the information of the grid-impedance for the controller should be added so that the designed system can adapt to different grid impedances.

- **Applying flexible power control to practical DG systems**

  To improve the grid-fault ride-through capability of DG systems during unbalanced voltage dips, flexible power control strategies have been proposed. Although comprehensive objective-oriented analysis as well as one application case with adaptive power control have been used to show the promising applicability of the power control strategies, more practical DG systems such as wind turbines or photovoltaic inverters could be used to examine and further develop the proposed strategies for specific applications.

- **Harmonic interaction analysis with more nonlinear models**

  The modeling and analysis of harmonic interactions of aggregated DG inverters gave an insight into the distortion impact of DG inverters in distorted grids. Still, the analysis is not comprehensive due to missing models of specific nonlinear loads. Especially for a existing distribution network, there are many power electronic based nonlinear loads. To make one further step, the harmonic interaction analysis can be extended by involving more nonlinear models so as to give more accurate estimation of the potential harmonic interaction problems.

- **Connection of a micro-grid to the utility grid**

  This thesis focused on a grid-interfacing laboratory system consisting of one parallel converter and one series converter, but the application of connecting a micro-grid to the utility grid with the grid-interfacing system has also been introduced. As a future development of the current laboratory system, a micro-grid can be constructed by adding more parallel converters and implementing a parallel operation control scheme. A grid-interfacing system can then be developed for connecting a micro-grid to the utility grid.

- **Laboratory research set-up for smart grids**

  With the emerging application of DG and the increasing interest on the concept "smart-grid", a future research tendency is the bottom-up application of power electronic converters in a smart-grid, i.e. power conversion from renewable energy to electricity and bi-directional power transfer between two power supply systems. Hence, following the previous recommendation "connection of a micro-grid to the utility grid", a second small-scale micro-grid can be developed and connected to the utility grid or the other micro-grid, thereby forming a laboratory research set-up for such a smart grid.

Part VI

Appendices

Appendix A

Derivation of decoupling transformation matrix

The matrix for decoupling transformation from phase quantities in abc-frame to orthogonal quantities in $\alpha\beta\gamma$-frame is derived in the following. With the decoupling transformation, it is able to command four modulation indices (named $m_{a,b,c,n}$) to the switching legs of four-leg PWM converters based on independent control of three modulation indices in the $\alpha\beta\gamma$-frame, namely $m_{\alpha,\beta,\gamma}$.

It is known that with the additional degree of freedom brought by the fourth leg of four-leg converter it is able to produce independent three-phase output voltages. By means of high frequency PWM control, then the three-phase converter output voltages are in proportional to three modulation indices $m_{an,bn,cn}$ in an average sense of each PWM period (see Section 3.3). However, independent control of these three modulation indices cannot be directly achieved in abc frame due to the coupling through neutral-leg modulation index m_n, as expressed by

$$
\begin{bmatrix} m_{an} \\ m_{bn} \\ m_{cn} \end{bmatrix} = \begin{bmatrix} m_a - m_n \\ m_b - m_n \\ m_c - m_n \end{bmatrix} = \begin{bmatrix} 1 & 0 & 0 & -1 \\ 0 & 1 & 0 & -1 \\ 0 & 0 & 1 & -1 \end{bmatrix} \begin{bmatrix} m_a \\ m_b \\ m_c \\ m_n \end{bmatrix}. \tag{A.1}
$$

Similar coupling exists in physical systems for other phase quantities like voltages and currents. Hence, a transformation matrix is required for decoupling these quantities.

Note that a four-leg converter reduces to be a three-leg converter when the average output of neutral leg is zero, ie. in (A.1) $m_n = 0$. Therefore, the expecting matrix should keep the conventional transformation (Clarke transformation) matrix used for α- and β-axis quantities in three-wire systems. Following that, we expect to have

$$\begin{bmatrix} m_\alpha \\ m_\beta \\ m_\gamma \end{bmatrix} = \sqrt{\frac{2}{3}} \begin{bmatrix} 1 & -1/2 & -1/2 \\ 0 & \sqrt{3}/2 & -\sqrt{3}/2 \\ y & y & y \end{bmatrix} \begin{bmatrix} m_{an} \\ m_{bn} \\ m_{cn} \end{bmatrix} \tag{A.2}$$

$$= \sqrt{\frac{2}{3}} \begin{bmatrix} 1 & -1/2 & -1/2 & 0 \\ 0 & \sqrt{3}/2 & -\sqrt{3}/2 & 0 \\ y & y & y & -3y \end{bmatrix} \begin{bmatrix} m_a \\ m_b \\ m_c \\ m_n \end{bmatrix}, \tag{A.3}$$

where y represents a value we are looking for in the following. The three constants in the third row of the matrix are given the same value y is to make γ-axis quantity only related to zero-sequence components (see section 2.2.3). Name the transformation matrix $\boldsymbol{T}_{\alpha\beta\gamma1}$, (A.3) is rewritten as

$$\begin{bmatrix} m_\alpha \\ m_\beta \\ m_\gamma \end{bmatrix} = \boldsymbol{T}_{\alpha\beta\gamma1} \begin{bmatrix} m_a \\ m_b \\ m_c \\ m_n \end{bmatrix} \tag{A.4}$$

and analogous to inverse Clarke transformation the desired inverse transformation could be also a transposed matrix of $\boldsymbol{T}_{\alpha\beta\gamma1}$, as given by

$$\begin{bmatrix} m_a \\ m_b \\ m_c \\ m_n \end{bmatrix} = \boldsymbol{T}_{\alpha\beta\gamma1}^{-1} \begin{bmatrix} m_\alpha \\ m_\beta \\ m_\gamma \end{bmatrix}, \tag{A.5}$$

with

$$\boldsymbol{T}_{\alpha\beta\gamma1}^{-1} = \sqrt{\frac{2}{3}} \begin{bmatrix} 1 & 0 & y \\ -1/2 & \sqrt{3}/2 & y \\ -1/2 & -\sqrt{3}/2 & y \\ 0 & 0 & -3y \end{bmatrix}. \tag{A.6}$$

Hence, we do not need to find a place-holder term so that the above transformation matrices can be square ones. Substituting (A.5) to (A.4) derives

$$\begin{bmatrix} m_\alpha \\ m_\beta \\ m_\gamma \end{bmatrix} = \boldsymbol{T}_{\alpha\beta\gamma1} \boldsymbol{T}_{\alpha\beta\gamma1}^{-1} \begin{bmatrix} m_\alpha \\ m_\beta \\ m_\gamma \end{bmatrix} \tag{A.7}$$

$$= \begin{bmatrix} 1 & 0 & 0 \\ 0 & 1 & 0 \\ 0 & 0 & 8y^2 \end{bmatrix} \begin{bmatrix} m_\alpha \\ m_\beta \\ m_\gamma \end{bmatrix}. \tag{A.8}$$

Apparently, by setting $y = 1/\sqrt{8}$, we derive the desired matrix for decoupling transformation from four output modulation indices $m_{a,b,c,n}$ to three independent control variables $m_{\alpha,\beta,\gamma}$. Note that the value of y differs from the corresponding constants in $\boldsymbol{T}_{\alpha\beta\gamma}$ of (2.10), where y equals -1/2 for getting amplitude-invariant

transformation between the zero-sequence component and the γ-axis component. The derived decoupling transformation and inverse transformation matrices are rewritten as

$$\boldsymbol{T}_{\alpha\beta\gamma 1} = \sqrt{\frac{2}{3}} \begin{bmatrix} 1 & -1/2 & -1/2 & 0 \\ 0 & \sqrt{3}/2 & -\sqrt{3}/2 & 0 \\ 1/\sqrt{8} & 1/\sqrt{8} & 1/\sqrt{8} & -3/\sqrt{8} \end{bmatrix}, \qquad (A.9)$$

$$\boldsymbol{T}_{\alpha\beta\gamma 1}^{-1} = \sqrt{\frac{2}{3}} \begin{bmatrix} 1 & 0 & 1/\sqrt{8} \\ -1/2 & \sqrt{3}/2 & 1/\sqrt{8} \\ -1/2 & -\sqrt{3}/2 & 1/\sqrt{8} \\ 0 & 0 & -3/\sqrt{8} \end{bmatrix}. \qquad (A.10)$$

Applying transformation matrix (A.9) to phase currents gives

$$\begin{bmatrix} i_\alpha \\ i_\beta \\ i_\gamma \end{bmatrix} = \boldsymbol{T}_{\alpha\beta\gamma 1} \begin{bmatrix} i_a \\ i_b \\ i_c \\ i_n \end{bmatrix}, \qquad (A.11)$$

where $i_{a,b,c,n}$ are three-phase currents and the neutral current, respectively. For a four-wire system $i_a + i_b + i_c + i_n = 0$, (A.11) can be reduced to

$$\begin{bmatrix} i_\alpha \\ i_\beta \\ i_\gamma \end{bmatrix} = \sqrt{\frac{2}{3}} \begin{bmatrix} 1 & -1/2 & -1/2 \\ 0 & \sqrt{3}/2 & -\sqrt{3}/2 \\ 4/\sqrt{8} & 4/\sqrt{8} & 4/\sqrt{8} \end{bmatrix} \begin{bmatrix} i_a \\ i_b \\ i_c \end{bmatrix}. \qquad (A.12)$$

For phase voltages, there are only three quantities $v_{an,bn,cn}$. The transformation therefore can be expressed as

$$\begin{bmatrix} v_\alpha \\ v_\beta \\ v_\gamma \end{bmatrix} = \boldsymbol{T}_{\alpha\beta\gamma 1} \begin{bmatrix} v_{an} \\ v_{bn} \\ v_{cn} \\ 0 \end{bmatrix}, \qquad (A.13)$$

by filling in a zero as place-holder, or just use the reduced transform in (A.2).

It is commented that there could be many variations of transformation matrices in principle, but the matrix presented here is the only one with its transposed matrix for inverse transformation.

Appendix B

Power calculation of zero-sequence components

The power introduced by zero-sequence components in a three-phase unbalanced system is similar to that in a single-phase system, always including a constant and an oscillating power. Therefore the following method can also be used for single-phase applications. For the zero-sequence components:

$$i^0 = \sqrt{2}I^0 \cos(\omega t + \theta^0), v^0 = \sqrt{2}V^0 \cos(\omega t + \varphi^0), \tag{B.1}$$

where I^0 and θ^0 are the amplitude and phase angle of the current; V^0 and φ^0 are the amplitude and phase angle of the voltage.

The instantaneous power of a three-phase system can be expressed as

$$p^0 = 3v^0 i^0 = \underbrace{3I^0 V^0 \cos(\theta^0 - \varphi^0)}_{P^0} + \underbrace{3I^0 V^0 \cos(2\omega t + \theta^0 + \varphi^0)}_{\tilde{p}^0_{2\omega}}. \tag{B.2}$$

By means of a T/4 delay, two sets of orthogonal signals can be generated, i.e.

$$i^0_\alpha = i^0 = \sqrt{2}I^0 \cos(\omega t + \theta^0), \quad i^0_\beta = \sqrt{2}I^0 \sin(\omega t + \theta^0),$$

$$v^0_\alpha = v^0 = \sqrt{2}V^0 \cos(\omega t + \varphi^0), \quad v^0_\beta = \sqrt{2}V^0 \sin(\omega t + \varphi^0). \tag{B.3}$$

Therefore, the average power P^0 and oscillating component of p^0 can be represented by

$$\tilde{p}^0_{2\omega} = \tfrac{3}{2}(v^0_\alpha i^0_\alpha - v^0_\beta i^0_\beta) = 3I^0 V^0 \cos(2\omega t + \theta^0 + \varphi^0), \tag{B.4}$$

$$P^0 = \tfrac{3}{2}(v^0_\alpha i^0_\alpha + v^0_\beta i^0_\beta) = 3I^0 V^0 \cos(\theta^0 - \varphi^0). \tag{B.5}$$

An orthogonal signal of $\tilde{p}^0_{2\omega}$ is also derived, by shifting signals,

$$\tilde{p}^0_{2\omega\perp} = \tfrac{3}{2}(v^0_\alpha i^0_\beta + v^0_\beta i^0_\alpha) = 3I^0 V^0 \sin(2\omega t + \theta^0 + \varphi^0). \tag{B.6}$$

Rewriting (B.4) and (B.6) in matrix form, we obtain

$$
\begin{bmatrix} \tilde{p}_{2\omega}^0 \\ \tilde{p}_{2\omega\perp}^0 \end{bmatrix} = \frac{3}{2} \begin{bmatrix} v_\alpha^0 & -v_\beta^0 \\ v_\beta^0 & v_\alpha^0 \end{bmatrix} \begin{bmatrix} i_\alpha^0 \\ i_\beta^0 \end{bmatrix}.
\tag{B.7}
$$

The inverse transformation of (B.7) is

$$
\begin{bmatrix} i_\alpha^0 \\ i_\beta^0 \end{bmatrix} = \frac{2/3}{\left(v_\alpha^0\right)^2 + \left(v_\beta^0\right)^2} \begin{bmatrix} v_\alpha^0 & v_\beta^0 \\ -v_\beta^0 & v_\alpha^0 \end{bmatrix} \begin{bmatrix} \tilde{p}_{2\omega}^0 \\ \tilde{p}_{2\omega\perp}^0 \end{bmatrix}.
\tag{B.8}
$$

Appendix C

List of symbols

Symbol	Description	Unit
ω_1	fundamental angular frequency	rad/s
ω_b	stationary-frame filter bandwidth (w.r.t -3dB)	rad/s
ω_c	central frequency	rad/s
ω_{cut}	cut-off frequency of a low-pass filter	rad/s
θ^-	phase angle of neg.-seq. current w.r.t neg.-seq. voltage	degree
θ^{+-}	phase angle of neg.-seq. voltage w.r.t pos.-seq. voltage	degree
φ	power factor angle	degree
τ_i	time constant of integrator	s
B^-	negative-sequence susceptance	S
C	capacitor	F
C_f	filtering capacitor	F
C_{dc}	dc-bus capacitor	F
e	feedback error	-
$\underline{e}_{\alpha\beta}$	complex variable of feedback error in $\alpha\beta$-frame	-
$\underline{E}$	phasor of feedback error signals	-
f_1	fundamental frequency	Hz
f_{sw}	switching frequency	Hz
f_{sp}	sampling frequency	Hz
f_{hp}	high-pass bandwidth	Hz
G	conductance	S
G_{inv}	gain of inverter bridge	-
i	current	A
i_{C_f}	current of the filter capacitor	A
i_f	feedback current	A
i_g	grid current	A
i_{ld}	load current	A
i_L	current of the filtering inductor	A

i_{Lp}	inductor current of the parallel converter	A
i_{Ls}	inductor current of the series converter	A
i_p	current of the parallel converter	A
i_s	current of the series converter	A
$\mathbf{i}$	current vector	A
I	current	A
$\underline{I}$	current phasor	-
I_{eq2}	equivalent current of all sources at bus 2	A
$I_\%$	relative current	-
K_{ff}	feedforward gain	-
K_{fI}	current feedback coefficient	-
K_I	integral gain	-
k_p	coefficient for instantaneous active power control	-
K_P	proportional gain	-
K_{Pin}	inner-loop proportional gain	-
k_q	coefficient for instantaneous reactive power control	-
K_{VUF}	voltage unbalance factor	-
l_{fd}	feeder length	m
L	inductor	H
L_f	filtering inductor	H
L_s	inductor of series converter	H
L_g	grid inductor	H
m	droop coefficient	S/V
$\tilde{p}$	active ripple power	W
p	instantaneous power	W
P	active power	W
q	instantaneous reactive power	Var
Q	reactive power	Var
$\tilde{q}$	reactive ripple power	Var
R	feeder resistance	Ω
R_{C_f}	ESR of the filtering capacitor	Ω
R_{L_f}	ESR of the filtering inductor	Ω
S	apparent power	VA
S_{rat}	rated apparent power	VA
t	time	s
T_N	turns ratio of the series transformer	-
T_s	sampling time	s
$U_\%$	relative voltage	-
V_{cm}	magnitude of the carrier waveform	V
V_{dc}	dc-bus voltage	V
$\triangle V_{dc}$	peak-peak dc voltage variation	V
$\underline{V}_{1\varphi}$	single-phase voltage phasor	V
$\underline{v}$	complex expression of voltage	V
$\underline{V}$	voltage phasor	-
V_o	voltage operating point	-
$\tilde{V}$	small-signal voltage	V

$\mathbf{v}$	voltage vector	V
v	voltage variable	V
$v_{1\varphi}$	single-phase voltage	V
v_C	capacitor voltage	V
v_g	grid voltage	V
v_p	voltage of the parallel converter	V
v_{inv}	output voltage of the inverter bridge	V
v_{par}	parallel voltage	V
v_{ser}	series voltage	V
v_α	alpha-axis component of voltage vector	V
v_β	beta-axis component of voltage vector	V
$\underline{v}_{\alpha\beta}$	complex expression of v_α and v_β	V
v_γ	gamma-axis component of voltage vector	V
w_i	weighting factor for current feedback	-
X	inductive impedance of a feeder	Ω
x	unknown feedback variable	-
y_{nm}	admittance between bus n and bus m	Ω
y_α	alpha-axis control output	-
y_β	beta-axis control output	-
$\underline{y}_{\alpha\beta}$	complex expression of y_α and y_β	-
Y^-	negative-sequence admittance	S
$\underline{Z}$	impedance phasor	-
$\mathbf{Z}$	impedance matrix	Ω
Z	impedance	Ω
Z_C	impedance of a capacitor	Ω
Z_{C_f}	impedance of a filtering capacitor	Ω
Z_{fd}	feeder impedance	Ω
Z_g	grid impedance	Ω
Z_{ld}	load impedance	Ω
Z_L	impedance of an inductor	Ω
Z_{Left2}	equivalent impedance at the left-hand-side of bus 2	Ω
Z_{L_f}	impedance of a filtering inductor	Ω
Z_{Right2}	equivalent impedance at the right-hand-side of bus 2	Ω
$\underline{Z}_g$	grid impedance in form of complex number	-
$|Z_\%|$	magnitude of output harmonic impedance limit	Ω

Operation	Description	
$*$	convolution product	
$\cdot$	dot product	
$\|\cdot\|$	mod of a vector	
a	operator $\mathrm{e}^{j\frac{2\pi}{3}}$	
$\underline{\mathbf{A}}$	symmetric-sequence composition matrix	
$\mathcal{L}[\cdot]$	Laplace transformation	
$\mathbf{R}(\varphi)$	phasor rotating transformation	
$\Re(\cdot)$	real part of a complex number	

$\underline{G}(s)$	complex transfer function of a controller
$G(s)$	transfer function of a controller
$\boldsymbol{T}_{\alpha\beta}$	abc frame to $\alpha\beta$-stationary frame transformation
$\boldsymbol{T}_{\alpha\beta\gamma}$	abc frame to $\alpha\beta\gamma$-stationary frame transformation
$\boldsymbol{T}_{\alpha\beta\gamma 1}$	decoupling transformation matrix for 4-leg inverter
$\boldsymbol{T}_r$	rotating transformation matrix

Subscript	Description
1	fundament component
2ω	twice the grid frequency
α	alpha-axis component in stationary frame
β	beta-axis component in stationary frame
γ	gamma-axis component in stationary frame
a, b, c	phase a, b, and c of three-phase system
d	d-axis component in synchronous frame
in	input
h	harmonics
k	harmonic number
mag	magnitude
max	maximum value
min	minimum value
n	harmonic, bus, or module number; natural line
N	nominal value
o	equivalent output
out	control output
p	active power regulation
pk	peak value
pl	system plant
pq	active and reactive power regulation
q	reactive power regulation
q	q-axis component in synchronous frame
0	zero-axis component in synchronous frame
$\_$	complex number
$\perp$	orthogonal signal

Superscript	Description
$+$	positive sequence
-	negative sequence
0	zero sequence
$\sim$	small-signal disturbances or ripple
$*$	reference signals
o	conjugation

Appendix D

List of acronyms

ac	alternating current
AARC	average active-reactive control
BPS	balanced positive-sequence
CHP	combined heat and power
dc	direct current
DB	deadbeat
DG	distributed generation
D/A	digital to analogue conversion
DSC	delayed signal cancelation
DVR	dynamic voltage restorer
ESR	equivalent series resistor
IGBT	insulated-gate bipolar transistor
KCL	Kirchhoff's current law
MOSFET	metal-oxide-semiconductor field-effect transistor
NSDR	negative-sequence-decoupled resonant
P	proportional
PBC	passivity-based control
PI	proportional and integral
PLL	phase locked loop
PNSC	positive-negative-sequence
PNSDR	positive-negative sequence-decoupled resonant
PoC	point of connection
PR	proportional and resonant
PSDR	positive-sequence-decoupled resonant
PV	photovoltaic
PWM	pulse width modulation
SDR	sequence-decoupled resonant
SOGI	second-order generalized integrators
SRF	synchronous reference frames
SSC	static series compensator

STATCOM	static compensator
THD	total harmonic distortion
UPQC	unified power quality conditioner
VSC	voltage source converters
VUF	voltage unbalance factor

Bibliography

[1] L. Freris and D. Infield, *Renewable energy in power systems.* Wiley, 2008.

[2] T. Ackermann, G. Andersson, and L. Soder, "Distributed generation: a definition," *Electric Power Systems Research*, vol. 57, pp. 195–204, 2001.

[3] S. Cobben, "Power quality implications at the point of connection," Ph.D. dissertation, Eindhoven uinversity of technology, 2007.

[4] R. Cai, "Flicker interaction studies and flicker meter improvement," Ph.D. dissertation, Eindhoven university of technology, 2009.

[5] L. H. Tey, P. L. So, and Y. C. Chu, "Improvement of power quality using adaptive shunt active filter," *IEEE Trans. Power Delivery*, vol. 20, no. 2, pp. 1558–1568, Apr. 2005.

[6] B. Singh, K. Al-Haddad, and A. Chandra, "A review of active filters for power quality improvement," *IEEE Trans. Ind. Electron.*, vol. 46, no. 5, pp. 960–971, Oct. 1999.

[7] P. Salmeron and R. S.Herrera, "Distorted and unbalanced systems compensation within instantaneous reactive power framework," *IEEE Trans. Power Delivery*, vol. 22, no. 3, pp. 1655–1662, Jul. 2006.

[8] D. M. Vilathgamuwa, P. C. Loh, and Y. Li, "Protection of microgrids during utility voltage sags," *IEEE Trans. Ind. Electron.*, vol. 53, no. 5, pp. 1427–1436, Oct. 2006.

[9] M. Bongiorno and J. Svensson, "Voltage dip mitigation using shunt-connected voltage source converter," *IEEE Trans. Power Electron.*, vol. 22, no. 5, pp. 1867–1874, Sep. 2007.

[10] M. Adredes, K. Heumann, and E. Watanabe, "A universal active power line conditioner," *IEEE Trans. Power Delivery*, vol. 13, no. 2, pp. 1581–1590, Apr. 1998.

[11] H. Fujita and H. Akagi, "The unified power quality conditioner: the integration of series- and shunt-active filters," *IEEE Trans. Power Electron.*, vol. 13, no. 2, pp. 315–322, Mar. 1998.

[12] S. Silva, P. Donoso-Garcia, P. Cortizo, and P. Seixas, "A three-phase line-interactive ups system implementation with series-parallel active power-line conditioning capabilities," *IEEE Trans. Ind. Appl.*, vol. 38, no. 6, pp. 1581–1590, Nov./Dec. 2002.

[13] B. Han, B. Bae, H. Kim, and S. Baek, "Combined operation of unified power-quality conditioner with distributed generation," *IEEE Trans. Power Delivery*, vol. 21, no. 1, pp. 330–338, Jan. 2006.

[14] D. Vannoy, M. McGranaghan, M. Halpin, W. Moncrief, and D. Sabin, "Roadmap for power-quality standards development," *IEEE Trans. Ind. Appl.*, vol. 43, no. 2, pp. 412–421, Mar./Apr. 2007.

[15] J. Morren, "Grid support by power electronic converters of distributed generation units," Ph.D. dissertation, Technische Universiteit Delft, 2006.

[16] M. C. Benhabib and S. Saadate, "A new robust experimentally validated phase locked loop for power electronic control," *European Power Electronics and Drives Journal*, vol. 15, no. 3, pp. 36–48, Aug. 2005.

[17] S.-K. Chung, "Phase-locked loop for grid-connected three-phase power conversion systems," *IET Electr. Power Appl.*, vol. 147, no. 3, pp. 213–219, May 2000.

[18] M. Karimi-Ghartemani and M. R. Iravani, "A method for synchronization of power electronic converters in polluted and variable-frequency environments," *IEEE Trans. Power Syst.*, vol. 19, no. 3, pp. 1263–1270, Aug. 2004.

[19] J. Svensson, "Synchronisation methods for grid-connected voltage source converters," *IET Gener. Transm. Distrib.*, vol. 148, no. 3, pp. 229–235, May 2001.

[20] J. Svensson, M. Bongiorno, and A. Sannino, "Practical implementation of delayed dignal cancellation method for phase-sequence separation," *IEEE Trans. Power Del.*, vol. 22, no. 1, pp. 18–26, Jan. 2007.

[21] R. Cutri and L. M. Junior, "A generalized instantaneous method for harmonics, positive and negative sequence detection/extraction," in *Conf. Record IEEE Industry Application Society (IAS) Annu. Meeting*, 2007, pp. 2294–2297.

[22] H. de Souza, F. Bradaschia, F. Neves, M. Cavalcanti, G. Azevedo, and J. de Arruda, "A method for extracting the fundamental-frequency positive-sequence voltage vector based on simple mathematical transformations," *IEEE Trans. Ind. Electron.*, vol. 56, no. 5, pp. 1539–1547, May 2009.

[23] D. Yazdani, M. Mojiri, A. Bakhshai, and G. Joos, "A fast and accurate synchronization technique for extraction of symmetrical components," *IEEE Trans. Power Electron.*, vol. 24, no. 3, pp. 674–684, Mar. 2009.

[24] H. Song and K. Nam, "Dual current control scheme for PWM converter under unbalanced input voltage conditions," *IEEE Trans. Ind. Electron.*, vol. 46, no. 5, pp. 953–959, Oct. 1999.

[25] Y. Suh, V. Tijeras, and T. Lipo, "A nonlinear control of the instantaneous power in dq synchronous frame for PWM AC/DC converter under generalized unbalanced operating conditions," in *Proc. IEEE IAS*, 2002, pp. 1189–1196.

[26] D. N. Zmood and D. G. Holmes, "Improved voltage regulation for current-source inverters," *IEEE Trans. Ind. Appl.*, vol. 37, no. 4, pp. 1028–1036, Jul./Aug. 2001.

[27] R. Bojoi, G. Griva, V. Bostan, M. Guerriero, F. Farina, and F. Profumo, "Current control strategy for power conditioners using sinusoidal signal integrators in synchronous reference frame," *IEEE Trans. Power Electron.*, vol. 20, no. 6, pp. 1402–1412, Nov. 2005.

[28] K. J. P. Macken, K. Vanthournout, J. V. den Keybus, G. Deconinck, and R. J. M. Belmans, "Distributed control of renewable generation units with integrated active filter," *IEEE Trans. Power Electron.*, vol. 19, no. 5, pp. 1353–1360, Sep. 2004.

[29] M. Bollen and A. Sannino, "Voltage control with inverter-based distributed generation," *IEEE Trans. Power Delivery*, vol. 20, no. 1, pp. 519–520, Jan. 2005.

[30] P. Cheng, C. Chen, T. Lee, and S. Kuo, "A cooperative unbalance compensation method for distributed generation interface converters," in *Conf. Record IEEE Industry Application Society (IAS) Annu. Meeting*, 2007, pp. 1567–1573.

[31] Y. Wang, L. Xu, and B. W. Williams, "Control of DFIG-based wind farms for network unbalance compensation," in *Proc. IEEE Power Electronics Specialist Conf. (PESC)*, 2008, pp. 113–119.

[32] *Grid Code for high and extra high voltage.*   E.ON Netz Gmbh, 2006.

[33] *The Grid Code.*   National Grid Electricity Transmission Plc, U.K., 2009.

[34] Y. Suh and T. A. Lipo, "A control scheme in hybrid synchronous-stationary frame for PWM AC/DC converter under generalized unbalanced operating conditions," *IEEE Trans. Ind. Appl.*, vol. 42, no. 3, pp. 825–835, 2006.

[35] B. Yin, R. Oruganti, S. Panda, and A. Bhat, "An output-power-control strategy for a three-phase PWM rectifier under unbalanced supply conditions," *IEEE Trans. Ind. Electron.*, vol. 55, no. 5, pp. 2140–2151, May 2008.

[36] J. Rodriguez, J. Pontt, and C. Silva, "Predictive current control of a voltage source inverter," *IEEE Trans. Ind. Electron.*, vol. 54, no. 01, pp. 495–503, Feb. 2007.

[37] P. Rodriguez, A. Timbus, R. Teodorescu, M. Liserre, and F. Blaabjerg, "Flexible active power control of distributed power generation systems during grid faults," *IEEE Trans. Ind. Electron.*, vol. 54, no. 5, pp. 2583–2592, Oct. 2007.

[38] J. Enslin and P. Heskes, "Harmonic interaction between a large number of distributed power inverters and the distribution network," *IEEE Trans. Power Electron.*, vol. 19, no. 6, pp. 1586–1593, Nov. 2004.

[39] P. Heskes and J. Duarte, "Harmonic reduction as ancillary service by inverters for distributed energy resources (DER) in electricity distribution networks," in *Proc. CIRED*, 2007, pp. 1–4.

[40] M. Benhabib, P. Wilczek, J. Myrzik, and J. Duarte, "Harmonic interactions and resonance problems in large scale networks," in *Proc. Power Systems Computation Conference*, 2008, pp. 1–8.

[41] Y. Li, D. M. Vilathgamuwa, and P. Loh, "A grid-interfacing power quality compensator for three-phase three-wire microgrid applications," *IEEE Trans. Power Electron.*, vol. 21, no. 4, pp. 1021–1031, Jul. 2006.

[42] ——, "Microgrid power quality enhancement using a three-phase four-wire grid-interfacing compensator," *IEEE Trans. Ind. Appl.*, vol. 41, no. 6, pp. 1707–1719, Jul. 2005.

[43] X. Yu and A. M. Khambadkone, "Combined active and reactive power control of power converter building block to facilitate the connection of microgrid to electric power system," in *Proc. IEEE Energy Conversion Congress and Exposition (ECCE)*, 2009, pp. 1444–1450.

[44] F. Wang, J. Duarte, and M. Hendrix, "Reconfiguring grid-interfacing converters for power quality improvement," in *Proc. IEEE Benelux Young Researchers Symposium in Electrical Power Engineering*, 2008, pp. 1–6.

[45] P. Mattavelli, "A closed-loop selective harmonic compensation for active filters," *IEEE Trans. Ind. Appl.*, vol. 37, no. 1, pp. 81–89, Jan./Feb. 2001.

[46] M. J. Newman, D. N. Zmood, and D. G. Holmes, "Stationary frame harmonic reference generation for active filter systems," *IEEE Trans. Ind. Appl.*, vol. 38, no. 6, pp. 1591–1599, Nov./Dec. 2002.

[47] V. Khadkikar and A. Chandra, "A novel structure for three-phase four-wire distribution system utilizing unified power quality conditioner (UPQC)," *IEEE Trans. Ind. Appl.*, vol. 45, no. 5, pp. 1897–1902, Sept./Oct. 2009.

[48] P. Rodriguez, J. Pou, J. Bergas, J. I. Candela, R. P. Burgos, and D. Boroyevich, "Decoupled double synchronous reference frame PLL for power converters control," *IEEE Trans. Power Electron.*, vol. 22, no. 2, pp. 584–592, Mar. 2007.

[49] D. N. Zmood, D. G. Holmes, and G. H. Bode, "Frequency-domain analysis of three-phase linear current regulators," *IEEE Trans. Ind. Appl.*, vol. 37, no. 2, pp. 601–610, Mar./Apr. 2001.

[50] X. Yuan, W. Merk, H. Stemmler, and J. Allmeling, "Stationary frame generalized integrators for current control of active power filters with zero steady-state error for current harmonics of concern under unbalanced and distorted operating conditions," *IEEE Trans. Ind. Appl.*, vol. 38, no. 2, pp. 523–532, Mar./Apr. 2002.

[51] P. Rodriguez, R. Teodorescu, I. Candela, A. Timbus, M. Liserre, and F. Blaabjerg, "New positive-sequence voltage detector for grid synchronization of power converters under faulty grid conditions," in *Proc. IEEE Power Electron. Spec. Conf.*, 2006, pp. 1–7.

[52] F. Wang, M. Benhabib, J. Duarte, and M. Hendrix, "High performance stationary frame filters for symmetrical sequences or harmonics separation under a variety of grid conditions," in *Proc. IEEE Applied Power Electronics Conference and Exposition (APEC)*, 2009, pp. 1570–1576.

[53] F. Wang, J. Duarte, and M. Hendrix, "Control of grid-interfacing inverters with integrated voltage unbalance correction," in *Proc. IEEE Power Electron. Spec. Conf. (PESC)*, 2008, pp. 310–316.

[54] ——, "Active and reactive power control schemes for distributed generation systems under voltage dips," in *Proc. IEEE Energy Conversion Congress and Exposition (ECCE)*, 2009, pp. 3564–3571.

[55] P. M. Andersson, *Analysis of faulted power systems*.   IEEE Press, 1995.

[56] *Voltage characteristics of electricity supplied by public distribution systems.* Std. EN 50160.

[57] M. Benhabib, F. Wang, and J. Duarte, "Improved robust phase locked-loop for utility grid applications," in *Proc. 13th European conference on power electronics and applications*, 2009, pp. 1–10.

[58] R. Datta and V. Ranganathan, "Direct power control of grid-connected wound rotor induction machine without rotor position sensors," *IEEE Trans. Power Electron.*, vol. 6, no. 3, pp. 390–399, May 2001.

[59] T. Noguchi, H. Tomiki, S. Kondo, and I. Takahashi, "Direct power control of PWM converter without power-source voltage sensors," *IEEE Trans. Ind. Appl.*, vol. 34, no. 3, pp. 473–479, May/June 1998.

[60] M. P. Kazmierkowski and L. Malesani, "Current control techniques for three-phase voltage-source PWM converters: A survey," *IEEE Trans. Ind. Electron.*, vol. 45, no. 3, pp. 691–703, Oct. 1998.

[61] J. Duarte, A. van Zwam, C. Wijnands, and A. Vandenput, "Reference frames fit for controlling PWM rectifiers," *IEEE Trans. Ind. Electron.*, vol. 46, no. 3, pp. 628–630, June 1999.

[62] S. Banerjee and G. Verghese, *Nonlinear phenomena in power electronics.* IEEE Press, 2001.

[63] H. Komurcugil and O. Kukrer, "Lyapunov-based control for three-phase PWM AC/DC voltage-source converters," *IEEE Trans. Power Electron.*, vol. 13, no. 5, pp. 801–813, Sept. 1998.

[64] D. Holmes and D. Martin, "Implementation of a direct digital predictive current controller for single and three phase voltage source inverters," in *Proc. IEEE IAS*, 1996, pp. 906–913.

[65] A. Timbus, M. Liserre, R. Teodorescu, P. Rodriguez, and F. Blaabjerg, "Evaluation of current controllers for distributed power generation systems," *IEEE Trans. Power Electron.*, vol. 24, no. 3, pp. 654–663, Mar. 2009.

[66] X. Wu, S. Panda, and J. Xu, "Analysis of the instantaneous power flow for three-phase PWM boost rectifier under unbalanced supply voltage conditions," *IEEE Trans. Power Electron.*, vol. 23, no. 4, pp. 1679–1691, July 2008.

[67] D. Zmood and D. Holmes, "Stationary frame current regulation of PWM inverters with zero steady-state error," *IEEE Trans. Power Electron.*, vol. 18, no. 3, pp. 814–822, May 2003.

[68] R. Teodorescu, F. Blaabjerg, M. Liserre, and P. Loh, "Proportional-resonant controllers and filters for grid-connected voltage-source converters," *IEE Proc.-Electr. Power Appl.*, vol. 153, no. 5, pp. 750–762, Sep. 2006.

[69] R. Teodorescu, F. Blaabjerg, M. Liserre, and U. Borup, "A new control structure for grid-connected PV inverters with zero steady-state error and selective harmonic compensation," in *Proc. IEEE Applied Power Electronics Conference and Exposition (APEC)*, 2004, pp. 580–586.

[70] F. Wang, M. Benhabib, J. Duarte, and M. Hendrix, "Sequence-decoupled resonant controller for three-phase grid-connected inverters," in *Proc. IEEE APEC*, 2009, pp. 121–127.

[71] K. Ogata, *Modern control engineering (4th edition).* Prentice Hall, 2002.

[72] C. Lascu, L. Asiminoaei, I. Boldea, and F. Blaabjerg, "High performance current controller for selective harmonic compensation in active power filters," *IEEE Trans. Power Electron.*, vol. 22, no. 5, pp. 1826–1834, Sep. 2007.

[73] M. Liserre, R. Teodorescu, and F. Blaabjer, "Stability of photovoltaic and wind turbine grid-connected inverters for a large set of grid impedance values," *IEEE Trans. Power Electron.*, vol. 21, no. 1, pp. 263–271, Jan. 2006.

[74] M. Ryan, R. D. Doncker, and R. Lorenz, "Decoupled control of a four-leg inverter via a new 4x4 transformation matrix," *IEEE Trans. Power Electron.*, vol. 16, no. 5, pp. 694–611, Sept. 2001.

[75] R. Zhang, V. Prasad, D. Boroyevich, and F. Lee, "Three-dimensional space vector modulation for four-leg voltage-source converters," *IEEE Trans. Power Electron.*, vol. 17, no. 3, pp. 314–325, May 2002.

[76] R. Zhang, *High performance power converter systems for nonlinear and unbalanced load/source.* Virginia Polytechnic Institute and State University, 1998.

[77] M. Ryan, R. Lorenz, and R. D. Doncker, "Modeling of multileg sine-wave inverters: a geometric approach," *IEEE Trans. Ind. Electron.*, vol. 46, no. 6, pp. 1183–1191, Dec. 1999.

[78] D. Holmes, T. Lipo, B. McGrath, and W. Kong, "Optimized design of stationary frame three phase ac current regulators," *IEEE Trans. Power Electron.*, vol. 24, no. 11, pp. 2417–2426, Nov. 2009.

[79] J. Salaet, S. Alepuz, A. Gilabert, and J. Bordonau, "Comparison between two methods of DQ transformation for single phase converters control application to a 3-level boost rectifier," in *Proc. IEEE Power Electron. Spec. Conf.*, 2004, pp. 214–220.

[80] L. Harnefors, "Modeling of three-phase dynamic systems using complex transfer functions and transfer matrices," *IEEE Trans. Ind. Electron.*, vol. 54, no. 4, pp. 2239–2248, Aug. 2007.

[81] F. Blaabjerg, R. Teodorescu, M. Liserre, and A. V. Timbus, "Overview of control and grid synchronization for distributed power generation systems," *IEEE Trans. Ind. Electron.*, vol. 53, no. 5, pp. 1398–1408, Oct. 2006.

[82] E. Twining and D. G. Holmes, "Grid current regulation of a three-phase voltage source inverter with an LCL input filter," *IEEE Trans. Power Electron.*, vol. 18, no. 3, pp. 888–895, May 2003.

[83] A. V. Jouanne and B. Banerjee, "Assessment of voltage unbalance," *IEEE Trans. Power Delivery*, vol. 16, no. 4, pp. 782–790, Oct. 2001.

[84] M. Prodanovic and T. C. Green, "Control and filter design of three-phase inverters for high power quality grid connection," *IEEE Trans. Power Electron.*, vol. 18, no. 1, pp. 373–380, Jan. 2003.

[85] K. K. Sen, "SSSC-static synchronous series compensator theory, modeling, and application," *IEEE Trans. Power Delivery*, vol. 13, no. 1, pp. 241–246, Jan. 1998.

[86] V. B. Bhavaraju and P. N. Enjeti, "An active line conditioner to balance voltages in a three-phase system," *IEEE Trans. Ind. Applicat.*, vol. 32, no. 2, pp. 287–292, Mar./Apr. 1996.

[87] C. Hochgraf and R. H. Lasseter, "Statcom controls for operation with un-balanced voltage," *IEEE Trans. Power Delivery*, vol. 13, no. 2, pp. 538–544, Apr. 1998.

[88] K. Li, J. Liu, Z. Wang, and B. Wei, "Strategies and operating point opti-mization of STATCOM control for voltage unbalance mitigation in three-phase three-wire systems," *IEEE Trans. Power Delivery*, vol. 22, no. 1, pp. 413–422, Jan. 2007.

[89] D. Graovac, V. A. Katic, and A. Rufer, "Power quality problems compensa-tion with universal power quality conditioning system," *IEEE Trans. Power Delivery*, vol. 22, no. 2, pp. 968–976, Apr. 2007.

[90] G. Joos, B.-T. Ooi, D. McGillis, F. D. Galiana, and R. Marceau, "The potential of distributed generation to provide ancillary services," in *Proc. IEEE Power Eng. Soc. Summer Meeting*, June 2000.

[91] F. Provoost, "Intelligent distribution network design," Ph.D. dissertation, Eindhoven university of technology, 2009.

[92] H. Tao, "Integration of sustainable energy sources through power electronic converters in small distributed electricity generation systems," Ph.D. disser-tation, Eindhoven university of technology, 2008.

[93] M. F. McGranaghan, D. R. Mueller, and M. J. Samotyj, "Voltage sags in industrial systems," *IEEE Trans. Ind. Appl.*, vol. 29, no. 2, pp. 397–403, Mar./Apr. 1993.

[94] L. Zhang and M. H. J. Bollen, "Characteristic of voltage dips (sags) in power systems," *IEEE Trans. Power Del.*, vol. 15, no. 2, pp. 827–832, Apr. 2000.

[95] *Guideline for generating plants' connection to and parallel operation with the medium-voltage network.* BDEW, 2008.

[96] A. Sannino, M. Bollen, and J. Svensson, "Voltage tolerance testing of three-phase voltage source converters," *IEEE Trans. Power Delivery*, vol. 20, no. 2, pp. 1633–1639, Apr. 2005.

[97] G. Saccomando and J. Svensson, "Transient operation of grid-connected voltage source under unbalanced voltage conditions," in *Proc. IEEE IAS*, 2001, pp. 2419–2424.

[98] F. A. Magueed, A. Sannino, and J. Svensson, "Transient performance of voltage source converter under unbalanced voltage dips," in *Proc. IEEE Power Electron. Spec. Conf.*, 2004, pp. 1163–1168.

[99] I. Etxeberria-Otadui, U. Viscarret, M. Caballero, A. Rufer, and S. Bacha, "New optimized PWM VSC control structures and strategies under unbal-anced voltage transients," *IEEE Trans. Ind. Electron.*, vol. 54, no. 5, pp. 2902–2914, Oct. 2007.

[100] H. Chong, R. Li, and J. Bumby, "Unbalanced-grid-fault ride-through control for a wind turbine inverter," *IEEE Trans. Ind. Appl.*, vol. 44, no. 3, pp. 845–856, May/Jun. 2008.

[101] H. Akagi, E. H. Watanabe, and M. Aredes, *Instantaneous power theory and applications to power conditioning.* IEEE Press, 2007.

[102] F. Wang, J. Duarte, and M. Hendrix, "Active power control strategies for inverter-based distributed power generation adapted to grid-fault ride-through requirements," in *Proc. EPE*, 2009, pp. 1–10.

[103] F. Peng and J. Lai, "Generalized instantaneous reactive power theory for three-phase power systems," *IEEE Trans. Instrum. Meas.*, vol. 45, no. 1, pp. 293–297, Feb. 1996.

[104] P. Rodriguez, A. V. Timbus, R. Teodorescu, M. Liserre, and F. Blaabjerg, "Reactive power control for improving wind turbine system behavior under grid faults," *IEEE Trans. Power Electron.*, vol. 24, no. 7, pp. 1798–1801, Jul. 2009.

[105] I. Gabe, V. Montagner, and H. Pinheiro, "Design and implementation of a robust current controller for VSI connected to the grid through an lcl filter," *IEEE Trans. Power Electron.*, vol. 24, no. 6, pp. 1444–1452, Jun. 2009.

[106] T. Abeyasekera, C. Johnson, D. Atkinson, and M. Armstrong, "Suppression of line voltage related distortion in current controlled grid connected inverters," *IEEE Trans. Power Electron.*, vol. 20, no. 6, pp. 1393–1402, Nov. 2005.

[107] *Recommended practice for utility interface of photovoltaic (PV) systems.* IEEE Std. 929-2000.

[108] *Recommended practices and requirements for harmonic control in electrical power systems.* IEEE Std. 519-1992.

[109] P. F. Ribeiro, etc. Task Force on Harmonics Modeling, and Simulation, "Guidelines for modeling power electronics in electric power engineering applications," *IEEE Trans. Power Delivery*, vol. 12, no. 1, pp. 505–514, Jan. 1997.

[110] ——, "Test systems for harmonics modeling and simulation," *IEEE Trans. Power Delivery*, vol. 14, no. 2, pp. 579–587, Apr. 1999.

[111] ——, "Modeling devices with nonlinear voltage-current characteristics for harmonic studies," *IEEE Trans. Power Delivery*, vol. 19, no. 4, pp. 1802–1811, Oct. 2004.

[112] ——, "Characteristics and modeling of harmonic sources - power electronic devices," *IEEE Trans. Power Delivery*, vol. 16, no. 4, pp. 791–800, Oct. 2001.

[113] D. Maksimovic, A. Stankovic, V. Thsottuvelil, and G. Verghese, "Modeling and simulation of power electronic converters," *Proc. IEEE*, vol. 89, no. 6, pp. 898–912, Jun. 2001.

[114] R. Erickson and D. Maksimovic, *Fundamentals of power electronics.* Springer Netherlands, 2001.

[115] M. Cespedes and J. Sun, "Renewable energy systems instability involving grid-parallel inverters," in *Proc. IEEE APEC*, 2009, pp. 1971–1977.

[116] J. Sun, "Small-signal methods for AC distributed power systems - a review," *IEEE Trans. Power Electron.*, vol. 24, no. 11, pp. 2545–2554, Nov. 2009.

[117] H. Saadat, *Power system analysis.* McGraw-Hill, 1999.

[118] *IEEE guide for service to equipment sensitive to momentary voltage disturbances.* IEEE Std. 1250-1995.

[119] L. Gyugyi, C. D. Schauder, S. Willams, T. Rietman, D. Torgerson, and A. Edris, "The unified power flow controller: a new approach to power transmission control," *IEEE Trans. Power Delivery*, vol. 10, no. 2, pp. 1085–1093, Apr. 1995.

[120] H. Farhangi, "The path of the smart grid," *IEEE Power and Energy Magazine*, vol. 8, no. 1, pp. 18–28, Jan./Feb. 2010.

[121] J. Guerrero, L. Vicuna, J. Matas, M. Castilla, and J. Miret, "A wireless controller to enhance dynamic performance of parallel inverters in distributed generation systems," *IEEE Trans. Power Electron.*, vol. 19, no. 5, pp. 1205–1213, Sept. 2004.

[122] Y. Li, D. M. Vilathgamuwa, and P. Loh, "Design, analysis, and real-time testing of a controller for multibus microgrid system," *IEEE Trans. Power Electron.*, vol. 19, no. 5, pp. 1195–1204, Sept. 2004.

[123] Y. Li and C.-N. Kao, "An accurate power control strategies for power-electronic-interfaced distributed generation units operating in a low-voltage multibus microgrid," *IEEE Trans. Power Electron.*, vol. 24, no. 12, pp. 2977–2988, Dec. 2009.

[124] P. Loh, M. Newman, D. Zmood, and D. Holmes, "A comparative analysis of multiloop voltage regulation strategies for single and three-phase ups systems," *IEEE Trans. Power Electron.*, vol. 18, no. 5, pp. 1176–1185, Sep. 2003.

[125] P. Loh and D. Holmes, "Analysis of multiloop control strategies for LC/CL/LCL-filtered voltage-source and current-source inverters," *IEEE Trans. Ind. Appl.*, vol. 41, no. 2, pp. 644–654, Mar./Apr. 2005.

[126] G. Shen, D. Xu, C. L, and X. Zhu, "An improved control strategy for grid-connected voltage source inverters with an LCL filter," *IEEE Trans. Power Electron.*, vol. 23, no. 4, pp. 1899–1906, Jul. 2008.

Samenvatting

Door de groeiende toepassing van gedistribueerde generatie (DG) zullen in de nabije toekomst grote aantallen DG systemen elektriciteit gaan leveren aan het openbare net. Deze systemen zijn in het algemeen niet bestand tegen een netonderbreking en ze kunnen mede daardoor ook niet gebruikt worden om ongewenste spanningsfluctuaties te verminderen.

Aan de ene kant zien we een toename in de hoeveelheid gevoelige en kritieke apparatuur bij de klanten, die de energieleverancier noodzaakt een netspanning van hoge kwaliteit af te leveren. Aan de andere kant neemt de aangesloten hoeveelheid ongebalanceerd en niet-lineair materieel, inclusief DG, sterk toe, waardoor de leveringskwaliteit van het distributienetwerk negatief beïnvloed wordt. Met het doel zich aan te passen aan het toekomstige distributienetwerk is de tendens dat netgekoppelde omzetters spanningskwaliteitsverbetering integreren met hun basis DG functionaliteit.

In dit proefschrift onderzoeken we de flexibele inzet van netinteractieve omzetters in distributienetwerken met het doel spanningskwaliteitsverbetering te krijgen aan zowel het net- als de verbruikerskant. Het onderzoek is bottom-up uitgevoerd, van het elementaire begin in de vermogenselektronische regeling, via het realiseren van de specifieke systeemfunctionaliteit, naar uiteindelijk de concepten en implementatie op systeemniveau.

Omdat dit essentieel is voor de regeling van netgekoppelde omzetters onderzoeken we zowel *stationary-frame* technieken voor spanningsdetectie en synchroniseren in vervuilde netten, als ook de asymmetrische stroomregeling. Eerst wordt een groep hoogperformante filters ter detectie van de fundamentele symmetrische sequenties en harmonischen onder diverse netcondities voorgesteld. De robuustheid van de voorgestelde filters voor geringe net-frequentieafwijkingen en hun vermogen zich aan grote frequentieveranderingen aan te passen wordt toegelicht. Daarna wordt bekeken hoe de *multi-reference-frame* stroomregeling overweg kan met ongebalanceerde netcondities. Complementair aan de bestaande proportioneel resonante (PR) regelaars worden, om de individuele symmetrische sequenties te beheersen, sequentieontkoppelde resonante (SDR) regelaars bekeken. Baserend op de modellering van een vierbrug netgekoppeld *multi-reference-frame* systeem zijn drie types regelaar, PI, PR, en proportioneel plus SDR, vergeleken.

Netinteractieve regeling van gedistribueerde energieopwekking is onderzocht op

de punten ongebalanceerde spanningscompensatie, netonderbrekingsgevoeligheid, flexibele vermogensoverdracht, en het modeleren van harmonische interactie. Een gedegen studie en analyse van deze interacties met het net toont aan dat op elektronische omzetters gebaseerde DG eenheden naast hun primaire taak van energielevering het net kunnen ondersteunen, maar ook dat er een potentieel negatieve invloed van hen uit kan gaan.

Voor het bereiken van een coöperatieve spanningsbalancering met gedistribueerde DG systemen zijn twee regelmethodes voorgesteld, namelijk de spanningsonbalansfactor regeling en de negatieve-sequentie admittantie regelaar. De negatieve-sequentie spanningen op het netaansluitpunt kunnen worden gecompenseerd en verbeterd door het regelen van de negatieve-sequentie stromen die tussen het net en de DG omzetters lopen.

Het voorstel is om gedurende kortdurende spanningsdalingen actief en reactief vermogen flexibel te regelen. Dit stelt DG systemen in staat de *ride-through* capaciteit van het net bij kortsluitingen te verhogen en geeft mogelijkheden om snel aan te passen aan de diverse eisen voor netspanningondersteuning. Door adaptieve weegfactoren te veranderen kan oscillerend vermogen gecompenseerd worden en zijn de netstromen eenvoudig beheersbaar. Voor het simultaan regelen van actief en reactief vermogen zijn twee elkaar wederzijds ondersteunende strategieën uitgewerkt, samen in staat tot een adapterende regeling die overweg kan met meervoudige beperkingen in praktische toepassingen. De contributie van nul-sequentie stromen aan actieve vermogensbeheersing is geanalyseerd als een complementaire toevoeging aan de voorgestelde, op positieve- en negatieve-sequentie gestoelde, regeling.

Harmonische interactie tussen DG omzetters en het net is gemodelleerd en geanalyseerd met een op impedanties baserende aanpak. Om de harmonische vervorming in een vervuild net te kunnen onderdrukken is voorgesteld om grenzen voor de uitgangsimpedantie van de DG omzetters te specificeren. De resultaten van modellering, analyse, en simulatie van een distri-butienetwerk met een aantal DG omzetters tonen dat de voorgestelde methode een simpele en effectieve manier is om harmonische quasi-resonante problemen kwantitatief te voorspellen.

Door het integreren van de voorgestelde regelstrategieën in een gemodificeerde conventionele serieparallel structuur komen we tot een groep van netgekoppelde systeemtopologieën die bruikbaar zijn voor DG applicaties, spanningskwaliteitsverbetering, en flexibele vermogensoverdracht. Een concreet laboratoriumsysteem detailleert de voorgestelde concepten en specificeert de praktische problemen die inherent zijn aan het gekozen regelaarontwerp. De introductie van *multi-level* regelaarobjectieven illustreert dat het voorgestelde systeem overweg kan met spanningsfluctuaties, het locale net verbetert, en het vermogenstransfer van en naar het openbare net garandeert terwijl tevens een hoge spanningskwaliteit voor de locale gebruikers in de systeemmodule gewaarborgd blijft. Een laboratoriumopstelling met twee omzetters demonstreert volledig de voorgestelde concepten en de praktische uitvoering daarvan.

Acknowledgements

This thesis would not have been possible without the extraordinary support of a number of people.

First of all, I would like to thank prof. Andé Vandenput, who passed away on 11 January 2008 after an unfortunate illness. I offer my gratitude to him for giving me the great opportunity to do research in the Electromechanics and Power Electronics (EPE) group. It was a short period of time to work together with him, but his carefulness, modesty, and kindness deeply impressed me.

I would also like to thank prof. Elena Lomonova for your support and efforts at the final stage, also the most important stage, of my thesis. Becoming my first promotor and reading my thesis are busy enough; spending plenty of your time on discussing many details to improve my thesis requires the patience of Job. Once again, I am grateful for that.

I want to express my sincere gratitude to my daily supervisor, dr. Jorge Duarte, who has guided and supported me through the past four years in many aspects concerning research and life. Your patience and guidance allowed me enough room to do research in my own way. Your encouragement and valuable suggestions helped me get through the project ahead of schedule. And your endless curiosity to science, nature, and culture has strongly infected me.

Of course, I could not have done this thesis without the full support and guidance of my weekly supervisor, Marcel Hendrix, a senior principal engineer of Philips Lighting. It was you who first interviewed me in Shanghai and accepted me to be a PhD student of our group in 2006. It was you who taught me a lot in both research and technical writing aspects with your patient discussions on the project and careful corrections on my papers. For these, I am very thankful to you.

I am heartily thankful to prof. Xiangning He, the supervisor of my Master thesis in Zhejiang University. Thank you for recommending me to the EPE group, otherwise I would not have been pursuing the PhD degree. And thank you for coming to be present as a committee member in my PhD defense from thousands of kilometers away. In particular, thank you so much for your continuous concern and help in the past years.

Additionally, I would like to show my gratitude to other committee members

Curriculum vitae

Fei Wang was born on November 17th 1981 in Jiangxi, China. He received his BSc degree in Applied Electronics and MSc degree in Power Electronics and Electrical Drives from Zhejiang University (Comprehensive National University in China), in September 2002 and March 2005, respectively. After graduating, he started his industrial career at Philips Lighting Electronics Global Development Center (Shanghai), where he worked on research and development of electronic ballasts for various types of fluorescent lamps with deep dimming level (2005-2006). In January 2007 he started as a PhD student in the group of Electromechanics and Power Electronics (EPE) at the Electrical Engineering department of the Eindhoven University of Technology (TU/e), where he researched into advanced power electronic control and grid-interfacing converter systems that led to this thesis. His research interests include inverter systems, micro-grids, distributed power generation and power quality.